

Todo list

■ Acknowledgements	8
■ write a quick placeholder introduction of a few pages	12
■ Power spectrum introduction – need to take from section above	14
■ C_ℓ stuff	14
■ write intro why relativistic effects important	18
■ remove this fluff, move to intro	22
■ check tidal bias + bias param	25
■ check this table	27
■ check the bias params, and provide expressions	32
■ move figures into section	32
■ leave some points about relativistic effects detect. in P vs B	35
■ expressions	36
■ incorporate appendix properly here	41
■ add the actual bias parans	42
■ add actual figure reference	43
■ YandP discussion	43
■ add actual table ref	43
■ chat about the new correction to the evolution bias, new paper	43
■ rerun figures with the other euclid bias model	44

■ tidy this, or move to dipole?	50
■ reference appendix	56
■ check where to put this	59
■ insert right equation reference	62
■ reference Pnoise figure	63
■ check the kmin labels, renamed one	63
■ reference kf equation	65
■ ref appendix in caption below	65
■ work on deriv here	84
■ fix this derivation garbage and double check	88
■ either ref appendix, or put coeffs here	93

Astronomy Unit
School of Physics and Astronomy
Queen Mary, University of London

Relativistic effects in the galaxy bispectrum

Eline Maaike de Weerd

Supervised by Dr. Chris Clarkson & Dr. Alkistis Pourtsidou

Submitted in partial fulfillment of the requirements of the Degree of
Doctor of Philosophy

Declaration

I, Eline Maaike de Weerd, confirm that the research included within this thesis is my own work or that where it has been carried out in collaboration with, or supported by others, that this is duly acknowledged below and my contribution indicated. Previously published material is also acknowledged below.

I attest that I have exercised reasonable care to ensure that the work is original, and does not to the best of my knowledge break any UK law, infringe any third party's copyright or other Intellectual Property Right, or contain any confidential material.

I accept that the College has the right to use plagiarism detection software to check the electronic version of the thesis.

I confirm that this thesis has not been previously submitted for the award of a degree by this or any other university. The copyright of this thesis rests with the author and no quotation from it or information derived from it may be published without the prior written consent of the author.

Details of collaboration and publications: Part of this work has been done in collaboration with Stefano Camera, Chris Clarkson, Sheean Jolicoeur, Roy Maartens, and Obinna Umeh. It is based on the following publications, all of which I have contributed to:

- The dipole of the galaxy bispectrum
C. Clarkson, E.M. De Weerd, S. Jolicoeur, R. Maartens, O. Umeh
Published: *MNRAS Letters* 486 (2019) L101, arXiv: 1812.09512 [astro-ph.CO]
- Detecting the relativistic galaxy bispectrum
R. Maartens, S. Jolicoeur, O. Umeh, E.M. De Weerd, C. Clarkson, S. Camera
Published: *JCAP*03(2020)065, arXiv: 1911.02398 [astro-ph.CO]

- Multipoles of the relativistic galaxy bispectrum
E.M. De Weerd, C. Clarkson, S. Jolicoeur, R. Maartens, O. Umeh
Published: *JCAP05(2020)018*, arXiv: 1912.11016 [astro-ph.CO]
- Detecting the relativistic bispectrum in 21cm intensity maps
S. Jolicoeur, R. Maartens, E.M. De Weerd, O. Umeh, C. Clarkson, S. Camera
Published: *JCAP06(2021)039*, arXiv: 2009.06197 [astro-ph.CO]
- Local primordial non-Gaussianity in the relativistic galaxy bispectrum
R. Maartens, S. Jolicoeur, O. Umeh, E.M. De Weerd, C. Clarkson
Published: *JCAP04(2021)013*, arXiv: 2011.13660 [astro-ph.CO]

Signature: Eline Maaike de Weerd

Date: xx.xx.2021

Abstract

Next-generation galaxy surveys will provide us with a wealth of high-precision cosmological data. To be able to use this information in an as unbiased manner as possible, theoretical accuracy must match the experimental precision. The three-point function, or bispectrum, is the first of the higher-order statistics beyond the power spectrum, and contains information both complementary and additional to what is contained in the power spectrum.

On large scales, the galaxy bispectrum will be a key probe for measuring primordial non-Gaussianity, improve constraints on cosmological parameters, and hence help discriminate between various models of inflation and other theories of the early universe. On these scales, a variety of relativistic effects come into play once the galaxy number-count fluctuation is projected onto the past light cone. It is important for these effects to be taken into account in our theoretical treatment of the bispectrum, as they will contaminate the primordial non-Gaussian signal and bias measurements.

In this thesis, we review the relativistic projection effects in the galaxy bispectrum, and examine in detail how these relativistic effects contribute to the invariant multipoles of the galaxy bispectrum about the observer's line of sight. The Fourier-space bispectrum is complex, with an imaginary part arising from the relativistic effects only, which generates odd multipoles. This means that detection of this imaginary part is a smoking gun signal of the relativistic contributions, and we show that such a signal is in principle detectable in future surveys, although with a higher signal-to-noise ratio for spectroscopic surveys compared to 21cm intensity mapping surveys. Finally, we include local primordial non-Gaussianity in the theoretical description of the relativistic bispectrum, separating the relativistic corrections from the primordial signal, and use the bispectrum in Fisher matrix forecasts for cosmological parameters.

Abbreviations and conventions

Estuans interius ira vehementi

Acknowledgements

Acknowledgements

Round up the usual suspects

Contents

Todo list	1
Abstract	6
Abbreviations and Conventions	7
Acknowledgements	8
1. Introduction	12
1.1. The standard cosmological model	12
1.2. Formation of structure	12
1.3. Statistics of galaxy clustering	12
1.4. The two-point function	13
1.4.1. The power spectrum	14
1.4.2. The angular power spectrum	14
1.5. The three-point function	15
1.5.1. The matter bispectrum	16
1.5.2. Matter bispectrum in observations	16
1.6. Galaxy bias	17
1.7. Primordial non-Gaussianity	17
2. Relativistic effects	18
2.1. Relativistic effects in LSS	21
2.2. First order in perturbation theory	21
2.3. Second order in perturbation theory	21
2.4. Relativistic contributions to the galaxy power spectrum	21
3. The dipole of the galaxy bispectrum	22
3.1. The dipole	22
3.2. Extracting the dipole	26
3.3. Squeezed, equilateral and flattened limits	28
3.4. The dipole in intensity mapping and galaxy surveys	32
3.5. Conclusions	32
4. Detectability in next-generation galaxy surveys	34
4.1. Detecting the leading-order relativistic signature	34
4.2. Signal-to-Noise	38
4.2.1. Relativistic contributions to the variance	39

Contents

4.2.2. Nonlinear effects	40
4.2.3. Summations over triangles	41
4.3. Next-generation galaxy surveys	42
4.3.1. Evolution bias and magnification bias	43
4.3.2. Relativistic signal-to-noise ratio	46
4.3.3. Inclusion of cosmological parameters	50
4.3.4. Conclusions	52
4.4. 21cm intensity mapping surveys	54
4.4.1. Relativistic effects in the 21cm IM bispectrum	55
4.4.2. Effects of foregrounds	60
4.4.3. Maximum and minimum scales probed	62
4.4.4. Instrumental noise	63
4.4.5. Future 21cm IM surveys	65
4.4.6. Forecasts for the relativistic signal-to-noise ratio	67
4.5. Conclusions	71
5. Higher order relativistic effects in the bispectrum	74
6. Multipoles of the bispectrum	75
6.1. The relativistic bispectrum	75
6.2. Extracting the multipoles	81
6.3. Analysis of the multipoles	93
6.3.1. Co-linear, squeezed and equilateral limits	93
6.3.2. Numerical analysis for next-generation surveys	95
6.4. Conclusion	106
7. Local primordial non-Gaussianity in the bispectrum	108
7.1. Galaxy clustering statistics and primordial non-Gaussianity	109
7.2. Local primordial non-Gaussianity in the galaxy bias	114
7.2.1. First-order bias	115
7.2.2. Second-order bias: Newtonian approximation	117
7.2.3. Second-order bias: relativistic corrections	119
7.2.4. Second-order metric and velocity potentials	121
7.3. Local primordial non-Gaussianity in the relativistic bispectrum	123
7.3.1. Matter bispectrum	123
7.3.2. Observed number density	124
7.3.3. Galaxy bispectrum	126
7.3.4. Numerical examples	129
7.4. Conclusions	133
8. Fisher forecasts	136
9. Summary	137
A. Beta coefficients	138

Contents

B. Beta coefficient tables	141
C. Upsilon coefficients	145
D. Presentation of kernel coefficients	147
E. Squeezed limit of multipoles	154
Bibliography	156
List of Figures	164
List of Tables	168

1. Introduction

Some introduction! General overview of the current observational state of things to make bispectrum work more relevant.

write a quick placeholder introduction
of a few pages

Waffling on about cosmology. What is the point? I am not sure myself. I am pretty sure that most of cosmological research is just solving ‘interesting’ mathematical problems– if interesting at all.

1.1. The standard cosmological model

Introduction to ‘history’ of cosmology. Introduce the standard Λ CDM model which is assumed throughout, etc.

1.2. Formation of structure

Fluctuations in early universe leading to formation of structure?

1.3. Statistics of galaxy clustering

Description of the role of statistics in cosmology

The galaxy bispectrum is the Fourier-space equivalent of the three-point function and is as such the first of the higher-order statistics beyond the power spectrum. Next-generation large scale structure such as Euclid (galaxy) and the SKA (21cm intensity mapping) will rely on a combination of the power spectrum and the bispectrum for high-precision measurements of primordial non-Gaussianity and for improvement of constraints on cosmological parameters. In particular, improvement on constraints on the primordial non-Gaussian parameter f_{NL} will be crucial for

1. Introduction

discrimination between various models of inflation and other theories of the early universe.

As it stands, our current understanding of the universe is that large scale structure of matter is a result of the growth of small primordial fluctuations which have functioned as seeds for structure growth in an otherwise homogeneous universe. These small fluctuations have been amplified by gravitational instability, resulting in the formation of the structure that we know as the cosmic web on cosmological scales. Tests of theories describing these primordial fluctuations are statistical in nature for the following reasons. For one, there is no direct observational access to primordial fluctuations, and additionally, the time-scales required to follow cosmological evolution of systems is much longer than that over which observations are realistically possible. In essence this means that observations on the past lightcone show different objects at different phases of their evolution, and as a result tests of the evolution of large scale structure must be carried out statistically.

A goal of theoretical cosmology is to make statistical predictions which depend on the statistical properties of primordial perturbations, which in turn lead to the formation of large scale structures in the universe. In these models, the observable universe is modelled simply as a stochastic realisation of a statistical ensemble of possibilities. The most widely considered models are based on the inflationary paradigm, and generically give rise to adiabatic Gaussian initial fluctuations. In this case, the origin of stochasticity lies in quantum fluctuations that were generated in the early universe.

1.4. The two-point function

A purely Gaussian field is fully described by the two-point correlation function or power spectrum. The two-point correlation function is defined as the joint ensemble average of the density at two different points \mathbf{x} and $\mathbf{x} + \mathbf{r}$, i.e.

$$\xi(r) = \langle \delta(\mathbf{x})\delta(\mathbf{x} + \mathbf{r}) \rangle, \quad (1.1)$$

which is dependent on the distance r between the two points only, due to statistical homogeneity and isotropy which are assumed throughout. Usually, the density contrast δ is expressed in terms of its Fourier space components, where our Fourier convention is

1. Introduction

$$\delta(\mathbf{x}) = \int \frac{d^3k}{(2\pi)^3} e^{i\mathbf{k}\cdot\mathbf{x}} \delta(\mathbf{k}), \quad (1.2)$$

where $\delta(\mathbf{k})$ are complex random variables. Note that there are generally two Fourier conventions that are used in literature on the galaxy statistics, which lead to a difference of $(2\pi)^3$ in the definition of the power spectrum or two-point function. The other choice of Fourier convention is to reverse where the factor of $(2\pi)^3$ goes in the Fourier transforms, that is, using $f(\mathbf{x}) = \int d^3k e^{i\mathbf{k}\cdot\mathbf{x}} f(\mathbf{k})$ and $f(\mathbf{k}) = \int \frac{d^3x}{(2\pi)^3} e^{-i\mathbf{k}\cdot\mathbf{x}} f(\mathbf{x})$ instead of our convention used here.

Since the density contrast is real, this means that we have

$$\delta(k) = \delta^*(-k). \quad (1.3)$$

Similarly, the correlators can also be computed in Fourier space, as follows,

$$\langle \delta(\mathbf{k})\delta(\mathbf{k}') \rangle = \int d^3x d^3r \langle \delta(\mathbf{x})\delta(\mathbf{x} + \mathbf{r}) \rangle e^{-i(\mathbf{k}+\mathbf{k}')\cdot\mathbf{x}-i\mathbf{k}'\cdot\mathbf{r}}. \quad (1.4)$$

This can be rewritten using the definition of the two-point correlation function as

$$\langle \delta(\mathbf{k})\delta(\mathbf{k}') \rangle = \int d^3x d^3r \xi(r) e^{-i(\mathbf{k}+\mathbf{k}')\cdot\mathbf{x}-i\mathbf{k}'\cdot\mathbf{r}}, \quad (1.5)$$

and, performing one of the integrals,

$$\langle \delta(\mathbf{k})\delta(\mathbf{k}') \rangle = (2\pi)^3 \delta^D(\mathbf{k} + \mathbf{k}') \int d^3r \xi(r) e^{i\mathbf{k}\cdot\mathbf{r}} \quad (1.6)$$

$$\equiv (2\pi)^3 \delta^D(\mathbf{k} + \mathbf{k}') P(k), \quad (1.7)$$

where $P(k)$ is by definition the density power spectrum.

1.4.1. The power spectrum

Power spectrum introduction – need to take from section above

1.4.2. The angular power spectrum

C_ℓ stuff

1.5. The three-point function

Higher-order correlation functions are defined as the connected part of the joint ensemble average of the density in an arbitrary number of locations. In principle it is possible define any order of correlation function like this, but they will rapidly become more computationally complex and expensive. In the case of a purely Gaussian field, the only non-vanishing connected part is the two-point correlation function. This is a direct consequence of Wick's theorem for Gaussian fields, and has a number of important consequences. Firstly it means that a purely Gaussian, statistically homogeneous and isotropic field is fully described by its two-point correlation function or power spectrum, and secondly it means that the statistical properties of any field, which is not necessarily linear, can be written in terms of combinations of two-point correlation functions – as long as the field is built from a Gaussian field δ . In a generic form, Wick's theorem can be expressed as

$$\begin{aligned} \langle \delta(\mathbf{k}_1) \dots \delta(\mathbf{k}_{2p+1}) \rangle &= 0 \\ \langle \delta(\mathbf{k}_1) \dots \delta(\mathbf{k}_{2p}) \rangle &= \sum_{[\text{all distinct pairs}]} \prod_{[p \text{ pairs } (i,j)]} \langle \delta(\mathbf{k}_i) \delta(\mathbf{k}_j) \rangle. \end{aligned} \quad (1.8)$$

More concretely, this means that for a purely Gaussian field, $\langle \delta(\mathbf{k}_1) \delta(\mathbf{k}_2) \delta(\mathbf{k}_3) \rangle = 0$. However, this changes in the presence of any sources of non-linearity. BLAH. An important consequence of non-linear evolution of structure is that the statistics of odd-number density fields are no longer vanishing. The leading odd-number statistic which will be non-zero in the case of non-linear evolution is the three-point correlation function or the bispectrum in Fourier space,

$$\langle \delta(\mathbf{k}_1) \delta(\mathbf{k}_2) \delta(\mathbf{k}_3) \rangle = (2\pi)^3 \delta^D(\mathbf{k}_1 + \mathbf{k}_2 + \mathbf{k}_3) [2F_2(\mathbf{k}_1, \mathbf{k}_2) P_L(\mathbf{k}_1) P_L(\mathbf{k}_2) + \text{2 c.p.}] \quad (1.9)$$

where F_2 is the Fourier space density evolution kernel, P_L is the linear power spectrum from the previous discussion, and redshift dependence is suppressed for brevity.

Some blah blah about higher order statistics and their importance in future surveys (higher precision data, non-Gaussianities in the universe and effects that give rise to nonlinearities)

1. Introduction

1.5.1. The matter bispectrum

The bispectrum is a non-Gaussian statistic, and as such is especially sensitive to any forms of non-linearity in the universe. It is an essential probe for e.g. primordial non-Gaussianity, though there are also other sources of non-Gaussianities in the universe. Primordial non-Gaussianity, which is often parametrised by the non-linear parameter f_{NL} , is predicted by different types of inflation and other theories of the early universe; meaning that improvement of constraints on f_{NL} could help discriminate between these theories and help shed light on the very early universe and the seeds of structure formation.

In this section we will go into more detail as to how various amplitudes and signs of the bispectrum correspond to real-space signatures. The bispectrum in Fourier space forms a closed triangle correlating three different wave-vectors and, unlike the power spectrum or two-point function, is able to correlate different scales. The matter bispectrum is unique from the thus far more well-studied CMB bispectrum in that it is able to form a three-dimensional map of the universe, whereas the cosmic microwave background provides a two-dimensional snapshot of the first light only. It is therefore essential to try and improve the theoretical description of the matter bispectrum if we are to utilise the wealth of information from next-generation high-precision galaxy surveys in as good and as unbiased a manner as possible.

Where the power spectrum is a measure of probability of, e.g. in the case of the galaxy power spectrum, finding galaxies at distance corresponding to separation of points r from each other, the bispectrum similarly maps this to a probability in a three-dimensional equivalent. That is, it can correspond directly to what we know as the cosmic web, and the galaxy or dark matter distributions therein. The bispectrum has degrees of freedom in both modulus of the wavevector i.e. scales of correlation, as well as the shape of the triangle itself. Different triangle shapes correspond to different real-space bispectrum signatures.

Theoretical blah about the matter bispectrum, definitions, showing how various bispectrum signals translate to real space shapes and modulations of signal

1.5.2. Matter bispectrum in observations

Bispectrum in observation – can skip over any CMB and just focus on lss

1. Introduction

1.6. Galaxy bias

(Very) brief overview of the relevant bias

1.7. Primordial non-Gaussianity

Types of primordial non-Gaussianity in the bispectrum, their signatures on various scales, scale dependence it introduces in the clustering bias etc.

cum sit enim proprium
viro sapienti
supra petram ponere
sedem fundamenti
stultus ego comparor
fluvio labenti
sub eodem tramite
nunquam permanenti

2. Relativistic effects

Relativistic effects in galaxy number counts at first and second order

write intro why relativistic effects important

copypastes of old introductions in papers:

The Fourier galaxy bispectrum is complex, with the imaginary part arising from leading-order relativistic corrections, due to Doppler, gravitational redshift and related line-of-sight effects in redshift space. The detection of the imaginary part of the bispectrum is potentially a smoking gun signal of relativistic contributions. Long-mode relativistic effects couple to short-mode Newtonian effects in the galaxy bispectrum, but not in the galaxy power spectrum. This is the basis for detectability of relativistic effects in the bispectrum of a single galaxy survey, whereas the power spectrum requires multiple galaxy surveys to detect the corresponding signal.

The bispectrum of number count fluctuations in redshift space will become an increasingly important complement to the power spectrum in the extraction of cosmological information from galaxy surveys, in the measurement of clustering bias parameters and in the breaking of degeneracies between the clustering amplitude and growth rate. Analysis of the Fourier galaxy bispectrum is already well advanced for existing survey data (e.g Gil-Marín et al. (2017); Sugiyama et al. (2018)) and for mock data of future surveys (e.g. Karagiannis et al. (2018); Yankelevich & Porciani (2019); Oddo et al. (2020); Sugiyama et al. (2020)).

We investigate the detectability of leading-order relativistic effects in the bispectrum of future 21cm intensity mapping surveys. The relativistic signal arises from Doppler and other line-of-sight effects in redshift space. In the power spectrum of a single tracer, these effects are suppressed by a factor \mathcal{H}^2/k^2 . By contrast, in the bispectrum the relativistic signal couples to short-scale modes, leading to an imaginary contribution that scales as \mathcal{H}/k , thus increasing the possibility of detection. Previous work has shown that this relativistic signal is detectable in a Stage IV H α galaxy survey. We show that the signal is also detectable by next-generation 21cm

2. Relativistic effects

intensity maps, but typically with a lower signal-to-noise, due to foreground and telescope beam effects.

Next-generation galaxy surveys will allow for precision measurements of the bispectrum, bringing new information to improve constraints on cosmological parameters and to break some of their degeneracies (see e.g. Scoccimarro (2015); Tellarini et al. (2016); Gil-Marín et al. (2017); Slepian et al. (2017); Gagrani & Samushia (2017); Sugiyama et al. (2018); Desjacques et al. (2018a); Child et al. (2018); Yankelevich & Porciani (2019); Schmit et al. (2019); Di Dio et al. (2019); Gualdi et al. (2019); Sarkar et al. (2019); Chudaykin & Ivanov (2019); Oddo et al. (2020); Sugiyama et al. (2020); Philcox & Eisenstein (2020); Durrer et al. (2020); Montanari & Camera (2021)).

These surveys will typically probe very large volumes in the Universe, including ultra-large scales ($k \lesssim k_{\text{eq}} \sim 0.01 \text{ Mpc}^{-1}$), which facilitates the detection of, or precision constraints on, primordial non-Gaussianity Tellarini et al. (2015); Watkinson et al. (2017); Majumdar et al. (2018); Karagiannis et al. (2018, 2020b); Bharadwaj et al. (2020) and relativistic effects Kehagias et al. (2015); Umeh et al. (2017); Di Dio et al. (2017); Jolicoeur et al. (2017); Bertacca et al. (2018); Jolicoeur et al. (2018); Koyama et al. (2018); Clarkson et al. (2019); Maartens et al. (2020); Jeong & Schmidt (2020).

Redshift-space distortions (RSD) are the dominant observational effect on the number counts or brightness temperature at first and second order in perturbations. There are local relativistic corrections to standard RSD, arising from Doppler and other line-of-sight gradient terms, together with their couplings. In Fourier space, the leading-order corrections scale as $i(\mathcal{H}/k)$. In the tree-level power spectrum of a single tracer, the only nonzero contribution from these Doppler-type effects is from their square, since the power spectrum is necessarily real. As a result, the Doppler-type effects are further suppressed in the auto-power spectrum, scaling as $(\mathcal{H}/k)^2$.

The tree-level bispectrum of a single tracer is not forced to be real and it couples Doppler-type effects with the standard ('Newtonian') density + RSD term. Consequently, the leading-order relativistic contribution to the bispectrum scales as $i(\mathcal{H}/k)$. This means that the leading-order relativistic signal is more detectable in the bispectrum than the power spectrum, for a single tracer. In Fourier space, the dominant relativistic effect is a purely imaginary part of the bispectrum, as shown

2. Relativistic effects

by Clarkson et al. (2019); Maartens et al. (2020). Our previous work Maartens et al. (2020) showed that it is detectable by a Stage IV spectroscopic galaxy survey.

Observations in large scale structure surveys pose a variety of challenges. As opposed to CMB observations, in which in great detail temperature fluctuations can be measured and mapped, LSS surveys have the downside that one observes galaxies and not the underlying density field. Since galaxies are a biased tracer of the underlying density field, this in itself imposes the problem of how galaxy clustering biases measurements. Furthermore, there are various sources of non-linearities in galaxy clustering, which give rise to non-trivial higher order correlations aside from the power spectrum. Where a purely Gaussian field is fully described by the power spectrum, that is, all statistical information about the field is contained therein and odd correlators vanish identically, in the case of non-Gaussianities the three-point correlations and higher are generated and are needed in addition to the power spectrum to describe the field at high enough accuracy.

For a highly non-linear regime it would probably be necessary to turn to full numerical simulations for an analysis, but in the intermediate, weakly non-linear regime, higher order perturbation theory can be used for our analysis. In this chapter I will discuss the relativistic effects on galaxy number counts at first and second order.

In a typical galaxy survey, the observer looks down the past lightcone and observes some number of galaxies dN , which are above some threshold luminosity L , in a redshift interval dz and within an element of solid angle $d\Omega_o$, about direction of observation \mathbf{n} .

The fractional perturbation of observed number counts Δ_g is defined by

$$\frac{dN(z, \mathbf{n}, > \ln L)}{dz d\Omega_o} = \frac{\chi^2(z)}{(1+z)^4 \mathcal{H}(z)} \bar{\mathcal{N}}(z, > \ln L) [1 + \Delta_g(z, \mathbf{n}, > \ln L)], \quad (2.1)$$

where \mathcal{H} is the conformal Hubble rate, χ is the comoving line-of-sight distance, and $\bar{\mathcal{N}}$ is the background magnitude-limited number density of sources. The dependence of Δ_g on $\ln L$ will be suppressed for brevity. Expanding Δ_g up to second order in perturbation theory as follows,

$$\Delta_g(z, \mathbf{n}) = \Delta_g^{(1)}(z, \mathbf{n}) + \frac{1}{2} [\Delta_g^{(2)}(z, \mathbf{n}) - \langle \Delta_g^{(2)}(z, \mathbf{n}) \rangle], \quad (2.2)$$

subtracting off the average value of $\Delta_g^{(2)}$ to ensure that $\langle \Delta_g \rangle = 0$.

2. Relativistic effects

2.1. Relativistic effects in LSS

2.2. First order in perturbation theory

see title

2.3. Second order in perturbation theory

see title again

**2.4. Relativistic contributions to the galaxy
power spectrum**

3. The dipole of the galaxy bispectrum

3.1. The dipole

In this chapter we examine the leading-order relativistic contributions in the galaxy bispectrum, which arise predominantly from RSD and other Doppler-type observational effects. These give rise to corrections at $\mathcal{O}(\mathcal{H}/k)$ in the galaxy bispectrum. Higher order \mathcal{H}/k contributions are, while being subdominant, still present in the galaxy bispectrum; and a full treatment of the bispectrum at all orders can be found from Chapter 5 onwards.

remove this fluff, move to intro

The dominant RSD effect on galaxy number counts at first order is given by $\delta_g(z, \mathbf{k}) = (b_1(z) + f(z)\mu^2)\delta(z, \mathbf{k})$, where $\mu = \mathbf{n} \cdot \frac{\mathbf{k}}{k}$, with \mathbf{n} the line of sight direction, f the growth rate, and b_1 is the linear bias. Henceforth the redshift dependence will be dropped for brevity as we are working at fixed redshift. At leading order, there is a Doppler type correction to this effect (Kaiser, 1987; McDonald, 2009; Challinor & Lewis, 2011) (see also (Raccanelli et al., 2018; Hall & Bonvin, 2017; Abramo & Bertacca, 2017)) proportional to $\mathbf{v} \cdot \mathbf{n}$, where \mathbf{v} is the peculiar velocity:¹

$$\delta_g(\mathbf{x}) = b_1\delta(\mathbf{x}) - \frac{1}{\mathcal{H}}\partial_r(\mathbf{v} \cdot \mathbf{n}) + A\mathbf{v} \cdot \mathbf{n} \rightarrow \quad (3.1)$$

$$\delta_g(\mathbf{k}) = \left(b_1 + f\mu^2 + iA f\mu \frac{\mathcal{H}}{k} \right) \delta(\mathbf{k}), \quad (3.2)$$

where

$$A = b_e + 3\Omega_m/2 - 3 + (2 - 5s)(1 - 1/r\mathcal{H}). \quad (3.3)$$

Here $b_e = \partial(a^3\bar{n}_g)/\partial \ln a$ is the evolution of comoving galaxy number density, $s = -(2/5)\partial \ln \bar{n}_g/\partial \ln L$ is the magnification bias (L is the threshold luminosity), r is the

¹(Challinor & Lewis, 2011) provides the relativistic correction to the coefficient of $\mathbf{v} \cdot \mathbf{n}$ given in (Kaiser, 1987; McDonald, 2009).

3. The dipole of the galaxy bispectrum

comoving radial distance ($\partial_r = \mathbf{n} \cdot \nabla$) and we have assumed a Λ CDM background ($\mathcal{H}'/\mathcal{H}^2 = 1 - 3\Omega_m/2$, where \mathcal{H} is the conformal Hubble rate, a prime is differentiation with respect to conformal time, Ω_m is the evolving density contrast). In the Fourier space expression (3.2) we can read off the relative contribution of each term by how they scale with k : terms like \mathcal{H}/k are suppressed on small scales when $\mathcal{H}/k \ll 1$ but become important around and above the equality scale.

Although the galaxy density contrast (3.2) is complex, the power spectrum of a single tracer is real:

$$\langle \delta_g(\mathbf{k}) \delta_g(-\mathbf{k}) \rangle = \left[(b_1 + f\mu^2)^2 + \left(A f \mu \frac{\mathcal{H}}{k} \right)^2 \right] \langle \delta(\mathbf{k}) \delta(-\mathbf{k}) \rangle,$$

since $\mu_{-\mathbf{k}} = -\mu_{\mathbf{k}}$ enforces a cancellation of the imaginary part, and the RSD contribution is separate from the Doppler term. However, if we consider the cross-power spectrum for *two* matter tracers, this cancellation breaks down, and there is an imaginary part in the cross-power (McDonald, 2009; Bonvin, 2014),

$$P_{g\tilde{g}}(k) = \left\{ \left[(b_1 + f\mu^2)(\tilde{b}_1 + f\mu^2) + A\tilde{A}f^2\mu^2 \frac{\mathcal{H}^2}{k^2} \right] + i f\mu \left[(\tilde{b}_1 + f\mu^2)A - (b_1 + f\mu^2)\tilde{A} \right] \frac{\mathcal{H}}{k} \right\} P(k).$$

While the Doppler contribution to P_g is $\mathcal{O}((\mathcal{H}/k)^2)$, the Doppler contribution to $P_{g\tilde{g}}$ mixes with the density and RSD to give an additional less suppressed part, i.e. $\mathcal{O}(\mathcal{H}/k)$. The nonzero multipoles of P_g are $\ell = 0, 2, 4$, whereas $P_{g\tilde{g}}$ has a nonzero dipole (as well as a smaller octupole). There are also further relativistic corrections to this dipole part of the cross power spectrum (Di Dio & Seljak, 2019).

A natural question is: what about the galaxy bispectrum? In the standard ‘Newtonian’ approximation, with only RSD, the galaxy bispectrum for a single tracer at fixed redshift has no dipole, and only has even multipoles (Scoccimarro et al., 1999; Nan et al., 2018). But with a lightcone corrected galaxy density contrast, the 3-point correlator, even for a *single* tracer, will no longer be an even function of $\mathbf{k}_a \cdot \mathbf{n}$ ($a = 1, 2, 3$). In order to compute the consequent contribution to the galaxy bispectrum, (3.1) is not sufficient: we need its second-order generalisation, $\delta_g \rightarrow \delta_g + \delta_g^{(2)}/2$.

At second order, the Doppler correction in (3.1) generalises to $A \mathbf{v}^{(2)} \cdot \mathbf{n}$, but there are also quadratic coupling terms. The couplings involve not only the Doppler effect, but also radial gradients of the potential (‘gravitational redshift’), volume

3. The dipole of the galaxy bispectrum

distortion effects, and second-order corrections to the density contrast. Most of these contributions are small, but those that scale as $(\mathcal{H}/k)\delta^2$ are not, even on equality scales. Except on super-equality scales we can often neglect any terms $\mathcal{O}((\mathcal{H}/k)^2)$ and higher, which makes the calculation considerably simpler. The treatment of higher-order terms is left to chapter 6.

The leading correction can be extracted from the general expressions that include all relativistic corrections to the Newtonian approximation, as given in Bertacca (2015) (see also Bertacca et al. (2014a); Yoo & Zaldarriaga (2014); Di Dio et al. (2014); Jolicoeur et al. (2017); Di Dio & Seljak (2019)),

$$\begin{aligned}\delta_{gD}^{(2)} = & A \mathbf{v}^{(2)} \cdot \mathbf{n} + 2C(\mathbf{v} \cdot \mathbf{n})\delta + 2\frac{E}{\mathcal{H}}(\mathbf{v} \cdot \mathbf{n})\partial_r(\mathbf{v} \cdot \mathbf{n}) \\ & + 2\frac{b_1}{\mathcal{H}}\phi\partial_r\delta + \frac{2}{\mathcal{H}^2}[\mathbf{v} \cdot \mathbf{n}\partial_r^2\phi - \phi\partial_r^2(\mathbf{v} \cdot \mathbf{n})] - \frac{2}{\mathcal{H}}\partial_r(\mathbf{v} \cdot \mathbf{v}),\end{aligned}\quad (3.4)$$

where ϕ is the gravitational potential, and the coefficients C and E are,

$$C = b_1(A + f) + b'_1/\mathcal{H} + 2(1 - 1/r\mathcal{H})\partial b_1/\partial \ln L, \quad (3.5)$$

and

$$E = 4 - 2A - \frac{3}{2}\Omega_m. \quad (3.6)$$

This is in agreement with the independent re-derivation of the leading correction given in Di Dio & Seljak (2019). We have corrected a typo in the last bracket of line 1 of Eq. (2.15): $-f_{\text{evo}} \rightarrow -2f_{\text{evo}} \equiv -2b_e$. Note that our \mathbf{n} is minus theirs, and they use the convention $\delta_g + \delta_g^{(2)}$. All but one of the contributions to this leading term contain Doppler contributions, so we label these terms with a D subscript. In this sense, they can be thought of as the relativistic correction to redshift space distortions, but their origin is considerably more subtle than in the Newtonian picture (Bertacca et al., 2014a; Di Dio & Seljak, 2019). These relativistic corrections all arise as projections along the line of sight \mathbf{n} . It is this projection that is responsible for the dipole in the observed bispectrum. Beyond these leading terms in (3.4) there are a host of local coupled terms which appear on larger scales.

We follow most work on the Fourier bispectrum and neglect the effect of lensing magnification. This is reasonable for correlations at the same redshift and when using very thin redshift bins allowed by spectroscopic surveys (Di Dio et al., 2019). We also use the standard plane-parallel approximation, which is reasonable on ultra-large scales. However, we note that wide-angle effects in the power spectrum can

3. The dipole of the galaxy bispectrum

be of the same order of magnitude as the Doppler-type effects in certain circumstances (Tansella et al., 2018), and these should be incorporated in a more complete treatment.

The galaxy bispectrum is defined in Fourier space by,

$$B_g(\mathbf{k}_1, \mathbf{k}_2, \mathbf{k}_3) = \mathcal{K}(\mathbf{k}_1)\mathcal{K}(\mathbf{k}_2)\mathcal{K}^{(2)}(\mathbf{k}_1, \mathbf{k}_2, \mathbf{k}_3)P(k_1)P(k_2) + 2 \text{ cyclic permutations.} \quad (3.7)$$

The first-order kernel $\mathcal{K} = \mathcal{K}_{\text{N}} + \mathcal{K}_{\text{D}}$ is given by the term in brackets in (3.2). At second order, $\mathcal{K}^{(2)} = \mathcal{K}_{\text{N}}^{(2)} + \mathcal{K}_{\text{D}}^{(2)}$, where the Newtonian kernel is (Verde et al., 1998)

$$\mathcal{K}_{\text{N}}^{(2)}(\mathbf{k}_1, \mathbf{k}_2, \mathbf{k}_3) = b_2 + b_1 F_2(\mathbf{k}_1, \mathbf{k}_2) + b_s S_2(\mathbf{k}_1, \mathbf{k}_2) + f \mu_3^2 G_2(\mathbf{k}_1, \mathbf{k}_2) + \mathcal{Z}_2(\mathbf{k}_1, \mathbf{k}_2). \quad (3.8)$$

Here $F_2(\mathbf{k}_1, \mathbf{k}_2)$ is the standard Newtonian mode-coupling kernel for ΛCDM (Villa & Rampf, 2016),

$$F_2(a, \mathbf{k}_1, \mathbf{k}_2) = 1 + \frac{F(a)}{D(a)^2} + \left(\frac{k_1}{k_2} + \frac{k_2}{k_1} \right) \mathbf{\hat{k}}_1 \cdot \mathbf{\hat{k}}_2 + \left[1 - \frac{F(a)}{D(a)^2} \right] \left(\mathbf{\hat{k}}_1 \cdot \mathbf{\hat{k}}_2 \right)^2, \quad (3.9)$$

where F is the second-order growth factor. For ΛCDM , the Einstein-De Sitter relation $F/D^2 = 3/7$ is a very good approximation. Using this approximation, F_2 is essentially time-independent. $G_2(\mathbf{k}_1, \mathbf{k}_2, \mathbf{k}_3)$ is the second-order velocity kernel,

$$G_2(a, \mathbf{k}_1, \mathbf{k}_2) = \frac{F'(a)}{D(a)D'(a)} + \left(\frac{k_1}{k_2} + \frac{k_2}{k_1} \right) \mathbf{\hat{k}}_1 \cdot \mathbf{\hat{k}}_2 + \left(2 - \frac{F'(a)}{D(a)D'(a)} \right) \left(\mathbf{\hat{k}}_1 \cdot \mathbf{\hat{k}}_2 \right)^2, \quad (3.10)$$

where, since we use the Einstein-De Sitter approximation $F/D^2 = 3/7$ in F_2 , we have $F'/(DD') = 6/7$ in G_2 . We use a local bias model (Desjacques et al., 2018b), which includes tidal bias kernel

$$S_2(\mathbf{k}_1, \mathbf{k}_2) = (\mathbf{\hat{k}}_1 \cdot \mathbf{\hat{k}}_2)^2 - \frac{1}{3}, \quad (3.11)$$

with tidal bias b_s . Finally, the kernel $\mathcal{Z}_2(\mathbf{k}_1, \mathbf{k}_2)$ incorporates the non-linear Kaiser RSD contribution (Verde et al., 1998; Scoccimarro et al., 1999),

$$\mathcal{Z}_2(\mathbf{k}_1, \mathbf{k}_2) = b_1 f(\mu_1 k_1 + \mu_2 k_2) \left(\frac{\mu_1}{k_1} + \frac{\mu_2}{k_2} \right) + f^2 \frac{\mu_1 \mu_2}{k_1 k_2} (\mu_1 k_1 + \mu_2 k_2)^2. \quad (3.12)$$

[check tidal bias + bias param](#)

3. The dipole of the galaxy bispectrum

The Doppler correction to (3.8) in Fourier space follows from (3.4) (Jolicoeur et al., 2018),

$$\begin{aligned} \mathcal{K}_{\text{D}}^{(2)}(\mathbf{k}_1, \mathbf{k}_2, \mathbf{k}_3) = & i \mathcal{H} \left[-\frac{3}{2} \left(\mu_1 \frac{k_1}{k_2^2} + \mu_2 \frac{k_2}{k_1^2} \right) \Omega_m b_1 + 2\mu_{12} \left(\frac{\mu_1}{k_2} + \frac{\mu_2}{k_1} \right) f^2 \right. \\ & \left(\frac{\mu_1}{k_1} + \frac{\mu_2}{k_2} \right) Cf - \frac{3}{2} \left(\mu_1^3 \frac{k_1}{k_2^2} + \mu_2^3 \frac{k_2}{k_1^2} \right) \Omega_m f \\ & \left. + \mu_1 \mu_2 \left(\frac{\mu_1}{k_2} + \frac{\mu_2}{k_1} \right) \left(\frac{3}{2} \Omega_m - Ef \right) f + \frac{\mu_3}{k_3} G_2(\mathbf{k}_1, \mathbf{k}_2, \mathbf{k}_3) Af \right], \quad (3.13) \end{aligned}$$

where $\mu_{ab} = \hat{\mathbf{k}}_a \cdot \hat{\mathbf{k}}_b$ and $\mu_a = \hat{\mathbf{k}}_a \cdot \mathbf{n}$. The Newtonian kernel (3.8) scales as $(\mathcal{H}/k)^0$, while the Doppler kernel (3.13) scales as (\mathcal{H}/k) . Using (3.8) and (3.13) in (3.7), and dropping terms that scale as $(\mathcal{H}/k)^2$ and $(\mathcal{H}/k)^3$, we find that

$$\begin{aligned} B_{gN}(\mathbf{k}_1, \mathbf{k}_2, \mathbf{k}_3) = & \mathcal{K}_N(\mathbf{k}_1) \mathcal{K}_N(\mathbf{k}_2) \mathcal{K}_N^{(2)}(\mathbf{k}_1, \mathbf{k}_2, \mathbf{k}_3) P(k_1) P(k_2) \\ & + 2 \text{ cyclic permutations}, \quad (3.14) \end{aligned}$$

$$\begin{aligned} B_{gD}(\mathbf{k}_1, \mathbf{k}_2, \mathbf{k}_3) = & \left\{ \mathcal{K}_N(\mathbf{k}_1) \mathcal{K}_N(\mathbf{k}_2) \mathcal{K}_{\text{D}}^{(2)}(\mathbf{k}_1, \mathbf{k}_2, \mathbf{k}_3) \right. \\ & \left. + [\mathcal{K}_N(\mathbf{k}_1) \mathcal{K}_D(\mathbf{k}_2) + \mathcal{K}_D(\mathbf{k}_1) \mathcal{K}_N(\mathbf{k}_2)] \mathcal{K}_N^{(2)}(\mathbf{k}_1, \mathbf{k}_2, \mathbf{k}_3) \right\} P(k_1) P(k_2) \\ & + 2 \text{ cyclic permutations}. \quad (3.15) \end{aligned}$$

Since (3.13) scales as \mathcal{H}/k it is purely imaginary, as all these contributions have at least one \mathbf{k} projected along the line of sight – i.e., they contain odd powers of μ_a 's. This means that *the leading relativistic correction in the observed galaxy Fourier bispectrum of a single tracer is a purely imaginary addition to the Newtonian approximation*. On larger scales, terms $\mathcal{O}((\mathcal{H}/k)^2)$ and higher appear in both the real and imaginary parts, with the kernels given in Umeh et al. (2017); Jolicoeur et al. (2017, 2018, 2019). We include the higher-order terms in our plots below, and a full treatment can be found in chapter 6.

3.2. Extracting the dipole

The bispectrum can be considered as a function of $k_1, k_2, k_3, \mu_1, \mu_2, \mu_3$ and φ , which is the azimuthal angle giving the orientation of the triangle relative to \mathbf{n} . In order to extract the dipole it is easiest to write $\mu_3 = -(k_1 \mu_1 + k_2 \mu_2)/k_3$, so that we can write $B_g = \sum_{i,j} \mathcal{B}_{ij} (i \mu_1)^i (i \mu_2)^j$, where $i, j = 0 \dots 6$ which factors out the angular dependence multiplying real coefficients \mathcal{B}_{ij} with no angular dependence. Then,

3. The dipole of the galaxy bispectrum

use the identity $\mu_2 = \mu_1 \cos \theta + \sqrt{1 - \mu_1^2} \sin \theta \cos \varphi$, where $\theta = \theta_{12}$ (and we define $\mu = \cos \theta$ – note that θ is the angle outside the triangle as the \mathbf{k}_a 's are head-to-tail). We use standard orthonormal spherical harmonics with the triangle lying in the $y - z$ plane, with \mathbf{k}_1 aligned along the z -axis (Nan et al., 2018), see Figure 3.1 for a schematic overview of the relevant angles and vectors of our decomposition. Then

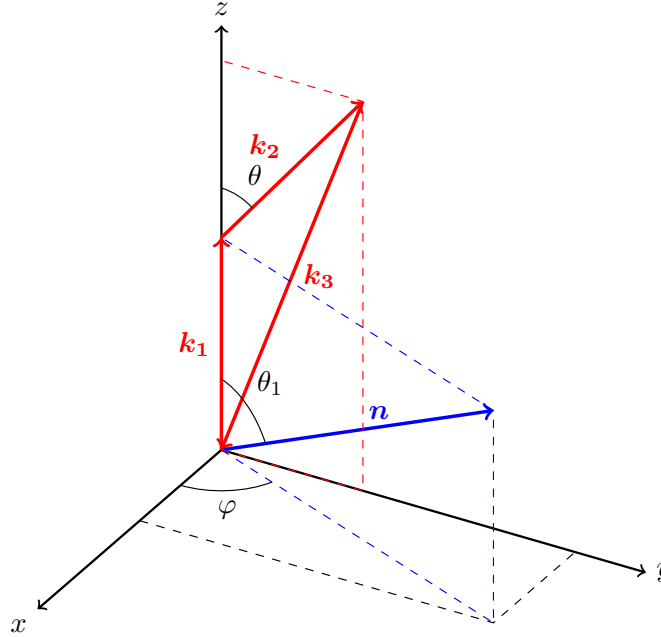


Figure 3.1.: Overview of the relevant vectors and angles for the Fourier-space bispectrum.

we have $Y_{\ell m}(\mu_1, \varphi)$, so that we can write $B_g = \sum_{\ell m} B_{\ell m} Y_{\ell m}(\mu_1, \varphi)$. The leading relativistic terms we consider here generate odd-power multipoles up to $\ell = 7$, and the full expression generates even and odd multipoles up to $\ell = 8$ – see Chapter 6. Different powers of $(i\mu_1)$ and $(i\mu_2)$ contribute to the dipole as follows,

[check this table](#)

$$\int d\Omega (i\mu_1)^a (i\mu_2)^b Y_{1m}^* = \delta_{m,0} \frac{i\sqrt{3\pi}}{15} \begin{bmatrix} 0 & 10\mu & 0 & -6\mu \\ 10 & 0 & -4\mu^2 - 2 & 0 & \dots \\ 0 & -6\mu & 0 & \frac{12\mu^3 + 18\mu}{7} \\ -6 & 0 & \frac{24\mu^2 + 6}{7} & 0 \\ \vdots & & & \ddots \end{bmatrix}$$

3. The dipole of the galaxy bispectrum

$$+ \delta_{m,\pm 1} \frac{\sqrt{6\pi}}{15} \begin{bmatrix} 0 & -5 & 0 & 3 & \dots \\ 0 & 0 & 2\mu & 0 & \dots \\ 0 & 1 & 0 & -\frac{6\mu^2+3}{7} & \dots \\ 0 & 0 & -\frac{6}{7}\mu & 0 & \dots \\ \vdots & & & & \ddots \end{bmatrix} \sin \theta, \quad (3.16)$$

where each matrix element corresponds to a particular combination of a, b , where the matrix indices run over the values $a = 0 \dots 6, b = 0 \dots 6$, with powers above 3 not written above; these are polynomials in μ up to order 6. From this we can read off the terms from \mathcal{K}_D contribute to differing $m = 0, \pm 1$. In particular, if $i + j$ is even – i.e., the real part of the bispectrum – there is no contribution: only the imaginary terms, corresponding to $i + j$ odd, contribute. For the monopole, only $i + j$ even contribute. Therefore, at $\mathcal{O}(\mathcal{H}/k)$, *the monopole of the bispectrum is the Newtonian part, while the dipole is purely from the relativistic corrections. The presence of the dipole is therefore a ‘smoking gun’ signal for the leading relativistic correction to the bispectrum.* At order $\mathcal{O}((\mathcal{H}/k)^2)$, relativistic terms appear in the monopole, which were considered in Umeh et al. (2017); Jolicoeur et al. (2017, 2018, 2019).

3.3. Squeezed, equilateral and flattened limits

It is relatively straightforward to understand the type of dipole generated in different triangular configurations in our conventions. In particular, for the $\mathcal{O}(\mathcal{H}/k)$ relativistic dipole:

- The squeezed case is zero for $m = 0$, and is non-zero for $m = \pm 1$. We see this directly from (3.16): with $\mu = -1$ the $m = 0$ contribution is anti-symmetric in i, j while \mathcal{B}_{ij} is symmetric in this limit.
- In the equilateral case, the dipole is zero (this is the case for all orders in \mathcal{H}/k).
- The flattened case ($k_1 = k_2 = k_3/2, \theta = 0$) is zero for $m = \pm 1$ (for all orders in \mathcal{H}/k), but is non-zero for $m = 0$. This can be seen directly from (3.16) with $\theta = 0$.

To show the equilateral case is zero is a lengthy calculation involving many cancellations. Let us illustrate instead the squeezed case. We write $k_1 = k_2 =$

3. The dipole of the galaxy bispectrum

$\sqrt{1+\varepsilon^2}k_S, k_3 = 2\varepsilon k_S$. In this case the triangle has small angle 2ε and equal angles $\pi/2 - \varepsilon$, where the squeezed limit is $\varepsilon \rightarrow 0$. It is convenient to replace $(1, 2, 3)$ by $(S, -S, L)$. Then to $O(\varepsilon)$, $k_{-S} = k_S, k_L = 2\varepsilon k_S, \mu_{-S} = -\mu_S - 2\varepsilon\mu_L, \mu_L = -\sqrt{1-\mu_S^2} \cos\varphi - \varepsilon\mu_S$. In this limit, the permutations of the relativistic kernels become

$$\begin{aligned} \mathcal{K}_D^{(2)}(\mathbf{k}_L, \mathbf{k}_S, \mathbf{k}_{-S}) &= i\mathcal{H} \left[-\frac{3}{2}\Omega_m b_1 \mu_S \frac{k_S}{k_L^2} + Cf \frac{\mu_L}{k_L} \right. \\ &\quad \left. - \frac{3}{2}\Omega_m f \mu_S^3 \frac{k_S}{k_L^2} + \left(\frac{3}{2}\Omega_m - Ef \right) f \mu_S^2 \frac{\mu_L}{k_L} \right] \end{aligned} \quad (3.17)$$

and $\mathcal{K}_D^{(2)}(\mathbf{k}_{-S}, \mathbf{k}_L, \mathbf{k}_S) = \mathcal{K}_D^{(2)}(\mathbf{k}_L, \mathbf{k}_S, \mathbf{k}_{-S})|_{\mu_S \rightarrow \mu_{-S}}$ while $\mathcal{K}_D^{(2)}(\mathbf{k}_S, \mathbf{k}_{-S}, \mathbf{k}_L) = 0$. In the squeezed limit of the cyclic sum (3.7), the terms $\mathcal{K}^{(2)}(\mathbf{k}_L, \mathbf{k}_S, \mathbf{k}_{-S})$ and $\mathcal{K}^{(2)}(\mathbf{k}_{-S}, \mathbf{k}_L, \mathbf{k}_S)$ appear only in the form $\mathcal{K}^{(2)}(\mathbf{k}_L, \mathbf{k}_S, \mathbf{k}_{-S}) + \mathcal{K}^{(2)}(\mathbf{k}_{-S}, \mathbf{k}_L, \mathbf{k}_S)$. This sum regularises the divergent $k_S/k_L = (2\varepsilon)^{-1}$ and $k_S/k_L^2 = (2\varepsilon k_L)^{-1}$ terms. We obtain the bispectrum in the squeezed limit,

$$\begin{aligned} B_g^{\text{sq}} &= b_{1S} b_{1L} b_{SL} P_L P_S + i b_{1S} \left\{ b_{SL} f A + \frac{3}{2} \Omega_m b_{1S} b_{1L} \right. \\ &\quad \left. + 2b_{1L} f C + b_{1L} \mu_S^2 \left[\frac{3}{2} \Omega_m - Ef \right] \right\} P_L P_S \mu_L \frac{\mathcal{H}}{k_L}, \end{aligned} \quad (3.18)$$

where $P_{S,L} = P(k_{S,L})$, $b_{1S,L} \equiv b_1 + f\mu_{S,L}^2$ and

$$b_{SL} \equiv 2b_2 + \frac{43}{21}b_1 - \frac{4}{21} + \left(2b_1 + \frac{5}{7} \right) f\mu_S^2 + f\mu_L^2 b_{1S}.$$

Note that only the first term in the squeezed bispectrum comes from the Newtonian limit.

The type of dipole extracted from this term is seen as follows. To this order we can write $\mu_S^2 = \mu_S \mu_{-S}$. Then, since $\mu_L = -2(\mu_S + \mu_{-S})/\varepsilon$, we see that the $m = 0$ term is zero because B_g^{sq} is symmetric in $\mu_S^i \mu_{-S}^j$ under $i \leftrightarrow j$, while the $m = 0$ term is antisymmetric in (3.16). This leaves just the $m = \pm 1$ contribution in (3.16).

3. The dipole of the galaxy bispectrum

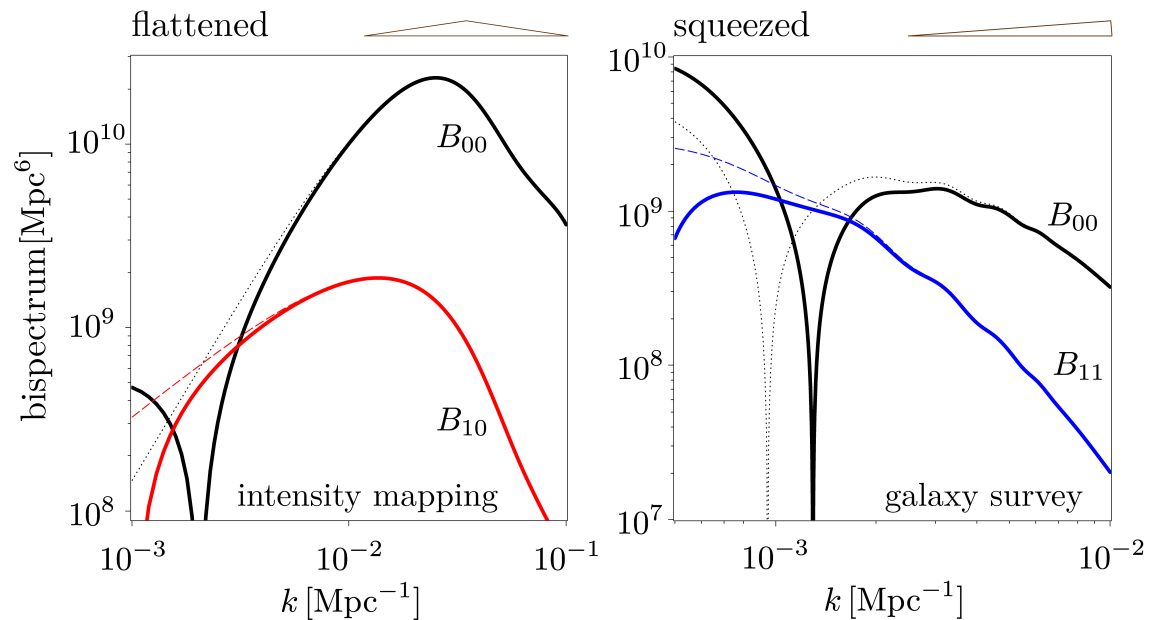


Figure 3.2.: The absolute value of the bispectrum dipole at $z = 1$ as a function of triangle size, in the flattened (Left, $\theta = 2^\circ$, for intensity mapping bias) and squeezed (Right, $\theta = 178^\circ$, for Euclid-like bias) configurations, with k_3 as the horizontal axis. Red is the $m = 0$ part and blue is $m = \pm 1$. Dashed (and dotted) lines show up to the $\mathcal{O}(\mathcal{H}/k)$ terms considered analytically here, while solid lines indicate larger-scale contributions. For reference the monopole is in black, with the dotted line the Newtonian part. (The zero-crossing in the monopole for the squeezed case is a result of the tidal bias.)

3. The dipole of the galaxy bispectrum

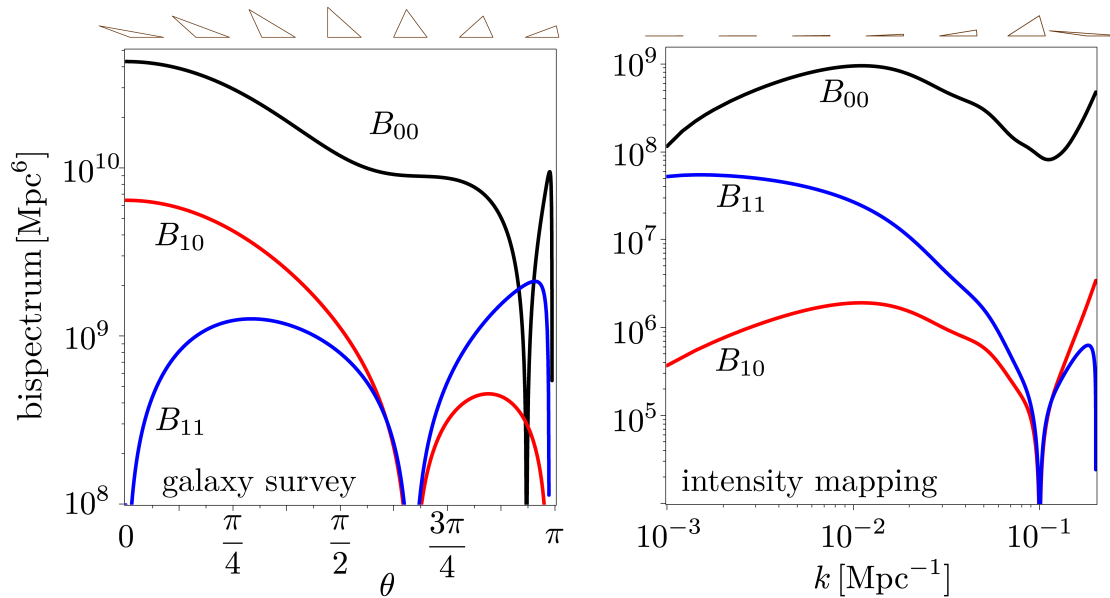


Figure 3.3.: (Left) We show the dipoles as a function of θ with a bias appropriate for a Euclid-like survey, for $k_1 = k_2 = 0.01 \text{ Mpc}^{-1}$. The left of the plot corresponds to the flattened case where the $m = 0$ (red) dipole reaches 10% of the monopole. (Right) We show the IM signal with $k_1 = k_2 = 0.1 \text{ Mpc}^{-1}$ versus the long mode k_3 . Except for very long modes $\theta \approx \pi$, our $\mathcal{O}(\mathcal{H}/k)$ truncation is a very good approximation in these examples.

3. The dipole of the galaxy bispectrum

3.4. The dipole in intensity mapping and galaxy surveys

We now consider the amplitude of the dipole relevant for upcoming galaxy surveys, which have different bias parameters. We consider two different types of survey: an SKA intensity mapping of 21 cm radio emission, as well as a Euclid-like optical/infrared spectroscopic survey. An intensity map of the 21cm emission of neutral hydrogen (HI) in the post-reionization Universe records the total emission in galaxies containing HI, without detecting individual galaxies. There is an equivalence between the brightness temperature contrast and number count contrast (Umeh et al., 2016). For IM we use the bias parameters at $z = 1$, $b_1 = 0.856, b_2 = -0.321, b'_1 = -0.5 \times 10^{-4}, b_e = -0.5, b'_e = 0, s = 2/5$ (Fonseca et al., 2018; Umeh et al., 2016) while for the spectroscopic survey we use $b_1 = 1.3, b_2 = -0.74, b'_1 = -1.6 \times 10^{-4}, b_e = -4, b'_e = 0, s = -0.95$ (Camera et al., 2018; Yankelevich & Porciani, 2019). For intensity mapping, $\partial b_1 / \partial \ln L = 0$ and we assume it is zero for simplicity for the spectroscopic survey. We use a LCDM model with standard parameters $\Omega_m = 0.314, h = 0.67, f_{\text{baryon}} = 0.157, n_s = 0.968$. Plots are presented using linear power spectra generated using CAMB (Lewis et al., 2000).

In Fig. (3.2) we show how changing the scale of a fixed triangle changes the amplitude of the dipole, with reference to the monopole. In the flattened case with $m = 0$ we see the signal peaks for triangles below the equality scale, while for squeezed shapes, with $m = \pm 1$, the signal is smaller, and peaks when the long mode approaches the Hubble scale. In Fig. (3.3) we change the shape with fixed $k_1 = k_2$ for both galaxy and IM surveys. We confirm our analytical results that the equilateral limit is zero, as well as the other limits. For triangles between right-angle and flattened the dipole is more than 10% of the monopole, and the signal is largest in the flattened case – except in the extreme squeezed limit (not shown).

check the bias params, and provide expressions

move figures into section

3.5. Conclusions

We have shown for the first time that the relativistic galaxy bispectrum has a leading correction which is a local dipole with respect to the observers line of sight. In contrast to the power spectrum, this dipole exists even for a single tracer. We have shown analytically how the dipole is generated for the leading terms, and numerically

3. The dipole of the galaxy bispectrum

we have included all local contributions, which show up above the equality scale. We have neglected integrated terms which will also contribute to the dipole, but their inclusion in a Fourier space bispectrum is non-trivial. Local relativistic corrections will induce all multipoles up to $\ell = 8$ at every m , in contrast to the Newtonian case which only induces even $\ell = 0, 2, 4$. We will investigate these new multipoles in a forthcoming publication.

We have shown that this dipole is large with respect to the monopole in both the flattened and squeezed limits, which excite different orders of the dipole orientation m . We have shown that even on equality scales it is about 10% of the monopole at $z = 1$ for flattened shapes which have the largest amplitude. In more squeezed cases where the short mode is ~ 10 Mpc the dipole can also be a large part of the IM signal. Furthermore, although we have only considered Gaussian initial conditions here, the dipole will be unaffected by non-Gaussianity at leading order because these corrections start at $\mathcal{O}((\mathcal{H}/k)^2)$, making our predictions relatively robust to this. This implies that the dipole of the bispectrum is a unique signature of general relativity on cosmological scales, and therefore offers a new observational window onto modifications of general relativity.

4. Detectability in next-generation galaxy surveys

In this chapter, we investigate whether the next generation of high-precision cosmological surveys will be able to make such a detection. First, we consider a Stage IV spectroscopic $H\alpha$ survey similar to Euclid, and we find that the cumulative signal to noise of this relativistic signature is $\mathcal{O}(10)$. Secondly, we look at some future 21cm intensity mapping surveys; MeerKAT, SKA, PUMA, and HIRAX. Due to foreground and telescope beam effects, the signal-to-noise ratio for intensity mapping surveys is typically lower than for spectroscopic $H\alpha$ surveys, though also still detectable.

4.1. Detecting the leading-order relativistic signature

Here we highlight a feature of the tree-level Fourier galaxy bispectrum which follows from the leading-order relativistic contribution – due to Doppler, gravitational redshift and related line-of-sight effects – that is omitted in the standard Newtonian analysis. These effects generate an imaginary part of the galaxy bispectrum, which can be understood as follows (see also McDonald (2009); Clarkson et al. (2019); Jeong & Schmidt (2020) for a more general discussion). The Doppler-type contributions to the galaxy density contrast involve one or three derivatives of scalars along the fixed line of sight \mathbf{n} [see (4.6), (4.7) below]. In Fourier space, with the plane-parallel approximation, we have $\mathbf{n} \cdot \nabla \rightarrow i \mathbf{n} \cdot \mathbf{k}$, and this leads to imaginary corrections to the galaxy density contrast, which do not cancel in the bispectrum, unlike in the power spectrum. At first order, we have $\delta_g = \delta_{gN} + \delta_{gD}$, where the Newtonian part δ_{gN} is real and scales as the linear matter density contrast δ . The relativistic Doppler-type part δ_{gD} scales as $i(\mathcal{H}/k)\delta$ (see McDonald (2009); Jeong

4. Detectability in next-generation galaxy surveys

et al. (2012); Abramo & Bertacca (2017); Clarkson et al. (2019) and below). At second order, the relativistic contribution $\delta_g^{(2)}$ scales as $i(\mathcal{H}/k)(\delta)^2$ (see Clarkson et al. (2019) and below).

In the case of the galaxy auto-power spectrum, $P_g \sim \langle |\delta_g|^2 \rangle$, the relativistic part is real and scales as $(\mathcal{H}/k)^2 P$: therefore we can neglect P_{gD} at leading order. By contrast, for the galaxy bispectrum, $B_g \sim \langle \delta_g \delta_g \delta_g^{(2)} \rangle$, a coupling of relativistic contributions to short-scale Newtonian terms (which is absent in P_g) produces a B_{gD} that is imaginary and scales as $i(\mathcal{H}/k)P^2$. We therefore expect these relativistic effects to be more accessible in the bispectrum than in the power spectrum, for the case of a single tracer of the matter distribution.

leave some points about relativistic effects detect. in P vs B

Although the galaxy bispectrum is statistically isotropic, the plane-parallel approximation in redshift space breaks 3-dimensional isotropy, since a preferred direction is imposed by the observer's fixed line of sight.

Let us introduce a more explicit analysis, as follows.

At tree-level, the Fourier galaxy bispectrum at a redshift z is given by

$$\langle \delta_g(z, \mathbf{k}_1) \delta_g(z, \mathbf{k}_2) \delta_g^{(2)}(z, \mathbf{k}_3) \rangle + 2 \text{ cp} = 2(2\pi)^3 B_g(z, \mathbf{k}_1, \mathbf{k}_2, \mathbf{k}_3) \delta^{\text{Dirac}}(\mathbf{k}_1 + \mathbf{k}_2 + \mathbf{k}_3), \quad (4.1)$$

where cp denotes cyclic permutation and the factor 2 on the right arises from the convention that the total number density contrast is $\delta_g + \delta_g^{(2)}/2$. In terms of the first- and second-order kernels, we have

$$B_g(z, \mathbf{k}_1, \mathbf{k}_2, \mathbf{k}_3) = \mathcal{K}^{(1)}(z, \mathbf{k}_1) \mathcal{K}^{(1)}(z, \mathbf{k}_2) \mathcal{K}^{(2)}(z, \mathbf{k}_1, \mathbf{k}_2, \mathbf{k}_3) P(z, k_1) P(z, k_2) + 2 \text{ cp}, \quad (4.2)$$

where P is the linear matter power spectrum. The $9 - 3 = 6$ degrees of freedom in the triangle condition $\mathbf{k}_1 + \mathbf{k}_2 + \mathbf{k}_3 = \mathbf{0}$ at each z are reduced to 5 by the fixed observer's line of sight direction \mathbf{n} . The bispectrum can be chosen at each z to be a function of the 3 magnitudes $k_a = (k_1, k_2, k_3)$ and 2 angles that define the orientation of the triangle (see Fig. 4.1):

$$B_g(z, \mathbf{k}_a) = B_g(z, k_a, \mu_1, \varphi). \quad (4.3)$$

Here $\mu_a = \mathbf{k}_a \cdot \mathbf{n} = \cos \theta_a$, and φ is the angle between the triangle plane and the $(\mathbf{n}, \mathbf{k}_1)$ -plane. The three angles $\theta_{ab} = \cos^{-1}(\mathbf{k}_a \cdot \mathbf{k}_b)$, are determined by k_a ; then $\mu_2 = \mu_1 \cos \theta_{12} + \sin \theta_{12} \sin \theta_{12} \cos \varphi$ is determined when φ is given, and $\mu_3 = -(\mu_1 k_1 + \mu_2 k_2)/k_3$.

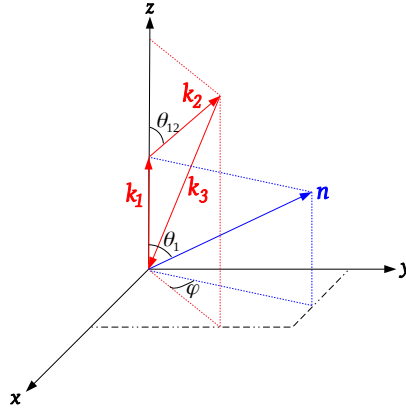


Figure 4.1.: Relevant vectors and angles for the Fourier bispectrum.

In the standard Newtonian approximation, $B_g = B_{gN}$, the kernels in (4.2) contain the galaxy bias and the redshift-space distortions (RSD) at first and second order Bernardeau et al. (2002); Karagiannis et al. (2018):

$$\mathcal{K}_N^{(1)}(\mathbf{k}_1) = b_1 + f\mu_1^2, \quad (4.4)$$

$$\mathcal{K}_N^{(2)}(\mathbf{k}_1, \mathbf{k}_2, \mathbf{k}_3) = b_1 F_2(\mathbf{k}_1, \mathbf{k}_2) + b_2 + f\mu_3^2 G_2(\mathbf{k}_1, \mathbf{k}_2) + fZ_2(\mathbf{k}_1, \mathbf{k}_2) + b_{s^2} S_2(\mathbf{k}_1, \mathbf{k}_2), \quad (4.5)$$

where we dropped the z -dependence for brevity. Here f is the linear matter growth rate, b_1, b_2 are the linear and second-order clustering biases, and b_{s^2} is the tidal bias. The kernel F_2 is for second-order density, G_2, Z_2 are for RSD, and S_2 is the kernel for tidal bias .

expressions

The Doppler-type relativistic corrections to the Newtonian number count contrast in redshift space are given at first order by Bonvin & Durrer (2011):

$$\delta_{gD} = A \mathbf{v} \cdot \mathbf{n}, \quad (4.6)$$

where $A(z)$ is given below in (4.12) and the momentum conservation equation has been used to eliminate the gravitational redshift: $\mathbf{n} \cdot \nabla \Phi \equiv \partial_r \Phi = -\mathbf{v}' \cdot \mathbf{n} - \mathcal{H} \mathbf{v} \cdot \mathbf{n}$. Here Φ is the gravitational potential, \mathbf{v} is the peculiar velocity, \mathcal{H} is the comoving Hubble parameter, and r is the line-of-sight comoving distance. Note that $\mathbf{v} \cdot \mathbf{n} = \partial_r V$, where V is the velocity potential ($v_i = \partial_i V$). At second order, and neglecting vector and tensor modes, it is shown in Clarkson et al. (2019) that (see also Di Dio

4. Detectability in next-generation galaxy surveys

& Seljak (2019))

$$\begin{aligned} \delta_{gD}^{(2)} = & A \mathbf{v}^{(2)\cdot} \mathbf{n} + 2C(\mathbf{v} \cdot \mathbf{n}) \delta + 2\frac{E}{\mathcal{H}}(\mathbf{v} \cdot \mathbf{n}) \partial_r(\mathbf{v} \cdot \mathbf{n}) + \frac{2}{\mathcal{H}^2} [(\mathbf{v} \cdot \mathbf{n}) \partial_r^2 \Phi - \Phi \partial_r^2(\mathbf{v} \cdot \mathbf{n})] \\ & - \frac{2}{\mathcal{H}} \partial_r(\mathbf{v} \cdot \mathbf{v}) + 2\frac{b_1}{\mathcal{H}} \Phi \partial_r \delta. \end{aligned} \quad (4.7)$$

The redshift-dependent coefficients C, E are given below in (4.13), (4.14).

In Fourier space, neglecting sub-leading $\mathcal{O}(\mathcal{H}^2/k^2)$ terms, we find from (4.2) that

$$B_{gD}(\mathbf{k}_1, \mathbf{k}_2, \mathbf{k}_3) = \left\{ \left[\mathcal{K}_{N}^{(1)}(\mathbf{k}_1) \mathcal{K}_{D}^{(1)}(\mathbf{k}_2) + \mathcal{K}_{D}^{(1)}(\mathbf{k}_1) \mathcal{K}_{N}^{(1)}(\mathbf{k}_2) \right] \mathcal{K}_{N}^{(2)}(\mathbf{k}_1, \mathbf{k}_2, \mathbf{k}_3) \right. \\ \left. + \mathcal{K}_{N}^{(1)}(\mathbf{k}_1) \mathcal{K}_{N}^{(1)}(\mathbf{k}_2) \mathcal{K}_{D}^{(2)}(\mathbf{k}_1, \mathbf{k}_2, \mathbf{k}_3) \right\} P(k_1) P(k_2) + 2 \text{ cp.} \quad (4.8)$$

The relativistic kernels follow from (4.6) and (4.7); they are given in Clarkson et al. (2019) as

$$\mathcal{K}_{D}^{(1)}(\mathbf{k}_1) = i \mathcal{H} f A \frac{\mu_1}{k_1}, \quad (4.9)$$

$$\begin{aligned} \mathcal{K}_{D}^{(2)}(\mathbf{k}_1, \mathbf{k}_2, \mathbf{k}_3) = & i \mathcal{H} f \left[A \frac{\mu_3}{k_3} G_2(\mathbf{k}_1, \mathbf{k}_2) + C \left(\frac{\mu_1}{k_1} + \frac{\mu_2}{k_2} \right) + \left(\frac{3}{2} \Omega_m - f E \right) \mu_1 \mu_2 \left(\frac{\mu_1}{k_2} + \frac{\mu_2}{k_1} \right) \right. \\ & \left. - \frac{3}{2} \Omega_m \left(\mu_1^3 \frac{k_1}{k_2^2} + \mu_2^3 \frac{k_2}{k_1^2} \right) + 2f \mathbf{k}_1 \cdot \mathbf{k}_2 \left(\frac{\mu_1}{k_1} + \frac{\mu_2}{k_2} \right) - \frac{3\Omega_m b_1}{2f} \left(\mu_1 \frac{k_1}{k_2^2} + \mu_2 \frac{k_2}{k_1^2} \right) \right]. \end{aligned} \quad (4.10)$$

It is clear from (4.8)–(4.10) and from the general expressions given in Umeh et al. (2017); Jolicoeur et al. (2017), that Doppler-type relativistic effects generate an imaginary correction to the Newtonian bispectrum:

$$\text{Re } B_g = B_{gN} + \mathcal{O}(\mathcal{H}^2/k^2), \quad i \text{ Im } B_g = B_{gD} + \mathcal{O}(\mathcal{H}^3/k^3). \quad (4.11)$$

The coefficients in (4.9) and (4.10) are Clarkson et al. (2019)

$$A = b_e - 2\mathcal{Q} + \frac{2(\mathcal{Q}-1)}{r\mathcal{H}} - \frac{\mathcal{H}'}{\mathcal{H}^2}, \quad (4.12)$$

$$C = b_1(A+f) + \frac{b'_1}{\mathcal{H}} + 2 \left(1 - \frac{1}{r\mathcal{H}} \right) \frac{\partial b_1}{\partial \ln L} \Big|_c, \quad (4.13)$$

$$E = 4 - 2A - \frac{3}{2}\Omega_m, \quad (4.14)$$

where a prime is a conformal time derivative, $\Omega_m = \Omega_{m0}(1+z)H_0^2/\mathcal{H}^2$, L is the

4. Detectability in next-generation galaxy surveys

luminosity, and $|_c$ denotes evaluation at the flux cut.

In addition to the clustering bias b_1 , the relativistic bispectrum is sensitive to the evolution bias and magnification bias, which are defined as Alonso et al. (2015b)

$$b_e = -\frac{\partial \ln n_g}{\partial \ln(1+z)}, \quad \mathcal{Q} = -\left.\frac{\partial \ln n_g}{\partial \ln L}\right|_c. \quad (4.15)$$

Here and below, n_g is the *comoving* galaxy number density. (Note that the alternative magnification bias parameter $s = 2\mathcal{Q}/5$ is often used.)

It is interesting to note that the magnification bias \mathcal{Q} enters the relativistic bispectrum, even though we have not included the effect of the integrated lensing magnification κ . The reason for this apparent inconsistency is that there is a (non-integrated) Doppler correction to κ at leading order Bonvin (2008); Bolejko et al. (2013).

4.2. Signal-to-Noise

The signal-to-noise ratio (SNR) for the bispectrum at some redshift z is in the Gaussian approximation of uncorrelated triangles given by (Scoccimarro et al., 2004),

$$\left[\frac{S}{N}(z)\right]^2 = \sum_{k_a, \mu_1, \varphi} \frac{1}{\text{Var}[B_g(z, k_a, \mu_1, \varphi)]} B_g(z, k_a, \mu_1, \varphi) B_g^*(z, k_a, \mu_1, \varphi), \quad (4.16)$$

where we have introduced the complex conjugate B_g^* as the galaxy bispectrum has an imaginary correction. Here $\text{Var}[B_g]$ is the variance of the bispectrum estimator (Chan & Blot, 2017),

$$\hat{B}_g(z, \mathbf{k}_a) = \frac{k_f^3}{V_{123}} \int_{\mathbf{k}_a} d^3\mathbf{q}_1 d^3\mathbf{q}_2 d^3\mathbf{q}_3 \delta^{\text{Dirac}}(\mathbf{q}_1 + \mathbf{q}_2 + \mathbf{q}_3) \delta_g(z, \mathbf{q}_1) \delta_g(z, \mathbf{q}_2) \delta_g(z, \mathbf{q}_3), \quad (4.17)$$

where integration is over the shells $k_a - \Delta k/2 \leq q_a \leq k_a + \Delta k/2$ and the shell volume is $V_{123} = \int_{\mathbf{k}_a} d^3\mathbf{q}_1 d^3\mathbf{q}_2 d^3\mathbf{q}_3 \delta^{\text{Dirac}}(\mathbf{q}_1 + \mathbf{q}_2 + \mathbf{q}_3)$.

In the Newtonian approximation, the Gaussian variance can be given as (Scocci-

4. Detectability in next-generation galaxy surveys

marro et al., 2004; Karagiannis et al., 2018),

$$\text{Var}[B_g(z, k_a, \mu_1, \varphi)] = s_B \frac{\pi k_f(z)^3}{k_1 k_2 k_3 (\Delta k)^3} \frac{N_{\mu_1} N_{\varphi}}{\Delta \mu_1 \Delta \varphi} \tilde{P}_{gN}(z, k_1, \mu_1) \tilde{P}_{gN}(z, k_2, \mu_2) \tilde{P}_{gN}(z, k_3, \mu_3), \quad (4.18)$$

where,

$$\tilde{P}_{gN}(z, k_a, \mu_a) = P_{gN}(z, k_a, \mu_a) + \frac{1}{n_g(z)}, \quad (4.19)$$

and $P_{gN} = (b_1 + f\mu_a^2)^2 P$ is the linear galaxy power spectrum. In (4.18), s_B is 6, 2, 1 respectively for equilateral, isosceles and non-isosceles triangles, and N_{μ_1}, N_{φ} are the ranges for μ_1, φ (which are sometimes reduced from their full values of 2 and 2π using symmetry arguments). The fundamental mode is determined by the comoving survey volume of the redshift bin centred at z , i.e. $k_f(z) = 2\pi V(z)^{-1/3}$, where $V(z) = 4\pi f_{\text{sky}}[r(z + \Delta z/2)^3 - r(z - \Delta z/2)^3]$.

For a survey with redshift bin centres ranging from z_{\min} to z_{\max} , the cumulative SNR is

$$\frac{S}{N}(\leq z) = \left\{ \sum_{z'=z_{\min}}^z \left[\frac{S}{N}(z') \right]^2 \right\}^{1/2}, \quad (4.20)$$

and then the total SNR is $S/N(\leq z_{\max})$.

4.2.1. Relativistic contributions to the variance

For the full bispectrum, including the relativistic part, (4.17) leads to a variance of the form

$$\text{Var}[B_g(z, \mathbf{k}_a)] \propto \tilde{P}_g(z, k_1, \mu_1) \tilde{P}_g(z, k_2, \mu_2) \tilde{P}_g(z, k_3, \mu_3). \quad (4.21)$$

In the Newtonian approximation, this gives (4.18). By (4.9), the galaxy number density contrast has an imaginary relativistic correction, $\delta_g = \delta_{gN} + \delta_{gD}$. However, since $P_g \sim \langle \delta_g(\mathbf{k}) \delta_g(-\mathbf{k}) \rangle = \langle |\delta_g(\mathbf{k})|^2 \rangle$, the galaxy power spectrum is given by McDonald (2009); Abramo & Bertacca (2017); Clarkson et al. (2019),

$$P_g = P_{gN} + P_{gD} = P_{gN} + \mathcal{O}(\mathcal{H}^2/k^2). \quad (4.22)$$

It follows from (4.21) and (4.22) that at leading order, the relativistic contribution to the variance can be neglected,

$$\text{Var}[B_g] = \text{Var}[B_{gN}] + \mathcal{O}(\mathcal{H}^2/k^2). \quad (4.23)$$

4. Detectability in next-generation galaxy surveys

Therefore the SNR for the Newtonian and relativistic parts of the bispectrum are,

$$\left(\frac{S}{N}\right)_N^2 = \sum_{k_a, \mu_1, \varphi} \frac{B_{gN} B_{gN}}{\text{Var}[B_{gN}]}, \quad (4.24)$$

$$\left(\frac{S}{N}\right)_D^2 = \sum_{k_a, \mu_1, \varphi} \frac{B_{gD} B_{gD}^*}{\text{Var}[B_{gN}]}. \quad (4.25)$$

4.2.2. Nonlinear effects

In order to avoid nonlinear effects of matter clustering, the maximum k is chosen as a scale where perturbation theory for the matter density contrast begins to break down. It is known that the matter bispectrum is more sensitive to nonlinearity than the matter power spectrum: at $z \sim 0$ nonlinearity sets in at $k \sim 0.1h/\text{Mpc}$ for the matter bispectrum, as opposed to $k \sim 0.2h/\text{Mpc}$ for the matter power spectrum. To account for the growth of k_{\max} with redshift, we use the redshift-dependence proposed in Smith et al. (2003) for the power spectrum, but with half the amplitude at $z = 0$,

$$k_{\max}(z) = 0.1h(1+z)^{2/(2+n_s)}. \quad (4.26)$$

The cut-off $k \leq k_{\max}(z)$ avoids a breakdown of perturbative accuracy in the matter correlations, but nonlinearities in the galaxy correlations due to RSD can affect longer wavelength modes. The effect of RSD on these scales is to damp the power – the ‘FoG’ effect. In order to take account of this, we follow Karagiannis et al. (2018); Yankelevich & Porciani (2019) and use the simple model of FoG damping,

$$P_g \rightarrow D_P P_g, \quad D_P(z, \mathbf{k}) = \exp\{-\text{frac12}[k\mu\sigma(z)]^2\}, \quad (4.27)$$

$$B_g \rightarrow D_B B_g, \quad D_B(z, \mathbf{k}_1, \mathbf{k}_2, \mathbf{k}_3) = \exp\left\{-\frac{1}{2}\left[k_1^2\mu_1^2 + k_2^2\mu_2^2 + k_3^2\mu_3^2\right]\sigma(z)^2\right\}, \quad (4.28)$$

where σ is the linear velocity dispersion.

On sufficiently large scales the non-Gaussian contribution to the bispectrum covariance can be approximated by including corrections to the power spectra appearing in the bispectrum variance (B.5). This is shown by Chan & Blot (2017) (see also Karagiannis et al. (2018)), using the approximation,

$$\text{Var}[B_g] \rightarrow \text{Var}[B_g] + \delta\text{Var}[B_g], \quad (4.29)$$

4. Detectability in next-generation galaxy surveys

$$\delta\text{Var}[B_g] = \frac{s_B \pi k_f^3 N_{\mu_1} N_\varphi}{k_1 k_2 k_3 (\Delta k)^3 \Delta \mu_1 \Delta \varphi} \left\{ \tilde{P}_{gN}(1) \tilde{P}_{gN}(2) \left[\tilde{P}_{gN}^{\text{NL}}(3) - \tilde{P}_{gN}(3) \right] + 2 \text{cp} \right\}. \quad (4.30)$$

Here $\tilde{P}_{gN}(a) \equiv \tilde{P}_{gN}(z, k_a, \mu_a)$ and $\tilde{P}_{gN}^{\text{NL}}(a) = (b + f\mu_a^2)^2 P^{\text{NL}} + n_g^{-1}$, where P^{NL} is the nonlinear matter power spectrum, computed with a modified Halofit emulator.

4.2.3. Summations over triangles

Sum [inline]discussion of yankelevich and porciani The counting of triangles $\mathbf{k}_1 + \mathbf{k}_2 + \mathbf{k}_3 = \mathbf{0}$ that contribute to the signal-to-noise involves a sum in k_a -space and a sum over orientations.

The triangle sides are chosen so that $k_1 \geq k_2 \geq k_3$, and must satisfy $k_1 - k_2 - k_3 \leq 0$. For the summation in k_a we choose the minimum and the step-length as

$$k_{\min}(z) = k_f(z) \quad \text{and} \quad \Delta k(z) = k_f(z), \quad (4.31)$$

as in Karagiannis et al. (2018); Yankelevich & Porciani (2019). Then the k_a sum is defined as Liguori et al. (2010); Oddo et al. (2020)

$$\sum_{k_a} = \sum_{k_1=k_{\min}}^{k_{\max}} \sum_{k_2=k_{\min}}^{k_1} \sum_{k_3=k_{\min}}^{k_2}. \quad (4.32)$$

The coordinates $(\mu_1 = \cos \theta_1, \varphi)$ describe all possible orientations of the triangle. We follow Karagiannis et al. (2018) and choose the ranges $N_{\mu_1} = 2, N_\varphi = 2\pi$. For a given μ_1 , a complete rotation in φ about \mathbf{k}_1 double counts the triangle falling onto the fixed $(\mathbf{n}, \mathbf{k}_1)$ -plane at $\varphi = 0$ and $\varphi = 2\pi$ (see Figure 4.1). Similarly, for a given φ , the end-points $\theta_1 = 0$ and $\theta_1 = \pi$ correspond to equivalent triangles, with $\mathbf{k}_a \rightarrow -\mathbf{k}_a$. This double-counting can be avoided by imposing suitable upper limits: $-1 \leq \mu_1 < 1$ and $0 \leq \varphi < 2\pi$. The signal to noise is quite sensitive to the step-lengths $\Delta\mu_1, \Delta\varphi$.

incorporate appendix properly here

Figure 4.2 shows the effect on the relativistic total SNR of changing the number of orientation bins, $n_{\mu_1} = N_{\mu_1}/\Delta\mu_1 = 2/\Delta\mu_1$ and $n_\varphi = N_\varphi/\Delta\varphi = 2\pi/\Delta\varphi$. It is apparent that reducing the number of bins increases the cumulative SNR. The cumulative SNR converges towards a minimum for $n_{\mu_1}, n_\varphi > 40$. We choose $n_{\mu_1} =$

4. Detectability in next-generation galaxy surveys

$n_\varphi = 50$, which is equivalent to eq. Following this, we find that a suitable choice for

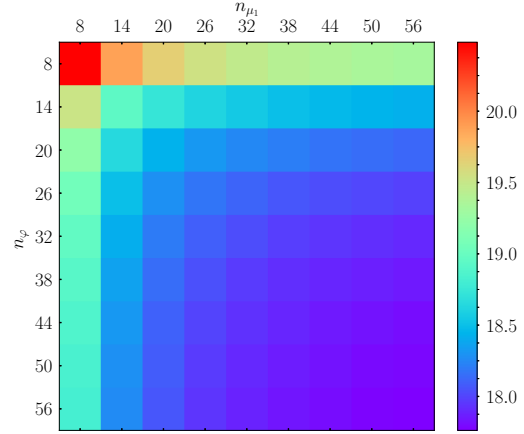


Figure 4.2.: Effect on total relativistic SNR of changing number of φ and μ_1 bins.

convergence is

$$\Delta\mu_1 = 0.04, \quad \Delta\varphi = \pi/25. \quad (4.33)$$

4.3. Next-generation galaxy surveys

We consider a Stage IV $H\alpha$ spectroscopic survey, with clustering bias, comoving volume, comoving number density and RSD damping parameter given by Table 1 in Yankelevich & Porciani (2019), over the redshift range $0.65 \leq z \leq 2.05$, with $\Delta z = 0.1$ bins. Fitting formulas for these quantities are,

$$b_1(z) = 0.9 + 0.4z, \quad b_2(z) = -0.741 - 0.125z + 0.123z^2 + 0.00637z^3, \quad (4.34)$$

$$b_{s^2}(z) = 0.0409 - 0.199z - 0.0166z^2 + 0.00268z^3, \quad (4.35)$$

$$V(z) = 8.85z^{1.65} \exp(-0.777z) h^{-3} \text{Gpc}^3, \quad (4.36)$$

$$n_g(z) = 0.0193z^{-0.0282} \exp(-2.81z) h^3 \text{Mpc}^{-3}, \quad (4.37)$$

$$\sigma(z) = (5.29 - 0.249z - 0.720z^2 + 0.187z^3) h^{-1} \text{Mpc}. \quad (4.38)$$

Figure 4.3 shows the values given in Yankelevich & Porciani (2019) together with the fitting curves. For the cosmological parameters, we use Planck 2018 Aghanim et al. (2018),

add the actual bias parans

4. Detectability in next-generation galaxy surveys

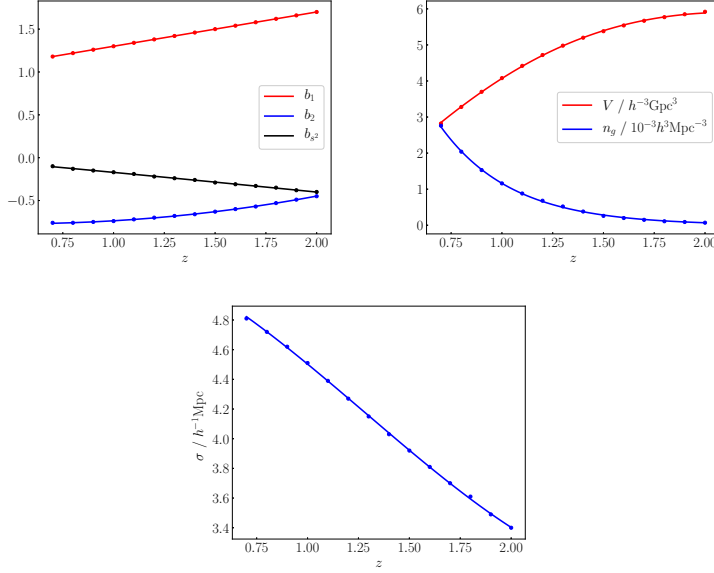


Figure 4.3.: Clustering bias parameters (*left*), comoving volume and number density (*middle*) and RSD damping parameter (*right*). Points are the data from Table 1 in Yankelevich & Porciani (2019).

$h = 0.6766, \Omega_{m0} = 0.3111, \Omega_{b0}h^2 = 0.02242, \Omega_{c0}h^2 = 0.11933, n_s = 0.9665, \sigma_8 = 0.8102, \gamma = 0.545, \Omega_{K0} = 0 = \Omega_{\nu0}$.

We checked that the SNR for the Newtonian bispectrum is consistent with Fig. 4

add actual figure reference

of Yankelevich & Porciani (2019),

YandP discussion

when we use their redshift-independent $k_{\max} = 0.15h \text{ Mpc}^{-1}$, and when we remove the flattened triangle shapes that are excluded by Yankelevich & Porciani (2019). When we include the flattened shapes, we checked that we recover the total number of triangles given in Table 1

add actual table ref

of Oddo et al. (2020).

4.3.1. Evolution bias and magnification bias

be, Q

4. Detectability in next-generation galaxy surveys

chat about the new correction to the evolution bias, new paper

rerun figures with the other euclid bias model

The relativistic bispectrum depends also on b_e and \mathcal{Q} , as shown in (4.10)–(4.14). These parameters do *not* appear in the Newtonian approximation, but they are crucial for the relativistic correction, and we need to evaluate them in a physically consistent way. We compute these parameters from the same luminosity function that is used to generate the number density shown in Fig. 4.3, i.e., Model 1 in Pozzetti et al. (2016):

$$\Phi(z, y) = \Phi_*(z) y^\alpha e^{-y}, \quad y \equiv \frac{L}{L_*}. \quad (4.39)$$

We have written Φ in terms of the redshift z and the normalised dimensionless luminosity y , where $L_* = L_{*0}(1+z)^\delta$ and L_{*0} is a characteristic luminosity. Here α is the faint-end slope, and Φ_* is a characteristic comoving density of $H\alpha$ emitters, modelled as

$$\frac{\Phi_*}{\Phi_{*0}} = \begin{cases} (1+z)^\epsilon & z \leq z_b, \\ (1+z_b)^{2\epsilon}(1+z)^{-\epsilon} & z > z_b. \end{cases} \quad (4.40)$$

The best-fit parameters for Model 1 are given by Pozzetti et al. (2016) as

$$\alpha = -1.35, \quad \delta = 2, \quad L_{*0} = 10^{41.5} \text{ erg s}^{-1}, \quad \Phi_{*0} = 10^{-2.8} \text{ Mpc}^{-3}, \quad \epsilon = 1, \quad z_b = 1.3. \quad (4.41)$$

The flux cut F_c translates to a luminosity cut:

$$L_c(z) = 4\pi F_c d_L(z)^2, \quad F_c = 3 \times 10^{-16} \text{ erg cm}^{-2} \text{ s}^{-1}, \quad (4.42)$$

where d_L is the background luminosity distance and the choice of F_c follows Yankelevich & Porciani (2019).

In order to compute b_e and \mathcal{Q} , we require the comoving number density

$$n_g(z) = \int_{y_c(z)}^{\infty} dy \Phi(z, y) = \Phi_*(z) \Gamma(\alpha + 1, y_c(z)), \quad (4.43)$$

where Γ is the upper incomplete Gamma function and

$$y_c(z) = \frac{4\pi F_c}{L_{*0}} r(z)^2 = \left[\frac{r(z)}{2.97 h \times 10^3 (\text{Mpc}/h)} \right]^2. \quad (4.44)$$

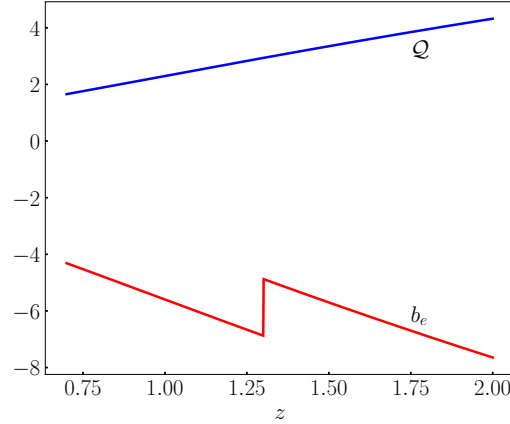


Figure 4.4.: Magnification and evolution bias (4.45), (4.46).

Using (4.44) and (4.39)–(4.42), we confirm that the analytical form (4.43) for n_g recovers the points from Table 1 in Yankelevich & Porciani (2019).

By (4.15), the magnification bias follows as

$$\mathcal{Q}(z) = \left(y \frac{\Phi}{n_g} \right)_c = \frac{y_c(z)^{\alpha+1} \exp[-y_c(z)]}{\Gamma(\alpha+1, y_c(z))}, \quad (4.45)$$

since $\partial/\partial \ln L = \partial/\partial \ln y$, and the evolution bias is

$$b_e(z) = -\frac{d \ln \Phi_*(z)}{d \ln(1+z)} + \frac{d \ln y_c(z)}{d \ln(1+z)} \mathcal{Q}(z). \quad (4.46)$$

Figure 4.4 shows the analytical forms (4.45) and (4.46) for b_e and \mathcal{Q} .

Table 4.1 collects the information in Figs. 4.3 and 4.4 to provide an extension of Table 1 in Yankelevich & Porciani (2019).

Finally, we need to deal with the luminosity derivative of the bias in (4.13). Simulations by Pan et al. (2019) indicate that the clustering bias of $H\alpha$ galaxies does not vary appreciably with luminosity near the fiducial luminosity L_{*0} in (4.41) and for $z \lesssim 2$ (see their Fig. 8). We therefore take

$$\left. \frac{\partial b_1}{\partial \ln L} \right|_c = 0, \quad (4.47)$$

in (4.13).

4. Detectability in next-generation galaxy surveys

Table 4.1.: Stage IV $H\alpha$ spectroscopic survey parameters.

z	b_1	b_2	b_{s^2}	b_e	\mathcal{Q}	n_g $10^{-3}h^3\text{Mpc}^{-3}$	V $h^{-3}\text{Gpc}^3$	σ $h^{-1}\text{Mpc}$
0.7	1.18	-0.766	-0.105	-4.31	1.66	2.76	2.82	4.81
0.8	1.22	-0.759	-0.127	-4.74	1.87	2.04	3.38	4.72
0.9	1.26	-0.749	-0.149	-5.17	2.08	1.53	3.70	4.62
1.0	1.30	-0.737	-0.172	-5.60	2.30	1.16	4.08	4.51
1.1	1.34	-0.721	-0.194	-6.02	2.51	0.880	4.42	4.39
1.2	1.38	-0.703	-0.217	-6.45	2.72	0.680	4.72	4.27
1.3	1.42	-0.682	-0.240	-6.76	2.94	0.520	4.98	4.15
1.4	1.46	-0.658	-0.262	-5.29	3.14	0.380	5.20	4.03
1.5	1.50	-0.631	-0.285	-5.70	3.35	0.260	5.38	3.92
1.6	1.54	-0.600	-0.308	-6.10	3.55	0.200	5.54	3.81
1.7	1.58	-0.567	-0.332	-6.50	3.75	0.150	5.67	3.70
1.8	1.62	-0.531	-0.355	-6.89	3.94	0.110	5.77	3.61
1.9	1.66	-0.491	-0.378	-7.27	4.13	0.0900	5.85	3.49
2.0	1.70	-0.449	-0.401	-7.64	4.32	0.0700	6.92	3.40

4.3.2. Relativistic signal-to-noise ratio

We can now evaluate the Doppler-type relativistic part of the bispectrum, (4.8)–(4.14), using (4.45)–(4.47). Then the SNR is computed using (4.20) and (4.25) together with (4.30). The results, for SNR in each z -bin, $S/N(z)$, and for the cumulative SNR, $S/N(\leq z)$, are shown in Fig. 4.5. Our forecasts indicate that the total SNR, $S/N(\leq z_{\max})$, for a Stage IV $H\alpha$ survey could be $\mathcal{O}(10)$, which is high enough for a detection in principle.

The relativistic SNR is sensitive in particular to two factors:

- Changes in the nonperturbative scale $k_{\max}(z)$: this sensitivity is due to the coupling of long-wavelength relativistic terms to short-wavelength Newtonian terms. We use a conservative and redshift-dependent k_{\max} , given in (4.26). In Fig. 4.6 we show the comparison of SNR using (4.26) and using the redshift-independent $k_{\max} = 0.15h/\text{Mpc}$. The redshift-independent model does not incorporate the increase in the nonperturbative scale with growing z , and therefore produces a lower SNR; however, the difference is not large.
- Changes in $b_e(z)$, $\mathcal{Q}(z)$: The effect on the relativistic SNR of changes in magnification bias and in evolution bias is illustrated in Fig. 4.7. In Figure 4.7 we illustrate the significant impact on cumulative SNR of changing b_e , \mathcal{Q} . We use a range of constant choices for b_e , \mathcal{Q} – which are not physically motivated.

4. Detectability in next-generation galaxy surveys

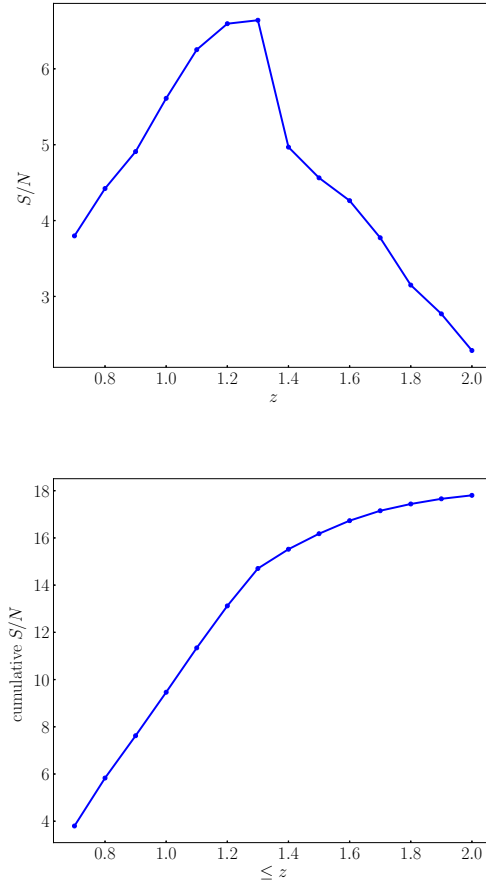


Figure 4.5.: Relativistic SNR per z -bin (*left*) and cumulative (*right*) for a Stage IV $H\alpha$ survey.

This shows the importance of modelling b_e , \mathcal{Q} self-consistently from the same luminosity function that produces the number density, as we have done.

The sensitivity of the relativistic SNR to k_{\max} reflects the importance of the coupling of the relativistic signal to Newtonian terms on short scales. How sensitive is the SNR to the signal on the largest scales? We can answer this by increasing k_{\min} from its fiducial value k_f , which is the maximal observable scale. The result is that there is only a small reduction when k_{\min}/k_f is increased by a factor up to 5, as shown in Fig. 4.8. Even with $k_{\min} = 10k_f$, the total SNR is ~ 10 . This means that the relativistic SNR does not depend critically on accessing the largest possible scales.

It is also interesting to investigate how important for the SNR is the second-order

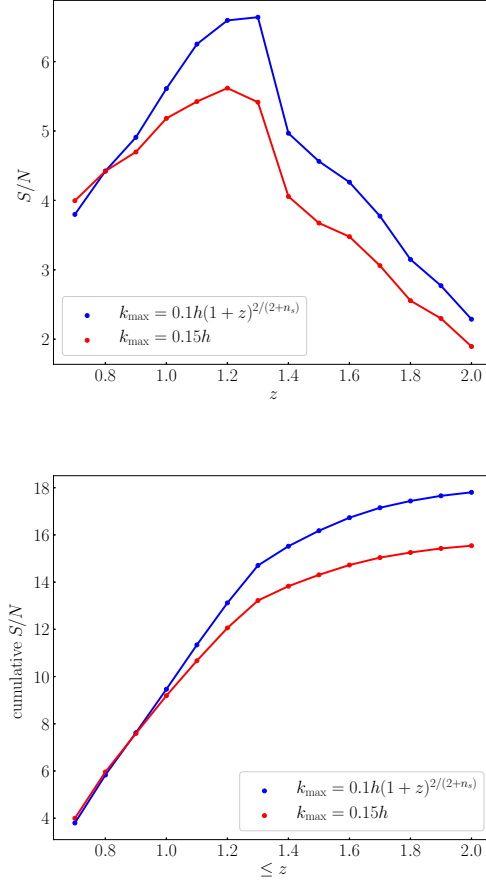


Figure 4.6.: Effect of changing k_{\max} on SNR per bin (*left*) and cumulative SNR (*right*).

relativistic contribution in the bispectrum, i.e. from terms of the form

$$\mathcal{K}_N^{(1)}(\mathbf{k}_1)\mathcal{K}_N^{(1)}(\mathbf{k}_2)\mathcal{K}_D^{(2)}(\mathbf{k}_1, \mathbf{k}_2, \mathbf{k}_3), \quad (4.48)$$

in (4.8), compared to the first-order contribution, i.e. from terms of the form

$$\left[\mathcal{K}_N^{(1)}(\mathbf{k}_1)\mathcal{K}_D^{(1)}(\mathbf{k}_2) + \mathcal{K}_D^{(1)}(\mathbf{k}_1)\mathcal{K}_N^{(1)}(\mathbf{k}_2) \right] \mathcal{K}_N^{(2)}(\mathbf{k}_1, \mathbf{k}_2, \mathbf{k}_3). \quad (4.49)$$

It is conceivable that the first-order Doppler-type contribution in (4.49) to B_g , which couples to first- and second-order Newtonian terms, dominates the SNR. However, we find that the first- and second-order relativistic parts of the bispectrum make comparable contributions to the SNR – see Fig. 4.9. We deduce that the second-order relativistic contribution in (4.48) cannot be neglected. Furthermore, this means that it must be accurately modelled, as we have done.

4. Detectability in next-generation galaxy surveys

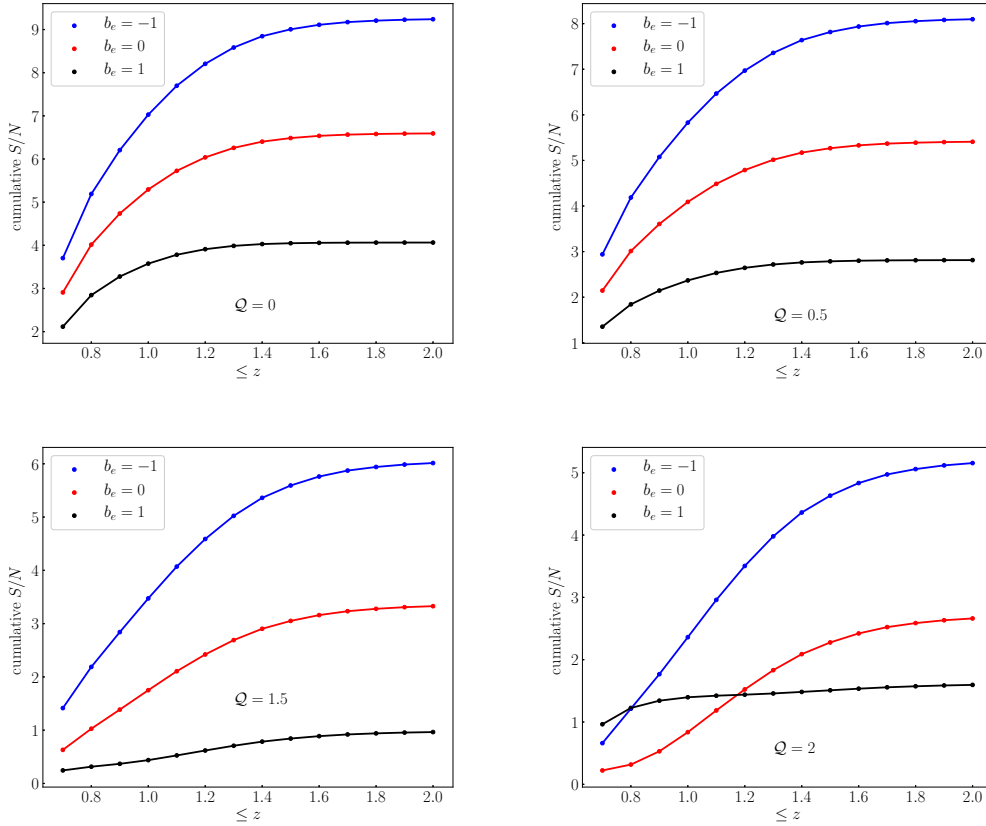


Figure 4.7.: Effect of changing Q and b_e on relativistic cumulative SNR.

Recently Jeong & Schmidt (2020) estimated the SNR for the leading relativistic part of the bispectrum. There are significant differences in their analysis compared to ours. In particular, they neglect most of the terms in $\delta_{gD}^{(2)}$ [see our (3.4)] which defines $\mathcal{K}_D^{(2)}$. In Jeong & Schmidt (2020), a significant number of terms is neglected in the relativistic second-order galaxy number count contrast, $\delta_{gD}^{(2)}$, given by our (3.4). (Note that our (3.4), derived in Clarkson et al. (2019), was independently confirmed by Di Dio & Seljak (2019)). They have the first term, $A \mathbf{v}^{(2)} \cdot \mathbf{n}$, on the right of (3.4). In the second term, $2C(\mathbf{v} \cdot \mathbf{n}) \delta$, they do not have the correct form of the coefficient C – they include only the first part, $b_1 A$, of C [see the right-hand side of eq 26?]. All terms after the second term in (3.4) are omitted by Jeong & Schmidt (2020). Note that none of the omitted terms is suppressed by a higher power of k^{-1} ; they all have the same scaling, i.e., $\propto (\mathcal{H}/k)(\delta)^2$. In detail, they omit the following terms:

$$\delta_{gD}^{(2)}(\text{us}) - \delta_{gD}^{(2)}(\text{Jeong \& Schmidt (2020)}) = 2 \left[b_1 f + \frac{b'_1}{\mathcal{H}} + 2 \left(1 - \frac{1}{r\mathcal{H}} \right) \frac{\partial b_1}{\partial \ln L} \Big|_c \right] (\mathbf{v} \cdot \mathbf{n}) \delta \quad (4.50)$$

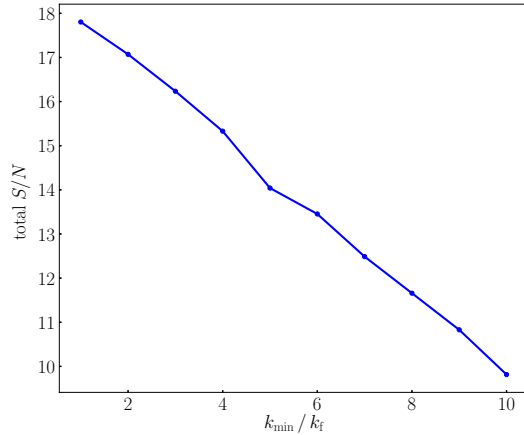


Figure 4.8.: Effect of changing k_{\min} on total relativistic SNR.

$$\begin{aligned}
 & + \frac{2}{\mathcal{H}} \left(4 - 2A - \frac{3}{2}\Omega_m \right) (\mathbf{v} \cdot \mathbf{n}) \partial_r(\mathbf{v} \cdot \mathbf{n}) \\
 & + \frac{2}{\mathcal{H}^2} [(\mathbf{v} \cdot \mathbf{n}) \partial_r^2 \Phi - \Phi \partial_r^2(\mathbf{v} \cdot \mathbf{n})] - \frac{2}{\mathcal{H}} \partial_r(\mathbf{v} \cdot \mathbf{v}) + 2 \frac{b_1}{\mathcal{H}} \Phi \partial_r \delta.
 \end{aligned}$$

In addition they do not use self-consistent models for b_e and \mathcal{Q} . These two differences could account for their conclusion that the relativistic signal is not detectable, in contrast to our result.

An interesting feature of the relativistic signal is that there is a significant contribution to the SNR from flattened triangle shapes. This is consistent with the results of Clarkson et al. (2019) for the dipole that is generated by the imaginary part of the bispectrum.

tidy this, or move to dipole?

4.3.3. Inclusion of cosmological parameters

A full treatment of cosmological constraints would marginalise over the standard cosmological parameters, together with the Alcock-Paczynski parameters and the clustering bias parameters. The constraints obtained would depend almost entirely on the Newtonian galaxy power spectrum and bispectrum (as analysed in Yankelevich & Porciani (2019)), given that the relativistic contribution to the power spectrum is below leading order, while in the bispectrum the relativistic SNR is an order of magnitude smaller than the Newtonian SNR.

Our focus here is instead on the detectability of the relativistic signal in the bispec-

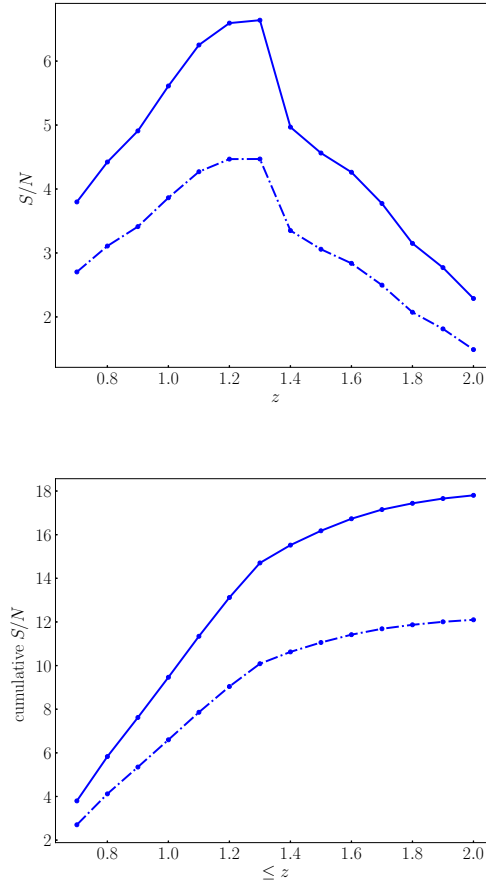


Figure 4.9.: As in Fig. 4.5, but showing the effect of omitting the second-order relativistic contribution (4.48) to the bispectrum (dot-dashed curves).

trum, assuming that P_{gN} and B_{gN} have been used to constrain the standard parameters. We now investigate the effect on this detectability when we include the parameters directly related to redshift-space effects, i.e., the growth index $\gamma = \ln f / \ln \Omega_m$ (with fiducial value 0.545), and the clustering amplitude σ_8 (with Planck 2018 fiducial). For forecasts we use the theoretical values of b_e, Q . In a galaxy survey, they would be measured directly from the observed luminosity function, and their measurement uncertainties would need to be marginalised over.

For the relativistic part of the bispectrum, we introduce a parameter A_D , with fiducial value 1:

$$B_g = B_{gN} + A_D B_{gD}. \quad (4.51)$$

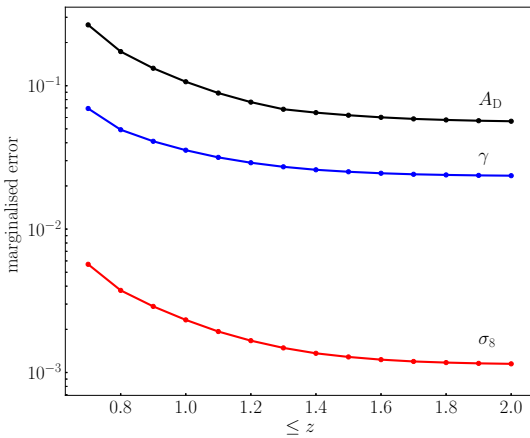


Figure 4.10.: Marginal errors (cumulative) on the relativistic contribution, growth index and clustering amplitude, using the full bispectrum.

Then the Fisher matrix for the parameters $\vartheta_\alpha = (A_D, \gamma, \sigma_8)$ is

$$F_{\alpha\beta} = \sum_{z, k_a, \mu_1, \varphi} \frac{1}{\text{Var}[B_g]} \frac{\partial B_g}{\partial \vartheta_{(\alpha}}} \frac{\partial B_g^*}{\partial \vartheta_{\beta}}, \quad (4.52)$$

where the round brackets denote symmetrisation. The cumulative marginal errors $\sigma_\alpha = [(F^{-1})_{\alpha\alpha}]^{1/2}$ are shown in Fig. 4.10. The fact that $\sigma_{A_D} \lesssim 0.1$ means that the relativistic effects remain detectable when the two additional cosmological parameters are marginalised over.

4.3.4. Conclusions

As shown by Clarkson et al. (2019), the tree-level galaxy bispectrum in Fourier space has an imaginary part which is a unique signal of the leading-order relativistic corrections in redshift space. These corrections arise from Doppler and other line-of-sight effects on the past lightcone [see (4.6), (3.4)]. In the galaxy bispectrum, the corrections scale as $i(\mathcal{H}/k)P^2$, where P is the linear matter power spectrum [see (4.8)–(4.10)]. By contrast, at leading order in the galaxy power spectrum, the relativistic correction is real and scales as $(\mathcal{H}/k)^2 P$ – i.e., it is suppressed by a further factor of \mathcal{H}/k . Only the cross-power spectrum of two different tracers produces an imaginary contribution that scales as $i(\mathcal{H}/k)P$ McDonald (2009).¹

¹See also Bonvin et al. (2014, 2016); Gaztanaga et al. (2017); Iršič et al. (2016); Hall & Bonvin (2017); Lepori et al. (2018); Bonvin & Fleury (2018); Lepori et al. (2020) for the corresponding

4. Detectability in next-generation galaxy surveys

For a single tracer, the $(\mathcal{H}/k)^2$ relativistic signal in the galaxy *power* spectrum is not detectable, even for a cosmic-variance limited survey Alonso et al. (2015b). The galaxy bispectrum of a single tracer, with its $i(\mathcal{H}/k)$ relativistic contribution, improves the chances of detectability. In addition, the relativistic contribution in the bispectrum couples to short-scale Newtonian terms – which means that the signal is not confined to very large scales, unlike the case of the power spectrum. We confirmed the expectations of detectability by showing that the signal to noise on the imaginary relativistic part is $\mathcal{O}(10)$ for a Stage IV $H\alpha$ spectroscopic survey similar to Euclid [see Fig. 4.5]. We checked that detectability is not compromised by including the uncertainties on two cosmological growth parameters, σ_8 and γ [Fig. 4.10], assuming that other cosmological and nuisance parameters are determined by the Newtonian power spectrum and bispectrum.

The relativistic SNR depends on the $k_{\max}(z)$ assumed, because of the coupling of relativistic effects to short-scale Newtonian terms [Fig. 4.6], and we made a conservative choice (4.26), which includes a redshift dependence to reflect the weakening of nonlinearity at higher z . Accurate modelling of nonlinear effects would allow us to increase the SNR – this is not at all specific to the relativistic signal, but is required for the standard analysis of RSD.

The relativistic SNR also relies on the largest available scales, but very little signal is lost if k_{\min}/k_f is increased by a factor up to 5, and even a factor of 10 increase leaves a detectable SNR [Fig. 4.8].

By contrast, the SNR depends strongly on accurate modelling of the second-order part of the relativistic correction [Fig. 4.9]. This includes both the theoretical form (3.4), and the two astrophysical parameters that do not appear in the Newtonian approximation of the galaxy bispectrum: the evolution bias b_e (measuring the deviation from comoving number conservation) and the magnification bias \mathcal{Q} (which is brought into play by a Doppler correction to standard lensing magnification). A key feature of our analysis is a physically self-consistent derivation of these quantities from the luminosity function [Fig. 4.4 and (4.45), (4.46)]. We showed that the SNR is very sensitive to these parameters [Fig. 4.7], which underlines the need for accurate physical modelling.

We assumed a Gaussian covariance in our computations, but we used the approximation of Chan & Blot (2017) to include non-Gaussian corrections.

effect in the two-point correlation function, and see Okoli et al. (2017) for an imaginary short-scale contribution from neutrino drag on haloes.

4. Detectability in next-generation galaxy surveys

Further work should include the window function which we have neglected. The imaginary part of the galaxy bispectrum generates a dipole, as shown in Clarkson et al. (2019). This suggests a multipole analysis that uses the relativistic dipole in addition to the monopole and quadrupole, which are unaffected by relativistic effects at leading order. The window function can also have an imaginary part Beutler et al. (2019), which will need to be corrected for. The dipole from the imaginary part of the bispectrum vanishes in equilateral configurations Clarkson et al. (2019), which may help to disentangle the relativistic dipole from that of the window function.

Our analysis, in common with other works on the Fourier bispectrum, implicitly uses the plane-parallel approximation, since the line-of-sight direction \mathbf{n} is fixed. At the cost of significant complexity, the approximation can be avoided, for example by using a Fourier-Bessel analysis of bispectrum multipoles Castorina & White (2018). Further work is needed to address this, but we note that errors from the approximation are mitigated in high redshift surveys such as the one considered here.

Finally, further work also needs to include the effects of lensing magnification, which are excluded in the standard Fourier analysis, but have been included in the galaxy angular bispectrum Kehagias et al. (2015); Di Dio et al. (2016, 2017, 2019) and in a spherical Bessel analysis Bertacca et al. (2018).

4.4. 21cm intensity mapping surveys

In this work, we investigate the detectability of the relativistic signal in the bispectrum of various planned 21cm intensity mapping surveys at post-reionisation redshifts. The 21cm emission line of neutral hydrogen (HI) is measured without detecting the individual galaxies that contain HI. This results in brightness temperature maps that trace the large-scale structure with exquisite redshift precision. In Section 2 we discuss the leading order relativistic form of the temperature contrast up to second order, and its contribution to the bispectrum. Section 3 describes the signal, modelled using the tree-level bispectrum with the addition of a phenomenological model to account for RSD ‘fingers-of-god’ nonlinearity. Foreground contamination overwhelms the signal, and cleaning techniques must be applied which lead to a loss of signal in regions of Fourier space, which we take into account. We also discuss the effects of telescope beams and the instrumental noise. Our forecast sig-

4. Detectability in next-generation galaxy surveys

nal to noise for future surveys is presented in Section 4, and we conclude in Section 5.

4.4.1. Relativistic effects in the 21cm IM bispectrum

The HI brightness temperature measured at redshift z in direction \mathbf{n} is related to the observed number of 21cm emitters per redshift per solid angle, N_{HI} , as follows (see Hall et al. (2013); Alonso et al. (2015b) for details):

$$T_{\text{HI}}(z, \mathbf{n}) = \text{const.} \frac{N_{\text{HI}}(z, \mathbf{n})}{d_A(z, \mathbf{n})^2}, \quad (4.53)$$

where d_A is the angular diameter distance.

The background HI brightness temperature follows from (4.53) as Villaescusa-Navarro et al. (2018)

$$\bar{T}_{\text{HI}}(z) = 189h \frac{(1+z)H_0}{\mathcal{H}(z)} \Omega_{\text{HI}}(z) \text{ mK}. \quad (4.54)$$

Here $h = H_0/(100 \text{ km/s})$, $\mathcal{H} = (\ln a)'$ is the conformal Hubble rate, and $\Omega_{\text{HI}}(z)$ is the comoving HI density in units of the critical density today, which is currently poorly constrained by observations and is modelled by simulations. We use the fit in Santos et al. (2017):

$$\bar{T}_{\text{HI}}(z) = 0.056 + 0.23z - 0.024z^2 \text{ mK}. \quad (4.55)$$

The temperature fractional perturbation ism

$$\Delta_{\text{HI}}(z, \mathbf{n}) = \frac{T_{\text{HI}}(z, \mathbf{n}) - \bar{T}_{\text{HI}}(z)}{\bar{T}_{\text{HI}}(z)}. \quad (4.56)$$

Using (4.53), this leads to the following perturbative expansion (our convention is $X + X^{(2)}/2$). (A clear and concise derivation of the following expressions for Δ and $\Delta^{(2)}$ is given in Appendix A of Di Dio & Seljak (2019).)

- **At first order** Hall et al. (2013):

$$\Delta \equiv \Delta_{\text{HI}}^{(1)} = \Delta_N + \Delta_D, \quad \Delta_N = b_1 \delta_m - \frac{1}{\mathcal{H}} \partial_r(\mathbf{v} \cdot \mathbf{n}), \quad \Delta_D = A(\mathbf{v} \cdot \mathbf{n}). \quad (4.57)$$

Here r is the radial comoving distance and $\mathbf{v} = \nabla V$ is the peculiar velocity. Δ_N is the standard density + RSD term, which scales as δ_m . Δ_D is the dominant

4. Detectability in next-generation galaxy surveys

relativistic correction, scaling as $i(\mathcal{H}/k)\delta_m$ in Fourier space. This Doppler term has coefficient

$$A = b_e - 2 - \frac{\mathcal{H}'}{\mathcal{H}^2} = -\frac{d \ln [(1+z)\bar{T}_{\text{HI}}]}{d \ln(1+z)}, \quad (4.58)$$

where the evolution bias is Fonseca et al. (2015),

$$b_e = -\frac{d \ln [(1+z)^{-1}\mathcal{H}\bar{T}_{\text{HI}}]}{d \ln(1+z)}. \quad (4.59)$$

We omit sub-leading relativistic corrections that scale as $(\mathcal{H}/k)^2\delta_m$.

- **At second order** Maartens et al. (2020) (see also Umeh et al. (2016); Di Dio et al. (2016); Umeh (2017); Clarkson et al. (2019); Di Dio & Seljak (2019)):

$$\Delta^{(2)} \equiv \Delta_{\text{HI}}^{(2)} = \Delta_{\text{N}}^{(2)} + \Delta_{\text{D}}^{(2)}, \quad (4.60)$$

$$\Delta_{\text{N}}^{(2)} = b_1\delta_m^{(2)} + b_2(\delta_m)^2 + b_{s^2}s^2 + \text{RSD}^{(2)}, \quad (4.61)$$

$$\begin{aligned} \Delta_{\text{D}}^{(2)} &= A(\mathbf{v}^{(2)} \cdot \mathbf{n}) + 2 \left[b_1(A+f) + \frac{b'_1}{\mathcal{H}} \right] (\mathbf{v} \cdot \mathbf{n}) \delta_m + \frac{1}{\mathcal{H}} (8 - 4A - 3\Omega_m) (\mathbf{v} \cdot \mathbf{n}) \partial_r(\mathbf{v} \cdot \mathbf{n}) \\ &+ \frac{2}{\mathcal{H}^2} [(\mathbf{v} \cdot \mathbf{n}) \partial_r^2 \Phi - \Phi \partial_r^2(\mathbf{v} \cdot \mathbf{n})] - \frac{2}{\mathcal{H}} \partial_r(\mathbf{v} \cdot \mathbf{v}) + 2 \frac{b_1}{\mathcal{H}} \Phi \partial_r \delta_m. \end{aligned} \quad (4.62)$$

In (4.61), $b_{s^2}s^2$ is the tidal bias contribution and $\text{RSD}^{(2)}$ is the standard second-order RSD contribution (see Maartens et al. (2020) for details). The bias parameters are computed via a halo model (see Appendix) and are shown in Figure 4.11, together with the evolution bias. In (4.62), we see the Doppler terms and the line-of-sight gradients that make up the dominant relativistic contribution. Φ is the gravitational potential and $\Omega_m = \Omega_{m0}(1+z)H_0^2/\mathcal{H}^2$. We neglect sub-dominant relativistic effects in $\Delta^{(2)}$ that scale as $(\mathcal{H}/k)^2(\delta_m)^2$.

reference appendix

- **Lensing contribution:**

At first order, there is no lensing contribution to Δ Hall et al. (2013). The general case of galaxy number density contrast contains a lensing contribution $2(\mathcal{Q} - 1)\kappa$ to Δ_g , where κ is the convergence Challinor & Lewis (2011). For HI emitters in intensity mapping, the magnification bias satisfies

$$\mathcal{Q} \equiv -\frac{\partial \ln \bar{N}_{\text{HI}}}{\partial \ln L} \Big|_{\text{c}} = 1, \quad (4.63)$$

4. Detectability in next-generation galaxy surveys

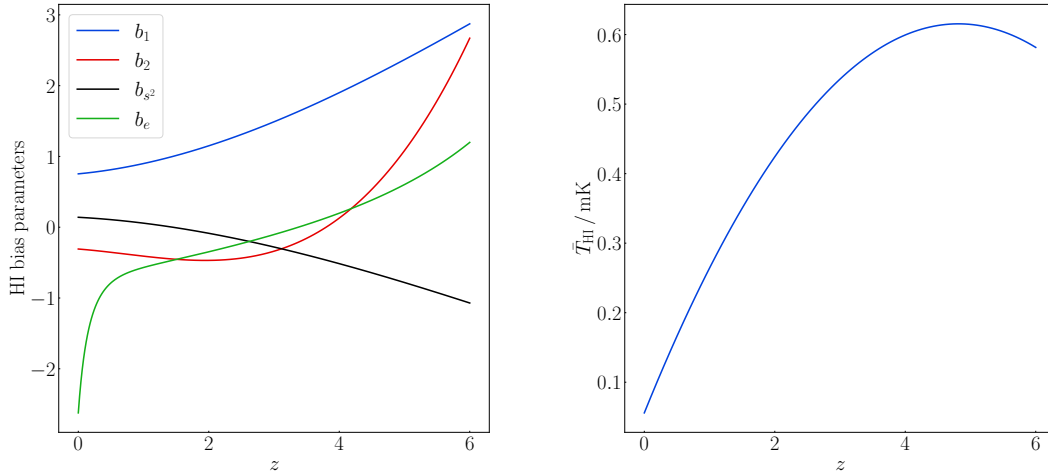


Figure 4.11.: HI clustering and evolution bias parameters (left) and background temperature (right).

where c indicates evaluation at the luminosity cut.

At second order, (4.53) shows that there is also no contribution to $\Delta^{(2)}$ from lensing convergence Di Dio et al. (2016); Jalilvand et al. (2019). We can recover this result from the full general expression for second-order number density contrast Bertacca et al. (2014a,b); Yoo & Zaldarriaga (2014); Di Dio et al. (2014); Bertacca (2015), by imposing (4.63) together with the conditions Di Dio et al. (2016)

$$\frac{\partial^2 \ln \bar{N}_{\text{HI}}}{\partial (\ln L)^2} \Big|_c = 0, \quad \frac{\partial b_1}{\partial \ln L} \Big|_c = 0. \quad (4.64)$$

There remains however a lensing deflection contribution $\nabla_{\perp a} \Delta \nabla_{\perp}^a \phi$ to $\Delta^{(2)}$, where $\nabla_{\perp a}$ is a screen-space gradient and ϕ is the lensing potential Umeh et al. (2016); Di Dio et al. (2016); Jalilvand et al. (2019). In the bispectrum the contribution of this term is negligible for equal-redshift correlations Di Dio et al. (2016); Durrer et al. (2020). Since we only consider the bispectrum at equal redshifts, we can safely neglect this term.

In Fourier space, the HI bispectrum at tree level is defined by,

$$\langle \Delta(z, \mathbf{k}_1) \Delta(z, \mathbf{k}_2) \Delta^{(2)}(z, \mathbf{k}_3) \rangle + 2 \text{ cp} = 2(2\pi)^3 B_{\text{HI}}(z, \mathbf{k}_1, \mathbf{k}_2, \mathbf{k}_3) \delta^{\text{Dirac}}(\mathbf{k}_1 + \mathbf{k}_2 + \mathbf{k}_3), \quad (4.65)$$

4. Detectability in next-generation galaxy surveys

where cp denotes cyclic permutation. It follows that,

$$B_{\text{HI}}(z, \mathbf{k}_1, \mathbf{k}_2, \mathbf{k}_3) = \mathcal{K}^{(1)}(z, \mathbf{k}_1)\mathcal{K}^{(1)}(z, \mathbf{k}_2)\mathcal{K}^{(2)}(z, \mathbf{k}_1, \mathbf{k}_2, \mathbf{k}_3)P_m(z, k_1)P_m(z, k_2) + 2 \text{ cp}, \quad (4.66)$$

where P_m is the linear matter power spectrum (computed using CLASS Blas et al. (2011)). From now on, we often drop the z dependence for brevity. The bispectrum kernels are as follows:

- **Standard (Newtonian) kernels:**

$$\mathcal{K}_{\text{N}}^{(1)}(\mathbf{k}_1) = b_1 + f\mu_a^2, \quad (4.67)$$

$$\mathcal{K}_{\text{N}}^{(2)}(\mathbf{k}_1, \mathbf{k}_2, \mathbf{k}_3) = b_1 F_2(\mathbf{k}_1, \mathbf{k}_2) + b_2 + f\mu_a^2 G_2(\mathbf{k}_1, \mathbf{k}_2) + f\mathcal{Z}_2(\mathbf{k}_1, \mathbf{k}_2) + b_{s^2} S_2(\mathbf{k}_1, \mathbf{k}_2), \quad (4.68)$$

where f is the linear matter growth rate, $\mu_a = \hat{\mathbf{k}}_a \cdot \mathbf{n}$ and the standard $F_2, G_2, \mathcal{Z}_2, S_2$ kernels are given in Maartens et al. (2020).

- **Leading-order relativistic kernels:**

$$\mathcal{K}_{\text{D}}^{(1)}(\mathbf{k}_1) = i\mathcal{H}fA \frac{\mu_a}{k_a}, \quad (4.69)$$

$$\begin{aligned} \mathcal{K}_{\text{D}}^{(2)}(\mathbf{k}_1, \mathbf{k}_2, \mathbf{k}_3) = & i\mathcal{H}f \left\{ A \frac{\mu_3}{k_3} G_2(\mathbf{k}_1, \mathbf{k}_2) + \left[b_1(A+f) + \frac{b'_1}{\mathcal{H}} \right] \left(\frac{\mu_1}{k_1} + \frac{\mu_2}{k_2} \right) \right. \\ & - \frac{3}{2}\Omega_m \left(\mu_1^3 \frac{k_1}{k_2^2} + \mu_2^3 \frac{k_2}{k_1^2} \right) + \left[\frac{3}{2}\Omega_m(1+f) + 2f(A-2) \right] \mu_1\mu_2 \left(\frac{\mu_1}{k_2} + \frac{\mu_2}{k_1} \right) \\ & \left. + 2f \hat{\mathbf{k}}_1 \cdot \hat{\mathbf{k}}_2 \left(\frac{\mu_1}{k_1} + \frac{\mu_2}{k_2} \right) - \frac{3\Omega_m b_1}{2f} \left(\mu_1 \frac{k_1}{k_2^2} + \mu_2 \frac{k_2}{k_1^2} \right) \right\}, \end{aligned} \quad (4.70)$$

where A is given by (4.58). These follow from (4.57) and (4.62), and agree with Maartens et al. (2020) when we impose (4.58), (4.63) and (4.64).

- **Complex bispectrum:**

From (4.67)–(4.70) we see that B_{HI} is complex: the imaginary part is given purely by local relativistic corrections, while at leading order, i.e. neglecting relativistic terms of $\mathcal{O}(\mathcal{H}^2/k^2)$, the real part is given purely by the standard Newtonian bispectrum:

$$\text{Re}(B_{\text{HI}}) = B_{\text{N}} = \mathcal{K}_{\text{N}}^{(1)}(\mathbf{k}_1)\mathcal{K}_{\text{N}}^{(1)}(\mathbf{k}_2)\mathcal{K}_{\text{N}}^{(2)}(\mathbf{k}_1, \mathbf{k}_2, \mathbf{k}_3)P_m(k_1)P_m(k_2) + 2 \text{ cp}, \quad (4.71)$$

4. Detectability in next-generation galaxy surveys

$$\begin{aligned} i \operatorname{Im}(B_{\text{HI}}) = B_D = & \left\{ \left[\mathcal{K}_N^{(1)}(\mathbf{k}_1) \mathcal{K}_D^{(1)}(\mathbf{k}_2) + \mathcal{K}_D^{(1)}(\mathbf{k}_1) \mathcal{K}_N^{(1)}(\mathbf{k}_2) \right] \mathcal{K}_N^{(2)}(\mathbf{k}_1, \mathbf{k}_2, \mathbf{k}_3) \right. \\ & \left. + \mathcal{K}_N^{(1)}(\mathbf{k}_1) \mathcal{K}_N^{(1)}(\mathbf{k}_2) \mathcal{K}_D^{(2)}(\mathbf{k}_1, \mathbf{k}_2, \mathbf{k}_3) \right\} P_m(k_1) P_m(k_2) + 2 \text{ cp.} \end{aligned} \quad (4.72)$$

It is apparent that $B_N \sim P_m^2$ while $B_D \sim i(\mathcal{H}/k)P_m^2$. Equation (4.72) makes explicit the coupling of relativistic and Newtonian terms in the bispectrum.

HI bias parameters

check where to put this

We follow Umeh et al. (2016) to compute b_1 and b_2 from a halo-model approach,

$$b_1 = 1 + \left\langle \frac{2p + (q\nu - 1)[1 + (q\nu)^p]}{\delta_{\text{cr}}[1 + (q\nu)^p]} \right\rangle_m, \quad (4.73)$$

$$b_2 = \frac{8}{21} (b_1 - 1) + \left\langle \frac{2p(2p + 2\nu q - 1) + q\nu(q\nu - 3)[1 + (q\nu)^p]}{\delta_{\text{cr}}^2[1 + (q\nu)^p]} \right\rangle_m, \quad (4.74)$$

where the parameters p , q and ν are related to the Sheth-Tormen distribution function (see Sheth et al. (2001); Sheth & Tormen (2002, 1999) for more details), and δ_{cr} is the critical density at which halos collapse spherically Kitayama & Suto (1996),

$$\delta_{\text{cr}}(z) = \frac{3(12\pi)^{2/3}}{20} [1 + 0.0123 \log \Omega_m(z)] \dots \quad (4.75)$$

The mass average is defined by

$$\langle X_h(z, \mathbf{x}) \rangle_m = \frac{\int_{M_-}^{M_+} dM X_h(z, \mathbf{x}, M) M_{\text{HI}}(M) n_h(z, \mathbf{x}, M)}{\int_{M_-}^{M_+} dM M_{\text{HI}}(M) n_h(z, \mathbf{x}, M)}, \quad (4.76)$$

where M is the mass of halos that can host HI gas, and M_{\pm} are the lower and upper mass limits, which are related to the circular velocities of the galaxies (Bull et al., 2015). n_h is the halo mass function (Sheth et al., 2001; Sheth & Tormen, 2002; Tellarini et al., 2015), and M_{HI} is the HI mass function, which is assumed to follow a power law (Santos et al., 2015),

$$M_{\text{HI}}(M) \propto M^{0.6}. \quad (4.77)$$

Figure 4.3 shows the numerical results from (4.73) and (4.74). Fitting formulas for

4. Detectability in next-generation galaxy surveys

the bias parameters are

$$b_1(z) = 0.754 + 0.0877z + 0.0607z^2 - 0.00274z^3, \quad (4.78)$$

$$b_2(z) = -0.308 - 0.0724z - 0.0534z^2 + 0.0247z^3. \quad (4.79)$$

Assuming that halo formation is a local process in Lagrangian space and that there is no initial tidal bias, the tidal bias is Tellarini et al. (2015),

$$b_{s^2} = \frac{4}{7}(1 - b_1). \quad (4.80)$$

4.4.2. Effects of foregrounds

Foreground contamination is the major systematic confronting 21cm intensity mapping. Cleaning techniques are very efficient at recovering the cosmological signal in regions of $(k_{\parallel}, k_{\perp})$ space (see e.g. Pober et al. (2014); Bull et al. (2015); Alonso et al. (2015a); Pober (2015); Wolz et al. (2015); Santos et al. (2015); Shaw et al. (2015); Obuljen et al. (2018); Ansari et al. (2018); Witzemann et al. (2019); Bacon et al. (2020); Asorey et al. (2020); Cunningham et al. (2020)). A realistic model of bispectrum measurements should include modelling of foreground removal. However, our focus is on the relativistic signal in the bispectrum and so we take a simpler approach – by excising the regions of $(k_{\parallel}, k_{\perp})$ space where foreground cleaning does not recover the signal efficiently.

HI intensity mapping surveys are planned for next-generation radio dish arrays, including MeerKAT², SKA1-MID³, and HIRAX⁴. We will also consider surveys with PUMA⁵ in its initial phase (Petite) (note that PUMA is currently still a proposal).

Intensity mapping surveys can be done in 2 survey modes:

- Single-dish (SD) mode: auto-correlation signals from single dishes are added.
- Interferometer (IF) mode: cross-correlation signals from array elements are combined.

In both SD- and IF-mode surveys, foreground cleaning effectively removes large-scale radial modes because of the smoothness in frequency of the main foreground

²www.sarao.ac.za/science/meerkat/

³www.skatelescope.org/

⁴hirax.ukzn.ac.za/

⁵www.puma.bnl.gov/

4. Detectability in next-generation galaxy surveys

emissions. In order to model the effects of foreground cleaning, we remove radial modes $k_{\parallel} \equiv \mu k$ that are smaller than a critical scale $k_{\parallel\text{fg}}$ Karagiannis et al. (2018). We impose this via an exponential damping factor Bull et al. (2015),

$$D_{\text{fg}}(k, \mu) = 1 - \exp \left[- \left(\frac{\mu k}{k_{\parallel\text{fg}}} \right)^2 \right] \quad \text{for SD and IF survey modes.} \quad (4.81)$$

Then,

$$P_{\text{HI}}(k, \mu, z) \rightarrow D_{\text{fg}}(k, \mu) P_{\text{HI}}(k, \mu, z), \quad (4.82)$$

$$B_{\text{HI}}(k_a, \mu_a, z) \rightarrow D_{\text{fg}}(k_1, \mu_1) D_{\text{fg}}(k_2, \mu_2) D_{\text{fg}}(k_3, \mu_3) B_{\text{HI}}(k_a, \mu_a, z). \quad (4.83)$$

The value of $k_{\parallel\text{fg}}$ can be reduced by techniques which reconstruct long modes from the information in measured short modes. This technique has been applied to HI intensity mapping by Zhu et al. (2018); Modi et al. (2019). Taking into account reconstruction, we choose,

$$k_{\parallel\text{fg}} = 0.01 h \text{ Mpc}^{-1}, \quad (4.84)$$

but we will also consider an optimistic case, $k_{\parallel\text{fg}} = 0.005 h \text{ Mpc}^{-1}$, that anticipates further developments of the reconstruction technique.

IF-mode surveys lose additional signal due to the fact that interferometers are chromatic, i.e. a fixed physical baseline length probes different angular scales at different frequencies. This causes smooth foregrounds to leak into high- k_{\perp} modes Obuljen et al. (2018); Alonso et al. (2017); Ansari et al. (2018). The signal loss may be accounted for by excluding the region known as the foreground wedge Pober (2015); Pober et al. (2014):

$$|k_{\parallel}| > k_{\text{wedge}}(z) k_{\perp} \quad \text{for IF survey mode,} \quad (4.85)$$

where $k_{\perp} = \sqrt{1 - \mu^2} k$ and k_{wedge} is modelled as,

$$k_{\text{wedge}}(z) = r(z) \mathcal{H}(z) \sin [0.61 N_w \theta_b(z)]. \quad (4.86)$$

The beam (defining the IF field of view) is given for a dish array by,

$$\theta_b(z) = 1.22 \frac{\lambda(z)}{D_d}, \quad (4.87)$$

where $\lambda(z) = \lambda_{21}(1 + z)$ and D_d is the dish diameter. N_w is the number of primary

4. Detectability in next-generation galaxy surveys

beams away from the beam centre that contaminate the signal. The wedge effect is a technical problem that can be mitigated (and in principle removed) by calibration of baselines Ghosh et al. (2018). Following Karagiannis et al. (2020b), we take

$$N_w = 0, 1, 3, \quad (4.88)$$

where 0 is the most optimistic possibility (wedge removed by calibration) and 3 is a pessimistic case.

4.4.3. Maximum and minimum scales probed

The nonlinearity limit $k \leq k_{\max}(z)$ given in (4.26), defines a minimum wavelength $2\pi/k_{\max}(z)$ that is independent of surveys and is determined purely by dark matter clustering. It applies to both SD- and IF-mode surveys. However, in the case of IF-mode surveys, there is also a lower limit on angular scales, i.e. an upper limit on transverse wavenumbers, via $k_{\perp} = 2\pi/(r\theta)$. This arises because the maximum baseline D_{\max} determines the angular resolution and the upper limit can be roughly estimated by a cut-off Bull et al. (2015); Alonso et al. (2017); Karagiannis et al. (2020b); Durrer et al. (2020),

$$k_{\perp\max}^{\text{IF}}(z) \approx \frac{2\pi D_{\max}}{r(z) \lambda(z)}. \quad (4.89)$$

In our computations, we do not use this cut-off since it is effectively imposed by the baseline density factor (see Section 4.4.4).

In principle, the maximum wavelength probed by HI intensity surveys at redshift z is $2\pi/k_f(z)$, where the fundamental mode k_f is determined by the comoving volume of the redshift bin, via equation. However, foreground cleaning imposes on both SD- and IF-mode surveys the limiting minimum radial wavenumber $k_{\parallel\text{fg}}$, given by (4.84). Since $k^2 = k_{\parallel}^2 + k_{\perp}^2$, this means that

$$k > k_{\parallel\text{fg}} \quad \text{which implies} \quad k > k_{\min} = \max \{k_f(z), k_{\parallel\text{fg}}\}. \quad (4.90)$$

In IF-mode surveys there is a further minimum wavenumber, corresponding to the maximum angular scale that can be probed. This limit depends on the minimum baseline and is given by Bull et al. (2015); Alonso et al. (2017); Karagiannis et al.

insert right equation reference

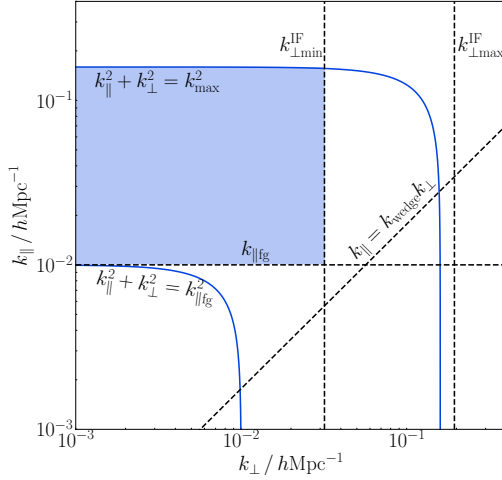


Figure 4.12.: Schematic of important scales in the k_{\parallel}, k_{\perp} -plane at fixed z . Shading indicates the included region for SD mode (light) and IF mode (dark).

(2020b); Durrer et al. (2020),

$$k_{\perp\text{min}}^{\text{IF}}(z) = \frac{2\pi}{r(z)\theta_b(z)}. \quad (4.91)$$

Since $k > k_{\perp}$, we have

$$k > k_{\min} = \max \{ k_{\perp\text{min}}^{\text{IF}}(z), k_f(z), k_{\parallel\text{fg}} \} \quad \text{for IF surveys.} \quad (4.92)$$

The scales from foreground cleaning and the maximum and minimum scales are shown schematically in Figure 4.12. This does not include the effects of the beam in SD mode; see Figure

reference Pnoise figure

below.

check the kmin labels, renamed one

4.4.4. Instrumental noise

In HI intensity mapping for the scales and redshifts we consider, the shot noise is much smaller than the instrumental noise for next-generation surveys⁶ and can be

⁶For the futuristic PUMA (Full) survey, the noise is low enough to be comparable to the shot noise Chen et al. (2019).

4. Detectability in next-generation galaxy surveys

safely neglected Castorina & Villaescusa-Navarro (2017); Villaescusa-Navarro et al. (2018). The noise power spectrum for the fractional temperature perturbation is then determined by instrumental noise and is given by Bull et al. (2015); Alonso et al. (2017):⁷

$$P_{\text{noise}}(z) = \frac{2\pi f_{\text{sky}}}{\nu_{21} t_{\text{tot}}} \frac{(1+z)r(z)^2}{\mathcal{H}(z)} \left[\frac{T_{\text{sys}}(z)}{\bar{T}_{\text{HI}}(z)} \right]^2 \frac{\alpha(z, k_{\perp})}{\beta(z, k_{\perp})^2} h^{-3} \text{Mpc}^3. \quad (4.93)$$

Here t_{tot} is the total observing time, and the system temperature may be modelled as (Ansari et al., 2018):

$$T_{\text{sys}}(z) = T_{\text{d}}(z) + T_{\text{sky}}(z) = T_{\text{d}}(z) + 2.7 + 25 \left[\frac{400 \text{ MHz}}{\nu_{21}} (1+z) \right]^{2.75} \text{ K}, \quad (4.94)$$

where T_{d} is the dish receiver temperature. (We consider only dish arrays.)

In (4.93), the dish density factor α and the effective beam β depend on the survey mode as follows Bull et al. (2015); Obuljen et al. (2018); Ansari et al. (2018); Jalilvand et al. (2020); Durrer et al. (2020),

$$\alpha_{\text{SD}} = \frac{1}{N_{\text{d}}}, \quad \beta_{\text{SD}} = \exp \left[-\frac{k_{\perp}^2 r(z)^2 \theta_{\text{b}}(z)^2}{16 \ln 2} \right], \quad (4.95)$$

$$\alpha_{\text{IF}} = \left[\frac{\lambda(z)^2}{A_{\text{e}}} \right]^2 \frac{1}{n_{\text{b}}(z, k_{\perp})}, \quad \beta_{\text{IF}} = \theta_{\text{b}}(z). \quad (4.96)$$

Here N_{d} is the number of dishes and A_{e} is the effective beam area,

$$A_{\text{e}} = 0.7 A_{\text{d}}, \quad A_{\text{d}} = \frac{\pi}{4} D_{\text{d}}^2. \quad (4.97)$$

The dimensionless n_{b} is the baseline density in the image plane (assuming azimuthal symmetry), which is determined by the array distribution. The total number of baselines is $\int d^2 \mathbf{u} n_{\text{b}}(u) = N_{\text{d}}(N_{\text{d}} - 1)/2$. A physical baseline length L is related to an image-plane scale u as

$$L = u\lambda = \frac{k_{\perp}r}{2\pi} \lambda. \quad (4.98)$$

Then the image-plane and physical distributions of the array are related by Ansari et al. (2018),

$$n_{\text{b}}(z, u) = \lambda(z)^2 n_{\text{b}}^{\text{phys}}(L). \quad (4.99)$$

⁷It is also possible to put the beam factor β in the signal, rather than in the noise; see e.g. Bernal et al. (2019) for a discussion.

4. Detectability in next-generation galaxy surveys

4.4.5. Future 21cm IM surveys

We consider surveys proposed for the following dish arrays:

- SD mode: MeerKAT, SKA1-MID.
- IF mode: HIRAX, PUMA (Petite).

The survey specifications are given in Table 4.2, based on Santos et al. (2017); Bacon et al. (2020); Slosar et al. (2019); Karagiannis et al. (2020b); Castorina et al. (2020). Limiting wavenumbers for large wavelengths are shown for these surveys in Figure 4.14: the fundamental wavenumber, [the minimum radial wavenumber \(4.84\)](#) reference kf equation from foreground cleaning and the IF-mode minimum wavenumber (4.91).

ref appendix in caption below

Table 4.2.: HI intensity mapping survey specifications. (For *, see Appendix stuff.)

Survey	Redshift range	f_{sky}	t_{tot}	T_d	D_d	N_d	D_{max}
			[10^3 hr]	[K]	[m]		[m]
MeerKAT L Band	0.10–0.58	0.10	4	*	13.5	64	–
MeerKAT UHF Band	0.40–1.45	0.10	4	*	13.5	64	–
SKA1-MID Band 1	0.35–3.05	0.48	10	*	15.0	197	–
SKA1-MID Band 2	0.10–0.49	0.48	10	*	15.0	197	–
HIRAX	0.75–2.00	0.36	10	50	6.0	1024	270
PUMA (Petite)	2.00–6.00	0.50	40	50	6.0	5000	600

Table 4.3.: Parameters in (4.100) (from Ansari et al. (2018)).

Survey	a	b	c	d	e	N_s
HIRAX	0.4847	–0.3300	1.3157	1.5974	6.8390	32
PUMA (Petite)	0.5698	–0.5274	0.8358	1.6635	7.3177	100

For the system temperature, we use the results of measurements and simulations for MeerKAT and SKA1-MID, given below in Table 4.4 and Figure 4.13. For HIRAX and PUMA, we use the fit (4.94). In IF mode, HIRAX is assumed to be a square-packed array, while PUMA is taken as hexagonal-packed in a circular area, with 50% fill factor. We follow Karagiannis et al. (2020b) and use the fitting formula from Ansari et al. (2018) for the baseline density of such arrays,

$$n_b^{\text{phys}}(L) = \left(\frac{N_s}{D_d} \right)^2 \frac{a + b(L/L_s)}{1 + c(L/L_s)^d} \exp [-(L/L_s)^e], \quad (4.100)$$

4. Detectability in next-generation galaxy surveys

Table 4.4.: System temperatures for MeerKAT and SKA1-MID, used in Figure 4.4 (from Fonseca et al. (2019)).

MeerKAT L Band		MeerKAT UHF Band		SKA1-MID Band 1		SKA1-MID Band 2	
z	$T_{\text{sys}} / \text{K}$	z	$T_{\text{sys}} / \text{K}$	z	$T_{\text{sys}} / \text{K}$	z	$T_{\text{sys}} / \text{K}$
0.136	19.2	0.420	20.3	0.403	27.2	0.115	16.4
0.183	19.7	0.495	21.0	0.470	26.9	0.168	16.6
0.235	20.3	0.578	21.7	0.539	26.8	0.223	16.8
0.291	20.9	0.671	22.5	0.612	26.9	0.280	17.0
0.352	21.5	0.775	23.5	0.767	27.5	0.341	17.2
0.420	22.3	0.893	24.7	0.850	28.1	0.403	17.6
0.495	23.1	1.03	26.1	0.938	28.8	0.470	18.0
0.578	24.0	1.18	27.9	1.03	29.8		
		1.37	30.3	1.12	30.8		
		1.45	31.5	1.22	32.1		
				1.33	33.5		
				1.44	35.2		
				1.55	37.1		
				1.67	39.2		
				1.80	41.6		
				1.93	44.2		
				2.07	47.2		
				2.22	50.6		
				2.37	54.4		
				2.54	58.6		
				2.69	63.4		
				2.87	68.8		
				3.05	74.8		

where $L_s = N_s D_d$ and $N_s^2 = N_d$. The parameters in (4.100) are given in Table 4.3, and $n_b^{\text{phys}}(L)$ is shown in Figure 4.15.

In the case of PUMA, we take account of the 50% fill factor as follows. We use double the number of dishes to define N_s for the computation of (4.100), i.e. $N_s^2 = 2 \times 5000$. Then we remove half of the dishes without changing the baseline, i.e. without changing the shape and ground-area of the array.

The noise power spectra of the surveys at fixed redshift are displayed in Figure 4.16. For SD-mode surveys, the poor angular resolution is reflected in the blow-up of noise due to the beam in (4.95). The minimum transverse scale for IF-mode surveys is shown as a sharp cut-off, as in (4.91), with effectively infinite noise. Figure 4.16 also shows the smooth blow-up of IF-mode noise on small transverse scales, which results from the fact that $n_b \rightarrow 0$ as the baseline approaches its maximum D_{\max} (see

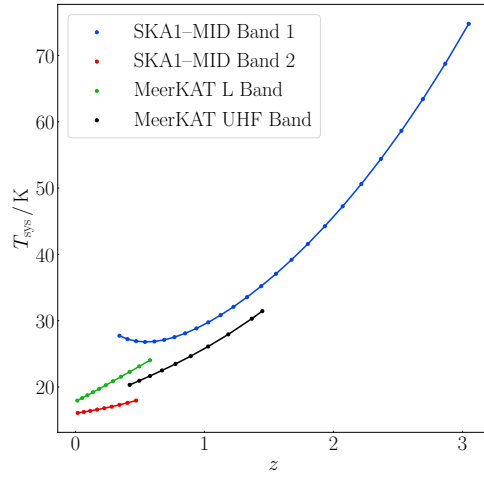


Figure 4.13.: T_{sys} for the different frequency bands of MeerKAT and SKA1 (from Table 4.4).

Figure 4.15). The unbounded increase of noise kills the signal, corresponding to the approximate cut-off scale (4.89).

4.4.6. Forecasts for the relativistic signal-to-noise ratio

Single-dish mode experiments

The SNR of the relativistic part of the bispectrum is shown in Figure 4.17, per z -bin and cumulative.

Table 4.5.: Total SNR for single-dish mode surveys.

Survey	Total SNR
MeerKAT UHF Band	2.5
MeerKAT L Band	1.8
MeerKAT L+UHF Bands	3.0
SKA1-MID Band 1	5.8
SKA1-MID Band 2	3.0
SKA1-MID Bands 1+2	6.6

The total SNR for the HI IM surveys in SD mode is $3 \lesssim \text{SNR} \lesssim 7$, with the high- z_{max} bands giving higher SNR. Table 4.5 displays the predicted total SNR for the SD-mode HI IM surveys. We can slightly improve the best total SNR by combining

4. Detectability in next-generation galaxy surveys

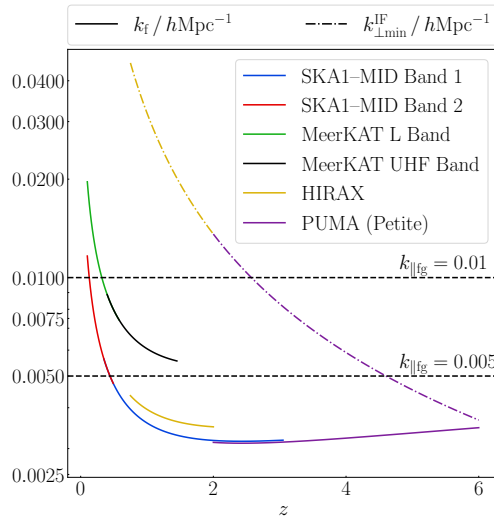


Figure 4.14.: Minimum wavenumbers for the surveys, where k is subject to (4.8) (SD) or (4.92) (IF).

measurements in the two bands, for both MeerKAT and SKA. In general, since we ignore cross-redshift correlations, we can sum in quadrature the per-bin values, $\text{SNR}(z_i)$, as if they were a collection of bins from the same set of observations. However, it must be noted that the two bands overlap in the redshift range $0.40 \leq z \leq 0.58$ for MeerKAT and $0.35 \leq z \leq 0.49$ for SKA. In that range, we follow a conservative approach and only consider the band yielding the largest value of SNR . The values obtained are shown in Table 4.5.

The best case, SKA1 Bands 1+2 gives a total $\text{SNR} \sim 6$ that is detectable, a few times smaller than the SNR predicted for a Stage IV $\text{H}\alpha$ (similar to *Euclid*) spectroscopic survey Maartens et al. (2020).

Interferometer mode experiments

Figure 4.18 shows the forecasts of the relativistic bispectrum SNR for HIRAX and PUMA, using three values of the wedge parameter N_w . HIRAX predicts SNR values slightly lower than an SKA SD-mode survey. The proposed PUMA survey (the ‘Petite’ or PUMA–5K phase of the full or PUMA–32K proposal) gives the highest SNR , at a level similar to a Stage IV $\text{H}\alpha$ (*Euclid*-like) spectroscopic survey. This SNR would safely detect the relativistic signal. Note that PUMA is more sensitive than HIRAX to the N_w parameter. Table 4.6 gives the predicted total SNR for the IF-mode surveys.

4. Detectability in next-generation galaxy surveys

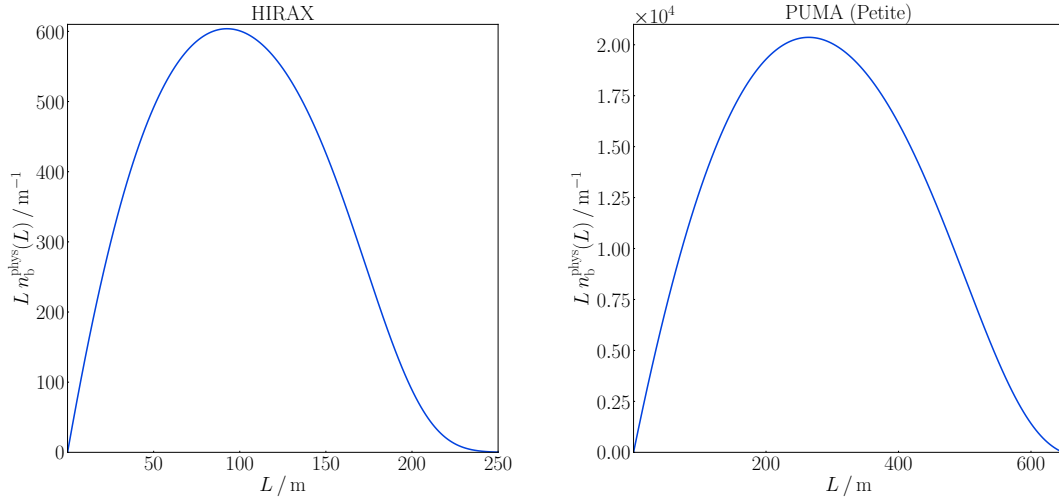


Figure 4.15.: Physical baseline density models for HIRAX (left) and PUMA (right).

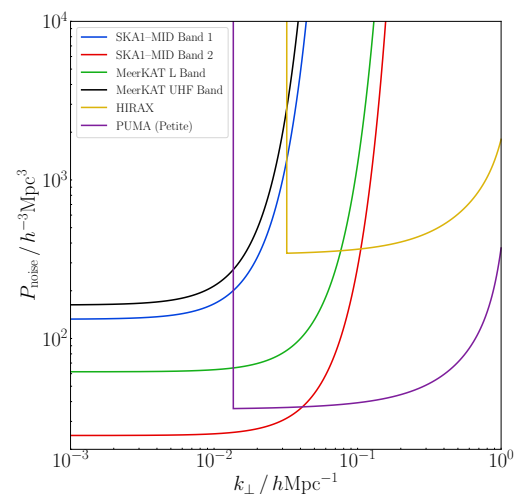


Figure 4.16.: Noise power spectra of the SD-mode surveys (at $z = 0.4$ for low- z_{max} bands and $z = 1$ for high- z_{max} bands) and IF-mode surveys (HIRAX at $z = 1$, PUMA at $z = 2$).

Table 4.6.: Total SNR for interferometer-mode surveys.

N_w Survey	0	1	3
HIRAX	5.4	5.4	5.3
PUMA (Petite)	14.5	14.0	12.0

4. Detectability in next-generation galaxy surveys

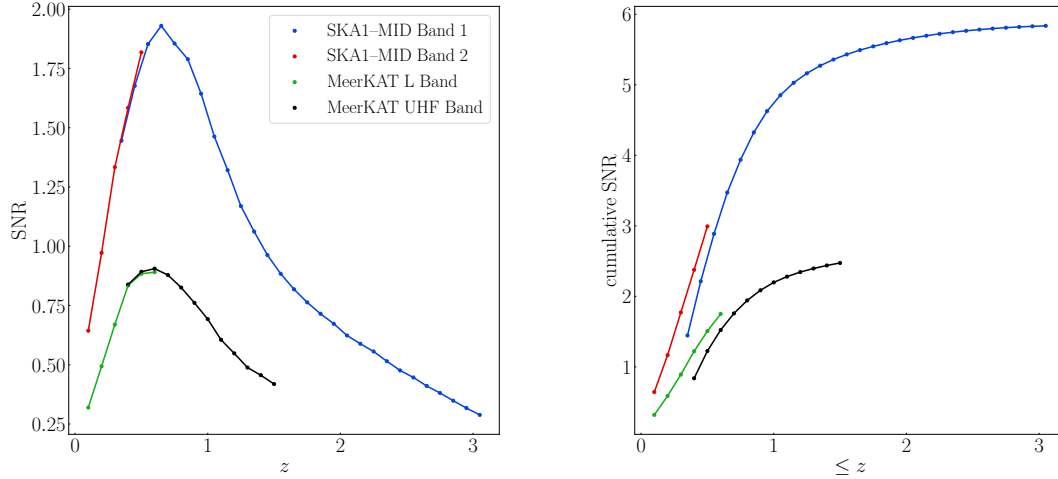


Figure 4.17.: SNR of the relativistic bispectrum per z -bin (*left*) and cumulative (*right*) for SD-mode surveys.

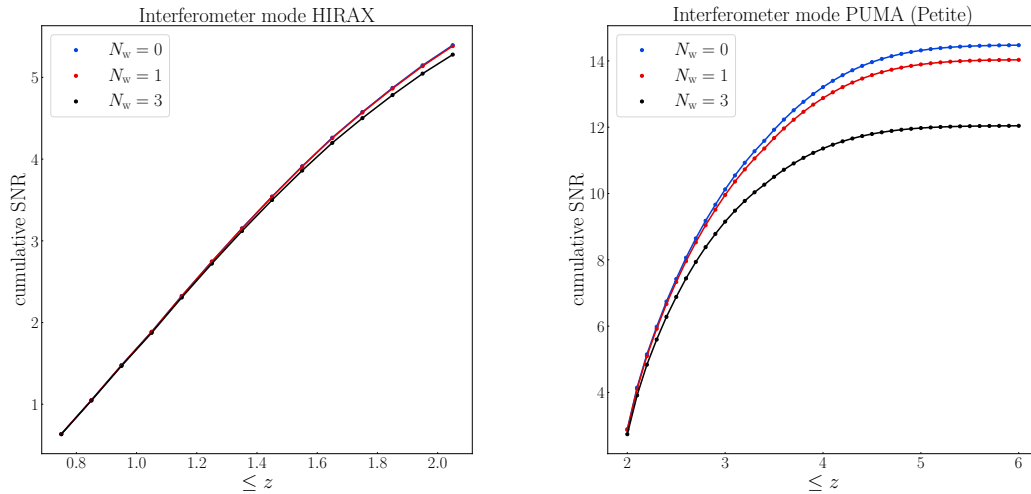


Figure 4.18.: Cumulative SNR of the relativistic bispectrum for IF-mode surveys.

Reducing the radial foreground cut

We investigate how much improvement in SNR results if we increase the number of very large scale modes by reducing the radial foreground cut to $k_{\parallel \text{fg}} = 0.005 \text{ hMpc}^{-1}$. Such a reduction may be achieved by future advances in reconstruction techniques.

It turns out that the SNR is relatively insensitive to this reduction in $k_{\parallel \text{fg}}$: very little gain in SNR is achieved, as shown in Tables 4.7 and 4.8.

4. Detectability in next-generation galaxy surveys

Table 4.7.: Total SNR for single-dish mode surveys with $k_{\parallel \text{fg}} = 0.005 \text{ } h\text{Mpc}^{-1}$.

Survey	Total SNR
MeerKAT UHF Band	2.8
MeerKAT L Band	2.0
MeerKAT L+UHF Bands	3.4
SKA1-MID Band 1	6.5
SKA1-MID Band 2	3.4
SKA1-MID Bands 1+2	7.3

Table 4.8.: Total SNR for interferometer-mode surveys with $k_{\parallel \text{fg}} = 0.005 \text{ } h\text{Mpc}^{-1}$.

N_w Survey	0	1	3
HIRAX	5.6	5.6	5.5
PUMA (Petite)	15.2	14.6	12.5

4.5. Conclusions

The imaginary part of the galaxy bispectrum at leading order is a unique signal that is purely relativistic Clarkson et al. (2019) – and that can be readily extracted from the full bispectrum. In Fourier space, the leading-order local lightcone effects that generate the Doppler-type signal scale as $i(\mathcal{H}/k)$ (see (4.69) and (4.70)). In the galaxy power spectrum for a single tracer, these Doppler-type contributions only occur squared, thus scaling as \mathcal{H}^2/k^2 . Only a cross-power spectrum analysis of two different tracers will generate an imaginary contribution McDonald (2009). For single tracers, the relativistic Doppler-type signal in the power spectrum is therefore highly suppressed and not detectable, even for a cosmic-variance limited survey Alonso et al. (2015b).

However, in the bispectrum of a single tracer, the $i(\mathcal{H}/k)$ relativistic signal survives because it couples with the Newtonian terms Clarkson et al. (2019). This increases the chance of detectability and, as shown by Maartens et al. (2020), the SNR forecast for a Stage IV H α galaxy spectroscopic survey (similar to *Euclid*) is ~ 17 .

We extended the analysis of Maartens et al. (2020) to HI intensity mapping spectroscopic surveys, which requires significant additions in order to deal with foreground contamination and the complexities of instrumental noise (that dominates over shot noise). As expected, loss of signal due to foreground cleaning and telescope beam effects reduces the SNR for the next-generation surveys on MeerKAT, SKA1-MID

4. Detectability in next-generation galaxy surveys

and HIRAX. We forecast a detectable SNR ~ 6 for SKA1 and ~ 5 for HIRAX. The proposed PUMA survey in its Petite or 5,000-dish first phase (before the futuristic full survey with 32,000 dishes) delivers a SNR ~ 14 , comparable to that of a Stage IV H α galaxy survey.

Surveys in single-dish mode (MeerKAT, SKA1) suffer from poor angular resolution so that the Newtonian short-scale transverse modes are suppressed. On the other hand, the interferometer-mode surveys (HIRAX, PUMA) do not probe ultra-large scales as well as SD-mode surveys because the maximum length scale is determined by the minimum baseline (4.91), as shown in Figure 4.16.

We investigated the effect of a more optimistic radial wavenumber cut and found that the improvement in SNR is small. This means that detection of the relativistic signal in the bispectrum does not require scales with $k \lesssim 0.01h/\text{Mpc}$.

There are some caveats to our results and pointers for future work:

- In common with nearly all work on the Fourier-space bispectrum that includes RSD, we implicitly make a flat-sky assumption, based on the fixed global direction \mathbf{n} . This is an issue when probing ultra-large scales – which applies not only to our case but also to all work on constraining primordial non-Gaussianity via the Fourier bispectrum. The flat-sky analysis loses accuracy as θ increases, where θ is the maximum opening angle to the three-point correlations at the given redshift. The corresponding comoving transverse scale is $k_{\perp}(z) = 2\pi / [r(z)\theta]$. There is a threshold scale θ_{fs} , beyond which the approximation fails – i.e., for $\theta > \theta_{\text{fs}}$, or equivalently, $k_{\perp} < k_{\perp\text{fs}}$, the SNR is not reliable.

For IF-mode surveys, the flat-sky assumption is reasonable if $\theta_{\text{fs}} > \theta_b$, where θ_b is the beam, given by (4.87). If we estimate that $\theta_{\text{fs}} \sim 10^\circ$ (see Matsubara (2000)), then this condition holds for HIRAX, and for PUMA up to redshift 3 (see Figure 4.14). Consequently, the flat-sky assumption is reasonable for HIRAX. However for PUMA at $z > 3$ and for the SD-mode surveys, there are modes with $k_{\perp} < k_{\perp\text{fs}}$ and the accuracy of the SNR will be affected for these modes.

Including wide-angle effects is a key target for future work that constrains relativistic effects or primordial non-Gaussianity via the bispectrum. In fact, this is also important for standard cosmological constraints. Corrections to the global flat-sky analysis of the Fourier bispectrum can be made by using a local

4. Detectability in next-generation galaxy surveys

flat-sky approximation Scoccimarro (2015); Sugiyama et al. (2018). Such corrections are typically approximate and do not incorporate the full wide-angle effect. Ultimately, one needs to use the full-sky 3-point correlation function or the full-sky angular bispectrum (see e.g. Kehagias et al. (2015); Di Dio et al. (2017, 2019); Durrer et al. (2020)) to properly include all wide-angle correlations. These alternatives are computationally much more intensive than the Fourier analysis.

- Also in common with other work on the Fourier power spectrum and bispectrum, we neglect cross-correlations among redshift bins. This is justified by the exquisite redshift accuracy of HI intensity mapping, allowing for sharp-edged redshift bins, which in turn implies small or no overlap between them. Integrated effects will in principle induce correlations along the line-of-sight direction, but this is not going to be relevant in our case since the dominant integrated contribution is weak lensing magnification, which vanishes in HI intensity mapping Hall et al. (2013); Alonso et al. (2015b); Di Dio et al. (2016); Jalilvand et al. (2019). Ultimately, only approximate solutions are possible in Fourier space and a complete treatment would require the angular bispectrum or 3-point correlation function.
- In the absence of a simulation-based model for the bispectrum RSD damping parameter σ_B , we set it equal to the power spectrum damping parameter σ_P , for which we used a fit from simulations given in Sarkar & Bharadwaj (2019). Realistically, we expect that $\sigma_B > \sigma_P$. We tested the impact on the SNR of increasing σ_B to $\sigma_B = 1.5 \sigma_P$ and found that it leads to only a small decrease in SNR.

5. Higher order relativistic effects in the bispectrum

In this chapter, we summarise previous work on relativistic projection effects in the observed galaxy bispectrum Umeh et al. (2017); Jolicoeur et al. (2017, 2018, 2019) going beyond the $\mathcal{O}(\mathcal{H}/k)$ approximation used in the previous chapters. For the bispectrum, similar to the power spectrum, effects from observing on the past lightcone need to be taken into account, as they distort the information which is contained in the underlying distribution of dark matter. These lightcone projection effects themselves can also provide new information. The major difference between the power spectrum and bispectrum analyses however, is that for the bispectrum, projection effects up to second order in perturbation theory are required.

Previously, the GR effects on the angular bispectrum of galaxies arising from lensing convergence has been computed in Di Dio et al. (2016), which neglects other ultra-large scale GR corrections to the galaxy overdensity. In Kehagias et al. (2015), a separate-universe approximation is used to compute the angular bispectrum of galaxies in the squeezed limit only, but including all GR lightcone effects.

6. Multipoles of the bispectrum

6.1. The relativistic bispectrum

Galaxy number count fluctuations are distorted due to the fact that we observe on the past lightcone. A well-known effect is the Kaiser redshift-space distortion (RSD) effect (Verde et al., 1998; Scoccimarro et al., 1999). Further distortions are due to lensing convergence, as well as due to Doppler, Sachs-Wolfe, Integrated Sachs-Wolfe (ISW), and time delay effects; all of which are suppressed on sub-equality scales. There are also couplings between these effects when one goes up to non-linear order.

The observed galaxy power spectrum at tree level involves only the projection effects at first order. However, the bispectrum, even at tree level, involves both first- and second-order relativistic projection effects.

introduction to the full theory : sheeans papers

Above the equality scale the galaxy bispectrum will be a key probe for measuring primordial non-Gaussianity which can help differentiate between different inflationary models and other theories of the early universe. On these scales a variety of relativistic effects come into play once the galaxy number-count fluctuation is projected onto our past lightcone. By decomposing the Fourier-space bispectrum into invariant multipoles about the observer's line of sight we examine in detail how the relativistic effects contribute to these. We show how to perform this decomposition analytically, which is significantly faster for subsequent computations. While all multipoles receive a contribution from the relativistic part, odd multipoles arising from the imaginary part of the bispectrum have no Newtonian contribution, making the odd multipoles a smoking gun for a relativistic signature in the bispectrum for single tracers. The dipole and the octopole are significant on equality scales and above where the Newtonian approximation breaks down. This breakdown is further

6. Multipoles of the bispectrum

signified by the fact that the even multipoles receive a significant correction on very large scales.

The bispectrum will play a key role in future galaxy surveys as an important probe of large-scale structure and for measuring primordial non-Gaussianity and galaxy bias Jeong & Komatsu (2009); Baldauf et al. (2011); Celoria & Matarrese (2020). It can help discriminate between different inflationary models and other theories of the early universe, and contains information that is complementary and additional to what is contained in the power spectrum. On super-equality scales, a variety of relativistic effects come into play once the galaxy number-count fluctuation is projected onto the past light cone. In the density contrast up to second order, relativistic effects arise from observing on the past lightcone, and they include all redshift, volume and lensing distortions and couplings between these. In Poisson gauge, these effects can be attributed to velocities (Doppler), gravitational potentials (Sachs-Wolfe, integrated SW, time delay) and lensing magnification and shear. In addition, there are corrections arising from a GR definition of galaxy bias Bertacca et al. (2014b). These effects generate corrections to the Newtonian approximation at order $\mathcal{O}(\mathcal{H}/k)$ and higher. Non-Gaussianity generated by these relativistic projection effects could closely mimic the signature of f_{NL} on large scales which gives a correction in the halo bias $\mathcal{O}((\mathcal{H}/k)^2)$, indicating the importance of precisely including all $\mathcal{O}(\mathcal{H}/k)$ and higher effects in theoretical modelling. So far, a variety of relativistic effects in the galaxy Fourier bispectrum has been taken into account, see Umeh et al. (2017); Jolicoeur et al. (2017, 2018, 2019); Clarkson et al. (2019); Maartens et al. (2020) under the assumption of the plane parallel approximation, and neglecting integrated effects. Other groups are working on this from different angles and approaches, for example by a spherical-Fourier formalism Bertacca et al. (2018), and calculating the angular galaxy bispectrum Di Dio et al. (2017, 2019). Crucially, we have shown that the relativistic part should be detectable in a survey like Euclid without resorting to the multi-tracer technique, which is needed for the power spectrum Maartens et al. (2020).

Once an observable like the galaxy number-count fluctuation is projected onto the past lightcone the orientation of the triangle in the Fourier space bispectrum becomes important. Analogously to how the Legendre multipole expansion is used for power spectrum analysis, one can expand the galaxy bispectrum in spherical harmonics, thus isolating the different invariant multipoles with respect to the observer's line of sight \mathbf{n} . We use the full spherical harmonics for the bispectrum rather than the Legendre polynomial expansion usually adopted for the power spectrum because of

6. Multipoles of the bispectrum

the azimuthal degrees of freedom associated with the orientation of the triangle with respect to the line of sight direction vector in Fourier space. In the power spectrum limit, there is only one angular degree of freedom after ensemble averaging. For the bispectrum, we have one angular and one azimuthal degree of freedom which when expanded in spherical harmonics leads to $(2\ell + 1)$ independent harmonics for each multipole value ℓ .

This has been done for the Newtonian bispectrum, which generates non-zero multipoles only for even ℓ (up to $\ell = 8$) due to redshift-space distortions Scoccimarro et al. (1999); Nan et al. (2018). Contrary to the Newtonian bispectrum, the relativistic galaxy bispectrum generates non-zero multipoles for both even and odd ℓ up to $\ell = 8$ and $m = 6$ where the odd multipoles are induced by the general relativistic effects only. This means that these multipoles are a crucial signature of relativistic projection effects. We provide, for the first time, a multipole decomposition of the Fourier space galaxy bispectrum with relativistic effects included. Additionally we show that the coefficients of this expansion can be worked out analytically. We provide an exact analytic formula for this multipole expansion of the galaxy bispectrum. Previously, we examined for the first time the dipole of the galaxy bispectrum in detail, showing that its amplitude can be more than 10% of that of the monopole even at equality scales Clarkson et al. (2019). In order to eliminate possible biases when analysing large scale structure data, it is important to include the relativistic effects. In addition to this, a variety of the effects that appear in the bispectrum are relativistic effects that have not been measured elsewhere and hence are interesting to study. By analysing the non-zero multipoles of the galaxy bispectrum both for a Euclid-like galaxy survey, and for an SKA-like HI intensity mapping survey, we show the behaviour of the higher multipoles and their corrections to the Newtonian bispectrum. In follow-up work, we are investigating possibilities of detecting the higher multipoles of the bispectrum. See for example Maartens et al. (2020) for detection prospects of the leading order relativistic effects; the dipole is expected to have the strongest GR signature.

The paper is organised as follows. We introduce the relativistic Fourier space bispectrum in section 6.1, and present the multipole expansion of the relativistic bispectrum in section 6.2. An analysis of the multipoles can be found in section 6.3. Finally, we summarise our conclusions in section 6.4.

In Fourier space, the observed galaxy bispectrum B_g at a fixed redshift z is given

6. Multipoles of the bispectrum

by Jolicoeur et al. (2017, 2018)

$$\langle \Delta_g(z, \mathbf{k}_1) \Delta_g(z, \mathbf{k}_2) \Delta_g(z, \mathbf{k}_3) \rangle = (2\pi)^3 B_g(z, \mathbf{k}_1, \mathbf{k}_2, \mathbf{k}_3) \delta^D(\mathbf{k}_1 + \mathbf{k}_2 + \mathbf{k}_3), \quad (6.1)$$

where $\Delta_g(z, \mathbf{k}_1)$ is the number count contrast at redshift z (see Jolicoeur et al. (2017) for the full expression). Here we work in the Poisson gauge; note that $\Delta_g = \delta_g + \text{RSD} + \text{GR}$ projection effects, where the RSD term is the Kaiser RSD up to second order, which is part of the Newtonian approximation. Since redshift is fixed, in what follows we drop redshift dependence for brevity. Furthermore, since the observed direction \mathbf{n} is fixed in what follows, the plane-parallel approximation is necessarily assumed. Then, at tree level, and for Gaussian initial conditions, the following combinations of terms contribute,

$$\langle \Delta_g(\mathbf{k}_1) \Delta_g(\mathbf{k}_2) \Delta_g(\mathbf{k}_3) \rangle = \frac{1}{2} \langle \Delta_g^{(1)}(\mathbf{k}_1) \Delta_g^{(1)}(\mathbf{k}_2) \Delta_g^{(2)}(\mathbf{k}_3) \rangle + 2 \text{ cyclic permutations.} \quad (6.2)$$

Using Wick's theorem, this gives an expression for the galaxy bispectrum Jolicoeur et al. (2017)

$$B_g(\mathbf{k}_1, \mathbf{k}_2, \mathbf{k}_3) = \mathcal{K}^{(1)}(\mathbf{k}_1) \mathcal{K}^{(1)}(\mathbf{k}_2) \mathcal{K}^{(2)}(\mathbf{k}_1, \mathbf{k}_2, \mathbf{k}_3) P(\mathbf{k}_1) P(\mathbf{k}_2) + 2 \text{ cyclic permutations,} \quad (6.3)$$

where P is the power spectrum of $\delta_T^{(1)}$, the first order dark matter density contrast in the total-matter gauge, which corresponds to an Eulerian frame. The first order kernel can be split into a Newtonian and a relativistic part as Jeong et al. (2012)

$$\mathcal{K}^{(1)} = \mathcal{K}_N^{(1)} + \mathcal{K}_{\text{GR}}^{(1)}, \quad \mathcal{K}_N^{(1)} = b_1 + f\mu^2, \quad \mathcal{K}_{\text{GR}}^{(1)} = i\mu \frac{\gamma_1}{k} + \frac{\gamma_2}{k^2}, \quad (6.4)$$

with $\mu = \hat{\mathbf{k}} \cdot \mathbf{n}$ ($\hat{\mathbf{k}} = \mathbf{k}/k$), b_1 is the first-order Eulerian galaxy bias coefficient, f is the linear growth rate of matter perturbations, and redshift-dependent coefficients γ_i are Jeong et al. (2012),

$$\frac{\gamma_1}{\mathcal{H}} = f \left[b_e - 2\mathcal{Q} - \frac{2(1-\mathcal{Q})}{\chi\mathcal{H}} - \frac{\mathcal{H}'}{\mathcal{H}^2} \right], \quad (6.5)$$

$$\frac{\gamma_2}{\mathcal{H}^2} = f(3 - b_e) + \frac{3}{2}\Omega_m \left[2 + b_e - f - 4\mathcal{Q} - \frac{2(1-\mathcal{Q})}{\chi\mathcal{H}} - \frac{\mathcal{H}'}{\mathcal{H}^2} \right]. \quad (6.6)$$

In equations (6.5) and (6.6), \mathcal{H} is the conformal Hubble rate $(\ln a)'$, where a prime denotes a derivative with respect to conformal time; b_e and \mathcal{Q} are the galaxy evolution and magnification biases respectively, χ is the line-of-sight comoving distance

6. Multipoles of the bispectrum

and $\Omega_m = \Omega_{m0}(1+z)H_0^2/\mathcal{H}^2$ is the matter density parameter. At first order, the gauge-independent GR definition of galaxy bias is made in the common comoving frame of galaxies and matter,

$$\delta_{gC}^{(1)} = b_1 \delta_C^{(1)} = b_1 \delta_T^{(1)}, \quad (6.7)$$

where subscript C is for the comoving gauge and T is for total matter gauge, which is a gauge corresponding to standard Newtonian perturbation theory. The bias relation in Poisson gauge is then obtained by transforming (6.7) to Poisson gauge Bertacca et al. (2014b); Jolicoeur et al. (2018):

$$\delta_g^{(1)} = \delta_{gC}^{(1)} + (3 - b_e)\mathcal{H}v^{(1)} = b_1 \delta_T^{(1)} + (3 - b_e)\mathcal{H}v^{(1)}, \quad (6.8)$$

where $v^{(1)}$ is the velocity potential. Since $v^{(1)} = f\mathcal{H}\delta_T^{(1)}/k^2$, the last term on the right of equation (6.8) leads to the $f(3 - b_e)$ term in γ_2/\mathcal{H}^2 , equation (6.6).

Similarly to the first order kernel, the second order kernel can be split into a Newtonian and a relativistic part. The second order part of the Newtonian kernel is well studied and is given as Bernardeau et al. (2002); Karagiannis et al. (2018); Scoccimarro et al. (1999); Verde et al. (1998)

$$\mathcal{K}_N^{(2)}(\mathbf{k}_1, \mathbf{k}_2, \mathbf{k}_3) = b_1 F_2(\mathbf{k}_1, \mathbf{k}_2) + b_2 + f\mu_3^2 G_2(\mathbf{k}_1, \mathbf{k}_2) + fZ_2(\mathbf{k}_1, \mathbf{k}_2) + b_{s2} S_2(\mathbf{k}_1, \mathbf{k}_2), \quad (6.9)$$

where $\mu_i = \mathbf{k}_i \cdot \mathbf{n}$, b_2 is the second-order Eulerian bias parameter, and b_{s2} is the tidal bias. F_2 and G_2 are the Fourier-space Eulerian kernels for second-order density contrast and velocity respectively Jolicoeur et al. (2017); Villa & Rampf (2016);

$$\begin{aligned} F_2(\mathbf{k}_1, \mathbf{k}_2) &= 1 + \frac{F}{D^2} + \left(\mathbf{k}_1 \cdot \mathbf{k}_2 \right) \left(\frac{k_1}{k_2} + \frac{k_2}{k_1} \right) + \left(1 - \frac{F}{D^2} \right) \left(\mathbf{k}_1 \cdot \mathbf{k}_2 \right)^2, \\ G_2(\mathbf{k}_1, \mathbf{k}_2) &= \frac{F'}{DD'} + \left(\mathbf{k}_1 \cdot \mathbf{k}_2 \right) \left(\frac{k_1}{k_2} + \frac{k_2}{k_1} \right) + \left(2 - \frac{F'}{DD'} \right) \left(\mathbf{k}_1 \cdot \mathbf{k}_2 \right)^2, \end{aligned} \quad (6.10)$$

where F is a second-order growth factor, which is given by the growing mode solution of,

$$F'' + \mathcal{H}F' - \frac{3}{2} \frac{H_0^2 \Omega_{m0}}{a} F = \frac{3}{2} \frac{H_0^2 \Omega_{m0}}{a} D^2. \quad (6.11)$$

In an Einstein-de Sitter background, $F = 3D^2/7$, which is a very good approximation for Λ CDM which we use here. The second-order RSD part of the Newtonian kernel is comprised of G_2 above and the kernel Z_2 Verde et al. (1998); Scoccimarro

6. Multipoles of the bispectrum

et al. (1999),

$$Z_2(\mathbf{k}_1, \mathbf{k}_2) = f \frac{\mu_1 \mu_2}{k_1 k_2} (\mu_1 k_1 + \mu_2 k_2)^2 + \frac{b_1}{k_1 k_2} [(\mu_1^2 + \mu_2^2) k_1 k_2 + \mu_1 \mu_2 (k_1^2 + k_2^2)] . \quad (6.12)$$

Finally, $S_2(\mathbf{k}_1, \mathbf{k}_2)$ is the kernel for the tidal bias,

$$S_2(\mathbf{k}_1, \mathbf{k}_2) = (\mathbf{k}_1 \cdot \mathbf{k}_2)^2 - \frac{1}{3} . \quad (6.13)$$

The Newtonian bias model is

$$\delta_{gT}^{(2)} = b_1 \delta_T^{(2)} + b_2 [\delta_T^{(1)}]^2 + b_{s^2} s^2 , \quad (6.14)$$

where $s^2 = s_{ij} s^{ij}$, and $s_{ij} = \Phi_{,ij} - \delta_{ij} \nabla^2 \Phi / 3$.

The relativistic part of the second order kernel was first derived in Umeh et al. (2017) in the simplest case and extended in Jolicoeur et al. (2017, 2018, 2019). Neglecting sub-dominant vector and tensor contributions, we have

$$\begin{aligned} \mathcal{K}_{\text{GR}}^{(2)}(\mathbf{k}_1, \mathbf{k}_2, \mathbf{k}_3) = & \frac{1}{k_1^2 k_2^2} \left\{ \beta_1 + E_2(\mathbf{k}_1, \mathbf{k}_2, \mathbf{k}_3) \beta_2 + i (\mu_1 k_1 + \mu_2 k_2) \beta_3 + i \mu_3 k_3 [\beta_4 + E_2(\mathbf{k}_1, \mathbf{k}_2, \mathbf{k}_3) \beta_5] \right. \\ & + \frac{k_1^2 k_2^2}{k_3^2} [F_2(\mathbf{k}_1, \mathbf{k}_2) \beta_6 + G_2(\mathbf{k}_1, \mathbf{k}_2) \beta_7] + (\mu_1 k_1 \mu_2 k_2) \beta_8 + \mu_3^2 k_3^2 (\beta_9 + E_2(\mathbf{k}_1, \mathbf{k}_2, \mathbf{k}_3) \beta_{10}) \\ & + (\mathbf{k}_1 \cdot \mathbf{k}_2) \beta_{11} + (k_1^2 + k_2^2) \beta_{12} + (\mu_1^2 k_1^2 + \mu_2^2 k_2^2) \beta_{13} \\ & + i \left[(\mu_1 k_1^3 + \mu_2 k_2^3) \beta_{14} + (\mu_1 k_1 + \mu_2 k_2) (\mathbf{k}_1 \cdot \mathbf{k}_2) \beta_{15} + k_1 k_2 (\mu_1 k_2 + \mu_2 k_1) \beta_{16} \right. \\ & \left. \left. + (\mu_1^3 k_1^3 + \mu_2^3 k_2^3) \beta_{17} + \mu_1 \mu_2 k_1 k_2 (\mu_1 k_1 + \mu_2 k_2) \beta_{18} + \mu_3 \frac{k_1^2 k_2^2}{k_3} G_2(\mathbf{k}_1, \mathbf{k}_2) \beta_{19} \right] \right\} . \end{aligned} \quad (6.15)$$

We have collected terms according to the overall powers of k involved. The β_i here are redshift- and bias-dependent coefficients, given in full in appendix REF BETA APPENDIX, which updates expressions in previous papers. We have defined the kernel E_2 which scales as k^0 (like F_2 , G_2 , and Z_2 do),

$$E_2(\mathbf{k}_1, \mathbf{k}_2, \mathbf{k}_3) = \frac{k_1^2 k_2^2}{k_3^4} \left[3 + 2 \left(\mathbf{k}_1 \cdot \mathbf{k}_2 \right) \left(\frac{k_1}{k_2} + \frac{k_2}{k_1} \right) + \left(\mathbf{k}_1 \cdot \mathbf{k}_2 \right)^2 \right] , \quad (6.16)$$

which incorporates some of the relativistic dynamical corrections to the intrinsic second-order terms.

6. Multipoles of the bispectrum

At second order, the GR bias model, which corrects the Newtonian bias model (6.14) is given by Umeh et al. (2019),

$$\delta_{gT}^{(2)} = b_1 \delta_T^{(2)} + b_2 \left[\delta_T^{(1)} \right]^2 + b_{s^2} s^2 + \delta_{C,GR}^{(2)}, \quad (6.17)$$

where the last term maintains gauge invariance on ultra-large scales, and is given by (using $\delta_C^{(1)} = \delta_T^{(1)}$)

$$\delta_{C,GR}^{(2)} = 2\mathcal{H}^2(3\Omega_m + 2f) \left[\delta_T^{(1)} \nabla^{-2} \delta_T^{(1)} - \frac{1}{4} \partial_i \nabla^{-2} \delta_T^{(1)} \partial^i \nabla^{-2} \delta_T^{(1)} \right]. \quad (6.18)$$

The GR correction (6.18) to the Newtonian bias model is contained in the GR kernel (6.15). Then, we also need to transform $\delta_{gT}^{(2)}$ to the Poisson gauge $\delta_g^{(2)}$, the expression for this is given in Jolicoeur et al. (2017),

$$\begin{aligned} \delta_g^{(2)} &= \delta_{gT}^{(2)} + (3 - b_e) \mathcal{H} v^{(2)} + \left[(b_e - 3) \mathcal{H}' + b'_e \mathcal{H} + (b_e - 3)^2 \mathcal{H}^2 \right] [v^{(1)}]^2 + (b_e - 3) \mathcal{H} v^{(1)} v^{(1)\prime} \\ &\quad + 2(3 - b_e) \mathcal{H} v^{(1)} \delta_{gT}^{(1)} - 2v^{(1)} \delta_{gT}^{(1)\prime} + 3(b_e - 3) \mathcal{H} v^{(1)} \Phi^{(1)}. \end{aligned} \quad (6.19)$$

All of the terms after $\delta_{gT}^{(2)}$ on the right of equation (6.19) scale as $(\mathcal{H}/k)^n \left[\delta_T^{(1)} \right]^2$, where $n = 2, 4$. Therefore they are omitted in the Newtonian approximation. These GR correction terms maintain gauge-independence on ultra-large scales, and they are included in the GR kernel (6.15).

6.2. Extracting the multipoles

Our goal is to extract the spherical harmonic multipoles of B_g with respect to the observer's line of sight. That is, for a fixed line of sight and triangle shape, the rotation of the plane of the triangle about \mathbf{n} generates invariant moments, the sum of which add up to the full bispectrum. This means that

$$B_g = \sum_{\ell m} B_{\ell m} Y_{\ell m}(\mathbf{n}), \quad (6.20)$$

where we follow Scoccimarro et al. (1999); Nan et al. (2018) in our choice of decomposition of the bispectrum (an alternative basis can be found in Sugiyama et al. (2018)). To define the $B_{\ell m}$ we need to define an orientation for the $Y_{\ell m}$ to give the polar and azimuthal angles over which to integrate. We choose a coordinate basis

6. Multipoles of the bispectrum

for the vectors that span the triangle as follows:

$$\mathbf{k}_1 = (0, 0, k_1) \quad (6.21)$$

$$\mathbf{k}_2 = (0, k_2 \sin \theta, k_2 \cos \theta), \quad (6.22)$$

$$\mathbf{k}_3 = (0, -k_2 \sin \theta, -k_1 - k_2 \cos \theta), \quad (6.23)$$

$$\mathbf{n} = (\sin \theta_1 \cos \varphi, \sin \theta_1 \sin \varphi, \cos \theta_1). \quad (6.24)$$

That is, we fix \mathbf{k}_1 along the z -axis, and require the other triangle vectors to lie in the y - z plane, see figure 6.1 for a sketch of the relevant vectors. Then we define $\mu_1 = \cos \theta_1$ and use φ , which is the azimuthal angle giving the orientation of the triangle relative to \mathbf{n} . $\theta_{12} = \theta$ is the angle between vectors \mathbf{k}_1 and \mathbf{k}_2 , and we define $\mu = \cos \theta = \mathbf{k}_1 \cdot \mathbf{k}_2$.

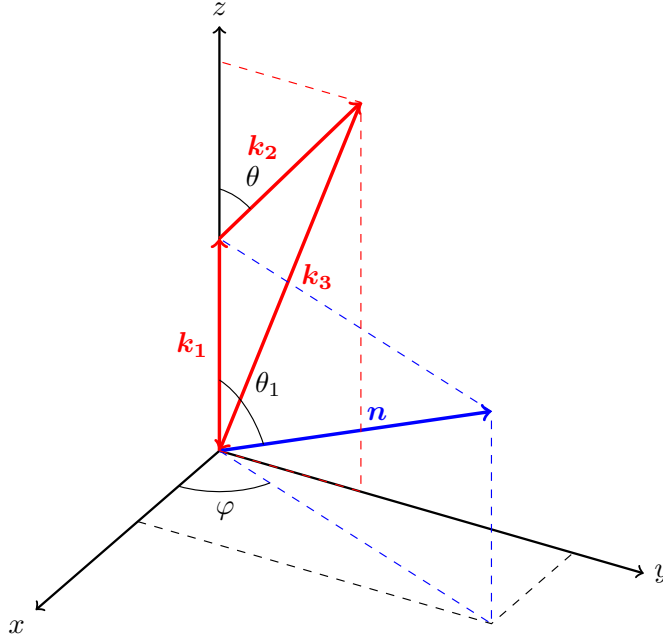


Figure 6.1.: Overview of the relevant vectors and angles for the Fourier-space bispectrum.

The bispectrum can then be expressed in terms of five variables, φ , μ_1 , θ , k_1 and k_2 , by using

$$\mu_2 = \sqrt{1 - \mu_1^2} \sin \theta \sin \varphi + \mu_1 \cos \theta, \quad (6.25)$$

$$\mu_3 = -\frac{k_1}{k_3} \mu_1 - \frac{k_2}{k_3} \mu_2. \quad (6.26)$$

6. Multipoles of the bispectrum

Then

$$B_g(\theta, k_1, k_2, \mu_1, \varphi) = \sum_{\ell m} B_{\ell m}(\theta, k_1, k_2) Y_{\ell m}(\mu_1, \varphi), \quad (6.27)$$

where we use standard orthonormal spherical harmonics,

$$Y_{\ell m}(\mu_1, \varphi) = \sqrt{\frac{2\ell+1}{4\pi}} \sqrt{\frac{(\ell-m)!}{(\ell+m)!}} P_{\ell}^m(\mu_1) e^{im\varphi}, \quad (6.28)$$

where the P_{ℓ}^m are the associated Legendre polynomials,

$$P_{\ell}^m(\mu_1) = \frac{(-1)^m}{2^{\ell} \ell!} (1 - \mu_1^2)^{m/2} \frac{d^{\ell+m}}{d\mu_1^{\ell+m}} (\mu_1^2 - 1)^{\ell}. \quad (6.29)$$

At this stage we can extract the multipoles numerically once a bias model and cosmological parameters are given. It is actually significantly quicker to perform this extraction algebraically however, as we now explain.

The bispectrum in general can be considered as a function of $k_1, k_2, k_3, \mu, \mu_1, \mu_2, \mu_3$ and φ . An alternative to the expansion (6.27) is

$$B_g(\mu, k_1, k_2; \mu_1, \mu_2) = \sum_{a=0}^6 \sum_{b=0}^6 \mathcal{B}_{ab}(\mu, k_1, k_2) (i\mu_1)^a (i\mu_2)^b, \quad (6.30)$$

where we used μ_2 instead of φ and $a, b = 0 \dots 6$, which is the maximum power of μ_1, μ_2 that can arise. This factors out all the angular dependence from the functions $\mathcal{B}_{ab}(\mu, k_1, k_2)$, where $\mu = \cos \theta$, which just depend on the triangle shape (and the cosmology). Note that by explicitly including factors of i in the sum, we have only real coefficients \mathcal{B}_{ab} . Schematically we can visualise \mathcal{B}_{ab} in matrix form, split into Newtonian and relativistic contributions as (a bullet denotes a non-zero entry, open circles denote zero entries, and dots are non-existent entries; here that means $a + b > 8$ as higher powers don't occur):

$$\mathcal{B}_{ab} \sim \underbrace{\begin{pmatrix} \bullet & \circ & \bullet & \circ & \bullet & \circ & \circ \\ \circ & \bullet & \circ & \bullet & \circ & \bullet & \circ \\ \bullet & \circ & \bullet & \circ & \bullet & \circ & \bullet \\ \circ & \bullet & \circ & \bullet & \circ & \bullet & \cdot \\ \bullet & \circ & \bullet & \circ & \bullet & \cdot & \cdot \\ \circ & \bullet & \circ & \bullet & \cdot & \cdot & \cdot \\ \circ & \circ & \bullet & \cdot & \cdot & \cdot & \cdot \end{pmatrix}}_{\text{Newtonian}} + \underbrace{\begin{pmatrix} \bullet & \bullet & \bullet & \bullet & \bullet & \bullet & \bullet \\ \bullet & \bullet & \bullet & \bullet & \bullet & \bullet & \circ \\ \bullet & \bullet & \bullet & \bullet & \bullet & \bullet & \circ \\ \bullet & \bullet & \bullet & \bullet & \bullet & \circ & \cdot \\ \bullet & \bullet & \bullet & \bullet & \circ & \cdot & \cdot \\ \bullet & \bullet & \bullet & \circ & \cdot & \cdot & \cdot \\ \bullet & \bullet & \circ & \cdot & \cdot & \cdot & \cdot \end{pmatrix}}_{\text{Relativistic}}. \quad (6.31)$$

6. Multipoles of the bispectrum

(Note that the matrix row and column labelling start at $a, b = 0, 0$ for the top left element.) Thus, the Newtonian contributions always have $a + b = \text{even} \leq 8$, contributing only to the real part of B_g , while there are relativistic contributions present for all $a + b \leq 7$. When $a + b$ is odd, this implies an imaginary component to the full bispectrum.

In terms of the powers of \mathcal{H}/k involved, we can visualise the maximum powers that appear in matrix form as follows:

$$\mathcal{B}_{ab} \sim \begin{pmatrix} k^{-8} & k^{-7} & k^{-6} & k^{-5} & k^{-4} & k^{-3} & k^{-2} \\ k^{-7} & k^{-6} & k^{-5} & k^{-4} & k^{-3} & k^{-2} & k^{-1} \\ k^{-6} & k^{-5} & k^{-4} & k^{-3} & k^{-2} & k^{-1} & k^0 \\ k^{-5} & k^{-4} & k^{-3} & k^{-2} & k^{-1} & k^0 & . \\ k^{-4} & k^{-3} & k^{-2} & k^{-1} & k^0 & . & . \\ k^{-3} & k^{-2} & k^{-1} & k^0 & . & . & . \\ k^{-2} & k^{-1} & k^0 & . & . & . & . \end{pmatrix}. \quad (6.32)$$

As in the matrix (6.31), the matrix row and column labelling in (6.32) starts at $(a, b) = (0, 0)$. We see that higher powers n of $(\mathcal{H}/k)^n$ appear for lower $a + b$. Newtonian contributions are all $(\mathcal{H}/k)^0$. Each element has only odd powers of \mathcal{H}/k if $a + b$ is odd, and similarly only even powers if $a + b$ is even.

The advantage of writing the bispectrum in this form is that we can derive analytic formulas for the multipoles. We need to find

$$\begin{aligned} B_{\ell m} &= \int d\Omega B_g Y_{\ell m}^* \\ &= \sum_{a,b} \mathcal{B}_{ab} X_{\ell m}^{ab}, \end{aligned} \quad (6.33)$$

where

$$X_{\ell m}^{ab} = \int_0^{2\pi} d\varphi \int_{-1}^1 d\mu_1 (i\mu_1)^a (i\mu_2)^b Y_{\ell m}^*(\mu_1, \varphi). \quad (6.34)$$

The derivation is as follows [Here we present a detailed derivation of the analytic result of the integration of](#)

$$X_{\ell m}^{ab} = \int_0^{2\pi} d\varphi \int_{-1}^1 d\mu_1 (i\mu_1)^a (i\mu_2)^b Y_{\ell m}^*(\mu_1, \varphi). \quad (6.35)$$

In the above, we have used that $\mu_1 = \cos \theta$, such that $Y_{\ell m}(\theta, \varphi) = Y_{\ell m}(\mu_1, \varphi)$. The

[work on deriv here](#)

6. Multipoles of the bispectrum

standard orthonormal spherical harmonics are defined as,

$$Y_{\ell m}(\mu_1, \varphi) = \sqrt{\frac{2\ell+1}{4\pi}} \sqrt{\frac{(\ell-m)!}{(\ell+m)!}} P_{\ell m}(\mu_1) e^{im\varphi}, \quad (6.36)$$

and the spherical harmonics are related to their complex conjugate as,

$$Y_{\ell,-m} = (-1)^m Y_{\ell,m}^*, \quad Y_{\ell,m}^* = (-1)^m Y_{\ell,-m}. \quad (6.37)$$

Equation (6.35) is separable. We can make this explicit as follows. First expressing μ_2 in terms of μ_1 using $\mu_2 = \sqrt{1 - \mu_1^2} \sin \theta \sin \varphi + \mu_1 \cos \theta$, where $\theta \equiv \theta_{12} \neq \theta_1$ – it is the angle between vectors \mathbf{k}_1 and \mathbf{k}_2 . Then we can expand $(i\mu_2)^b$ using the binomial series,

$$\begin{aligned} (i\mu_2)^b &= i^b (\sqrt{1 - \mu_1^2} \sin \theta \sin \varphi + \mu_1 \cos \theta)^b \\ &= i^b \sum_{g=0}^b \binom{b}{g} \left[\sqrt{1 - \mu_1^2} \sin \theta \sin \varphi \right]^g [\mu_1 \cos \theta]^{b-g} \\ &= i^b \sum_{g=0}^b \binom{b}{g} (1 - \mu_1^2)^{g/2} \mu_1^{b-g} \sin^g \varphi \sin^g \theta \cos^{b-g} \theta. \end{aligned} \quad (6.38)$$

Using this, we have,

$$\begin{aligned} X_{\ell m}^{ab} &= i^{a+b} \sum_{g=0}^b \sin^g \theta \cos^{b-g} \theta \binom{b}{g} \int_0^{2\pi} d\varphi \int_{-1}^1 d\mu (1 - \mu^2)^{g/2} \mu^{a+b-g} \times \\ &\quad \sin^g \varphi Y_{\ell m}^*(\mu, \varphi), \end{aligned} \quad (6.39)$$

where we have dropped subscript on $\mu_1 \equiv \mu$ for brevity. Now using the definition of the complex-conjugated standard spherical harmonics,

$$\begin{aligned} Y_{\ell m}^* &= (-1)^m Y_{\ell,-m} \\ &= (-1)^m \sqrt{\frac{2\ell+1}{4\pi}} \sqrt{\frac{(\ell+m)!}{(\ell-m)!}} P_{\ell,-m}(\mu) e^{-im\varphi} \end{aligned} \quad (6.40)$$

and the associated Legendre polynomials $P_{\ell m}$ can be rewritten for negative m as,

$$P_{\ell,-m} = (-1)^m \frac{(\ell-m)!}{(\ell+m)!} P_{\ell,m}, \quad (6.41)$$

6. Multipoles of the bispectrum

such that,

$$Y_{\ell m}^* = \sqrt{\frac{2\ell+1}{4\pi}} \sqrt{\frac{(\ell-m)!}{(\ell+m)!}} P_{\ell m}(\mu) e^{-im\varphi}. \quad (6.42)$$

This makes the separability of the integral (6.35) explicit,

$$\begin{aligned} X_{\ell m}^{ab} = & i^{a+b} \sum_{g=0}^b \binom{b}{g} \sin^g \theta \cos^{b-g} \theta \sqrt{\frac{2\ell+1}{4\pi}} \sqrt{\frac{(\ell-m)!}{(\ell+m)!}} \int_0^{2\pi} d\varphi \sin^g \varphi e^{-im\varphi} \times \\ & \int_{-1}^1 d\mu (1-\mu^2)^{g/2} \mu^{a+b-g} P_{\ell m}(\mu). \end{aligned} \quad (6.43)$$

Now these two integrals can be solved independently. Starting with the integral over μ , splitting the interval $\int_{-1}^1 = \int_{-1}^0 + \int_0^1$, the \int_{-1}^1 term can be rewritten using a change of variables and the parity of the associated Legendre polynomials as,

$$\begin{aligned} & \int_{-1}^0 d\mu (1-\mu^2)^{g/2} \mu^{a+b-g} P_{\ell m}(\mu) \\ &= - \int_0^{-1} d\mu (1-\mu^2)^{g/2} \mu^{a+b-g} P_{\ell m}(\mu) \\ &= \int_0^1 d\tilde{\mu} (1-\tilde{\mu}^2)^{g/2} (-\tilde{\mu})^{a+b-g} P_{\ell m}(-\tilde{\mu}) \\ &= (-1)^{\ell+m+a+b-g} \int_0^1 d\mu (1-\mu)^{g/2} \mu^{a+b-g} P_{\ell m}(\mu), \end{aligned} \quad (6.44)$$

where we have used that $P_{\ell m}(-x) = (-1)^{\ell+m} P_{\ell m}(x)$, and renamed $\tilde{\mu} = \mu$ in the last line. The full integral over μ then can be written as,

$$[1 + (-1)^{\ell+m+a+b-g}] \int_0^1 d\mu (1-\mu^2)^{g/2} \mu^{a+b-g} P_{\ell m}(\mu). \quad (6.45)$$

The associated Legendre polynomials can be written in closed form, using,

$$\begin{aligned} P_{\ell m}(\mu) &= (-1)^m P_{\ell}^m \\ &= (-1)^m (-1)^m 2^\ell (1-\mu^2)^{m/2} \sum_{k=m}^{\ell} \frac{k!}{(k-m)!} \mu^{k-m} \binom{\ell}{k} \binom{\frac{1}{2}(\ell+k-1)}{\ell} \\ &\quad 2^\ell (1-\mu^2)^{m/2} \sum_{k=m}^{\ell} \frac{k!}{(k-m)!} \mu^{k-m} \binom{\ell}{k} \binom{\frac{1}{2}(\ell+k-1)}{\ell}, \end{aligned} \quad (6.46)$$

6. Multipoles of the bispectrum

such that,

$$\begin{aligned} & [1 + (-1)^{\ell+m+a+b-g}] (-1)^m 2^\ell \sum_{k=m}^{\ell} \frac{k!}{(k-m)!} \binom{\ell}{k} \binom{\frac{1}{2}(\ell+k-1)}{\ell} \times \\ & \int_0^1 d\mu (1-\mu^2)^{\frac{1}{2}(m+g)} \mu^{a+b+k-g-m}. \end{aligned} \quad (6.47)$$

Changing variables $\xi = \mu^2$, omitting the prefactor for brevity, we get,

$$\int_0^1 d\xi \frac{1}{2} (1-\xi)^{\frac{1}{2}(m+g)} \xi^{\frac{1}{2}(a+b+k-g-m-1)}. \quad (6.48)$$

Comparing to the Beta function,

$$B(x, y) = \int_0^1 dt (1-t)^{y-1} t^{x-1}, \quad (6.49)$$

we can identify $x = \frac{1}{2}(a+b+k-g-m+1)$ and $y = \frac{1}{2}(m+g+2)$. The Beta function can be expressed in terms of Gamma functions $B(x, y) = \frac{\Gamma(x)\Gamma(y)}{\Gamma(x+y)}$, which in turn can be written in terms of factorials, for any positive integer n this relation is $\Gamma(n) = (n-1)!$. We will express the result in terms of Gamma functions as,

$$\begin{aligned} & \int_{-1}^1 d\mu (1-\mu^2)^{g/2} \mu^{a+b-g} P_{\ell m}(\mu) \\ &= [1 + (-1)^{\ell+m+a+b-g}] (-1)^m 2^\ell \sum_{k=m}^{\ell} \frac{k!}{(k-m)!} \binom{\ell}{k} \binom{\frac{1}{2}(\ell+k-1)}{\ell} \times \\ & \left\{ \Gamma \left[\frac{1}{2}(m+g+2) \right] \Gamma \left[\frac{1}{2}(a+b+k-g-m+1) \right] \right\} \cdot \left\{ \Gamma \left[\frac{1}{2}(a+b+k+3) \right] \right\}^{-1}. \end{aligned} \quad (6.50)$$

Now to solve the integral over φ ,

$$\int_0^{2\pi} d\varphi \sin^g \varphi e^{-im\varphi}. \quad (6.51)$$

Write $\sin^g \varphi$ in terms of e using the usual trig identities and binomial expansion as,

$$\sin^g \varphi = \frac{1}{(2i)^g} \sum_{n=0}^g \binom{g}{n} e^{i(g-n)\varphi} (-1)^n e^{-in\varphi} \quad (6.52)$$

6. Multipoles of the bispectrum

to get,

$$\begin{aligned}
& \int_0^{2\pi} d\varphi \frac{1}{(2i)^g} \sum_{n=0}^g \binom{g}{n} (-1)^n e^{i\varphi(g-m-2n)} \\
&= \frac{1}{(2i)^g} \sum_{n=0}^g \binom{g}{n} (-1)^n \int_0^{2\pi} d\varphi e^{i\varphi(g-m-2n)} \\
&= \frac{1}{(2i)^g} \sum_{n=0}^g \binom{g}{n} (-1)^n (2\pi) \delta_{g-m-2n,0}.
\end{aligned} \tag{6.53}$$

The Kronecker δ picks out the term in the sum which satisfies $g - m - 2n = 0 \Rightarrow n = \frac{1}{2}(g - m)$, s.t.

$$\int_0^{2\pi} d\varphi \sin^g \varphi e^{-im\varphi} = \frac{1}{(2i)^g} \binom{g}{\frac{1}{2}(g-m)} (2\pi) (-1)^{\frac{1}{2}(g-m)} \tag{6.54}$$

where n must be a positive integer (or zero), so $g \geq m$ and $g - m$ even.

Putting together blah blah

fix this derivation garbage and double check

leads to identity, done To do this we use the identity for $m \geq 0$,

$$\begin{aligned}
X_{\ell m}^{ab} &= 2^{\ell+m-1} i^{a+b+m} \sqrt{\frac{\pi(2\ell+1)(\ell-m)!}{(\ell+m)!}} \\
&\times \sum_{p=m}^{\frac{1}{2}(b+m)} \sum_{q=m}^{\ell} \frac{[1 + (-1)^{a+b+q}] b! \cos^{b+m-2p} \theta \sin^{2p-m} \theta}{4^p (b+m-2p)! (\ell-q)! (p-m)! (q-m)!} \frac{\Gamma[\frac{1}{2}(q+\ell+1)]}{\Gamma[\frac{1}{2}(q-\ell+1)]} \frac{\Gamma[\frac{1}{2}(a+b+q-2p+1)]}{\Gamma[\frac{1}{2}(a+b+q+3)]}
\end{aligned} \tag{6.55}$$

for $m \leq b$ and zero otherwise. For $m < 0$, the result follows a similar pattern, using the simple relation $X_{\ell-m}^{ab} = (-1)^{a+b+m} X_{\ell m}^{ax'b*}$.

The resulting expressions for $B_{\ell m}$ are rather massive, in part because the cyclic permutations become mixed together, so we do not present them here. We can visualise

6. Multipoles of the bispectrum

these in matrix form split into their Newtonian and relativistic contributions:

$$B_{\ell m} = \underbrace{\begin{pmatrix} \bullet & \cdot \\ \circ & \circ & \cdot \\ \bullet & \bullet & \bullet & \cdot & \cdot & \cdot & \cdot & \cdot & \cdot \\ \circ & \circ & \circ & \circ & \cdot & \cdot & \cdot & \cdot & \cdot \\ \bullet & \bullet & \bullet & \bullet & \bullet & \cdot & \cdot & \cdot & \cdot \\ \circ & \circ & \circ & \circ & \circ & \circ & \cdot & \cdot & \cdot \\ \bullet & \cdot & \cdot \\ \circ & \cdot \\ \bullet & \circ \end{pmatrix}}_{\text{Newtonian}} + \underbrace{\begin{pmatrix} \bullet & \cdot \\ \bullet & \bullet & \cdot \\ \bullet & \bullet & \bullet & \cdot & \cdot & \cdot & \cdot & \cdot & \cdot \\ \bullet & \bullet & \bullet & \bullet & \cdot & \cdot & \cdot & \cdot & \cdot \\ \bullet & \bullet & \bullet & \bullet & \bullet & \cdot & \cdot & \cdot & \cdot \\ \bullet & \bullet & \bullet & \bullet & \bullet & \bullet & \cdot & \cdot & \cdot \\ \bullet & \cdot & \cdot \\ \bullet & \circ \end{pmatrix}}_{\text{Relativistic}}. \quad (6.56)$$

Again, the matrix indices start at $(0, 0)$ in the top left, $(\ell, m) = (0, 0)$. In the matrix (6.56), consistent with previous matrix visualisations, a closed bullet represents a non-zero entry, while an open circle denotes a vanishing entry. The dots denote the non-existent elements of the matrix, here they are matrix elements where $m > \ell$ and hence do not exist. So, the Newtonian bispectrum only induces even multipoles up to and including $\ell = 8$, while the relativistic part induces even and odd multipoles up to $\ell = 7$ with multipoles higher than $\ell = 8$ vanishing exactly. Both the Newtonian and the relativistic part terminate at $m = \pm 6$, because $m \leq b \leq 6$, as can be seen from (6.55). Note that for $m < 0$ the pattern is the same. In terms of (\mathcal{H}/k) powers, the highest that appear for each ℓ is $(\mathcal{H}/k)^{8-\ell}$, while the leading contribution is $(\mathcal{H}/k)^0$ or ¹ if the leading contribution is Newtonian or relativistic. These powers are even (odd) if ℓ is even (odd), as explained previously along with the visualisation of the powers \mathcal{H}/k in equation (6.32).

Presentation of the matrix \mathcal{B}_{ab}

Here we describe in more detail how to calculate the matrix of coefficients \mathcal{B}_{ab} . These are far too large to write down, but most of the complexity comes from the k_i permutations and the fact that they are made irreducible from substituting for μ_3 . However, the core part can be shown from which they can easily be calculated. First we note that once μ_3 is substituted for, we can write the first cyclic permutation of

6. Multipoles of the bispectrum

the product of the kernels as

$$\mathcal{K}_{123} = \mathcal{K}^{(1)}(k_1, \mu_1) \mathcal{K}^{(1)}(k_2, \mu_2) \mathcal{K}^{(2)}(k_1, k_2, k_3, \mu_1, \mu_2) = \sum_{a=0}^5 \sum_{b=0}^5 (\mathrm{i} \mu_1)^a (\mathrm{i} \mu_2)^b \mathcal{K}_{ab}(k_1, k_2, k_3), \quad (6.57)$$

where $\mathcal{K}_{ab}(k_1, k_2, k_3) = \mathcal{K}_{ab}(k_2, k_1, k_3)$ is a set of real μ -independent coefficients which we give below, and here the maximum value of $a, b = 5$. Given \mathcal{K}_{123} we can derive the permutations \mathcal{K}_{321} and \mathcal{K}_{312} as

$$\mathcal{K}_{321} = \sum_{a,b} \sum_{c=0}^a \binom{a}{c} \frac{k_1^{a-c} k_2^c}{k_3^a} (-1)^a (\mathrm{i} \mu_1)^{a-c} (\mathrm{i} \mu_2)^{b+c} \mathcal{K}_{ab}(k_3, k_2, k_1), \quad (6.58)$$

$$\mathcal{K}_{312} = \sum_{a,b} \sum_{c=0}^a \binom{a}{c} \frac{k_1^{a-c} k_2^c}{k_3^a} (-1)^a (\mathrm{i} \mu_1)^{a+b-c} (\mathrm{i} \mu_2)^c \mathcal{K}_{ab}(k_3, k_1, k_2), \quad (6.59)$$

where, as in general, the range of $a, b = 0 \dots 6$. Given these, the full bispectrum is just $B_g = \mathcal{K}_{123} P_1 P_2 + 2$ permutations, but now explicitly written in terms of sums over powers of μ_1, μ_2 . From this \mathcal{B}_{ab} can be found by inspection. The difference in dimension between the permutations originates from the other cyclic permutations being added, where one substitutes $\mu_3 = -(k_1 \mu_1 + k_2 \mu_2) / k_3$. In (6.58) the largest power of μ_2 is 6, and (6.59) has the largest power of μ_1 as 6.

To present $\mathcal{K}_{ab}(k_1, k_2, k_3)$ we will show powers of \mathcal{H}/k separately, and write $\mathcal{K}_{ab}(k_1, k_2, k_3) = \sum_{n=0}^8 \mathcal{K}_{ab}^{(n)}(k_1, k_2, k_3)$ where n represents the power of \mathcal{H}/k . Then the Newtonian and leading GR correction part look like (again, a bullet denotes a non-zero entry)

$$\mathcal{K}_{ab}^{(0)} = \begin{pmatrix} \bullet & \circ & \bullet & \circ & \bullet & \circ \\ \circ & \bullet & \circ & \bullet & \circ & \bullet \\ \bullet & \circ & \bullet & \circ & \bullet & \circ \\ \circ & \bullet & \circ & \bullet & \circ & \bullet \\ \bullet & \circ & \bullet & \circ & \bullet & \circ \\ \circ & \bullet & \circ & \bullet & \circ & \circ \end{pmatrix} \quad \mathcal{K}_{ab}^{(1)} = \begin{pmatrix} \circ & \bullet & \circ & \bullet & \circ & \bullet \\ \bullet & \circ & \bullet & \circ & \bullet & \circ \\ \circ & \bullet & \circ & \bullet & \circ & \bullet \\ \bullet & \circ & \bullet & \circ & \bullet & \circ \\ \circ & \bullet & \circ & \bullet & \circ & \circ \\ \bullet & \circ & \bullet & \circ & \circ & \circ \end{pmatrix} \quad (6.60)$$

where, writing $F = F_2(\mathbf{k}_1, \mathbf{k}_2)$, $G = G_2(\mathbf{k}_1, \mathbf{k}_2)$, $S = S_2(\mathbf{k}_1, \mathbf{k}_2)$,

$$\mathcal{K}_{00}^{(0)} = b_1^2 (b_{s^2} S + b_2) + F b_1^3 \quad (6.61)$$

$$\mathcal{K}_{02}^{(0)} = -b_1 f \left[b_1^2 + b_{s^2} S + b_2 + \left(F + \frac{G k_2^2}{k_3^2} \right) b_1 \right] \quad (6.62)$$

$$\mathcal{K}_{04}^{(0)} = b_1 f^2 \left(\frac{G k_2^2}{k_3^2} + b_1 \right) \quad (6.63)$$

6. Multipoles of the bispectrum

$$\mathcal{K}_{11}^{(0)} = -b_1^2 f \left[\frac{(k_1^2 + k_2^2) b_1}{k_1 k_2} + \frac{2Gk_1 k_2}{k_3^2} \right] \quad (6.64)$$

$$\mathcal{K}_{13}^{(0)} = b_1 f^2 \left[\frac{(k_1^2 + 2k_2^2) b_1}{k_1 k_2} + \frac{2Gk_1 k_2}{k_3^2} \right] \quad (6.65)$$

$$\mathcal{K}_{15}^{(0)} = -\frac{b_1 f^3 k_2}{k_1} \quad (6.66)$$

$$\mathcal{K}_{20}^{(0)} = -b_1 f \left[b_1^2 + b_{s^2} S + b_2 + \left(F + \frac{Gk_1^2}{k_3^2} \right) b_1 \right] \quad (6.67)$$

$$\mathcal{K}_{22}^{(0)} = f^2 \left[4b_1^2 + b_{s^2} S + b_2 + \left(F + \frac{G(k_1^2 + k_2^2)}{k_3^2} \right) b_1 \right] \quad (6.68)$$

$$\mathcal{K}_{24}^{(0)} = -f^3 \left(\frac{Gk_2^2}{k_3^2} + 3b_1 \right) \quad (6.69)$$

$$\mathcal{K}_{31}^{(0)} = b_1 f^2 \left[\frac{b_1 (2k_1^2 + k_2^2)}{k_1 k_2} + \frac{2Gk_1 k_2}{k_3^2} \right] \quad (6.70)$$

$$\mathcal{K}_{33}^{(0)} = -f^3 \left[\frac{2b_1 (k_1^2 + k_2^2)}{k_1 k_2} + \frac{2Gk_1 k_2}{k_3^2} \right] \quad (6.71)$$

$$\mathcal{K}_{35}^{(0)} = \frac{f^4 k_2}{k_1} \quad (6.72)$$

$$\mathcal{K}_{40}^{(0)} = b_1 f^2 \left(b_1 + \frac{Gk_1^2}{k_3^2} \right) \quad (6.73)$$

$$\mathcal{K}_{42}^{(0)} = -f^3 \left(3b_1 + \frac{Gk_1^2}{k_3^2} \right) \quad (6.74)$$

$$\mathcal{K}_{44}^{(0)} = 2f^4 \quad (6.75)$$

$$\mathcal{K}_{51}^{(0)} = -\frac{b_1 f^3 k_1}{k_2} \quad (6.76)$$

$$\mathcal{K}_{53}^{(0)} = \frac{f^4 k_1}{k_2}. \quad (6.77)$$

Similarly, the leading GR correction $\mathcal{O}(\mathcal{H}/k)$ coefficients are,

$$\mathcal{K}_{01}^{(1)} = b_1 \gamma_1 \frac{(b_2 + b_{s^2} S)}{k_2} + b_1^2 \left(\frac{F\gamma_1 + \beta_{16}}{k_2} + \frac{\beta_{15}\mu}{k_1} + \frac{\beta_{14}k_2}{k_1^2} - \frac{\beta_{19}Gk_2}{k_3^2} \right) \quad (6.78)$$

$$\mathcal{K}_{03}^{(1)} = b_1 f \left[\frac{(\beta_{19} - \gamma_1) Gk_2}{k_3^2} - \frac{\beta_{16}}{k_2} - \frac{\beta_{15}\mu}{k_1} - \frac{\beta_{14}k_2}{k_1^2} \right] - b_1^2 \left(\frac{f\gamma_1}{k_2} + \frac{\beta_{17}k_2}{k_1^2} \right) \quad (6.79)$$

$$\mathcal{K}_{05}^{(1)} = \frac{b_1 f \beta_{17} k_2}{k_1^2} \quad (6.80)$$

$$\mathcal{K}_{10}^{(1)} = b_1 \gamma_1 \frac{(b_2 + b_{s^2} S)}{k_1} + b_1^2 \left[\left(-\frac{G\beta_{19}}{k_3^2} + \frac{\beta_{14}}{k_2^2} \right) k_1 + \frac{\beta_{15}\mu}{k_2} + \frac{F\gamma_1 + \beta_{16}}{k_1} \right] \quad (6.81)$$

$$\mathcal{K}_{12}^{(1)} = -\gamma_1 f \frac{(b_{s^2} S + b_2)}{k_1} - b_1^2 \left[\gamma_1 f \left(\frac{k_1}{k_2^2} + \frac{2}{k_1} \right) + \frac{\beta_{18}}{k_1} \right] \quad (6.82)$$

6. Multipoles of the bispectrum

$$+ b_1 f \left\{ \left[\left(-\frac{2k_1}{k_3^2} - \frac{k_2^2}{k_1 k_3^2} \right) \gamma_1 + \frac{k_1 \beta_{19}}{k_3^2} \right] G - \frac{F \gamma_1}{k_1} - \frac{\beta_{14} k_1}{k_2^2} - \frac{\beta_{15} \mu}{k_2} - \frac{\beta_{16}}{k_1} \right\} \quad (6.83)$$

$$\mathcal{K}_{14}^{(1)} = b_1 f \frac{2\gamma_1 f + \beta_{18}}{k_1} + \frac{G k_2^2 \gamma_1 f^2}{k_1 k_3^2} \quad (6.84)$$

$$\mathcal{K}_{21}^{(1)} = -\gamma_1 f \frac{(b_{s^2} S + b_2)}{k_2} - b_1^2 \left[\gamma_1 f \left(\frac{2}{k_2} + \frac{k_2}{k_1^2} \right) + \frac{\beta_{18}}{k_2} \right] \quad (6.85)$$

$$+ b_1 f \left\{ \left[\left(-\frac{k_1^2}{k_2 k_3^2} - \frac{2k_2}{k_3^2} \right) \gamma_1 + \frac{k_2 \beta_{19}}{k_3^2} \right] G - \frac{F \gamma_1}{k_2} - \frac{\beta_{16}}{k_2} - \beta_{14} \left(\frac{\mu}{k_1} + \frac{k_2}{k_1^2} \right) \right\} \quad (6.86)$$

$$\mathcal{K}_{23}^{(1)} = b_1 f \left[\left(\frac{4}{k_2} + \frac{2k_2}{k_1^2} \right) \gamma_1 f + \frac{\beta_{18}}{k_2} + \frac{\beta_{17} k_2}{k_1^2} \right] + f^2 \left[G (3\gamma_1 - \beta_{19}) \frac{k_2}{k_3^2} + \frac{\beta_{16}}{k_2} + \frac{\beta_{15} \mu}{k_1} + \frac{\beta_{14} k_2}{k_1^2} \right] \quad (6.87)$$

$$\mathcal{K}_{25}^{(1)} = -f^2 (\gamma_1 f + \beta_{17}) \frac{k_2}{k_1^2} \quad (6.88)$$

$$\mathcal{K}_{30}^{(1)} = -b_1^2 \left(\frac{f \gamma_1}{k_1} + \frac{\beta_{17} k_1}{k_2^2} \right) + b_1 f \left[G (-\gamma_1 + \beta_{19}) \frac{k_1}{k_3^2} - \frac{\beta_{14} k_1}{k_2^2} - \frac{\beta_{15} \mu}{k_2} - \frac{\beta_{16}}{k_1} \right] \quad (6.89)$$

$$\mathcal{K}_{32}^{(1)} = b_1 f \left[\left(\frac{2k_1}{k_2^2} + \frac{4}{k_1} \right) \gamma_1 f + \frac{\beta_{17} k_1}{k_2^2} + \frac{\beta_{18}}{k_1} \right] + f^2 \left[G (3\gamma_1 - \beta_{19}) \frac{k_1}{k_3^2} + \frac{\beta_{14} k_1}{k_2^2} + \frac{\beta_{15} \mu}{k_2} + \frac{\beta_{16}}{k_1} \right] \quad (6.90)$$

$$\mathcal{K}_{34}^{(1)} = -\frac{f^2 (3f \gamma_1 + \beta_{18})}{k_1} \quad (6.91)$$

$$\mathcal{K}_{41}^{(1)} = b_1 f \frac{(2\gamma_1 f + \beta_{18})}{k_2} + \frac{G \gamma_1 f^2 k_1^2}{k_2 k_3^2} \quad (6.92)$$

$$\mathcal{K}_{43}^{(1)} = -\frac{f^2 (3f \gamma_1 + \beta_{18})}{k_2} \quad (6.93)$$

$$\mathcal{K}_{50}^{(1)} = \frac{b_1 \beta_{17} f k_1}{k_2^2} \quad (6.94)$$

$$\mathcal{K}_{52}^{(1)} = -\frac{f^2 k_1 (f \gamma_1 + \beta_{17})}{k_2^2}. \quad (6.95)$$

The remaining matrices are of the form

$$\mathcal{K}_{ab}^{(2)} = \begin{pmatrix} \bullet & \circ & \bullet & \circ & \bullet & \circ \\ \circ & \bullet & \circ & \bullet & \circ & \bullet \\ \bullet & \circ & \bullet & \circ & \bullet & \circ \\ \circ & \bullet & \circ & \bullet & \circ & \circ \\ \bullet & \circ & \bullet & \circ & \circ & \circ \\ \circ & \bullet & \circ & \circ & \circ & \circ \end{pmatrix} \quad \mathcal{K}_{ab}^{(3)} = \begin{pmatrix} \circ & \bullet & \circ & \bullet & \circ & \bullet \\ \bullet & \circ & \bullet & \circ & \bullet & \circ \\ \circ & \bullet & \circ & \bullet & \circ & \circ \\ \bullet & \circ & \bullet & \circ & \circ & \circ \\ \circ & \bullet & \circ & \circ & \circ & \circ \\ \bullet & \circ & \circ & \circ & \circ & \circ \end{pmatrix} \quad \mathcal{K}_{ab}^{(4)} = \begin{pmatrix} \bullet & \circ & \bullet & \circ & \bullet & \circ \\ \circ & \bullet & \circ & \bullet & \circ & \circ \\ \bullet & \circ & \bullet & \circ & \circ & \circ \\ \circ & \bullet & \circ & \circ & \circ & \circ \\ \bullet & \circ & \circ & \circ & \circ & \circ \\ \circ & \circ & \circ & \circ & \circ & \circ \end{pmatrix} \quad \mathcal{K}_{ab}^{(5)} = \begin{pmatrix} \circ & & & & & \\ & \bullet & & & & \\ & & \circ & & & \\ & & & \bullet & & \\ & & & & \circ & \\ & & & & & \bullet \end{pmatrix}$$

6. Multipoles of the bispectrum

$$\mathcal{K}_{ab}^{(6)} = \begin{pmatrix} \bullet & \circ & \bullet & \circ & \circ & \circ \\ \circ & \bullet & \circ & \circ & \circ & \circ \\ \bullet & \circ & \circ & \circ & \circ & \circ \\ \circ & \circ & \circ & \circ & \circ & \circ \\ \circ & \circ & \circ & \circ & \circ & \circ \\ \circ & \circ & \circ & \circ & \circ & \circ \end{pmatrix} \quad \mathcal{K}_{ab}^{(7)} = \begin{pmatrix} \circ & \bullet & \circ & \circ & \circ & \circ \\ \bullet & \circ & \circ & \circ & \circ & \circ \\ \circ & \circ & \circ & \circ & \circ & \circ \\ \circ & \circ & \circ & \circ & \circ & \circ \\ \circ & \circ & \circ & \circ & \circ & \circ \\ \circ & \circ & \circ & \circ & \circ & \circ \end{pmatrix} \quad \mathcal{K}_{ab}^{(8)} = \begin{pmatrix} \bullet & \circ & \circ & \circ & \circ & \circ \\ \circ & \circ & \circ & \circ & \circ & \circ \\ \circ & \circ & \circ & \circ & \circ & \circ \\ \circ & \circ & \circ & \circ & \circ & \circ \\ \circ & \circ & \circ & \circ & \circ & \circ \\ \circ & \circ & \circ & \circ & \circ & \circ \end{pmatrix}. \quad (6.96)$$

Their coefficients are extracted in similar fashion, and can be found in full in appendix [REF APPENDIX Kab COEFF](#)

either ref appendix, or put coeffs here

6.3. Analysis of the multipoles

Here we present an analysis of the behaviour of the multipoles.

6.3.1. Co-linear, squeezed and equilateral limits

To help understand further the multipoles we can evaluate their equilateral ($k_1 = k_2 = k_3$), co-linear ($\theta = 0$ or $\theta = \pi$) and squeezed limits analytically. Non-zero co-linear multipoles exist only for $m = 0$ components. This is the one limit that is easy to evaluate by hand – it follows directly from (6.55). The equilateral case is significantly more complicated to evaluate. Non-zero equilateral multipoles exist for all even m , for any ℓ , the one exception being the $m = 0$ part of the dipole, for which the equilateral configuration is identically zero. These are summarised in Fig. 6.2, together with the powers of k which appear in each multipole.

The squeezed limit was explicitly evaluated in Clarkson et al. (2019) for the leading $\mathcal{O}(\mathcal{H}/k_L)$ contribution, where k_L is the long mode, which we expand further here. Note that in what follows, we have assumed that the small-scale modes are sufficiently sub-equality scale, and that the large-scale modes are larger than the equality scale. The leading corrections in the even multipoles require us going beyond leading order $\mathcal{O}(\mathcal{H}/k_L)$ in the squeezed limit. We let

$$k_1 = k_2 = k_S, \quad k_3 = \epsilon k_S, \quad (6.97)$$

6. Multipoles of the bispectrum

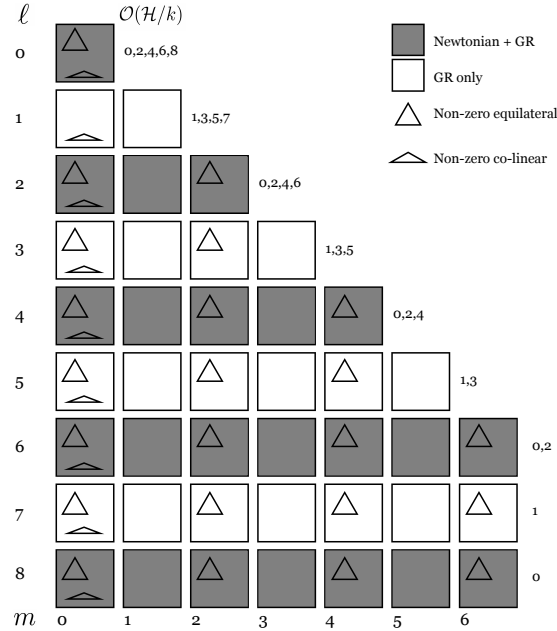


Figure 6.2.: Overview of all non-zero multipoles for the bispectrum, which includes ℓ from 0 to 8, and m from $-\ell$ to ℓ ; the pattern here is the same for $m < 0$, so only $m \geq 0$ are displayed. Denoted in the figure are whether components are Newtonian+GR or GR only, triangle shapes indicating whether given components are non-vanishing in flattened (co-linear) or equilateral limits. Note how the dipole is unique in having the equilateral case vanish for every value of m . Also given is which powers of \mathcal{H}/k appear in each of the multipoles.

to write the wavenumber in terms of the short mode $k_S \gg k_L$, which implies

$$\mu = -1 + \frac{\epsilon^2}{2}. \quad (6.98)$$

We then take the limit as $\epsilon \rightarrow 0$ with the short mode k_S fixed, and keep only the leading terms in \mathcal{H}/k_L , neglecting factors of \mathcal{H}/k_S and $P(k_S)^2$. For each multipole we are then left with the squeezed limit as a polynomial in \mathcal{H}/k_L . The leading

6. Multipoles of the bispectrum

contributions are:

$$\underbrace{\left(\frac{\mathcal{H}}{k_L}\right)^0 \begin{pmatrix} \bullet & \cdot \\ \circ & \circ & \cdot \\ \bullet & \circ & \bullet & \cdot & \cdot & \cdot & \cdot & \cdot & \cdot \\ \circ & \circ & \circ & \circ & \cdot & \cdot & \cdot & \cdot & \cdot \\ \bullet & \circ & \bullet & \circ & \bullet & \cdot & \cdot & \cdot & \cdot \\ \circ & \circ & \circ & \circ & \circ & \circ & \cdot & \cdot & \cdot \\ \bullet & \circ & \bullet & \circ & \bullet & \circ & \circ & \cdot & \cdot \\ \circ & \cdot \\ \bullet & \circ & \bullet & \circ & \bullet & \circ & \circ & \circ & \circ \end{pmatrix}}_{\text{Newtonian part}} + \underbrace{\left(\frac{\mathcal{H}}{k_L}\right)^1 \begin{pmatrix} \circ & \cdot \\ \circ & \bullet & \cdot \\ \circ & \circ & \circ & \cdot & \cdot & \cdot & \cdot & \cdot & \cdot \\ \circ & \bullet & \circ & \bullet & \cdot & \cdot & \cdot & \cdot & \cdot \\ \circ & \circ & \circ & \circ & \circ & \cdot & \cdot & \cdot & \cdot \\ \circ & \bullet & \circ & \bullet & \circ & \circ & \cdot & \cdot & \cdot \\ \circ & \cdot & \cdot \\ \circ & \bullet & \circ & \bullet & \circ & \circ & \circ & \circ & \cdot \\ \circ & \circ \end{pmatrix}}_{\text{GR contributions (6.99)}} + \underbrace{\left(\frac{\mathcal{H}}{k_L}\right)^2 \begin{pmatrix} \bullet & \cdot \\ \circ & \circ & \cdot \\ \bullet & \circ & \bullet & \cdot & \cdot & \cdot & \cdot & \cdot & \cdot \\ \circ & \circ \\ \bullet & \circ & \bullet & \circ & \bullet & \circ & \circ & \circ & \circ \\ \circ & \circ \\ \bullet & \circ & \bullet & \circ & \bullet & \circ & \circ & \circ & \circ \\ \circ & \circ \\ \bullet & \circ & \bullet & \circ & \bullet & \circ & \circ & \circ & \circ \end{pmatrix}}_{\text{GR contributions (6.99)}}$$

Here, the matrices represent the ℓ, m values from $\ell = 0, m = 0$ (top left entry). We see that the Newtonian part has non-zero squeezed limits for some even m , terminating at $m = 4$. GR corrections come in up to $m = 3$ for $\ell \leq 7$. For odd m these contributions come in for the leading terms $\mathcal{O}(\mathcal{H}/k)$, while for m even the order is lower, $\mathcal{O}((\mathcal{H}/k)^2)$. Note that we assume primordial Gaussianity. In the presence of primordial non-Gaussianity, the squeezed limit has higher powers of \mathcal{H}/k . Current work investigates how primordial non-Gaussianity will change our results. The effect of local primordial non-Gaussianity on the Newtonian galaxy bispectrum is presented in Umeh et al. (2017).

6.3.2. Numerical analysis for next-generation surveys

Here we present a numerical analysis of the multipoles of the galaxy bispectrum. We use three different survey models, two of which are appropriate for future surveys; i.e. SKA HI intensity mapping, and a Stage IV $H\alpha$ spectroscopic galaxy survey similar to Euclid. The third model we consider is a simplified ‘toy model’ for illustrative purposes. The parameters we use are introduced below.

Evolution and magnification bias are defined as Alonso et al. (2015b),

$$b_e = -\frac{\partial \ln n_g}{\partial \ln(1+z)}, \quad \mathcal{Q} = -\frac{\partial \ln n_g}{\partial \ln L} \Big|_c, \quad (6.100)$$

where n_g is the comoving galaxy number density, L the luminosity, and $|_c$ denotes evaluation at the flux cut.

6. Multipoles of the bispectrum

For an HI intensity mapping survey, we estimate the bias from the halo model following Umeh et al. (2016). This yields the following fitting formulae for first and second order bias,

$$b_1^{\text{HI}}(z) = 0.754 + 0.0877z + 0.0607z^2 - 0.00274z^3, \quad (6.101)$$

$$b_2^{\text{HI}}(z) = -0.308 - 0.0724z - 0.0534z^2 + 0.0247z^3. \quad (6.102)$$

For the tidal bias, we assume zero initial tidal bias which relates b_{s^2} to b_1 as,

$$b_{s^2}^{\text{HI}}(z) = -\frac{4}{7}(b_1(z) - 1), \quad (6.103)$$

so that,

$$b_{s^2}^{\text{HI}}(z) = 0.141 - 0.0501z - 0.0347z^2 + 0.00157z^3. \quad (6.104)$$

The HI intensity mapping evolution bias is given by the background HI brightness temperature Fonseca et al. (2018),

$$b_e^{\text{HI}}(z) = -\frac{d \ln [(1+z)^{-1} \mathcal{H} \bar{T}_{\text{HI}}]}{d \ln [1+z]}, \quad (6.105)$$

where \bar{T}_{HI} is given by the fitting formula,

$$\bar{T}_{\text{HI}}(z) = (5.5919 + 23.242z - 2.4136z^2) \times 10^{-2} \text{ mK}. \quad (6.106)$$

The effective magnification bias for HI intensity mapping is Fonseca et al. (2018)

$$Q^{\text{HI}} = 1.0, \quad (6.107)$$

and clustering bias is independent of luminosity,

$$\frac{\partial b_1^{\text{HI}}}{\partial \ln L} = 0. \quad (6.108)$$

We consider a Stage IV $H\alpha$ spectroscopic survey similar to Euclid, and use the clustering biases given in Maartens et al. (2020),

$$b_1^{H\alpha}(z) = 0.9 + 0.4z, \quad (6.109)$$

$$b_2^{H\alpha}(z) = -0.741 - 0.125z + 0.123z^2 + 0.00637z^3, \quad (6.110)$$

$$b_{s^2}^{H\alpha}(z) = 0.0409 - 0.199z - 0.0166z^2 + 0.00268z^3. \quad (6.111)$$

6. Multipoles of the bispectrum

The magnification bias and evolution bias are Maartens et al. (2020),

$$\mathcal{Q}^{H\alpha}(z) = \frac{y_c(z)^{\alpha+1} \exp[-y_c(z)]}{\Gamma(\alpha+1, y_c(z))}, \quad (6.112)$$

$$b_e^{H\alpha}(z) = -\frac{d \ln \Phi_*(z)}{d \ln(1+z)} + \frac{d \ln y_c(z)}{d \ln(1+z)} \mathcal{Q}^{H\alpha}(z), \quad (6.113)$$

where $\alpha = -1.35$, Γ is the upper incomplete gamma function, Φ_* is given in Maartens et al. (2020) and $y_c(z) = [\chi(z)/(2.97h \times 10^3) (\text{Mpc}/h)]^2$. Table 1 in Maartens et al. (2020) summarises the numerical values of the bias parameters discussed above. Finally, we follow Maartens et al. (2020) and take

$$\left. \frac{\partial b_1^{H\alpha}}{\partial \ln L} \right|_{\text{c}} = 0. \quad (6.114)$$

For the simple model of galaxy bias, we use

$$b_1(z) = \sqrt{1+z}, \quad (6.115)$$

$$b_2(z) = -0.3\sqrt{1+z}, \quad (6.116)$$

$$b_{s^2}(z) = -\frac{4}{7}(b_1(z) - 1), \quad (6.117)$$

$$b_e = 0, \quad (6.118)$$

$$\mathcal{Q} = 0. \quad (6.119)$$

For cosmological parameters we use Planck 2018 Aghanim et al. (2018), giving the best-fit parameters $h = 0.6766$, $\Omega_{m0} = 0.3111$, $\Omega_{b0}h^2 = 0.02242$, $\Omega_{c0}h^2 = 0.11933$, $n_s = 0.9665$, $\gamma = \ln f / \ln \Omega_m = 0.545$. The linear matter power spectrum is calculated using CAMB Lewis et al. (2000).

We examine numerically three different triangular configurations, the squeezed, co-linear, and equilateral triangles, as a function of triangle size. For our numerical analysis, we choose a moderately squeezed triangle shape with $\theta \approx 178^\circ$, which corresponds to $k_3 = k$, $k_1 = k_2 = 28k$ (such that long mode k_3 is the reference wavevector, and the other vectors are defined in relation to the long mode). For the co-linear case, we use flattened isosceles triangles with $\theta \approx 2.3^\circ$, corresponding to $k_3 = k$, $k_1 = k_2 = 0.5001k$. All plots are at redshift $z = 1$, with the exception of figure 6.9, where we look at the amplitude as a function of redshift.

Firstly, we consider the total amplitude of the different multipoles with respect to the

6. Multipoles of the bispectrum

Newtonian monopole, plotting the total power contained in each of the multipoles and normalising by the Newtonian monopole of the galaxy bispectrum,

$$b_\ell(k_1, k_2, \theta) = \frac{1}{B_{N,00}(k_1, k_2, \theta)} \sqrt{\frac{1}{2\ell+1} \sum_{m=-\ell}^{\ell} |B_{\ell m}(k_1, k_2, \theta)|^2}. \quad (6.120)$$

We present this for all multipoles $\ell = 0 \dots 8$ and separately for each of the triangle shapes introduced above (i.e. fixing triangle shape, and varying size by varying k), as well as for both bias models which are relevant for future surveys. The results can be viewed in figures 6.3, 6.4 and 6.5.

We have created colour-intensity plots to give an overview of the relative amplitudes of the first few multipoles of the galaxy bispectrum, $\ell = 0 \dots 3$. Because of the simple relationship between $B_{\ell m}$ and $B_{\ell, -m}$, we do not show plots for negative m . These as well are done for both HI intensity mapping bias and $H\alpha$ bias. The results are shown in figures 6.6 and 6.7 for the Euclid-like survey and for SKA intensity mapping respectively.

To further investigate the dependence on triangle shape we investigate the reduced bispectrum. We define the reduced bispectrum as

$$Q_{\ell m}(k_1, k_2, \theta) = \frac{B_{\ell m}(k_1, k_2, \theta)}{P_0(k_1)P_0(k_2) + P_0(k_2)P_0(k_3) + P_0(k_1)P_0(k_3)}, \quad (6.121)$$

where P_0 is the monopole of the galaxy power spectrum,

$$P_0(k) = \frac{1}{2} \int_{-1}^1 d\mu P_g(\mathbf{k}), \quad (6.122)$$

with the galaxy power spectrum $P_g(\mathbf{k}) = (b_1 + f\mu^2)^2 P$, P being the linear dark matter power spectrum. (An alternative definition would be to use the relativistic galaxy power spectrum which would induce small changes $O((\mathcal{H}/k)^2)$ on Hubble scales.) The reduced bispectrum Q is hence dependent on magnitude of wavevectors \mathbf{k}_1 and \mathbf{k}_2 , and the angle between these $(\pi - \theta)$. We fix $k_1 = 0.1 \text{ Mpc}^{-1}$ and $k_1 = 0.01 \text{ Mpc}^{-1}$, and use differently coloured lines to indicate the ratio of k_2/k_1 , which ranges from isosceles triangles in which $k_1 = k_2$, to $k_2/k_1 = 4.5$. The angle θ ranges from $[0, \pi]$, except for the isosceles shape, for which we stop at $\theta = \pi - 0.01$ (for $k_1 = 0.1 \text{ Mpc}^{-1}$), and at $\theta = \pi - 0.02$ (for $k_1 = 0.01 \text{ Mpc}^{-1}$). The reason for this is the inclusion of relativistic \mathcal{H}/k contributions, which cause unobservable divergences as $k \rightarrow 0$, occurring here for the isosceles shape when the angle between

6. Multipoles of the bispectrum

\mathbf{k}_1 and \mathbf{k}_2 goes to π and $k_3 \rightarrow 0$.

The bias used is again that for the Euclid-like $H\alpha$ spectroscopic survey. Results are in figure 6.8. The layout is similar to figures 6.6 and 6.7, with $\ell = 0 \dots 3$ plotted. Once again, negative m are not shown.

Lastly, we fix triangle shape and size, and plot the relative total power (as defined in (6.120)) as a function of redshift, where redshift ranges from $z = 0.1 \dots 2.0$. This is done for the toy model for bias only. The three panels in figure 6.9 show the results for $\ell = 0 \dots 3$, for each of the three wavevector triangles discussed earlier; equilateral, squeezed and flattened shapes. Solid and dashed lines indicate the relative total power for $k_1 = 0.1 \text{ Mpc}^{-1}$ and $k_1 = 0.01 \text{ Mpc}^{-1}$ respectively.

6. Multipoles of the bispectrum

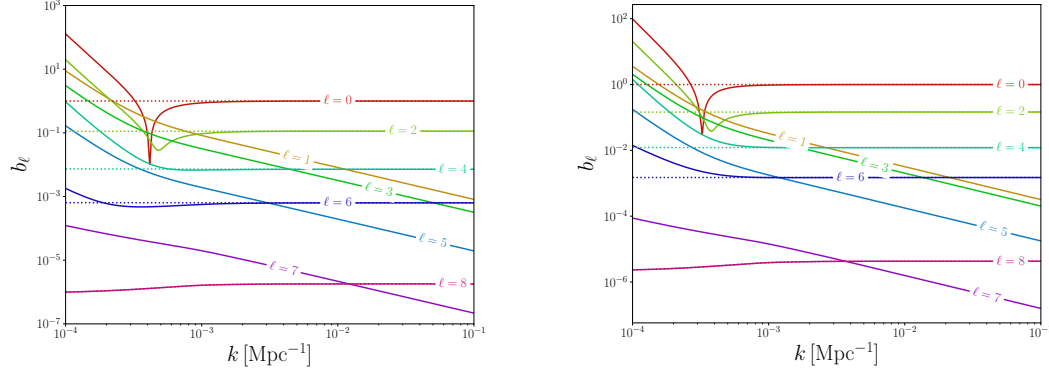


Figure 6.3.: Normalised total power for squeezed configuration for Euclid-like (left) and SKA HI intensity mapping (right) surveys. Long mode k_3 is plotted along the x -axis.

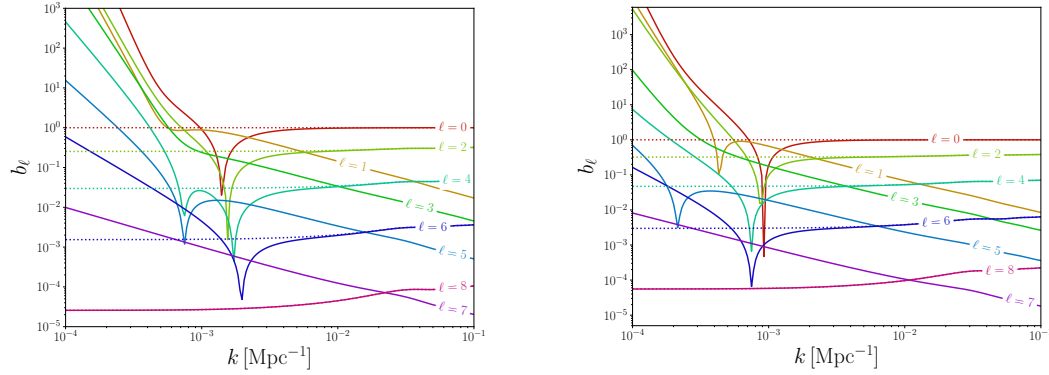


Figure 6.4.: Total power for flattened configuration for Euclid-like (left) and SKA HI intensity mapping (right) surveys. Long mode k_3 is plotted along the x -axis.

6. Multipoles of the bispectrum

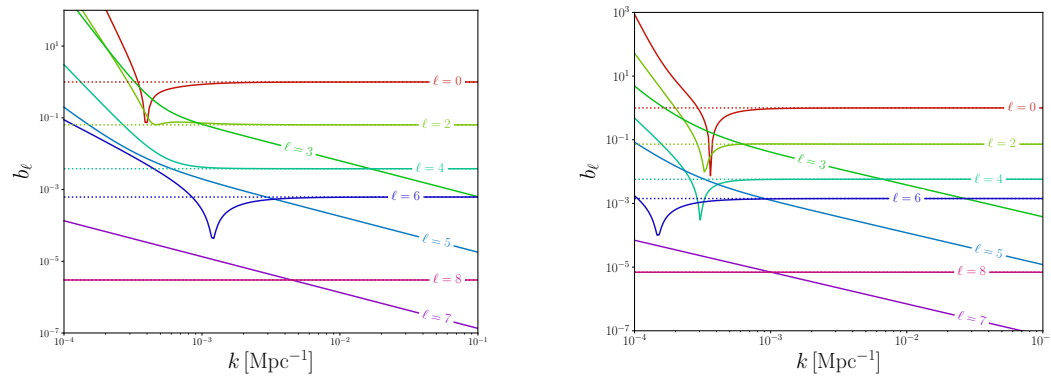


Figure 6.5.: Total power for equilateral configuration for Euclid-like (left) and SKA HI intensity mapping (right) surveys. Since the dipole vanishes in this limit, the $\ell = 1$ line is absent.

6. Multipoles of the bispectrum

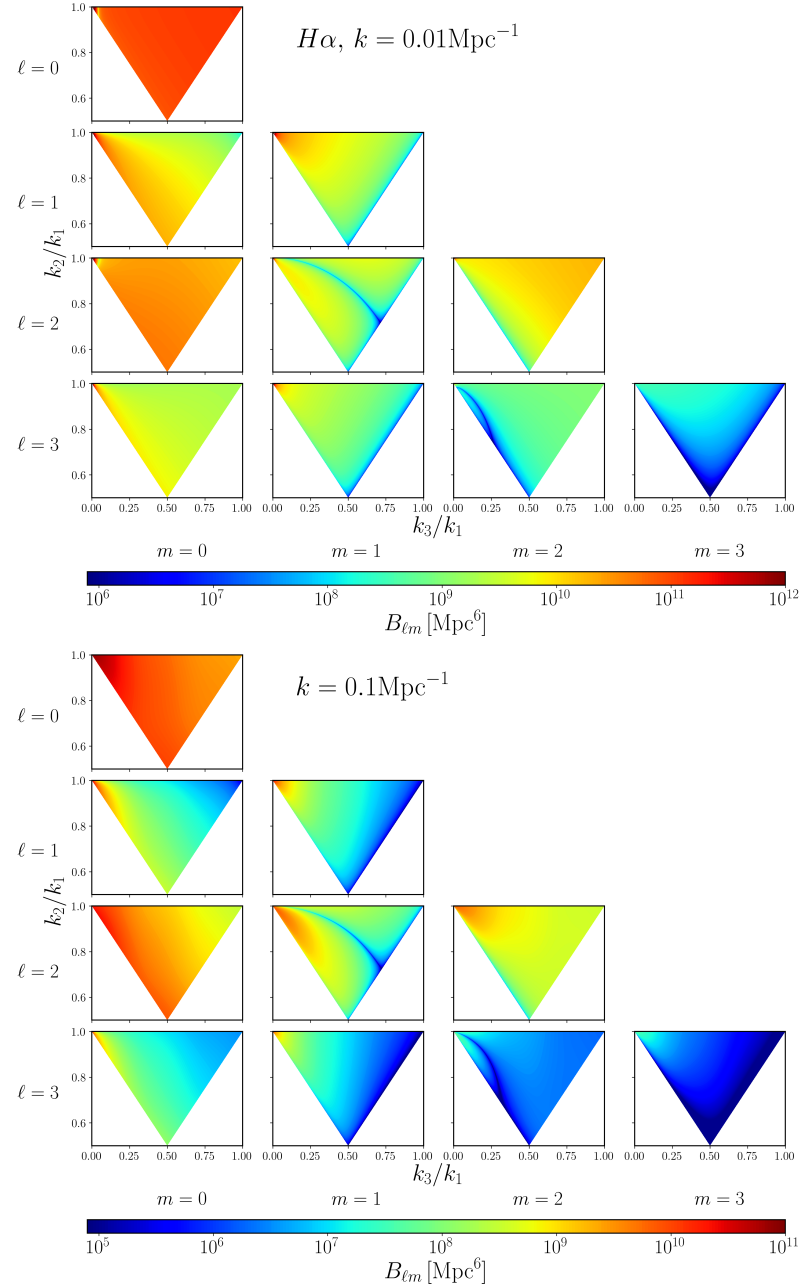


Figure 6.6.: A selection of multipoles of the galaxy bispectrum, $B_{\ell m}$, with $\ell = 0 \dots 3$ and $m = 0 \dots \ell$ as indicated in the figure. Bias model used is that for $H\alpha$ /Euclid-like survey. k_1 is kept fixed, the value of which is given alongside the plot, and the x and y axes vary respectively k_3 and k_2 with respect to the fixed k_1 . The upper left corner of the wedge shape is the squeezed limit, the upper right corner is the equilateral configuration, and the lower corner is the co-linear configuration. Note the difference in range of the colour bars.

6. Multipoles of the bispectrum

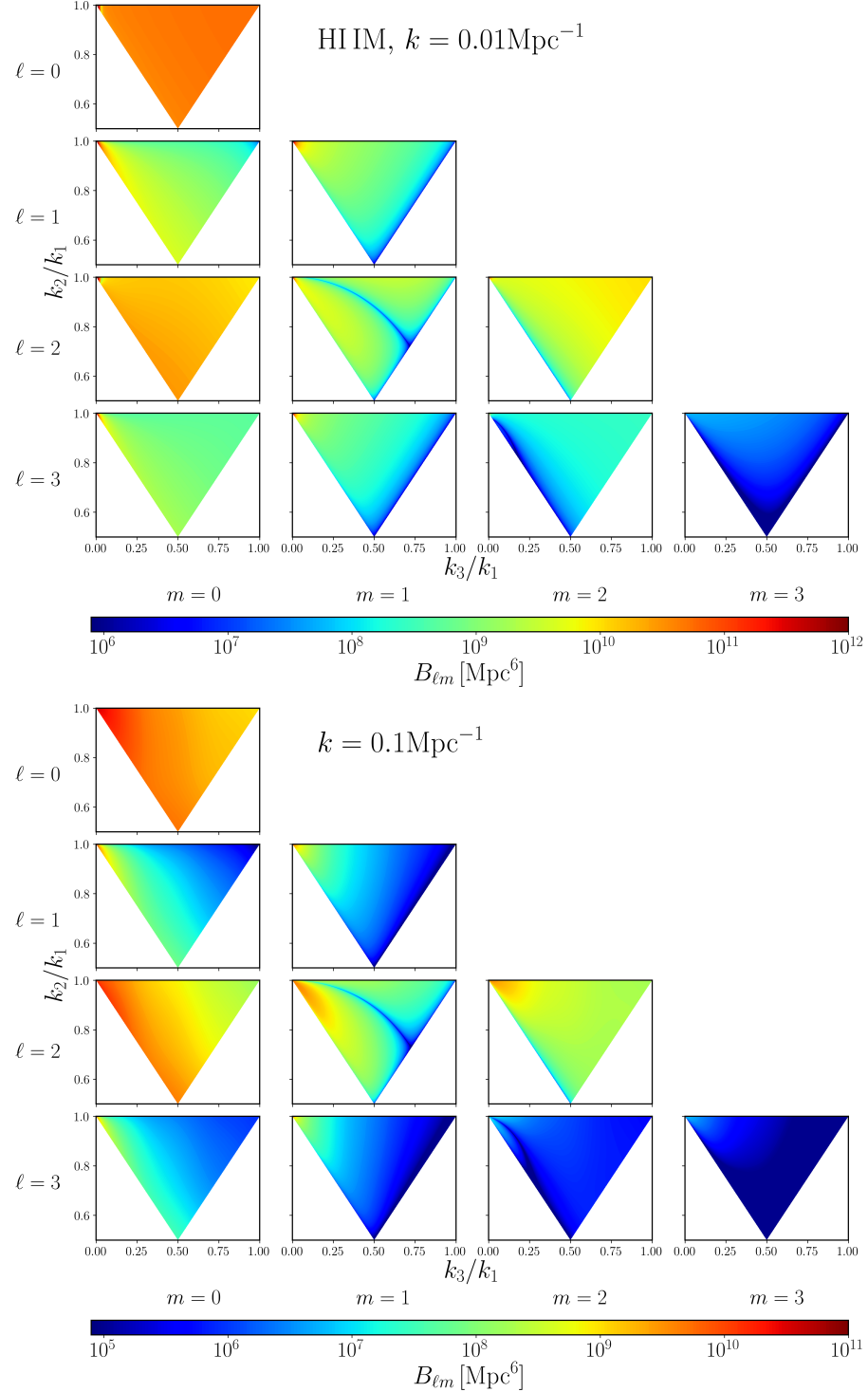


Figure 6.7.: Selected multipoles of the galaxy bispectrum, similar to figure 6.6, but with the bias model appropriate for intensity mapping. The value of fixed k_1 is indicated on the figures. The upper left corner of a wedge shape is the squeezed limit, the upper right corner is the equilateral configuration, and the lower corner is the co-linear configuration.

6. Multipoles of the bispectrum

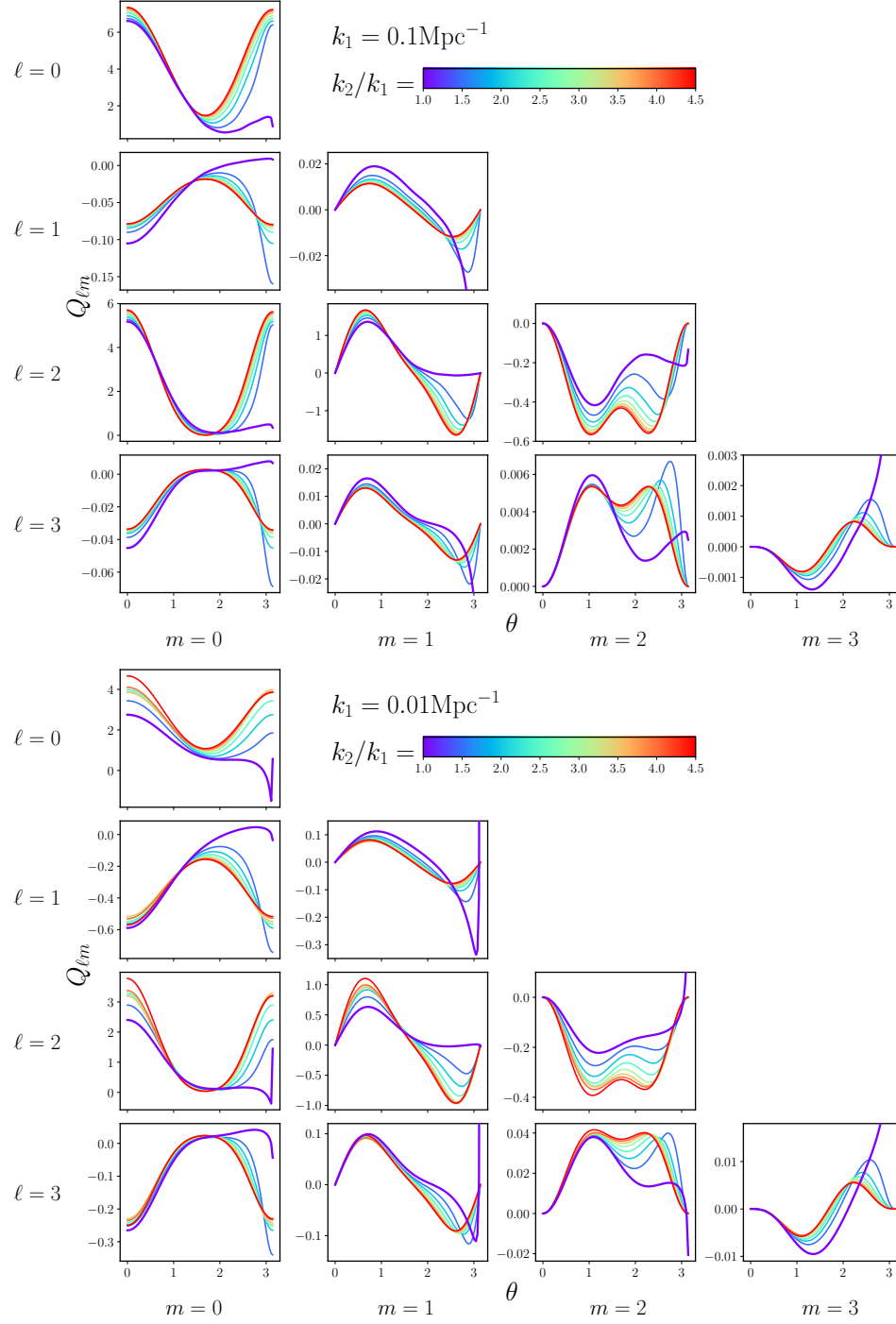


Figure 6.8.: Results for the reduced bispectrum $Q_{\ell m}$, where $\ell = 0 \dots 3$ and negative m not shown. The multipoles ℓ, m are indicated on the figure, as well as the value of k_1 which is kept fixed. The colourbar and different colours denote the ratio of k_2/k_1 , where the slightly thicker purple line is the isosceles triangle, which diverges as $\theta \rightarrow \pi$ since there $k_3 \rightarrow 0$.

6. Multipoles of the bispectrum

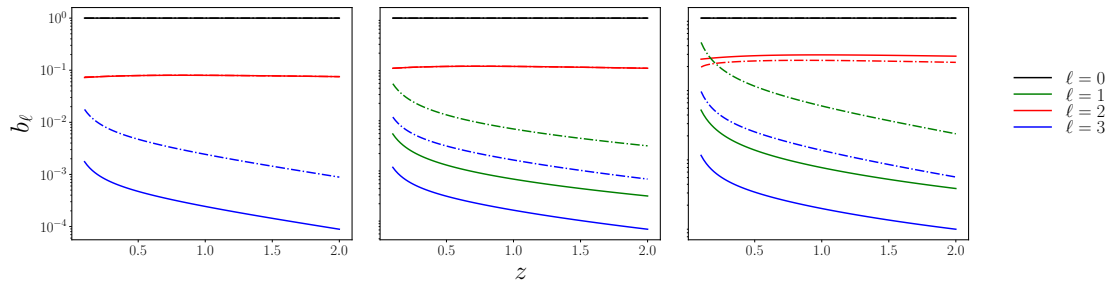


Figure 6.9.: Total power contained in the relativistic bispectrum normalised by the Newtonian monopole as a function of redshift z ranging from 0.1 to 2. The three panels are the equilateral configuration (left, with $\ell = 1$ vanishing), squeezed (middle) and co-linear flattened configuration (right). Solid lines for $k = 0.1 \text{ Mpc}^{-1}$, and dash-dotted for $k = 0.01 \text{ Mpc}^{-1}$.

Figures 6.3, 6.4 and 6.5 show the amplitude of the total power as defined in (6.120). For each ℓ this contains all orientations per multipole divided by the amplitude of the Newtonian monopole. Values of ℓ are labelled on the figure, with the dotted lines denoting the Newtonian contribution (for even ℓ only). For small scales (larger wavenumber k), the Newtonian contributions are generally larger than the relativistic b_ℓ (i.e. odd ℓ), however at larger scales, above equality, the relative power contained in relativistic contributions increases. This shows up in the even multipoles as a divergence between the dotted (purely Newtonian) lines and solid (GR-corrected) lines. In the odd multipoles, we see an increase in amplitude, which at the largest scales become larger than the purely Newtonian signal. This is dependent on bias model and triangular configuration.

The colour-intensity maps in figures 6.6 and 6.7 show the amplitude of the relativistic bispectrum over the k_3/k_1 , k_2/k_1 plane. The amplitude of the bispectrum signal peaks in the squeezed limit where $k_1 = k_2$, $k_3 \rightarrow 0$ which is in the top left corner in these plots. For the odd multipoles $\ell = 1$ and $\ell = 3$, the amplitude of the dipole is higher than the $\ell = 3$ case in most configurations. The amplitude of the relativistic bispectrum is also higher for larger scales (smaller k). For $\ell = 1$, the equilateral configuration, which lies in the upper right corner of the plots, is vanishing as we established analytically. We can also observe from these plots that there is a rough trend that more power is contained in the lower m multipoles.

The reduced bispectrum is plotted in figure 6.8, showing large relativistic contributions to the bispectrum odd-multipoles especially at large scales. This also shows the significant dependence on the triangle shape, depending on the orientation of the harmonic.

6. Multipoles of the bispectrum

Finally figure 6.9 shows the total power divided by the Newtonian monopole, as a function of redshift. The model for bias used here is not physically realistic, but this illustrates the generic behaviour with redshift we can expect. It is interesting to observe how, when going towards lower redshift, the power in the relativistic corrections to the bispectrum grows compared to the Newtonian signal. This is especially noticeable in squeezed and flattened shapes where the dipole approaches or surpasses the $\ell = 2$ line. Of course, at low redshift the plane-parallel assumption that we have used becomes a worse approximation.

6.4. Conclusion

We have considered in detail for the first time the multipole decomposition of the observed relativistic galaxy bispectrum. In section 6.2 we have shown how the multipoles may be derived analytically, with an analytic formula given in equation (6.55), and have illustrated how they behave in the squeezed, equilateral and co-linear limits (which includes the flattened case) in section 6.3. We have shown how the amplitude of the relativistic signals behaves for two types of upcoming surveys – a Euclid-like galaxy survey, and an SKA intensity mapping survey. Our key findings are:

odd multipoles Relativistic effects generate a hierarchy of odd multipoles which are absent in the Newtonian picture, plus an additional contribution to all multipoles up to $\ell = 7$. In particular we find that the octopole is similar in amplitude to the dipole; it is only about a factor of 5 or so smaller than the dipole. These are both larger than the Newtonian hexadecapole on large scales. Higher multipoles are suppressed. This effect can be seen clearly in figures 6.3, 6.4, 6.5.

powers of k The leading power of the relativistic correction in each ℓ harmonic is $(\mathcal{H}/k)^1$ for odd multipoles and $(\mathcal{H}/k)^2$, for even multipoles. Furthermore, all odd multipoles contain the leading (\mathcal{H}/k) correction, while lower values of ℓ contain the higher powers of \mathcal{H}/k , going up to $(\mathcal{H}/k)^7$ for $\ell = 1$ (though these are probably unobservable). An overview of occurring powers of k is given in figure 6.2.

special limits the co-linear case ($\theta = 0$ or π) only generates non-zero $m = 0$ multipoles and vanishes for all other values of m . The equilateral case is always zero for m odd, and is always zero for the special case of the dipole. For the

6. Multipoles of the bispectrum

squeezed limit we have leading (\mathcal{H}/k) relativistic corrections for ℓ and $m \leq 3$ odd.

multipoles with shape We computed the amplitude of each ℓ, m over the range of triangle shapes in figures 6.6, 6.7. For each ℓ most of the power is contained in the lower m multipoles.

multipoles with scale We analysed the total power in each multipole as a function of scale for 3 triangle shapes at $z = 1$. Roughly speaking the even- ℓ are dominated by the Newtonian part and have little scale dependence relative to the Newtonian monopole, though this changes approaching the Hubble scale. For odd- ℓ the leading relativistic part dominates and the dipole reaches the size of the Newtonian quadrupole around equality scales.

redshift dependence Relative to the Newtonian monopole, all the relativistic multipoles decay with redshift, while the quadrupole is roughly constant. For large squeezed triangles the dipole is comparable in size to the quadrupole for small redshift as shown in figure 6.9.

Of course, the analysis here is limited by the fact we have neglected wide angle effects which will alter the multipoles. Integrated effects will also contribute, but their effect will be suppressed when we analyse the multipoles. We leave these contributions for future work. Also currently under investigation is detectability of the galaxy bispectrum, with the leading order contribution examined in Maartens et al. (2020).

7. Local primordial non-Gaussianity in the bispectrum

Next-generation galaxy and 21cm intensity mapping surveys will rely on a combination of the power spectrum and bispectrum for high-precision measurements of primordial non-Gaussianity. In turn, these measurements will allow us to distinguish between various models of inflation. However, precision observations require theoretical precision at least at the same level. We extend the theoretical understanding of the galaxy bispectrum by incorporating a consistent general relativistic model of galaxy bias at second order, in the presence of local primordial non-Gaussianity. The influence of primordial non-Gaussianity on the bispectrum extends beyond the galaxy bias and the dark matter density, due to redshift-space effects. The standard redshift-space distortions at first and second order produce a well-known primordial non-Gaussian imprint on the bispectrum. Relativistic corrections to redshift-space distortions generate new contributions to this primordial non-Gaussian signal, arising from: (1) a coupling of first-order scale-dependent bias with first-order relativistic observational effects, and (2) linearly evolved non-Gaussianity in the second-order velocity and metric potentials which appear in relativistic observational effects. Our analysis allows for a consistent separation of the relativistic ‘contamination’ from the primordial signal, in order to avoid biasing the measurements by using an incorrect theoretical model. We show that the bias from using a Newtonian analysis of the squeezed bispectrum could be $\Delta f_{\text{NL}} \sim 5$ for a Stage IV H α survey.

7.1. Galaxy clustering statistics and primordial non-Gaussianity

Galaxy number counts are distorted by projection effects that arise from observing on the past lightcone. The dominant perturbative effect on sub-Hubble scales is from redshift-space distortions (RSD) Sargent & Turner (1977); Kaiser (1987), which constitute the standard Newtonian approximation to projection effects. Lensing magnification produces the best-known relativistic correction to RSD Villumsen (1995), but there are further relativistic effects Yoo et al. (2009); Yoo (2010); Challinor & Lewis (2011); Bonvin & Durrer (2011). The basic idea is the following. The number of sources, dN , above the luminosity threshold that are counted by the observer in a solid angle element about unit direction \mathbf{n} and in a redshift interval about a central redshift z , is given by

$$dN = N_g dz d\Omega_{\mathbf{n}} = n_g dV. \quad (7.1)$$

The second equality relates the observed quantities to those measured in the rest frame of the source. N_g is the number that is counted by the observer per redshift per solid angle, while n_g is the number per proper volume, which is not observed by the observer but is the quantity that would be measured at the source. Similarly, dV is not the observed volume element but the corresponding proper volume element at the source.

Then the observed number density contrast, $\Delta_g = (N_g - \bar{N}_g)/\bar{N}_g$, is related to the proper number density contrast at the source, $\delta_g = (n_g - \bar{n}_g)/\bar{n}_g$, by volume, redshift and luminosity perturbations. At first order in Poisson gauge, the gauge-independent relation (7.1) leads to

$$\begin{aligned} \Delta_g &= \delta_g + \text{RSD} + \text{lensing effect} + \text{other relativistic effects} \\ &= \delta_g - \frac{1}{\mathcal{H}} \mathbf{n} \cdot \nabla (\mathbf{v} \cdot \mathbf{n}) + 2(1 - \mathcal{Q})\kappa + A(\mathbf{v} \cdot \mathbf{n}) + B\Psi + \int d\chi C\Psi' + \int d\chi E\Psi. \end{aligned} \quad (7.2)$$

Here $\mathcal{H} = d \ln a / d\eta = (\ln a)'$ is the conformal Hubble rate, $\mathbf{v} = \nabla V$ is the peculiar velocity (V is not to be confused with the often-used alternative $v = |\mathbf{v}|$), κ is the integrated lensing convergence, \mathcal{Q} is the magnification bias, χ is the comoving line-of-sight distance and the integrals are from source to observer. The perturbed

7. Local primordial non-Gaussianity in the bispectrum

metric is given by

$$a^{-2}ds^2 = -(1 + 2\Phi)d\eta^2 + (1 - 2\Psi)dx^2, \quad (7.3)$$

and we have assumed $\Phi = \Psi$. The time-dependent factors A, B, C, E in (7.2) correspond respectively to Doppler, Sachs-Wolfe, integrated Sachs-Wolfe and time-delay effects. In Fourier space the Doppler term scales as $\partial V \propto (\mathcal{H}/k)\delta_m$, while the remaining terms scale as $\Psi \propto (\mathcal{H}/k)^2\delta_m$. Thus the other relativistic effects are suppressed on sub-Hubble scales, unlike the lensing effect, which scales as $\partial^2\Psi \propto \delta_m$.

The case of 21cm intensity mapping follows from the number count expressions by using the ‘dictionary’ given in Hall et al. (2013); Alonso et al. (2015b); Fonseca et al. (2015) at first order and in Umeh et al. (2016); Di Dio et al. (2016); Jolicoeur et al. (2020) at second order.

The physical definition of linear Gaussian galaxy bias is in the joint matter-galaxy rest frame, which corresponds to the comoving gauge (‘C gauge’),¹ so that (omitting luminosity dependence for brevity),

$$\delta_{gC}(a, \mathbf{x}) = b_1(a)\delta_{mC}(a, \mathbf{x}). \quad (7.4)$$

This relation is gauge-independent because C gauge corresponds to the physical rest frame. When transforming to other gauges, δ_g is in general no longer proportional to δ_m Challinor & Lewis (2011); Bruni et al. (2012); Jeong et al. (2012). For example, in the Poisson gauge of (7.2) and (7.3),

$$\delta_g = b_1\delta_{mC} + (3 - b_e)\mathcal{H}V, \quad b_e = \frac{\partial \ln(a^3\bar{n}_g)}{\partial \ln a}, \quad (7.5)$$

where b_e is known as the evolution bias, which encodes the non-conservation of the background comoving galaxy number density. The velocity potential V scales as Ψ by the Euler equation, $V \propto \Psi \propto (\mathcal{H}/k)^2\delta_m$, and therefore the gauge correction $(3 - b_e)\mathcal{H}V$ is only non-negligible on Hubble scales and may be neglected in a Newtonian approximation.

Local primordial non-Gaussianity (PNG) generates scale-dependent linear bias, with constant parameter f_{NL} Dalal et al. (2008); Matarrese & Verde (2008):

$$b_1(a) \rightarrow b_1(a) + 3\delta_{\text{crit}}\Omega_{m0}H_0^2 \frac{[b_1(a) - 1]}{D(a)} g_{\text{in}} \frac{f_{NL}}{T(k)k^2}. \quad (7.6)$$

¹In the Λ CDM model the comoving and synchronous gauges coincide.

7. Local primordial non-Gaussianity in the bispectrum

The threshold density contrast for collapse is usually taken to be $\delta_{\text{crit}} = 1.686$, and the growth factor D is normalised to 1 today ($a_0 = 1$), i.e. $\delta_m(a, \mathbf{k}) = D(a)\delta_{m0}(\mathbf{k})$. The growth suppression factor for the potential Ψ is $g = D/a$, which is thus also normalised as $g_0 = 1$, with initial value g_{in} deep in the matter era, and T is the transfer function. Note that (7.6) follows the CMB convention for f_{NL} Baldauf et al. (2011); Desjacques et al. (2018b); g_{in} can be removed from (7.6) if D is normalised as $D_{\text{in}} = a_{\text{in}}$. In a Λ CDM model we have the useful relation Villa & Rampf (2016)

$$\frac{g_{\text{in}}}{g} = \frac{3}{5} \left(1 + \frac{2f}{3\Omega_m} \right), \quad (7.7)$$

where the growth rate of linear matter perturbations, $f = d \ln D / d \ln a$, is very well approximated by $f(a) = \Omega_m(a)^{0.545}$.

The PNG component of galaxy bias in (7.6) scales as H_0^2/k^2 on ultra-large scales, i.e. above the equality scale, $k < k_{\text{eq}}$, where $T \approx 1$. It is strongly suppressed on scales $k \gg k_{\text{eq}}$ by $T(k)$. PNG has a similar impact on the power spectrum to the impact of ultra-large-scale relativistic effects. This means that relativistic effects contaminate the primordial signal – leading to biases if a Newtonian approximation is used to model the galaxy power spectrum (see Bruni et al. (2012); Jeong et al. (2012); Camera et al. (2015b)). The relativistic galaxy power spectrum has been used to analyse and predict the capability of future galaxy and intensity mapping surveys to measure the local PNG parameter f_{NL} , while avoiding the bias that is inherent in a Newtonian analysis (see e.g. Bruni et al. (2012); Jeong et al. (2012); Lopez-Honorez et al. (2012); Yoo et al. (2012); Raccanelli et al. (2014); Camera et al. (2015a,b); Raccanelli et al. (2016); Alonso et al. (2015b); Alonso & Ferreira (2015); Fonseca et al. (2015, 2017); Abramo & Bertacca (2017); Lorenz et al. (2018); Fonseca et al. (2018); Ballardini et al. (2019); Grimm et al. (2020); Bernal et al. (2020); Wang et al. (2020)).

The tree-level bispectrum requires the number counts in redshift space up to second order. In the Newtonian approximation, the projection effects are the second-order RSD terms (see e.g. Tellarini et al. (2016)). The relativistic corrections to RSD at second-order are extremely complicated, since they involve quadratic couplings of all the first-order terms, as well as introducing new terms that do not enter at first order, such as the transverse peculiar velocity, the lensing deflection angle and the lensing shear Bertacca et al. (2014a,b); Yoo & Zaldarriaga (2014); Di Dio et al. (2014); Bertacca (2015). There are further relativistic corrections that are not projection effects. Firstly, the Newtonian model of second-order galaxy bias in

7. Local primordial non-Gaussianity in the bispectrum

the comoving frame requires a relativistic correction, unlike the first-order bias (see Section 7.2). Secondly, and similar to the first-order case, the second-order galaxy bias relation needs relativistic gauge corrections when using non-comoving gauges such as the Poisson gauge. These are second-order extensions of equations like (7.5). In summary, the second-order relativistic corrections to the galaxy bispectrum in the Gaussian case are:

- relativistic projection corrections to the Newtonian RSD Bertacca et al. (2014a,b); Yoo & Zaldarriaga (2014); Di Dio et al. (2014); Bertacca (2015);
- relativistic corrections to the Newtonian bias model in the comoving frame at second order, which were only recently derived Umeh et al. (2019); Umeh & Koyama (2019);
- relativistic gauge corrections to the second-order number density when using non-comoving gauges Bertacca et al. (2014a,b).

As in the case of the power spectrum, local PNG affects the bispectrum on very large scales, which is also where the relativistic effects are strongest. This leads again to a contamination of the primordial signal by relativistic effects, necessitating a relativistic analysis. A Gaussian primordial universe could be mistakenly interpreted as non-Gaussian if a Newtonian model is used for the bispectrum in analysis of the data, as shown by Kehagias et al. (2015); Umeh et al. (2017); Jolicoeur et al. (2017); Koyama et al. (2018).

There are important differences between the power spectrum and bispectrum:

- At first order, there is no relativistic correction to the bias model in comoving gauge – the relativistic correction arises at second order Umeh et al. (2019); Umeh & Koyama (2019). Therefore the tree-level bispectrum contains a relativistic correction to the bias model, but the tree-level power spectrum does not.
- There is no PNG signal in the primordial *matter* power spectrum at tree level, so that the local PNG signal in the tree-level galaxy power spectrum is sourced only by scale-dependent bias.
- By contrast, local PNG in the galaxy bispectrum is sourced by scale-dependent bias, by the primordial matter bispectrum and by RSD at second order (see Tellarini et al. (2016) and Section 7.2.4 below).

7. Local primordial non-Gaussianity in the bispectrum

- Second-order relativistic corrections to RSD induce new local PNG effects in the bispectrum, via (1) a coupling of first-order scale-dependent bias to first-order relativistic projection effects, and (2) the linearly evolved PNG in second-order velocity and metric potentials, which appear in relativistic projection effects (absent in the standard Newtonian analysis).

Since local PNG affects the power spectrum and bispectrum differently, a Newtonian analysis could mistakenly identify inconsistencies between the power spectrum and bispectrum f_{NL} measurements, which could wrongly lead to an inference of hidden systematics or deviations from general relativity.

PNG in the galaxy bispectrum has been extensively investigated in the Newtonian approximation. Most work has used the Fourier bispectrum, implicitly incorporating a plane-parallel assumption (see e.g. Verde et al. (2000); Scoccimarro et al. (2004); Sefusatti et al. (2006); Sefusatti & Komatsu (2007); Giannantonio & Porciani (2010); Baldauf et al. (2011); Tellarini et al. (2015, 2016); Desjacques et al. (2018b); Watkinson et al. (2017); Majumdar et al. (2018); Karagiannis et al. (2018); Yankelevich & Porciani (2019); Sarkar et al. (2019); Karagiannis et al. (2020b); Bharadwaj et al. (2020); Karagiannis et al. (2020a); Moradinezhad Dizgah et al. (2020)) and we follow this approximation. Our previous work Umeh et al. (2017) included the local (non-integrated) relativistic effects in the Fourier bispectrum for the first time. This was extended by our work Jolicoeur et al. (2017, 2018, 2019); Clarkson et al. (2019); Maartens et al. (2020); de Weerd et al. (2020); Jolicoeur et al. (2020); Umeh et al. (2020), all in the case of primordial Gaussianity. Here we incorporate local PNG into the relativistic bispectrum. This involves applying the recent results of Umeh et al. (2019); Umeh & Koyama (2019) on relativistic corrections to the second-order galaxy bias model. In addition, we derive the new local PNG terms induced by a coupling of first-order scale-dependent bias and first-order relativistic projection effects and by linearly evolved second-order relativistic projection effects.

The paper is structured as follows. Section 7.2.4 reviews the relativistic correction to the galaxy bias, including the case of local PNG. In addition, we show how the linearly evolved second-order metric and velocity potentials carry a primordial non-Gaussian signal, which is imprinted in the bispectrum by relativistic projection effects. In Section 7.3, after presenting the relativistic correction to the matter bispectrum, we discuss the number density contrast in redshift space, which brings into play the relativistic projection effects. We combine the various results to derive the relativistic galaxy bispectrum, including all local PNG effects, and we show

7. Local primordial non-Gaussianity in the bispectrum

examples of the galaxy bispectrum for a Stage IV H α spectroscopic survey. We summarise and conclude in Section 7.4.

Conventions used: We assume a flat Λ CDM model, based on general relativity and perturbed up to second order, in which the matter is pressure-free and irrotational on perturbative scales. Generalisations to allow dynamical dark energy and relativistic modified gravity are straightforward, but are not included. For numerical calculations, we use the Planck 2018 best-fit parameters Aghanim et al. (2018). Perturbed quantities are expanded as $X + X^{(2)}/2$, and may be split as $X_N + X_{GR} + X_{nG}$, and similarly at second order, where N denotes the Newtonian approximation, GR denotes the relativistic correction and nG denotes the local PNG contribution. GR corrections are highlighted in magenta. Our definition of the metric potentials in (7.3) leads to the first-order Poisson equation

$$\nabla^2 \Psi = +\frac{3}{2}\Omega_m \mathcal{H}^2 \delta_C, \quad (7.8)$$

where $\Phi = \Psi$ in Λ CDM. Here and in the remainder of the paper, we omit the subscript m on the matter density contrast for brevity. At second order, the perturbed metric in Poisson gauge is given by

$$a^{-2} ds^2 = -[1 + 2\Psi + \Phi^{(2)}] d\eta^2 + [1 - 2\Psi - \Psi^{(2)}] d\mathbf{x}^2. \quad (7.9)$$

Here we have neglected the relativistic vector and tensor modes that are generated by scalar mode coupling, so that we only consider the relativistic scalar contribution to the bispectrum. This approximation is justified by the fact that the relativistic vector contribution to the bispectrum is typically 2 orders of magnitude below the relativistic scalar contribution on observable scales, while the relativistic tensor contribution is typically an order of magnitude below that of the vector contribution (see Jolicoeur et al. (2019)).

7.2. Local primordial non-Gaussianity in the galaxy bias

Local PNG is defined as a simple form of nonlinearity in the primordial curvature perturbation, which is local in configuration space. In terms of the gravitational

7. Local primordial non-Gaussianity in the bispectrum

potential deep in the matter era, we have

$$-\left[\Psi_{\text{in}}(\mathbf{x}) + \frac{1}{2}\Psi_{\text{in}}^{(2)}(\mathbf{x})\right] = \varphi_{\text{in}}(\mathbf{x}) + f_{\text{NL}}[\varphi_{\text{in}}(\mathbf{x})^2 - \langle\varphi_{\text{in}}^2\rangle], \quad (7.10)$$

where φ_{in} is the first-order Gaussian part. The standard definition of f_{NL} uses a convention for Ψ that is different to ours, with a minus on the right of the Poisson equation (7.8). In order to keep the standard sign of f_{NL} , we made a sign change on the left of (7.10). (f_{NL} in Villa & Rampf (2016); Koyama et al. (2018); Umeh & Koyama (2019) is of opposite sign to the standard sign that we use.)

7.2.1. First-order bias

In (7.10), the Gaussian part of the potential deep in the matter era (but after decoupling) is related to the linear primordial potential by the transfer function:

$$\varphi_{\text{in}}(\mathbf{k}) = T(k)\varphi_{\text{p}}(\mathbf{k}) \quad \text{for } a_{\text{p}} \ll a_{\text{eq}} \ll a_{\text{in}}. \quad (7.11)$$

Here $\varphi_{\text{p}}(\mathbf{k}) = -9\Psi(a_{\text{p}}, \mathbf{k})/10$, where the factor 9/10 ensures conservation of the curvature perturbation on super-Hubble scales. After equality, the potential evolves with the growth suppression factor, so that

$$\varphi(a, \mathbf{k}) = \frac{g(a)}{g_{\text{in}}}\varphi_{\text{in}}(\mathbf{k}) \quad \text{for } a \geq a_{\text{in}} > a_{\text{dec}}. \quad (7.12)$$

We relate the late-time matter density contrast to the primordial potential via the Poisson equation (7.8), using (7.7), (7.11) and (7.12):

$$\delta_{\text{C}}(a, \mathbf{k}) = \mathcal{M}(a, k)\varphi_{\text{p}}(\mathbf{k}) \quad \text{where} \quad \mathcal{M}(a, k) = \frac{10}{3\mathcal{H}(a)^2[3\Omega_m(a) + 2f(a)]}k^2T(k). \quad (7.13)$$

This relation is illustrated in Fig. 7.1. The matter and number density contrasts can be written as

$$\delta_{\text{C}} = \delta_{\text{C},\text{N}} \quad \text{and} \quad \delta_{g\text{C}} = \delta_{g\text{C},\text{N}} + \delta_{g\text{C},\text{nG}}. \quad (7.14)$$

This follows since there is no GR correction to either contrast and no PNG in the

7. Local primordial non-Gaussianity in the bispectrum

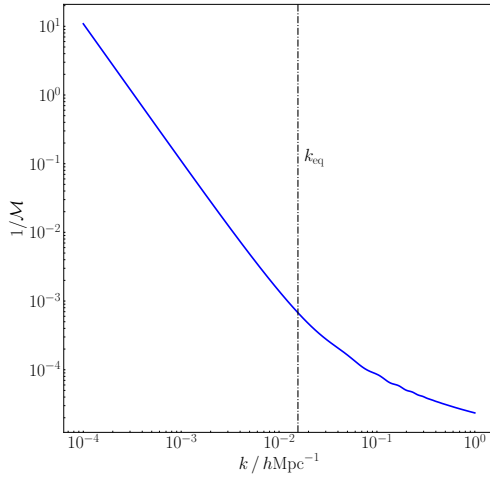


Figure 7.1.: $\mathcal{M}^{-1} = \varphi_p / \delta_C^{(1)}$ at $z = 1$.

Gaussian matter density contrast:

$$\delta_{C,GR} = 0 = \delta_{gC,GR}, \quad \delta_{C,nG} = 0. \quad (7.15)$$

Then it follows that

$$\delta_{gC} = \delta_{gC,N} + \delta_{gC,nG} = b_{10} \delta_C + b_{01} \varphi_p, \quad (7.16)$$

where the Gaussian and non-Gaussian bias coefficients are

$$b_{10} = b_1, \quad b_{01} = 2f_{NL}\delta_{crit}(b_{10} - 1). \quad (7.17)$$

The relations (7.13)–(7.17) then recover (7.6).

At first order, there is *no* GR correction to the bias relation expressed in the matter-galaxy rest frame. This is no longer true at second order.

The first-order metric potential is Gaussian by (7.10) and has no GR correction by (7.15) and the Poisson equation. From the Euler equation ($V' + \mathcal{H}V = -\Psi$) it follows that the velocity also has no GR and no PNG corrections:

$$\Psi = \Psi_N, \quad V = V_N. \quad (7.18)$$

7. Local primordial non-Gaussianity in the bispectrum

7.2.2. Second-order bias: Newtonian approximation

At second order, the galaxy bias is physically defined in comoving gauge, but any gauge may be used in general relativity. Standard Newtonian perturbation theory is often given in an Eulerian frame, and so it is useful for comparison to express the bias in a suitable Eulerian frame. We use Poisson gauge here, following Umeh et al. (2017); Tram et al. (2016); Jolicoeur et al. (2017, 2018, 2019); Clarkson et al. (2019); Maartens et al. (2020); de Weerd et al. (2020), but with the galaxy and matter density contrasts in total-matter gauge ('T gauge'). The total-matter gauge is a convenient Eulerian choice for the density contrasts, since it has the same spatial coordinates as the Poisson gauge at first order and the same time-slicing as the comoving gauge at first and second orders Bartolo et al. (2016); Villa & Rampf (2016); Tram et al. (2016). As a result, at first order the total-matter density contrasts coincide with those of the comoving gauge: $\delta_T = \delta_C$, $\delta_{gT} = \delta_{gC}$, and we can rewrite (7.16) as

$$\delta_{gT} = \delta_{gT,N} + \delta_{gT,nG} \quad (7.19)$$

$$= b_{10} \delta_T + b_{01} \varphi_p = \left(b_{10} + \frac{b_{01}}{\mathcal{M}} \right) \delta_T. \quad (7.20)$$

At second order, the total-matter and Poisson matter density contrasts agree in the Newtonian approximation: $\delta_{T,N}^{(2)} = \delta_N^{(2)}$, while the comoving and total-matter Newtonian density contrasts are related via a purely spatial gauge transformation Bertacca et al. (2015); Villa & Rampf (2016); Jolicoeur et al. (2017); Umeh et al. (2019):

$$\delta_{T,N}^{(2)} = \delta_{C,N}^{(2)} + 2\xi^i \partial_i \delta_C, \quad \delta_{gT,N}^{(2)} = \delta_{gC,N}^{(2)} + 2\xi^i \partial_i \delta_{gC}, \quad (7.21)$$

where

$$\xi^i = \partial^i \nabla^{-2} \delta_C = \partial^i \nabla^{-2} \delta_T. \quad (7.22)$$

(The GR parts of the second-order density contrasts in comoving and total-matter gauges are equal; see below.)

For the small scales involved in local clustering of matter density, the Poisson equation at second order has the same Newtonian form as at first order. Then we can extend (7.13) up to second order to define the linearly evolved local PNG part of the density contrast, whose nonlinearity is purely primordial:

$$\delta_{T,nG}^{(2)} = \mathcal{M} \varphi_p^{(2)} = 2f_{NL} \mathcal{M} \varphi_p * \varphi_p, \quad (7.23)$$

7. Local primordial non-Gaussianity in the bispectrum

where the $*$ denotes a convolution in Fourier space. This leads to

$$\delta_{\text{T,nG}}^{(2)} = 2f_{\text{NL}} \mathcal{M}(a, k) \int \frac{d\mathbf{k}'}{(2\pi)^3} \frac{\delta_{\text{T}}(a, \mathbf{k}')}{\mathcal{M}(a, k')} \frac{\delta_{\text{T}}(a, \mathbf{k} - \mathbf{k}')}{\mathcal{M}(a, |\mathbf{k} - \mathbf{k}'|)}. \quad (7.24)$$

In order to include the nonlinearity due to gravitational evolution, we add the standard Newtonian contribution for Gaussian initial conditions to the local PNG part:

$$\begin{aligned} & \delta_{\text{T,N}}^{(2)}(a, \mathbf{k}) + \delta_{\text{T,nG}}^{(2)}(a, \mathbf{k}) \\ &= \int \frac{d\mathbf{k}'}{(2\pi)^3} \left[F_2(a, \mathbf{k}', \mathbf{k} - \mathbf{k}') + 2f_{\text{NL}} \frac{\mathcal{M}(a, k')}{\mathcal{M}(a, k') \mathcal{M}(a, |\mathbf{k} - \mathbf{k}'|)} \right] \delta_{\text{T}}(a, \mathbf{k}') \delta_{\text{T}}(a, \mathbf{k} - \mathbf{k}'). \end{aligned} \quad (7.25)$$

The standard Newtonian mode-coupling kernel for Λ CDM is Villa & Rampf (2016):

$$F_2(a, \mathbf{k}_1, \mathbf{k}_2) = 1 + \frac{F(a)}{D(a)^2} + \left(\frac{k_1}{k_2} + \frac{k_2}{k_1} \right) \mathbf{\hat{k}}_1 \cdot \mathbf{\hat{k}}_2 + \left[1 - \frac{F(a)}{D(a)^2} \right] (\mathbf{\hat{k}}_1 \cdot \mathbf{\hat{k}}_2)^2, \quad (7.26)$$

where F is the second-order growth factor. The Einstein–de Sitter relation $F/D^2 = 3/7$ is a very good approximation in Λ CDM. We use this approximation, in which F_2 is effectively time independent.

At second order, the standard Newtonian bias model, including tidal bias in the Gaussian part and all local PNG contributions, is given by (see Desjacques et al. (2018b) for a comprehensive treatment):

$$\begin{aligned} \delta_{g\text{T,N}}^{(2)} + \delta_{g\text{T,nG}}^{(2)} &= b_{10} \delta_{\text{T,N}}^{(2)} + b_{20} (\delta_{\text{T}})^2 + b_s s^2 \\ &+ b_{10} \delta_{\text{T,nG}}^{(2)} + b_{11} \delta_{\text{T}} \varphi_{\text{p}} + b_n \xi^i \partial_i \varphi_{\text{p}} + b_{02} (\varphi_{\text{p}})^2. \end{aligned} \quad (7.27)$$

The (Eulerian) bias parameters in the case of Gaussian initial conditions are in the first line on the right-hand side: the linear and quadratic biases, b_{10} and b_{20} , and the tidal bias b_s , where

$$s^2 = s_{ij} s^{ij}, \quad s_{ij} = \left(\partial_i \partial_j - \frac{1}{3} \delta_{ij} \nabla^2 \right) \nabla^{-2} \delta_{\text{T}}. \quad (7.28)$$

The second line of (7.27) contains the local PNG contribution, with three new bias parameters b_{11}, b_n, b_{02} . The first term is the primordial dark matter contribution, from (7.25); note that $\tilde{\delta}_{\text{T,N}}^{(2)}$ is proportional to f_{NL} . The b_{11}, b_n terms scale as $(\mathcal{H}^2/k^2)(\delta_{\text{T}})^2$, while the b_{02} term is $\mathcal{O}(\mathcal{H}^4/k^4)$. The new bias parameters vanish when $f_{\text{NL}} = 0$; in the presence of local PNG, they are given by Tellarini et al. (2015);

7. Local primordial non-Gaussianity in the bispectrum

Desjacques et al. (2018b); Umeh & Koyama (2019):

$$b_{11} = 4f_{\text{NL}} \left[\delta_{\text{crit}} b_{20} + \left(\frac{13}{21} \delta_{\text{crit}} - 1 \right) (b_{10} - 1) + 1 \right], \quad (7.29)$$

$$b_n = 4f_{\text{NL}} \left[\delta_{\text{crit}} (1 - b_{10}) + 1 \right], \quad (7.30)$$

$$b_{02} = 4f_{\text{NL}}^2 \delta_{\text{crit}} \left[\delta_{\text{crit}} b_{20} - 2 \left(\frac{4}{21} \delta_{\text{crit}} + 1 \right) (b_{10} - 1) \right]. \quad (7.31)$$

Note that the expressions for the bias coefficients in (7.29)–(7.31), as well as for b_{01} in (7.17), are based on a universal halo mass function. (For recent work on the limits of the universality assumption, see Barreira et al. (2020); Barreira (2020).)

7.2.3. Second-order bias: relativistic corrections

The relativistic second-order galaxy bias model has been derived in Umeh et al. (2019) (Gaussian case) and Umeh & Koyama (2019) (with local PNG). The key feature to bear in mind is the following:

GR corrections in the galaxy number density contrast $\delta_{gT}^{(2)}$ do not change the galaxy bias terms in (7.27), which contain all the local PNG effects.

This separation between GR effects and local PNG in the number density can be understood as follows.

- The intrinsic nonlinearity of GR modulates the galaxy number density via large-scale modes. However, this does not affect small-scale clustering: GR effects do *not* modulate the variance of small-scale density modes Koyama et al. (2018); Dai et al. (2015); de Putter et al. (2015).
- By contrast, local PNG imprints a primordial long-short coupling that induces a long-mode modulation of the variance and thus changes the galaxy bias.

As a consequence, we expect that relativistic corrections to the bias relation should be independent of non-Gaussianity and apply only on ultra-large scales (for a different view, see Matarrese et al. (2021)). These two features are consistent with the behaviour of (7.27) under change of gauge:

The Newtonian bias relation (7.27) is gauge-independent only on small scales.

Relativistic corrections to (7.27) are needed to enforce gauge-independence of the bias relation on ultra-large scales.

7. Local primordial non-Gaussianity in the bispectrum

As shown in Umeh et al. (2019); Umeh & Koyama (2019), gauge-independence requires the addition to (7.27) of the relativistic part of the second-order matter density contrast. The relativistic modes are super-Hubble at equality and arise from nonlinear GR corrections to the Newtonian Poisson equation Bruni et al. (2014); Bartolo et al. (2016); Villa & Rampf (2016); Tram et al. (2016):

$$\delta_{\text{C,GR}}^{(2)} = \delta_{\text{T,GR}}^{(2)} = \frac{20}{3} \delta_{\text{T}} \varphi_{\text{in}} - \frac{5}{3} \xi^i \partial_i \varphi_{\text{in}} \equiv \delta_{g\text{T,GR}}^{(2)}. \quad (7.32)$$

Here φ_{in} is the ultra-large scale potential deep in the matter era,

$$\varphi_{\text{in}}(\mathbf{k}) = \varphi_{\text{in}}(\mathbf{k} | k < k_{\text{eq}}). \quad (7.33)$$

When we relate φ_{in} to the density contrast today, via (7.11) and (7.13), we need to impose $T = 1$ on the transfer function, by (7.33).

The relativistic second-order galaxy bias model of Umeh & Koyama (2019) can be written in T-gauge as

$$\delta_{g\text{T}}^{(2)} = \delta_{g\text{T,N}}^{(2)} + \delta_{g\text{T,nG}}^{(2)} + \delta_{g\text{T,GR}}^{(2)}, \quad (7.34)$$

where

$$\delta_{g\text{T,N}}^{(2)} = b_{10} \delta_{\text{T,N}}^{(2)} + b_{20} (\delta_{\text{T}})^2 + b_s s^2, \quad (7.35)$$

$$\delta_{g\text{T,nG}}^{(2)} = b_{10} \delta_{\text{T,nG}}^{(2)} + b_{11} \delta_{\text{T}} \varphi_{\text{p}} + b_n \xi^i \partial_i \varphi_{\text{p}} + b_{02} (\varphi_{\text{p}})^2, \quad (7.36)$$

$$\delta_{g\text{T,GR}}^{(2)} = \frac{20}{3} \delta_{\text{T}} \varphi_{\text{in}} - \frac{5}{3} \xi^i \partial_i \varphi_{\text{in}}. \quad (7.37)$$

Here (7.35) and (7.36) recover the Newtonian relation (7.27).

Both the local PNG and GR terms scale as $(\mathcal{H}^2/k^2)(\delta_{\text{T}})^2$, so that the GR correction *cannot* be neglected. Although they are of the same order of magnitude, there is a key distinction between them: local PNG induces a short-long mode coupling, and thus affects the primordial potential φ_{p} on small scales, while the GR corrections affect only the ultra-large-scale primordial modes. In the absence of local PNG, i.e. for $f_{\text{NL}} = 0$, the GR terms survive and constitute the relativistic bias correction in the case of Gaussian initial conditions, as derived in Umeh et al. (2019).

Finally, we transform (7.20) and (7.34) to Poisson gauge:

$$\delta_g = \delta_{g\text{T}} + (3 - b_e) \mathcal{H} V, \quad (7.38)$$

$$\delta_g^{(2)} = \delta_{g\text{T}}^{(2)} + (3 - b_e) \mathcal{H} V^{(2)} + [(b_e - 3) \mathcal{H}' + (b_e - 3)(b_e - 4) \mathcal{H}^2 + b'_e \mathcal{H}] (V)^2$$

7. Local primordial non-Gaussianity in the bispectrum

$$+ 2(3 - b_e) \mathcal{H}V \delta_{gT} - 2V \delta'_{gT} + 2(3 - b_e) \mathcal{H}V \Psi, \quad (7.39)$$

where the GR corrections in magenta scale as $(\mathcal{H}^2/k^2) \delta_T$ at first order, and as $(\mathcal{H}^2/k^2)(\delta_T)^2$ or $(\mathcal{H}^4/k^4)(\delta_T)^2$ at second order. For (7.39) we followed Bertacca et al. (2014b); Jolicoeur et al. (2017); de Weerd et al. (2020), but we significantly simplified their expressions, using the first-order Euler equation $V' + \mathcal{H}V = -\Psi$ and the relation

$$V = -\frac{2f}{3\Omega_m \mathcal{H}} \Psi, \quad (7.40)$$

which follows from the continuity equation, $\delta'_T = -\nabla^2 V$, and the Poisson equation. We also included the evolution bias terms that are omitted in Umeh & Koyama (2019).

7.2.4. Second-order metric and velocity potentials

At second order, the number density contrast has a GR correction in addition to a PNG correction, as shown in (7.34). Unlike the first-order case, the metric and velocity potentials at second order also have nonzero GR and PNG corrections:

$$\Psi^{(2)} = \Psi_N^{(2)} + \Psi_{GR}^{(2)} + \Psi_{nG}^{(2)}, \quad (7.41)$$

$$\Phi^{(2)} = \Phi_N^{(2)} + \Phi_{GR}^{(2)} + \Psi_{nG}^{(2)}, \quad (7.42)$$

$$V^{(2)} = V_N^{(2)} + V_{GR}^{(2)} + V_{nG}^{(2)}, \quad (7.43)$$

where we note that

$$\Phi_N^{(2)} = \Psi_N^{(2)} \quad \text{and} \quad \Phi_{nG}^{(2)} = \Psi_{nG}^{(2)}. \quad (7.44)$$

The GR corrections are derived in (Villa & Rampf, 2016) (which only considers modes $k < k_{eq}$). Here we derive the PNG contributions, which include modes $k > k_{eq}$.

The PNG corrections to metric and velocity potentials are linearly evolved, i.e., their nonlinearity is purely primordial, the same as in the case of the density contrast. They follow from constraint and energy conservation equations applied to the linearly evolved PNG part of the matter density contrast, $\delta_{T,nG}^{(2)}$. As we argued in deriving (7.24), $\delta_{T,nG}^{(2)}$ obeys the linear Newtonian Poisson equation. The same applies to the linearly evolved $\Psi_{nG}^{(2)}$. From the Newtonian Poisson equation we find

7. Local primordial non-Gaussianity in the bispectrum

that

$$\begin{aligned}\Psi_{\text{nG}}^{(2)}(a, \mathbf{k}) &= -\frac{3\Omega_m(a)\mathcal{H}(a)^2}{2k^2} \delta_{\text{T,nG}}^{(2)}(a, \mathbf{k}) \\ &= -\frac{10}{3}f_{\text{NL}} \left[1 + \frac{2f(a)}{3\Omega_m(a)} \right]^{-1} T(k) (\varphi_{\text{p}} * \varphi_{\text{p}})(\mathbf{k}),\end{aligned}\quad (7.45)$$

where we used (7.13) and (7.24).

By (7.45), $\Psi_{\text{nG}}^{(2)}$ grows as $(1 + 2f/3\Omega_m)^{-1}$, and thus

$$\Psi_{\text{nG}}^{(2)\prime} = -\frac{2f}{(3\Omega_m + 2f)} \left(\frac{f'}{f} + \mathcal{H} + 2\frac{\mathcal{H}'}{\mathcal{H}} \right) \Psi_{\text{nG}}^{(2)}. \quad (7.46)$$

The first-order linear equation (7.40), based on energy conservation and the Poisson equation, extends to second order for the linearly evolved PNG parts of the velocity and the potential. This determines the PNG part of the velocity:

$$V_{\text{nG}}^{(2)} = -\frac{2f}{3\Omega_m \mathcal{H}} \Psi_{\text{nG}}^{(2)}. \quad (7.47)$$

The linearly evolved PNG part of the second-order RSD term then follows as

$$\partial_{\parallel}^2 V_{\text{nG}}^{(2)}(a, \mathbf{k}) = -2f_{\text{NL}} \mathcal{H}(a)f(a)\mu^2 \mathcal{M}(a, k) (\varphi_{\text{p}} * \varphi_{\text{p}})(\mathbf{k}), \quad (7.48)$$

where $\partial_{\parallel} = \mathbf{n} \cdot \nabla$ and $\mu = \frac{\mathbf{k}}{|\mathbf{k}|} \cdot \mathbf{n}$. Finally, the first-order linear relation $\Phi = \Psi$ extends to second order for the linearly evolved PNG part of $\Phi^{(2)}$, giving the second equality of (7.44).

7. Local primordial non-Gaussianity in the bispectrum

7.3. Local primordial non-Gaussianity in the relativistic bispectrum

7.3.1. Matter bispectrum

The primordial contribution of matter, independent of halo formation, is given by the Newtonian approximation (7.25), corrected by the GR contribution in (7.32):

$$\delta_T^{(2)} = \delta_{T,N}^{(2)} + \delta_{T,nG}^{(2)} + \frac{20}{3} \delta_T \varphi_{in} - \frac{5}{3} \xi^i \partial_i \varphi_{in}. \quad (7.49)$$

The kernels in Fourier space corresponding to the GR terms in (7.49) are:

$$\delta_T \varphi_{in} \rightarrow -\frac{(k_1^2 + k_2^2)}{2k_1^2 k_2^2}, \quad \xi^i \partial_i \varphi_{in} \rightarrow -\frac{\mathbf{k}_1 \cdot \mathbf{k}_2}{k_1^2 k_2^2}. \quad (7.50)$$

Then the tree-level matter bispectrum $\langle \delta_T \delta_T \delta_T^{(2)} \rangle$ at equal times is given by

$$B_m(\mathbf{k}_1, \mathbf{k}_2, \mathbf{k}_3) = \left\{ F_2(\mathbf{k}_1, \mathbf{k}_2) + 2f_{NL} \frac{\mathcal{M}(k_3)}{\mathcal{M}(k_1)\mathcal{M}(k_2)} \right. \\ \left. - (3\Omega_m + 2f)\mathcal{H}^2 \frac{[2(k_1^2 + k_2^2) - \mathbf{k}_1 \cdot \mathbf{k}_2]}{2k_1^2 k_2^2} \right\} P(k_1)P(k_2) + 2 \text{ cp}, \quad (7.51)$$

where we omit the time dependence for brevity, and ‘cp’ denotes cyclic permutation. Here $P \equiv P_T$ is the linear matter power spectrum and

$$\frac{\mathcal{M}(k_3)}{\mathcal{M}(k_1)\mathcal{M}(k_2)} = \frac{3}{10} (3\Omega_m + 2f) \mathcal{H}^2 \frac{T(k_3)}{T(k_1)T(k_2)} \frac{k_3^2}{k_1^2 k_2^2}. \quad (7.52)$$

The standard Newtonian result (see e.g. Tellarini et al. (2015)) is modified in GR by the magenta terms in (7.51). For Gaussian initial conditions, the GR correction is suppressed by \mathcal{H}^2/k^2 relative to the Newtonian approximation, but *in the non-Gaussian case, the GR correction is of the same order of magnitude as the local PNG term.*

7. Local primordial non-Gaussianity in the bispectrum

7.3.2. Observed number density

The observed number density contrast is $\Delta_g + \Delta_g^{(2)}/2$, which modifies the source quantity $\delta_g + \delta_g^{(2)}/2$ by RSD and other redshift space effects. It can be split into Newtonian, relativistic and non-Gaussian parts as follows.

- The **first order** parts are:

$$\Delta_{gN} = b_{10}\delta_{T,N} - \frac{1}{\mathcal{H}}\partial_{\parallel}^2 V, \quad (7.53)$$

$$\Delta_{gnG} = b_{01}\varphi_p, \quad (7.54)$$

$$\begin{aligned} \Delta_{gGR} = & \left[b_e - 2\mathcal{Q} + \frac{2(\mathcal{Q}-1)}{\chi\mathcal{H}} - \frac{\mathcal{H}'}{\mathcal{H}^2} \right] (\partial_{\parallel}V - \Psi) \\ & + (2\mathcal{Q}-1)\Psi + \frac{1}{\mathcal{H}}\Psi' + (3-b_e)\mathcal{H}V. \end{aligned} \quad (7.55)$$

Recall that δ_T , V and Ψ have no GR and no PNG corrections, by (7.15) and (7.18).

- The **second-order Newtonian** part of the observed number density contrast is formed from the density contrast and RSD terms and their couplings:

$$\begin{aligned} \Delta_{gN}^{(2)} = & \delta_{gT,N}^{(2)} - \frac{1}{\mathcal{H}}\partial_{\parallel}^2 V_N^{(2)} \\ & - 2\frac{b_{10}}{\mathcal{H}} \left[\delta_T \partial_{\parallel}^2 V + \partial_{\parallel}V \partial_{\parallel}\delta_T \right] + \frac{2}{\mathcal{H}^2} \left[(\partial_{\parallel}^2 V)^2 + \partial_{\parallel}V \partial_{\parallel}^3 V \right]. \end{aligned} \quad (7.56)$$

- The **second-order relativistic** part is Jolicoeur et al. (2017, 2018):

$$\begin{aligned} \Delta_{gGR}^{(2)} = & \delta_{gT,GR}^{(2)} - \frac{1}{\mathcal{H}}\partial_{\parallel}^2 V_{GR}^{(2)} + \left[b_e - 2\mathcal{Q} + \frac{2(\mathcal{Q}-1)}{\chi\mathcal{H}} - \frac{\mathcal{H}'}{\mathcal{H}^2} \right] \left[\partial_{\parallel}V_{N+GR}^{(2)} - \Phi_{N+GR}^{(2)} \right] \\ & + 2(\mathcal{Q}-1)\Psi_{N+GR}^{(2)} + \Phi_{N+GR}^{(2)} + \frac{1}{\mathcal{H}}\Psi_{N+GR}^{(2)'} + (3-b_e)\mathcal{H}V_{N+GR}^{(2)} \\ & + \text{very many terms quadratic in first-order quantities}, \end{aligned} \quad (7.57)$$

where

$$V_{N+GR}^{(2)} \equiv V_N^{(2)} + V_{GR}^{(2)}, \quad (7.58)$$

and similarly for the metric potentials.

The Newtonian parts of the metric potentials $\Psi^{(2)}$, $\Phi^{(2)}$ appear in the GR part of $\Delta_g^{(2)}$ because there is *no Newtonian projection effect involving these potentials*. For the velocity potential, the Newtonian part $V_N^{(2)}$ is present only

7. Local primordial non-Gaussianity in the bispectrum

in the RSD term in (7.56); the remaining velocity terms occur *only in the GR part* of $\Delta_g^{(2)}$ and therefore $V_N^{(2)}$ is included in the GR terms.

The quadratic terms in (7.57) are given in full by Jolicoeur et al. (2017). For convenience, Appendix REFERENCE APPENDIX presents all of the terms in (7.57), correcting some errors in Jolicoeur et al. (2017).

- The **second-order local PNG** part is

$$\begin{aligned} \Delta_{gnG}^{(2)} = & \delta_{gT,nG}^{(2)} - \frac{1}{\mathcal{H}} \partial_{\parallel}^2 V_{nG}^{(2)} \\ & + \left[b_e - 2\mathcal{Q} + \frac{2(\mathcal{Q}-1)}{\chi\mathcal{H}} - \frac{\mathcal{H}'}{\mathcal{H}^2} \right] \left[\partial_{\parallel} V_{nG}^{(2)} - \Psi_{nG}^{(2)} \right] + (2\mathcal{Q}-1)\Psi_{nG}^{(2)} + \frac{1}{\mathcal{H}} \Psi_{nG}^{(2)\prime} + (3-b_e)\mathcal{H}V_{nG}^{(2)} \\ & - 2\frac{b_{01}}{\mathcal{H}} \left(\varphi_p \partial_{\parallel}^2 V + \partial_{\parallel} V \partial_{\parallel} \varphi_p \right) \\ & + b_{01} \left(c_1 \Psi \varphi_p + c_2 V \varphi_p + c_3 \varphi_p \partial_{\parallel} V + c_4 \Psi \partial_{\parallel} \varphi_p \right). \end{aligned} \quad (7.59)$$

In this expression, lines 1 and 2 contain the linearly evolved second-order terms whose nonlinearity is purely primordial. Lines 3 and 4 contain the quadratic coupling terms.

Line 1 is the Newtonian density + RSD part, given by (7.27) and (7.48).

Line 2 arises from *GR projection terms that are absent in the Newtonian approximation*: these terms are given by (7.44)–(7.48).

Line 3 arises from the first quadratic RSD term in line 2 of (7.56), given by the coupling of $\delta_{T,nG}$ to velocity gradients.

Line 4 arises from the *coupling of $\delta_{T,nG}$ to first-order GR projection terms*. The coefficients $c_I(a)$ are explicitly given below and in Appendix REFERENCE APPENDIX.

Apart from the b_{02} term in $\delta_{gT,nG}^{(2)}$, the Newtonian terms in (7.59) scale as $(\mathcal{H}^2/k^2)(\delta_T)^2$ and dominate the GR correction terms, which scale as $i(\mathcal{H}^3/k^3)(\delta_T)^2$ or $(\mathcal{H}^4/k^4)(\delta_T)^2$.

In summary the local PNG part at second order has the following origins:

- * the primordial matter density contrast;
- * the scale-dependent bias;

7. Local primordial non-Gaussianity in the bispectrum

- * the linearly evolved second-order projection effects in velocity and metric potentials – from RSD and from GR corrections;
- * the coupling of first-order scale-dependent bias with first-order projection effects – from RSD and from GR corrections.

7.3.3. Galaxy bispectrum

At leading order the observed galaxy bispectrum is defined by (Umeh et al., 2017)

$$2\langle \Delta_g(\mathbf{k}_1)\Delta_g(\mathbf{k}_2)\Delta_g^{(2)}(\mathbf{k}_3) \rangle + 2 \text{ cp} = (2\pi)^3 B_g(\mathbf{k}_1, \mathbf{k}_2, \mathbf{k}_3) \delta^{\text{Dirac}}(\mathbf{k}_1 + \mathbf{k}_2 + \mathbf{k}_3), \quad (7.60)$$

where here, and below, we omit the time dependence for brevity and we assume equal-time correlations. The bispectrum can be written in terms of Fourier kernels as

$$B_g(\mathbf{k}_1, \mathbf{k}_2, \mathbf{k}_3) = \mathcal{K}(\mathbf{k}_1) \mathcal{K}(\mathbf{k}_2) \mathcal{K}^{(2)}(\mathbf{k}_1, \mathbf{k}_2, \mathbf{k}_3) P(k_1)P(k_2) + 2 \text{ cp}, \quad (7.61)$$

where

$$\Delta_g(\mathbf{k}) = \mathcal{K}(\mathbf{k}) \delta_{\text{T}}(\mathbf{k}), \quad (7.62)$$

$$\Delta_g^{(2)}(\mathbf{k}_3) = \int \frac{d\mathbf{k}_1}{(2\pi)^3} d\mathbf{k}_2 \delta^{\text{Dirac}}(\mathbf{k}_1 + \mathbf{k}_2 - \mathbf{k}_3) \mathcal{K}^{(2)}(\mathbf{k}_1, \mathbf{k}_2, \mathbf{k}_3) \delta_{\text{T}}(\mathbf{k}_1) \delta_{\text{T}}(\mathbf{k}_2). \quad (7.63)$$

In (Jolicoeur et al., 2018), the Newtonian and GR kernels are presented, including all local relativistic effects, from projection, evolution and bias, but in the case of Gaussian initial conditions. Here we have updated these results and extended them to include the effects of local PNG. From Section 7.3.2, we find the following kernels.

- At **first order**, using (7.53)–(7.55) and (7.62):

$$\mathcal{K}_{\text{N}}(\mathbf{k}_a) = b_{10} + f\mu_a^2, \quad (7.64)$$

$$\mathcal{K}_{\text{GR}}(\mathbf{k}_a) = i\mu_a \frac{\gamma_1}{k_a} + \frac{\gamma_2}{k_a^2}, \quad (7.65)$$

$$\mathcal{K}_{\text{nG}}(\mathbf{k}_a) = \frac{b_{01}}{\mathcal{M}(k_a)}, \quad (7.66)$$

7. Local primordial non-Gaussianity in the bispectrum

where $\mu_a = \hat{\mathbf{k}}_a \cdot \mathbf{n}$ and

$$\frac{\gamma_1}{\mathcal{H}} = f \left[b_e - 2\mathcal{Q} - \frac{2(1-\mathcal{Q})}{\chi\mathcal{H}} - \frac{\mathcal{H}'}{\mathcal{H}^2} \right], \quad (7.67)$$

$$\frac{\gamma_2}{\mathcal{H}^2} = f(3-b_e) + \frac{3}{2}\Omega_m \left[2 + b_e - f - 4\mathcal{Q} - \frac{2(1-\mathcal{Q})}{\chi\mathcal{H}} - \frac{\mathcal{H}'}{\mathcal{H}^2} \right]. \quad (7.68)$$

- The **second-order Newtonian part** follows from (7.56) and (7.63) (see e.g. Tellarini et al. (2016)):

$$\begin{aligned} \mathcal{K}_{\text{N}}^{(2)}(\mathbf{k}_1, \mathbf{k}_2, \mathbf{k}_3) &= b_{10}F_2(\mathbf{k}_1, \mathbf{k}_2) + b_{20} + f\mu_3^2G_2(\mathbf{k}_1, \mathbf{k}_2) + b_sS_2(\mathbf{k}_1, \mathbf{k}_2) \quad (7.69) \\ &\quad + b_{10}f(\mu_1k_1 + \mu_2k_2)\left(\frac{\mu_1}{k_1} + \frac{\mu_2}{k_2}\right) + f^2\frac{\mu_1\mu_2}{k_1k_2}(\mu_1k_1 + \mu_2k_2)^2, \end{aligned}$$

where

$$G_2(\mathbf{k}_1, \mathbf{k}_2) = \frac{F'}{DD'} + \left(\frac{k_1}{k_2} + \frac{k_2}{k_1}\right)\hat{\mathbf{k}}_1 \cdot \hat{\mathbf{k}}_2 + \left(2 - \frac{F'}{DD'}\right)(\hat{\mathbf{k}}_1 \cdot \hat{\mathbf{k}}_2)^2, \quad (7.70)$$

$$S_2(\mathbf{k}_1, \mathbf{k}_2) = (\hat{\mathbf{k}}_1 \cdot \hat{\mathbf{k}}_2)^2 - \frac{1}{3}. \quad (7.71)$$

Since we use the approximation $F/D^2 = 3/7$ in F_2 , we have $F'/(DD') = 6/7$ in G_2 .

- The **second-order relativistic part** follows from (7.57) and (7.63) (see (Jolicoeur et al., 2018), with some errors that are corrected here):

$$\begin{aligned} \mathcal{K}_{\text{GR}}^{(2)}(\mathbf{k}_1, \mathbf{k}_2, \mathbf{k}_3) &= \frac{1}{k_1^2 k_2^2} \left\{ \beta_1 + E_2(\mathbf{k}_1, \mathbf{k}_2, \mathbf{k}_3) \beta_2 \right. \quad (7.72) \\ &\quad + i \left[(\mu_1 k_1 + \mu_2 k_2) \beta_3 + \mu_3 k_3 (\beta_4 + E_2(\mathbf{k}_1, \mathbf{k}_2, \mathbf{k}_3) \beta_5) \right] \\ &\quad + \frac{k_1^2 k_2^2}{k_3^2} \left[F_2(\mathbf{k}_1, \mathbf{k}_2) \beta_6 + G_2(\mathbf{k}_1, \mathbf{k}_2) \beta_7 \right] + (\mu_1 k_1 \mu_2 k_2) \beta_8 \\ &\quad + \mu_3^2 k_3^2 [\beta_9 + E_2(\mathbf{k}_1, \mathbf{k}_2, \mathbf{k}_3) \beta_{10}] + (\mathbf{k}_1 \cdot \mathbf{k}_2) \beta_{11} \\ &\quad + (k_1^2 + k_2^2) \beta_{12} + (\mu_1^2 k_1^2 + \mu_2^2 k_2^2) \beta_{13} \\ &\quad + i \left[(\mu_1 k_1^3 + \mu_2 k_2^3) \beta_{14} + (\mu_1 k_1 + \mu_2 k_2) (\mathbf{k}_1 \cdot \mathbf{k}_2) \beta_{15} \right. \\ &\quad \left. \left. + k_1 k_2 (\mu_1 k_2 + \mu_2 k_1) \beta_{16} + (\mu_1^3 k_1^3 + \mu_2^3 k_2^3) \beta_{17} \right] \right\} \end{aligned}$$

7. Local primordial non-Gaussianity in the bispectrum

$$+ \mu_1 \mu_2 k_1 k_2 (\mu_1 k_1 + \mu_2 k_2) \beta_{18} + \mu_3 \frac{k_1^2 k_2^2}{k_3} G_2(\mathbf{k}_1, \mathbf{k}_2) \beta_{19} \Big] \Big\},$$

where

$$E_2(\mathbf{k}_1, \mathbf{k}_2, \mathbf{k}_3) = \frac{k_1^2 k_2^2}{k_3^4} \left[3 + 2 \left(\frac{k_1}{k_2} + \frac{k_2}{k_1} \right) \mathbf{k}_1 \cdot \mathbf{k}_2 + (\mathbf{k}_1 \cdot \mathbf{k}_2)^2 \right]. \quad (7.73)$$

The kernel (7.72) is derived from the many terms in $\Delta_g^{(2)}(\mathbf{x})$, as given in Bertacca et al. (2014a); Bertacca (2015) (we neglect the integrated terms). For convenience, in Table B.1, Appendix B, we summarise which terms in $\Delta_g^{(2)}(\mathbf{x})$ contribute to which of the terms in (7.72). The time-dependent functions β_I are also given in Appendix REF APPENDIX.

- The **second-order local PNG part** follows from (7.59):

$$\begin{aligned} \mathcal{K}_{\text{nG}}^{(2)}(\mathbf{k}_1, \mathbf{k}_2, \mathbf{k}_3) = & 2 f_{\text{NL}} (b_{10} + f \mu_3^2) \frac{\mathcal{M}_3}{\mathcal{M}_1 \mathcal{M}_2} + f b_{01} (\mu_1 k_1 + \mu_2 k_2) \left(\frac{\mu_1}{k_1 \mathcal{M}_2} + \frac{\mu_2}{k_2 \mathcal{M}_1} \right) \\ & + b_n N_2(\mathbf{k}_1, \mathbf{k}_2) + \frac{b_{11}}{2} \left(\frac{1}{\mathcal{M}_1} + \frac{1}{\mathcal{M}_2} \right) + \frac{b_{02}}{\mathcal{M}_1 \mathcal{M}_2} \\ & + \frac{\mathcal{M}_3}{\mathcal{M}_1 \mathcal{M}_2} \left(\frac{\Upsilon_1}{k_3^2} + i \frac{\mu_3}{k_3} \Upsilon_2 \right) + \Upsilon_3 \left(\frac{1}{k_1^2 \mathcal{M}_2} + \frac{1}{k_2^2 \mathcal{M}_1} \right) \\ & + i \left[\Upsilon_4 \left(\frac{\mu_1 k_1}{k_2^2 \mathcal{M}_1} + \frac{\mu_2 k_2}{k_1^2 \mathcal{M}_2} \right) + \Upsilon_5 \left(\frac{\mu_1}{k_1 \mathcal{M}_2} + \frac{\mu_2}{k_2 \mathcal{M}_1} \right) \right], \end{aligned} \quad (7.74)$$

where $\mathcal{M}_a \equiv \mathcal{M}(k_a)$ and

$$N_2(\mathbf{k}_1, \mathbf{k}_2) = \frac{1}{2} \left(\frac{k_1}{k_2 \mathcal{M}_1} + \frac{k_2}{k_1 \mathcal{M}_2} \right) \mathbf{k}_1 \cdot \mathbf{k}_2. \quad (7.75)$$

In the first line of (7.74), the first term is a sum of the matter density term in line 2 of (7.27) and the linearly evolved PNG part of the second-order RSD term [line 1 of (7.59)]. The second term is the quadratic RSD term from line 3 of (7.59).

The second line gives the scale-dependent bias contribution from (7.27). The first two lines recover the Newtonian approximation (see Tellarini et al. (2015)).

Lines 3 and 4 in magenta are the PNG contributions that arise from relativistic projection effects, as explained in Section 7.3.2. These projection terms in the non-Gaussian kernel involve new time-dependent functions Υ_I , which are given in Appendix REFERENCE APPENDIX. The terms in $\Delta_g^{(2)}(\mathbf{x})$ corresponding

7. Local primordial non-Gaussianity in the bispectrum

to those in (7.74), lines 3 and 4, are summarised in Table C.1, Appendix REFERENCE APPENDIX.

The Newtonian terms scale as $(\mathcal{H}^2/k^2)(\delta_T)^2$ except for the b_{02} term which scales as $(\mathcal{H}^4/k^4)(\delta_T)^2$. The relativistic Υ_1, Υ_3 terms scale as $(\mathcal{H}^4/k^4)(\delta_T)^2$, while the $\Upsilon_2, \Upsilon_4, \Upsilon_5$ terms are $\mathcal{O}(\mathcal{H}^3/k^3)$.

Note that Υ_1, Υ_2 are proportional to f_{NL} , and $\Upsilon_3, \Upsilon_4, \Upsilon_5$ are proportional to b_{01} (which itself is proportional to f_{NL}).

For Gaussian initial conditions, $\mathcal{K}_{nG}^{(2)}$ vanishes:

$$f_{NL} = 0 \Rightarrow b_{01} = b_n = b_{11} = b_{02} = \Upsilon_I = 0 \Rightarrow \mathcal{K}_{nG}^{(2)}(\mathbf{k}_1, \mathbf{k}_2, \mathbf{k}_3) = 0. \quad (7.76)$$

7.3.4. Numerical examples

The GR corrections to the Newtonian bispectrum, for both Gaussian and local PNG cases, are sensitive to the following astrophysical parameters of the tracer: Gaussian bias b_{10} , PNG bias b_{01} , and magnification bias \mathcal{Q} , together with their first derivatives in time and luminosity; evolution bias b_e and its first time derivative. This can be seen from the kernels presented above, with the details given in Appendices B and C.

In order to illustrate the GR corrections, we need to use physically self-consistent values for these parameters, as well as for the second-order Newtonian clustering bias parameters b_{20} and b_s . For a Stage IV H α spectroscopic survey, similar to Euclid, we use Maartens et al. (2020) for the clustering biases, evolution bias and magnification bias. We neglect the luminosity derivatives of first-order clustering bias and magnification bias. For the PNG biases b_{11}, b_n, b_{02} we use (7.29)–(7.31).

We start by showing the contribution of GR corrections to the monopole of the reduced bispectrum,

$$Q_g^{00}(k_1, k_2, k_3) = \frac{B_g^{00}(k_1, k_2, k_3)}{P(k_1)P(k_2) + P(k_3)P(k_1) + P(k_2)P(k_3)}, \quad (7.77)$$

where de Weerd et al. (2020)

$$B_g^{\ell m}(k_1, k_2, k_3) = \int_0^{2\pi} d\phi \int_{-1}^1 d\mu_1 B_g(k_1, k_2, k_3, \mu_1, \phi) Y_{\ell m}^*(\mu_1, \phi). \quad (7.78)$$

7. Local primordial non-Gaussianity in the bispectrum

Here ϕ, μ_1 determine the orientation of the triangle relative to the line of sight. Figure 7.2 shows the monopole for squeezed configurations. We use fixed equal sides $k_1 = k_2 = 0.1 h/\text{Mpc}$ and varying long mode $k_3 < k_1 = k_2$. The isosceles triangle is increasingly squeezed as k_3 decreases. The left panel shows the Newtonian approximation (dash-dot lines) and the right panel shows the monopole without the GR bias correction (7.37).

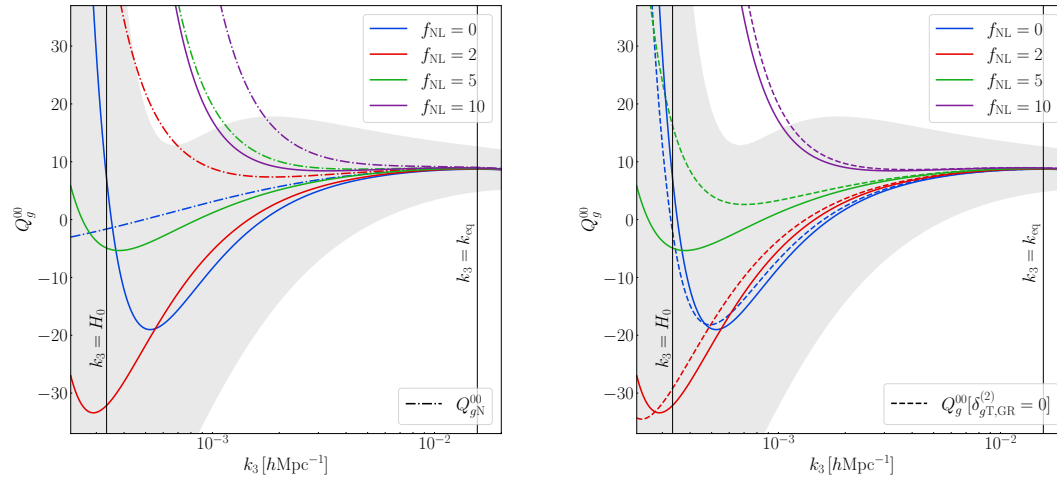


Figure 7.2.: Monopole of the reduced bispectrum for a Stage IV H α survey at $z = 1$, for various f_{NL} , with $k_1 = k_2 = 0.1 h/\text{Mpc}$. Shading indicates the 1σ uncertainty (neglecting shot noise) for the $f_{\text{NL}} = 0$ case (solid blue curve). *Left:* Comparing the full relativistic monopole to the Newtonian approximation (dash-dot curves). *Right:* Comparing the full relativistic monopole to the monopole without the GR correction to second-order galaxy bias, (7.32) (dashed curves).

The shading in Figure 7.2 is defined by the cosmic variance limited error σ_B on the $f_{\text{NL}} = 0$ monopole, given by Gagrani & Samushia (2017):

$$(\sigma_B)^2 = \frac{\mathcal{V}^{\text{com}}}{\pi k_1 k_2 k_3 \Delta k} \int d\mu_1 d\phi P_g(k_1, \mu_1) P_g(k_2, \mu_2) P_g(k_3, \mu_3), \quad (7.79)$$

where the galaxy power spectrum, from (7.64)–(7.66), is

$$P_g(k_a, \mu_a) = \left| b_{10} + f \mu_a^2 + \frac{\gamma_2}{k_a^2} + i \mu_a \frac{\gamma_1}{k_a} \right|^2 P(k_a). \quad (7.80)$$

In (7.79), \mathcal{V}^{com} is the comoving volume of the redshift bin, Δk is chosen as the fundamental mode, $2\pi(\mathcal{V}^{\text{com}})^{-1/3}$, $k_1 = k_2 = 0.1 h/\text{Mpc}$, and Clarkson et al. (2019)

7. Local primordial non-Gaussianity in the bispectrum

$\mu_2 = \mu_1 \cos \theta_{12} + \sqrt{1 - \mu_1^2} \sin \theta_{12} \cos \phi$, $\mu_3 = -(k_1 \mu_1 + k_2 \mu_2)/k_3$. Here θ_{12} is the tail-to-tail angle between \mathbf{k}_1 and \mathbf{k}_2 , so that the squeezed limit is $\theta_{12} = \pi$.

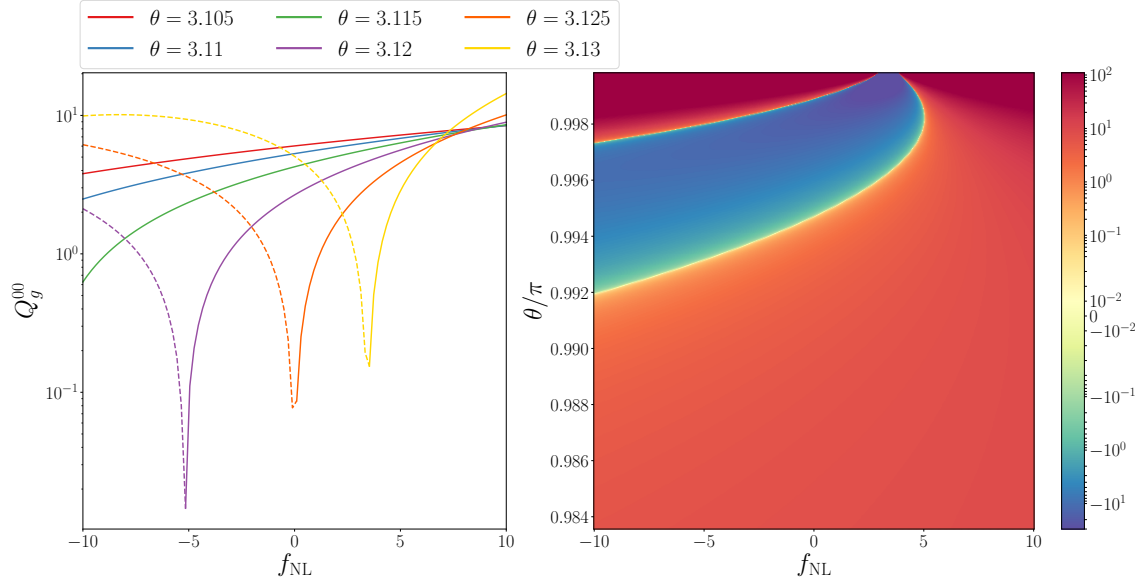


Figure 7.3.: Monopole of reduced bispectrum for isosceles triangles, as in Figure 7.2. *Left:* As a function of f_{NL} , for various values of $\theta \equiv \theta_{12}$, where $\theta = \pi$ is the squeezed limit. Dashed curves indicate negative values. *Right:* 2D colour map as a function of f_{NL} and θ/π .

The effect of f_{NL} is strongest in the monopole and competes with the GR contribution on ultra-large scales, since they both affect the Newtonian Gaussian bispectrum at $\mathcal{O}(\mathcal{H}^2/k^2)$. We see this in Figure 7.2 left panel, which shows the monopole of the reduced bispectrum for an increasingly squeezed isosceles triangle. In the Gaussian case (blue) we see that the Newtonian reduced monopole (dot-dash blue) becomes negative when the long mode is close to the Hubble scale, due to the effects of second-order galaxy bias. The Gaussian GR correction to the Newtonian approximation is negative for super-equality long modes until close to the Hubble scale (this was pointed out in Jolicoeur et al. (2019)). GR effects drive the reduced monopole (solid blue) below zero for $H_0 \lesssim k_3 \lesssim 0.002 h/\text{Mpc}$ (the locations of the zero-crossings are dependent on the Gaussian bias parameters, evolution bias and magnification bias).

As f_{NL} is increased above zero, the amplitude of the Newtonian reduced monopole (dot-dash curves) increases monotonically. When GR effects are taken into account, the reduced monopole is pushed upwards, but remains negative on observable scales for $f_{\text{NL}} \lesssim 5$, until it becomes always positive for $f_{\text{NL}} > 5$ – the precise turnaround value of f_{NL} depends on astrophysical parameters. This means that for $f_{\text{NL}} \lesssim 5$,

7. Local primordial non-Gaussianity in the bispectrum

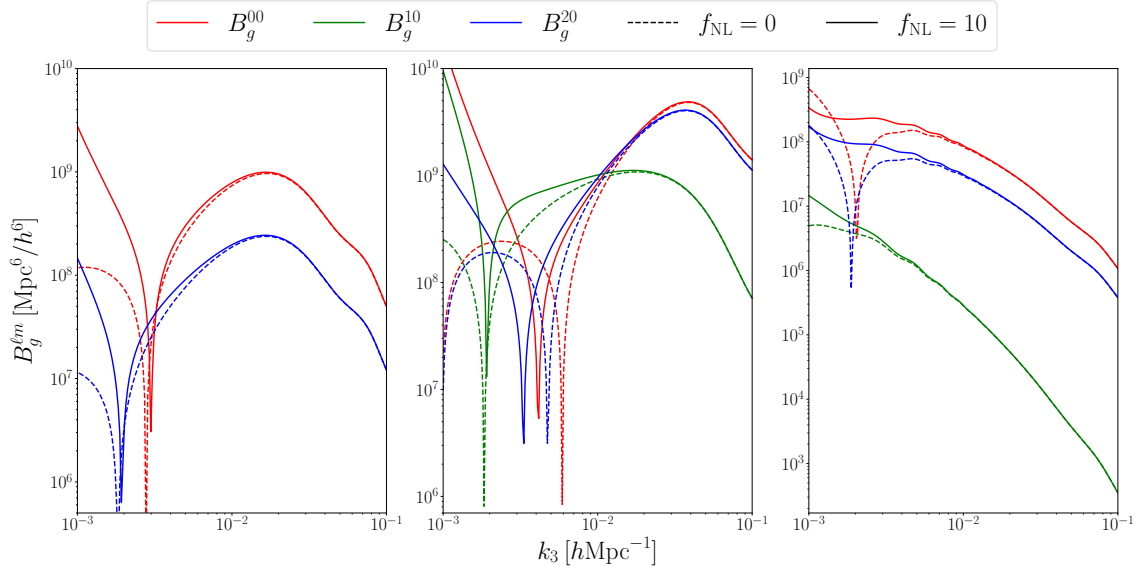


Figure 7.4.: First few nonzero multipoles for fixed triangle shape as a function of k_3 , with $f_{\text{NL}} = 10$ (solid) and $f_{\text{NL}} = 0$ (dashed). *Left:* Equilateral configuration, $k_1 = k_2 = k_3$. *Middle:* Flattened configuration, $k_1 = k_2 \approx k_3/2$, with $\theta_{12} = 2^\circ$. *Right:* Squeezed configuration with $\theta_{12} = 178^\circ$ and $k_1 = k_2 = k_3/(2 \sin \theta_{12}) \approx 14 k_3$.

local PNG *decreases* the amplitude of the reduced monopole on observable scales, in contrast to the Newtonian approximation. Comparing the green solid and blue dot-dash curves shows that *the Newtonian approximation is very close to the true reduced monopole with $f_{\text{NL}} \sim 5$* . For a universe with $f_{\text{NL}} \sim 5$, a Newtonian analysis of the squeezed bispectrum would conclude that the primordial universe is Gaussian. Similarly, a universe with $f_{\text{NL}} \sim 10$ would appear to have $f_{\text{NL}} \sim 5$ in a Newtonian approximation.

The GR contribution to the monopole is made up of: $\mathcal{O}(\mathcal{H}^2/k^2)$ Gaussian projection terms, $\mathcal{O}(\mathcal{H}^2/k^2)$ second-order galaxy bias correction (the same for Gaussian and PNG cases) and $\mathcal{O}(\mathcal{H}^4/k^4)$ second-order local PNG contributions from GR projection effects. The last contribution is effectively negligible on observable scales. In the right panel of Figure 7.2 we show that the GR bias correction is dominated by the Gaussian GR projection terms: the effect of removing the GR correction to second-order galaxy bias is small. Note that the GR bias correction has a similar effect to a small negative value of f_{NL} .

In Figure 7.3 we include negative f_{NL} and explore how local PNG changes the monopole of the reduced bispectrum as we approach the squeezed limit, $\theta_{12} \rightarrow \pi$. For $f_{\text{NL}} \geq 0$, the results provide a different perspective on Figure 7.2 left panel. For

7. Local primordial non-Gaussianity in the bispectrum

negative f_{NL} , local PNG and GR effects act together to drive the monopole negative, so that the zero-crossing of the monopole occurs for smaller θ_{12} , equivalently larger k_3 .

Figure 7.4 shows the effect of f_{NL} on the first three multipoles of the relativistic galaxy bispectrum, also including equilateral and flattened triangle shapes. In general, the Newtonian RSD effect induces only even multipoles, while the GR corrections modify the even multipoles and induce new odd multipoles. We show here the $m = 0$ dipole (absent without GR corrections) and quadrupole (mainly Newtonian), compared to the monopole.

For the equilateral shape (left panel), the dipole vanishes exactly in the Gaussian case Clarkson et al. (2019); de Weerd et al. (2020) and nonzero f_{NL} does not changes this result. The effect of f_{NL} on the quadrupole is very similar to the case of the monopole.

For the flattened shape (middle panel), the dipole is the dominant part of the bispectrum for $0.002 \lesssim k_3/(h\text{Mpc}^{-1}) \lesssim 0.01$, and we see that $f_{\text{NL}} > 0$ increases this effect further. The dipole B_g^{1m} is purely relativistic: it vanishes in the Newtonian approximation Clarkson et al. (2019); Maartens et al. (2020); Jolicoeur et al. (2020).

Finally, in the squeezed case (right panel), the effect on the monopole of $f_{\text{NL}} = 10$ is consistent with Figure 7.2. The quadrupole has a similar behaviour, and dominates the dipole. It is interesting that the three multipoles are approximately equal at scales near $k = 0.002 h/\text{Mpc}$. Once again, this value is sensitive to astrophysical parameters.

7.4. Conclusions

Upcoming galaxy surveys and 21cm intensity mapping surveys will deliver high-precision cosmological measurements and constraints, based on a combination of the power spectrum and bispectrum. This advance demands a commensurate advance in theoretical precision. Here we contribute to the development of theoretical precision by deriving for the first time the local relativistic corrections to the tree-level redshift-space bispectrum in the presence of local primordial non-Gaussianity (PNG).

At first order in perturbations, there are no relativistic corrections to the comoving matter and galaxy density contrasts – and therefore no correction to the galaxy

7. Local primordial non-Gaussianity in the bispectrum

clustering bias relation. There are also no relativistic corrections to the velocity and metric potentials. Consequently, there is no relativistic contribution to local PNG. The only relativistic correction is to the Newtonian projection effect, i.e. standard redshift-space distortions (RSD).

At second-order, relativistic corrections go beyond projection effects to alter the galaxy bias relation and local PNG in the galaxy bispectrum. In summary, there are:

- relativistic projection corrections to the Newtonian RSD at first and second order;
- relativistic corrections to the Newtonian bias model in the comoving frame at second order;
- second-order relativistic projection corrections to the local PNG carried by Newtonian RSD – from a coupling of first-order scale-dependent bias to first-order relativistic projection effects, and from the linearly evolved local PNG in second-order velocity and metric potentials.

Our previous work Umeh et al. (2017); Jolicoeur et al. (2017, 2018, 2019); Clarkson et al. (2019); Maartens et al. (2020); de Weerd et al. (2020); Jolicoeur et al. (2020) presented local (non-integrated) relativistic effects in the case of primordial Gaussianity and without the relativistic correction to galaxy bias. We have made corrections to these earlier results. In addition, we have presented for the first time the galaxy bispectrum with relativistic corrections to galaxy clustering bias and new local PNG contributions that are encoded in relativistic projection effects. Our main results are given in Fourier space in (7.69)–(7.74), with further details in Appendices B and C.

In Figures 7.2 and 7.3 we show examples of the squeezed monopole of the reduced relativistic bispectrum for a Stage IV H α survey similar to Euclid, using physical models for the astrophysical parameters (clustering biases, evolution bias, magnification bias). These figures reveal various interesting relativistic features. In particular, they show the bias in the estimate of f_{NL} from using a Newtonian analysis. This bias is given by

$$f_{\text{NL}}^{\text{Newt}} = f_{\text{NL}} + \Delta f_{\text{NL}}. \quad (7.81)$$

For the Stage IV survey at $z = 1$, the bias can be roughly estimated by eye as $\Delta f_{\text{NL}} \sim 5$, for the long mode above the equality scale. Although the precise level of bias is

7. Local primordial non-Gaussianity in the bispectrum

sensitive to astrophysical parameters and redshift, the point is that next-generation precision demands that relativistic corrections are included in the bispectrum.

In common with nearly all work on the Fourier-space bispectrum with RSD and PNG, we implicitly make a flat-sky assumption, based on the fixed global direction \mathbf{n} . As a consequence, wide-angle correlations are not included, so that the flat-sky analysis loses accuracy as θ increases, where θ is the maximum opening angle to the three-point correlations at the given redshift. This leads to a systematic bias in the separation of observational effects from the PNG signal, and therefore in the best-fit value of f_{NL} . Including wide-angle effects is a key target for future work. Corrections to the global flat-sky analysis of the Fourier bispectrum can be made by using a local or ‘moving’ line of sight Scoccimarro (2015); Sugiyama et al. (2018); Shirasaki et al. (2021). However, corrections of this type are approximate and do not incorporate all the wide-angle effects. Ultimately, one needs to use the full-sky 3-point correlation function or the full-sky angular bispectrum (see e.g. Kehagias et al. (2015); Di Dio et al. (2017, 2019); Durrer et al. (2020)) to properly include all wide-angle correlations. A major problem is that both of these alternatives are computationally more intensive.

8. Fisher forecasts

Mihi cordis gravitas
res videtur gravis;
iocus est amabilis
dulciorque favis;
quicquid Venus imperat,
labor est suavis,
quae numquam in cordibus
habitat ignavis.

9. Summary

summary

mortuus in anima
curam gero cutis

A. Beta coefficients

In this appendix, we present the β_I functions that appear in the second-order relativistic Fourier space kernel of the galaxy bispectrum.

$$\begin{aligned}
\frac{\beta_1}{\mathcal{H}^4} = & \frac{9}{4}\Omega_m^2 \left[6 - 2f \left(2b_e - 4\mathcal{Q} - \frac{4(1-\mathcal{Q})}{\chi\mathcal{H}} - \frac{2\mathcal{H}'}{\mathcal{H}^2} \right) - \frac{2f'}{\mathcal{H}} + b_e^2 + 5b_e - 8b_e\mathcal{Q} + 4\mathcal{Q} + 16\mathcal{Q}^2 \right. \\
& - 16 \frac{\partial\mathcal{Q}}{\partial \ln \bar{L}} - 8 \frac{\mathcal{Q}'}{\mathcal{H}} + \frac{b'_e}{\mathcal{H}} + \frac{2}{\chi^2\mathcal{H}^2} \left(1 - \mathcal{Q} + 2\mathcal{Q}^2 - 2 \frac{\partial\mathcal{Q}}{\partial \ln \bar{L}} \right) \\
& - \frac{2}{\chi\mathcal{H}} \left(3 + 2b_e - 2b_e\mathcal{Q} - 3\mathcal{Q} + 8\mathcal{Q}^2 - \frac{3\mathcal{H}'}{\mathcal{H}^2}(1-\mathcal{Q}) - 8 \frac{\partial\mathcal{Q}}{\partial \ln \bar{L}} - 2 \frac{\mathcal{Q}'}{\mathcal{H}} \right) \\
& \left. + \frac{\mathcal{H}'}{\mathcal{H}^2} \left(-7 - 2b_e + 8\mathcal{Q} + \frac{3\mathcal{H}'}{\mathcal{H}^2} \right) - \frac{\mathcal{H}''}{\mathcal{H}^3} \right] \\
& + \frac{3}{2}\Omega_m f \left[5 - 2f(4 - b_e) + \frac{2f'}{\mathcal{H}} + 2b_e \left(5 + \frac{2(1-\mathcal{Q})}{\chi\mathcal{H}} \right) - \frac{2b'_e}{\mathcal{H}} - 2b_e^2 + 8b_e\mathcal{Q} - 28\mathcal{Q} \right. \\
& - \frac{14(1-\mathcal{Q})}{\chi\mathcal{H}} - \frac{3\mathcal{H}'}{\mathcal{H}^2} + 4 \left(2 - \frac{1}{\chi\mathcal{H}} \right) \frac{\mathcal{Q}'}{\mathcal{H}} \left. \right] \\
& + \frac{3}{2}\Omega_m f^2 \left[-2 + 2f - b_e + 4\mathcal{Q} + \frac{2(1-\mathcal{Q})}{\chi\mathcal{H}} + \frac{3\mathcal{H}'}{\mathcal{H}^2} \right] \\
& + f^2 \left[12 - 7b_e + b_e^2 + \frac{b'_e}{\mathcal{H}} + (b_e - 3) \frac{\mathcal{H}'}{\mathcal{H}^2} \right] - \frac{3}{2}\Omega_m \frac{f'}{\mathcal{H}} \tag{A.1}
\end{aligned}$$

$$\begin{aligned}
\frac{\beta_2}{\mathcal{H}^4} = & \frac{9}{2}\Omega_m^2 \left[-1 + b_e - 2\mathcal{Q} - \frac{2(1-\mathcal{Q})}{\chi\mathcal{H}} - \frac{\mathcal{H}'}{\mathcal{H}^2} \right] + 3\Omega_m f \left[-1 + 2f - b_e + 4\mathcal{Q} + \frac{2(1-\mathcal{Q})}{\chi\mathcal{H}} + \frac{3\mathcal{H}'}{\mathcal{H}^2} \right] \\
& + 3\Omega_m f^2 \left[-1 + b_e - 2\mathcal{Q} - \frac{2(1-\mathcal{Q})}{\chi\mathcal{H}} - \frac{\mathcal{H}'}{\mathcal{H}^2} \right] + 3\Omega_m \frac{f'}{\mathcal{H}} \tag{A.2} \\
\frac{\beta_3}{\mathcal{H}^3} = & \frac{9}{4}\Omega_m^2 (f - 2 + 2\mathcal{Q}) \\
& + \frac{3}{2}\Omega_m f \left[-2 - f \left(-3 + f + 2b_e - 3\mathcal{Q} - \frac{4(1-\mathcal{Q})}{\chi\mathcal{H}} - \frac{2\mathcal{H}'}{\mathcal{H}^2} \right) - \frac{f'}{\mathcal{H}} \right]
\end{aligned}$$

A. Beta coefficients

$$\begin{aligned}
& + 3b_e + b_e^2 - 6b_e\mathcal{Q} + 4\mathcal{Q} + 8\mathcal{Q}^2 - 8\frac{\partial \mathcal{Q}}{\partial \ln \bar{L}} - 6\frac{\mathcal{Q}'}{\mathcal{H}} + \frac{b'_e}{\mathcal{H}} \\
& + \frac{2}{\chi^2 \mathcal{H}^2} \left(1 - \mathcal{Q} + 2\mathcal{Q}^2 - 2\frac{\partial \mathcal{Q}}{\partial \ln \bar{L}} \right) + \frac{2}{\chi \mathcal{H}} \left(-1 - 2b_e + 2b_e\mathcal{Q} + \mathcal{Q} - 6\mathcal{Q}^2 \right. \\
& \left. + \frac{3\mathcal{H}'}{\mathcal{H}^2} (1 - \mathcal{Q}) + 6\frac{\partial \mathcal{Q}}{\partial \ln \bar{L}} + 2\frac{\mathcal{Q}'}{\mathcal{H}} \right) - \frac{\mathcal{H}'}{\mathcal{H}^2} \left(3 + 2b_e - 6\mathcal{Q} - \frac{3\mathcal{H}'}{\mathcal{H}^2} \right) - \frac{\mathcal{H}''}{\mathcal{H}^3} \\
& + f^2 \left[-3 + 2b_e \left(2 + \frac{(1 - \mathcal{Q})}{\chi \mathcal{H}} \right) - b_e^2 + 2b_e\mathcal{Q} - 6\mathcal{Q} - \frac{b'_e}{\mathcal{H}} - \frac{6(1 - \mathcal{Q})}{\chi \mathcal{H}} \right. \\
& \left. + 2 \left(1 - \frac{1}{\chi \mathcal{H}} \right) \frac{\mathcal{Q}'}{\mathcal{H}} \right] \tag{A.3}
\end{aligned}$$

$$\frac{\beta_4}{\mathcal{H}^3} = \frac{9}{2} \Omega_m f \left[-b_e + 2\mathcal{Q} + \frac{2(1 - \mathcal{Q})}{\chi \mathcal{H}} + \frac{\mathcal{H}'}{\mathcal{H}^2} \right] \tag{A.4}$$

$$\frac{\beta_5}{\mathcal{H}^3} = 3\Omega_m f \left[b_e - 2\mathcal{Q} - \frac{2(1 - \mathcal{Q})}{\chi \mathcal{H}} - \frac{\mathcal{H}'}{\mathcal{H}^2} \right] \tag{A.5}$$

$$\frac{\beta_6}{\mathcal{H}^2} = \frac{3}{2} \Omega_m \left[2 - 2f + b_e - 4\mathcal{Q} - \frac{2(1 - \mathcal{Q})}{\chi \mathcal{H}} - \frac{\mathcal{H}'}{\mathcal{H}^2} \right] \tag{A.6}$$

$$\frac{\beta_7}{\mathcal{H}^2} = f(3 - b_e) \tag{A.7}$$

$$\frac{\beta_8}{\mathcal{H}^2} = 3\Omega_m f(2 - f - 2\mathcal{Q}) + f^2 \left[4 + b_e - b_e^2 + 4b_e\mathcal{Q} - 6\mathcal{Q} - 4\mathcal{Q}^2 + 4\frac{\partial \mathcal{Q}}{\partial \ln \bar{L}} + 4\frac{\mathcal{Q}'}{\mathcal{H}} - \frac{b'_e}{\mathcal{H}} \right.$$

$$\begin{aligned}
& - \frac{2}{\chi^2 \mathcal{H}^2} \left(1 - \mathcal{Q} + 2\mathcal{Q}^2 - 2\frac{\partial \mathcal{Q}}{\partial \ln \bar{L}} \right) - \frac{2}{\chi \mathcal{H}} \left(3 - 2b_e + 2b_e\mathcal{Q} - \mathcal{Q} - 4\mathcal{Q}^2 + \frac{3\mathcal{H}'}{\mathcal{H}^2} (1 - \mathcal{Q}) \right. \\
& \left. + 4\frac{\partial \mathcal{Q}}{\partial \ln \bar{L}} + 2\frac{\mathcal{Q}'}{\mathcal{H}} \right) - \frac{\mathcal{H}'}{\mathcal{H}^2} \left(3 - 2b_e + 4\mathcal{Q} + \frac{3\mathcal{H}'}{\mathcal{H}^2} \right) + \frac{\mathcal{H}''}{\mathcal{H}^3} \right] \tag{A.8}
\end{aligned}$$

$$\frac{\beta_9}{\mathcal{H}^2} = -\frac{9}{2} \Omega_m f \tag{A.9}$$

$$\frac{\beta_{10}}{\mathcal{H}^2} = 3\Omega_m f \tag{A.10}$$

$$\frac{\beta_{11}}{\mathcal{H}^2} = 3\Omega_m \left(\frac{1}{2} + f \right) + f - f^2 \left[-1 + b_e - 2\mathcal{Q} - \frac{2(1 + \mathcal{Q})}{\chi \mathcal{H}} - \frac{\mathcal{H}'}{\mathcal{H}^2} \right] \tag{A.11}$$

$$\begin{aligned}
& \frac{\beta_{12}}{\mathcal{H}^2} = \frac{3}{2} \Omega_m \left[-2 + b_1 \left(2 + b_e - 4\mathcal{Q} - \frac{2(1 - \mathcal{Q})}{\chi \mathcal{H}} - \frac{\mathcal{H}'}{\mathcal{H}^2} \right) + \frac{b'_1}{\mathcal{H}} + 2 \left(2 - \frac{1}{\chi \mathcal{H}} \right) \frac{\partial b_1}{\partial \ln \bar{L}} \right. \\
& \left. - f \left[2 + b_1(f - 3 + b_e) + \frac{b'_1}{\mathcal{H}} \right] \right] \tag{A.12}
\end{aligned}$$

$$\frac{\beta_{13}}{\mathcal{H}^2} = \frac{9}{4} \Omega_m^2 + \frac{3}{2} \Omega_m f \left[1 - 2f + 2b_e - 6\mathcal{Q} - \frac{4(1 - \mathcal{Q})}{\chi \mathcal{H}} - \frac{3\mathcal{H}'}{\mathcal{H}^2} \right] + f^2(3 - b_e) \tag{A.13}$$

A. Beta coefficients

$$\frac{\beta_{14}}{\mathcal{H}} = -\frac{3}{2}\Omega_m b_1 \quad (\text{A.14})$$

$$\frac{\beta_{15}}{\mathcal{H}} = 2f^2 \quad (\text{A.15})$$

$$\frac{\beta_{16}}{\mathcal{H}} = f \left[b_1 \left(f + b_e - 2\mathcal{Q} - \frac{2(1-\mathcal{Q})}{\chi\mathcal{H}} - \frac{\mathcal{H}'}{\mathcal{H}^2} \right) + \frac{b'_1}{\mathcal{H}} + 2 \left(1 - \frac{1}{\chi\mathcal{H}} \right) \frac{\partial b_1}{\partial \ln \bar{L}} \right] \quad (\text{A.16})$$

$$\frac{\beta_{17}}{\mathcal{H}} = -\frac{3}{2}\Omega_m f \quad (\text{A.17})$$

$$\frac{\beta_{18}}{\mathcal{H}} = \frac{3}{2}\Omega_m f - f^2 \left[3 - 2b_e + 4\mathcal{Q} + \frac{4(1-\mathcal{Q})}{\chi\mathcal{H}} + \frac{3\mathcal{H}'}{\mathcal{H}^2} \right] \quad (\text{A.18})$$

$$\frac{\beta_{19}}{\mathcal{H}} = f \left[b_e - 2Q - \frac{2(1-\mathcal{Q})}{\chi\mathcal{H}} - \frac{\mathcal{H}'}{\mathcal{H}^2} \right] \quad (\text{A.19})$$

B. Beta coefficient tables

Here we present a table of individual terms in the observed density fluctuation $\Delta_g^{(2)}$, with the corresponding β function β_I in the second column (N for standard Newtonian terms), Fourier space kernel \mathcal{F} , and the coefficients of the terms that appear in $\Delta_g^{(2)}$ in the fourth column.

Table B.1.: Individual terms in the observed $\Delta_g^{(2)}(a, \mathbf{x})$ [see (7.56), (7.57)] for $f_{\text{NL}} = 0$ are shown in column 1. The related β_I functions in (7.72) are listed in column 2. The Fourier-space kernels \mathcal{F} corresponding to column 1, given by $\int d\mathbf{k}' \mathcal{F}(\mathbf{k}', \mathbf{k} - \mathbf{k}') \delta_T(\mathbf{k}') \delta_T(\mathbf{k} - \mathbf{k}') / (2\pi)^3$, are shown in column 3. Column 4 gives the coefficients of the terms in $\Delta_g^{(2)}$ (column 1). The line-of-sight derivative is $\partial_{\parallel} = \mathbf{n} \cdot \nabla$ and $\Phi = \Psi$. The superscript (1) on first-order quantities has been omitted and N denotes Newtonian. This table updates the one in Jolicoeur et al. (2017).

TERM	β	FOURIER KERNEL	COEFFICIENT
$\delta_{T,N}^{(2)}$	N	$F_2(\mathbf{k}_1, \mathbf{k}_2)$	b_{10}
$(\delta_T)^2$	N	1	b_{20}
s^2	N	$S_2(\mathbf{k}_1, \mathbf{k}_2)$	b_s
$\partial_{\parallel}^2 V_N^{(2)}$	N	$f^2 \mathcal{H} \mu_3^2 G_2(\mathbf{k}_1, \mathbf{k}_2)$	$-1/\mathcal{H}$
$\delta_T \partial_{\parallel}^2 V$	N	$-f \mathcal{H} (\mu_1^2 + \mu_2^2)/2$	$-2b_{10}/\mathcal{H}$
$\partial_{\parallel} V \partial_{\parallel} \delta_T$	N	$-f \mathcal{H} \mu_1 \mu_2 (k_1^2 + k_2^2)/(2k_1 k_2)$	$-2b_{10}/\mathcal{H}$
$\partial_{\parallel} V \partial_{\parallel}^3 V$	N	$f^2 \mathcal{H}^2 (\mu_1 \mu_2^3 k_2^2 + \mu_2 \mu_1^3 k_1^2)/(k_1 k_2)$	$2/\mathcal{H}^2$
$[\partial_{\parallel}^2 V]^2$	N	$f^2 \mathcal{H}^2 \mu_1^2 \mu_2^2$	$2/\mathcal{H}^2$
$(\Psi)^2$	β_1	$9\Omega_m^2 \mathcal{H}^4 / (4k_1^2 k_2^2)$	\mathcal{A}_1
ΨV	β_1	$-3\Omega_m \mathcal{H}^3 f / (2k_1^2 k_2^2)$	\mathcal{A}_2
$V V'$	β_1	$f \mathcal{H}^3 (3\Omega_m - 2f) / (2k_1^2 k_2^2)$	$(b_e - 3)\mathcal{H}$
$(V)^2$	β_1	$f^2 \mathcal{H}^2 / (k_1^2 k_2^2)$	$(b_e - 3)^2 \mathcal{H}^2 + b'_e \mathcal{H} + (b_e - 3)\mathcal{H}'$
$V_{\text{GR}}^{(2)}$	β_1, β_2	$-3\Omega_m \mathcal{H}^3 [3 - 2E_2(\mathbf{k}_1, \mathbf{k}_2, \mathbf{k}_3)] / (4k_1^2 k_2^2)$	$(3 - b_e)\mathcal{H}$
$\Phi_{\text{GR}}^{(2)}$	β_1, β_2	$3\Omega_m \mathcal{H}^4 [f - C_1 + C_1 E_2(\mathbf{k}_1, \mathbf{k}_2, \mathbf{k}_3)] / (2k_1^2 k_2^2)$	$1 - b_e + 2\mathcal{Q} + \mathcal{R}$
$\Psi_{\text{GR}}^{(2)}$	β_1, β_2	$3\Omega_m \mathcal{H}^4 [C_1 - 3f + 2f^2 + 2f E_2(\mathbf{k}_1, \mathbf{k}_2, \mathbf{k}_3)] / (2k_1^2 k_2^2)$	$2(\mathcal{Q} - 1)$

B. Beta coefficient tables

$\Psi_{\text{GR}}^{(2)'} \partial_{\parallel}$	β_1, β_2	$3\Omega_m \mathcal{H}^5 [C_2 + C_3 E_2(\mathbf{k}_1, \mathbf{k}_2, \mathbf{k}_3)] / (2k_1^2 k_2^2)$	$1/\mathcal{H}$
$V \partial_{\parallel} V$	β_3	$i f^2 \mathcal{H}^2 (\mu_1 k_1 + \mu_2 k_2) / (2k_1^2 k_2^2)$	\mathcal{A}_3
$\Psi \partial_{\parallel} V$	β_3	$-i 3f \Omega_m \mathcal{H}^3 (\mu_1 k_1 + \mu_2 k_2) / (4k_1^2 k_2^2)$	\mathcal{A}_4
$\Psi \partial_{\parallel} \Phi$	β_3	$i 9\Omega_m^2 \mathcal{H}^4 (\mu_1 k_1 + \mu_2 k_2) / (8k_1^2 k_2^2)$	$2(f - 2 + 2\mathcal{Q})/\mathcal{H}$
$\partial_{\parallel} V_{\text{GR}}^{(2)}$	β_4, β_5	$-i 3\Omega_m \mathcal{H}^3 [3 - 2E_2(\mathbf{k}_1, \mathbf{k}_2, \mathbf{k}_3)] \mu_3 k_3 / (4k_1^2 k_2^2)$	$b_e - 2Q - \mathcal{R}$
$\Psi_N^{(2)} = \Phi_N^{(2)}$	β_6	$-3\Omega_m \mathcal{H}^2 F_2(\mathbf{k}_1, \mathbf{k}_2) / (2k_3^2)$	$4\mathcal{Q} - 1 - b_e + \mathcal{R}$
$\Psi_N^{(2)'} = \Phi_N^{(2)'} \partial_{\parallel}$	β_6	$-3\Omega_m \mathcal{H}^3 (2f - 1) F_2(\mathbf{k}_1, \mathbf{k}_2) / (2k_3^2)$	$1/\mathcal{H}$
$V_N^{(2)}$	β_7	$f \mathcal{H} G_2(\mathbf{k}_1, \mathbf{k}_2) / k_3^2$	$(3 - b_e) \mathcal{H}$
$(\partial_{\parallel} V)^2$	β_8	$-f^2 \mathcal{H}^2 \mu_1 \mu_2 / (k_1 k_2)$	\mathcal{A}_5
$\partial_{\parallel} V \partial_{\parallel} \Psi$	β_8	$3f \Omega_m \mathcal{H}^3 \mu_1 \mu_2 / (2k_1 k_2)$	$2(2 - f - 2\mathcal{Q})/\mathcal{H}$
$\partial_{\parallel}^2 V_{\text{GR}}^{(2)}$	β_9, β_{10}	$i 3\Omega_m \mathcal{H}^3 [3 - 2E_2(\mathbf{k}_1, \mathbf{k}_2, \mathbf{k}_3)] \mu_3^2 k_3^2 / (4k_1^2 k_2^2)$	$-1/\mathcal{H}$
$\partial_i V \partial^i V$	β_{11}	$-f^2 \mathcal{H}^2 \mathbf{k}_1 \cdot \mathbf{k}_2 / (k_1^2 k_2^2)$	$b_e - 1 - 2\mathcal{Q} - \mathcal{R}$
$\partial_i V \partial^i \Psi$	β_{11}	$3f \Omega_m \mathcal{H}^3 \mathbf{k}_1 \cdot \mathbf{k}_2 / (2k_1^2 k_2^2)$	$2/\mathcal{H}$
$\Psi \delta_T$	β_{12}	$-3\Omega_m \mathcal{H}^2 (k_1^2 + k_2^2) / (4k_1^2 k_2^2)$	$2b_{10}(4\mathcal{Q} + \mathcal{R} - 2 - b_e) - \mathcal{S}$
$V \delta_T$	β_{12}	$f \mathcal{H} (k_1^2 + k_2^2) / (2k_1^2 k_2^2)$	$b'_{10} + 2b_{10}(3 - b_e - f) \mathcal{H}$
$\delta_{gT, \text{GR}}^{(2)}$	β_{11}, β_{12}	$(3\Omega_m + 2f) \mathcal{H}^2 [\mathbf{k}_1 \cdot \mathbf{k}_2 - 2(k_1^2 + k_2^2)] / (2k_1 k_2)$	1
$\Psi \partial_{\parallel}^2 V$	β_{13}	$3f \Omega_m \mathcal{H}^3 (\mu_1^2 k_1^2 + \mu_2^2 k_2^2) / (4k_1^2 k_2^2)$	$2[1 - 2f + 2b_e - 6\mathcal{Q} - 2\mathcal{R} - (\mathcal{H}'/\mathcal{H}^2)]/\mathcal{H}$
$\Psi \partial_{\parallel}^2 \Psi$	β_{13}	$-9\Omega_m^2 \mathcal{H}^4 (\mu_1^2 k_1^2 + \mu_2^2 k_2^2) / (4k_1^2 k_2^2)$	$-2/\mathcal{H}^2$
$V \partial_{\parallel}^2 V$	β_{13}	$-f^2 \mathcal{H}^3 (\mu_1^2 k_1^2 + \mu_2^2 k_2^2) / (2k_1^2 k_2^2)$	$2(b_e - 3)/\mathcal{H}$
$\Psi \partial_{\parallel} \delta_T$	β_{14}	$-i 3\Omega_m \mathcal{H}^2 (\mu_1 k_1^3 + \mu_2 k_2^3) / (4k_1^2 k_2^2)$	$2b_{10}/\mathcal{H}$
$\partial_i V \partial_{\parallel} \partial^i V$	β_{15}	$-i f^2 \mathcal{H}^2 \mathbf{k}_1 \cdot \mathbf{k}_2 (\mu_1 k_1 + \mu_2 k_2) / (2k_1^2 k_2^2)$	$-4/\mathcal{H}$
$\delta_T \partial_{\parallel} V$	β_{16}	$i f \mathcal{H} (\mu_1 k_2 + \mu_2 k_1) / (2k_1 k_2)$	$2b_{10}(f + b_e - 2\mathcal{Q} - \mathcal{R}) + \mathcal{S}$
$\Phi \partial_{\parallel}^3 V$	β_{17}	$i 3f \Omega_m \mathcal{H}^3 (\mu_1^3 k_1^3 + \mu_2^3 k_2^3) / (4k_1^2 k_2^2)$	$-2/\mathcal{H}^2$
$\partial_{\parallel} V \partial_{\parallel}^2 V$	β_{18}	$-i f^2 \mathcal{H}^2 (\mu_1 \mu_2^2 k_2 + \mu_2 \mu_1^2 k_1) / (2k_1 k_2)$	$2[3 - 2b_e + 4\mathcal{Q} + 2\mathcal{R} + (\mathcal{H}'/\mathcal{H}^2)]/\mathcal{H}$
$\partial_{\parallel} V \partial_{\parallel}^2 \Psi$	β_{18}	$i 3f \Omega_m \mathcal{H}^3 (\mu_1 \mu_2^2 k_2 + \mu_2 \mu_1^2 k_1) / (4k_1 k_2)$	$2/\mathcal{H}^2$
$\partial_{\parallel} V_N^{(2)}$	β_{19}	$i f \mathcal{H} \mu_3 G_2(\mathbf{k}_1, \mathbf{k}_2) / k_3$	$b_e - 2Q - \mathcal{R}$

B. Beta coefficient tables

Here the \mathcal{C} functions in the Fourier kernels are

$$\mathcal{C}_1 = 2f - f^2 - 3\Omega_m , \quad (\text{B.1})$$

$$\mathcal{C}_2 = 2f - 1 + (1-f) \left[6\Omega_m + f(1-2f) - 2f \frac{\mathcal{H}'}{\mathcal{H}^2} \right] , \quad (\text{B.2})$$

$$\mathcal{C}_3 = 2f \left(2f - 1 + \frac{\mathcal{H}'}{\mathcal{H}^2} \right) + 2 \frac{f'}{\mathcal{H}} , \quad (\text{B.3})$$

the \mathcal{A} functions in the coefficients are

$$\begin{aligned} \mathcal{A}_1 = & -3 + 2f \left(2 - 2b_e + 4\mathcal{Q} + \frac{4(1-\mathcal{Q})}{\chi\mathcal{H}} + \frac{2\mathcal{H}'}{\mathcal{H}^2} \right) - \frac{2f'}{\mathcal{H}} + b_e^2 + 6b_e - 8b_e\mathcal{Q} + 4\mathcal{Q} \\ & + 16\mathcal{Q}^2 - 16 \frac{\partial\mathcal{Q}}{\partial \ln L} - 8 \frac{\mathcal{Q}'}{\mathcal{H}} + \frac{b'_e}{\mathcal{H}} + \frac{2}{\chi^2\mathcal{H}^2} \left(1 - \mathcal{Q} + 2\mathcal{Q}^2 - 2 \frac{\partial\mathcal{Q}}{\partial \ln L} \right) \\ & - \frac{2}{\chi\mathcal{H}} \left[4 + 2b_e - 2b_e\mathcal{Q} - 4\mathcal{Q} + 8\mathcal{Q}^2 - \frac{3\mathcal{H}'}{\mathcal{H}^2}(1-\mathcal{Q}) - 8 \frac{\partial\mathcal{Q}}{\partial \ln L} - 2 \frac{\mathcal{Q}'}{\mathcal{H}} \right] \\ & + \frac{\mathcal{H}'}{\mathcal{H}^2} \left(-8 - 2b_e + 8\mathcal{Q} + \frac{3\mathcal{H}'}{\mathcal{H}^2} \right) - \frac{\mathcal{H}''}{\mathcal{H}^3} , \end{aligned} \quad (\text{B.4})$$

$$\begin{aligned} \mathcal{A}_2 = & 2\mathcal{H} \left[-\frac{15}{2} + f(3-b_e) - \frac{3}{2}b_e - 2b_e \frac{(1-\mathcal{Q})}{\chi\mathcal{H}} + \frac{b'_e}{\mathcal{H}} + b_e^2 - 4b_e\mathcal{Q} + 12\mathcal{Q} + \frac{6(1-\mathcal{Q})}{\chi\mathcal{H}} \right. \\ & \left. - 2 \left(2 - \frac{1}{\chi\mathcal{H}} \right) \frac{\mathcal{Q}'}{\mathcal{H}} \right] \end{aligned} \quad (\text{B.5})$$

$$\begin{aligned} \mathcal{A}_3 = & 2\mathcal{H} \left[-3 + 4b_e + \frac{2b_e(1-\mathcal{Q})}{\chi\mathcal{H}} - b_e^2 + 2b_e\mathcal{Q} - 6\mathcal{Q} - \frac{b'_e}{\mathcal{H}} - \frac{6(1-\mathcal{Q})}{\chi\mathcal{H}} \right. \\ & \left. + 2 \left(1 - \frac{1}{\chi\mathcal{H}} \right) \frac{\mathcal{Q}'}{\mathcal{H}} \right] , \end{aligned} \quad (\text{B.6})$$

$$\begin{aligned} \mathcal{A}_4 = & 4 + 2f \left[-3 + f + 2b_e - 3\mathcal{Q} - \frac{4(1-\mathcal{Q})}{\chi\mathcal{H}} - \frac{2\mathcal{H}'}{\mathcal{H}^2} \right] + \frac{2f'}{\mathcal{H}} - 6b_e - 2b_e^2 + 12b_e\mathcal{Q} - 8\mathcal{Q} \\ & - 16\mathcal{Q}^2 + 16 \frac{\partial\mathcal{Q}}{\partial \ln L} + 12 \frac{\mathcal{Q}'}{\mathcal{H}} - 2 \frac{b'_e}{\mathcal{H}} - \frac{4}{\chi^2\mathcal{H}^2} \left(1 - \mathcal{Q} + 2\mathcal{Q}^2 - 2 \frac{\partial\mathcal{Q}}{\partial \ln L} \right) \\ & - \frac{4}{\chi\mathcal{H}} \left(-1 - 2b_e + 2b_e\mathcal{Q} + \mathcal{Q} - 6\mathcal{Q}^2 + \frac{3\mathcal{H}'}{\mathcal{H}^2}(1-\mathcal{Q}) + 6 \frac{\partial\mathcal{Q}}{\partial \ln L} + 2 \frac{\mathcal{Q}'}{\mathcal{H}} \right) \\ & + \frac{2\mathcal{H}'}{\mathcal{H}^2} \left(3 + 2b_e - 6\mathcal{Q} - \frac{3\mathcal{H}'}{\mathcal{H}^2} \right) + \frac{2\mathcal{H}''}{\mathcal{H}^3} , \end{aligned} \quad (\text{B.7})$$

$$\begin{aligned} \mathcal{A}_5 = & -4 - b_e + b_e^2 - 4b_e\mathcal{Q} + 6\mathcal{Q} + 4\mathcal{Q}^2 - 4 \frac{\partial\mathcal{Q}}{\partial \ln L} - 4 \frac{\mathcal{Q}'}{\mathcal{H}} + \frac{b'_e}{\mathcal{H}} \\ & + \frac{2}{\chi^2\mathcal{H}^2} \left(1 - \mathcal{Q} + 2\mathcal{Q}^2 - 2 \frac{\partial\mathcal{Q}}{\partial \ln L} \right) \end{aligned}$$

B. Beta coefficient tables

$$+ \frac{2}{\chi\mathcal{H}} \left[3 - 2b_e + 2b_e\mathcal{Q} - 3\mathcal{Q} - 4\mathcal{Q}^2 + \frac{3\mathcal{H}'}{\mathcal{H}^2}(1 - \mathcal{Q}) + 4\frac{\partial\mathcal{Q}}{\partial\ln L} + 2\frac{\mathcal{Q}'}{\mathcal{H}} \right] \\ + \frac{\mathcal{H}'}{\mathcal{H}^2} \left(3 - 2b_e + 4\mathcal{Q} + \frac{3\mathcal{H}'}{\mathcal{H}^2} \right) - \frac{\mathcal{H}''}{\mathcal{H}^3}, \quad (\text{B.8})$$

and the functions \mathcal{R}, \mathcal{S} in the coefficients are

$$\mathcal{R} = \frac{2(1 - \mathcal{Q})}{\chi\mathcal{H}} + \frac{\mathcal{H}'}{\mathcal{H}^2}, \quad (\text{B.9})$$

$$\mathcal{S} = 4 \left(2 - \frac{1}{\chi\mathcal{H}} \right) \frac{\partial b_{10}}{\partial\ln L}. \quad (\text{B.10})$$

The magnification bias is defined by Alonso et al. (2015b); Di Dio et al. (2016); Maartens et al. (2020):

$$\mathcal{Q} = -\frac{\partial \ln \bar{n}_g}{\partial \ln L} \Bigg|_c, \quad (\text{B.11})$$

where L is the background luminosity and the derivative is evaluated at the flux cut. Similarly, $\partial b_{10}/\partial \ln L$ is understood to be evaluated at the flux cut. We use a short-hand notation for the second luminosity derivative of \bar{n}_g :

$$\frac{\partial \mathcal{Q}}{\partial \ln L} \equiv -\frac{\partial^2 \ln \bar{n}_g}{\partial (\ln L)^2} \Bigg|_c. \quad (\text{B.12})$$

C. Upsilon coefficients

Υ_I functions in (7.74)

$$\begin{aligned} \frac{1}{f_{\text{NL}}} \frac{\Upsilon_1}{\mathcal{H}^2} &= 2(3 - b_e)f + 3\Omega_m \left[1 + b_e - 4\mathcal{Q} - \frac{2(1 - \mathcal{Q})}{\chi\mathcal{H}} - \frac{\mathcal{H}'}{\mathcal{H}^2} \right] \\ &\quad + \frac{6\Omega_m}{(3\Omega_m + 2f)} \left[\frac{f'}{\mathcal{H}} + \left(1 + 2\frac{\mathcal{H}'}{\mathcal{H}^2} \right) f \right] \end{aligned} \quad (\text{C.1})$$

$$\frac{1}{f_{\text{NL}}} \frac{\Upsilon_2}{\mathcal{H}} = 2f \left[b_e - 2\mathcal{Q} - \frac{2(1 - \mathcal{Q})}{\chi\mathcal{H}} - \frac{\mathcal{H}'}{\mathcal{H}^2} \right] \quad (\text{C.2})$$

$$\begin{aligned} \frac{1}{b_{01}} \frac{\Upsilon_3}{\mathcal{H}^2} &= \frac{3}{2}\Omega_m \left[2 + b_e - 4\mathcal{Q} + \frac{2(1 - \mathcal{Q})}{\chi\mathcal{H}} + \frac{\mathcal{H}'}{\mathcal{H}^2} + 2 \left(2 - \frac{1}{\chi\mathcal{H}} \right) \frac{\partial \ln b_{01}}{\partial \ln L} \right] \\ &\quad + f \left[3 - f - b_e + \frac{1}{2} \frac{\partial \ln b_{01}}{\partial \ln a} \right] \end{aligned} \quad (\text{C.3})$$

$$\frac{1}{b_{01}} \frac{\Upsilon_4}{\mathcal{H}} = -\frac{3}{2}\Omega_m \quad (\text{C.4})$$

$$\frac{1}{b_{01}} \frac{\Upsilon_5}{\mathcal{H}} = f \left[f + b_e - 2\mathcal{Q} - \frac{2(1 - \mathcal{Q})}{\chi\mathcal{H}} - \frac{\mathcal{H}'}{\mathcal{H}^2} + 2 \left(2 - \frac{1}{\chi\mathcal{H}} \right) \frac{\partial \ln b_{01}}{\partial \ln L} \right] \quad (\text{C.5})$$

Note that $\Upsilon_2 = 2f_{\text{NL}}\gamma_1$.

Table C.1.: The $f_{\text{NL}} \neq 0$ terms from relativistic projection effects [see (7.74)].

TERM	Υ	FOURIER KERNEL	COEFFICIENT
$V_{\text{nG}}^{(2)}$	Υ_1	$2f_{\text{NL}} \mathcal{H} \mathcal{M}_3 / (\mathcal{M}_1 \mathcal{M}_2 k_3^2)$	$(3 - b_e)\mathcal{H}$
$\Psi_{\text{nG}}^{(2)} = \Phi_{\text{nG}}^{(2)}$	Υ_1	$-3f_{\text{NL}} \Omega_m \mathcal{H}^2 \mathcal{M}_3 / (\mathcal{M}_1 \mathcal{M}_2 k_3^2)$	$4\mathcal{Q} - 1 - b_e + \mathcal{R}$

C. Upsilon coefficients

$\Psi_{\text{nG}}^{(2)'} \partial_{\parallel} V_{\text{nG}}^{(2)}$	Υ_1	$6f_{\text{NL}}[f' + (\mathcal{H} + 2\mathcal{H}'/\mathcal{H})f]\Omega_m\mathcal{H}^2\mathcal{M}_3/[(3\Omega_m + 2f)(\mathcal{M}_1\mathcal{M}_2k_3^2)]$	$1/\mathcal{H}$
$\partial_{\parallel} V_{\text{nG}}^{(2)}$	Υ_2	$i 2f_{\text{NL}} \mathcal{H} f \mu_3 \mathcal{M}_3 / (\mathcal{M}_1 \mathcal{M}_2 k_3)$	$b_e - 2Q - \mathcal{R}$
$\Psi \varphi_{\text{P}}$	Υ_3	$-3\Omega_m \mathcal{H}^2 [(k_1^2/\mathcal{M}_1) + (k_2^2/\mathcal{M}_2)] / (4k_1^2 k_2^2)$	$b_{01}[8\mathcal{Q} + 2\mathcal{R} - 2b_e - 4 - \mathcal{S}/(b_{10} - 1)]$
$V \varphi_{\text{P}}$	Υ_3	$f \mathcal{H} [(k_1^2/\mathcal{M}_1) + (k_2^2/\mathcal{M}_2)] / (2k_1^2 k_2^2)$	$b_{01}[2(3 - b_e - f)\mathcal{H} + b'_{10}/(b_{10} - 1)]$
$\Psi \partial_{\parallel} \varphi_{\text{P}}$	Υ_4	$-i 3\Omega_m \mathcal{H}^2 [(\mu_1 k_1^3/\mathcal{M}_1) + (\mu_2 k_2^3/\mathcal{M}_2)] / (4k_1^2 k_2^2)$	$2b_{01}/\mathcal{H}$
$\varphi_{\text{P}} \partial_{\parallel} V$	Υ_5	$i f \mathcal{H} [(\mu_1 k_2/\mathcal{M}_2) + (\mu_2 k_1/\mathcal{M}_1)] / (2k_1 k_2)$	$b_{01}[2f + 2b_e - 4\mathcal{Q} - 2\mathcal{R} + \mathcal{S}/(b_{10} - 1)]$

D. Presentation of kernel coefficients

Here we present the higher order \mathcal{H}/k kernels for the first of the cyclic permutations. It is worth noting that these cannot be exactly manipulated to obtain the coefficients for the other two cyclic permutations, since making the replacements $\mu_1 \rightarrow \mu_2, \mu_3$ introduces additional powers of μ_i , giving rise to slightly different coefficients \mathcal{K}_{ab} . It is however easy enough to extract the coefficients for these permutations following the same method. Below we focus on only the first of the cyclic permutations, that is, the 123 permutation, as outlined before. Schematic representations of the higher order Newtonian and GR kernels are given, along with their corresponding coefficients. Like before, for brevity we use shorthand notations; $F = F_2(\mathbf{k}_1, \mathbf{k}_2)$, $G = G_2(\mathbf{k}_1, \mathbf{k}_2)$, and $S = S_2(\mathbf{k}_1, \mathbf{k}_2)$. Superscript n on $\mathcal{K}_{ab}^{(n)}$ denotes the power $(\mathcal{H}/k)^n$.

$$\mathcal{K}_{ab}^{(2)} = \begin{pmatrix} \bullet & \circ & \bullet & \circ & \bullet & \circ \\ \circ & \bullet & \circ & \bullet & \circ & \bullet \\ \bullet & \circ & \bullet & \circ & \bullet & \circ \\ \circ & \bullet & \circ & \bullet & \circ & \circ \\ \bullet & \circ & \bullet & \circ & \circ & \circ \\ \circ & \bullet & \circ & \circ & \circ & \circ \end{pmatrix}, \quad (\text{D.1})$$

with coefficients,

$$\begin{aligned} \mathcal{K}_{00}^{(2)} &= b_1 b_{s^2} S \gamma_2 \left(\frac{1}{k_1^2} + \frac{1}{k_2^2} \right) + b_1^2 \left\{ [\gamma_2 (1 + F) + \beta_{12}] \left[\frac{1}{k_1^2} + \frac{1}{k_2^2} \right] + \frac{\mu \beta_{11}}{k_1 k_2} + \frac{F \beta_6 + G \beta_7}{k_3^2} \right\} \\ \mathcal{K}_{02}^{(2)} &= \frac{f b_{s^2} S \gamma_2}{k_1^2} - b_1 f \left[\frac{\gamma_2 (1 + F) + \beta_{12}}{k_1^2} + \frac{G \gamma_2 k_2^2}{k_1^2 k_3^2} + \frac{\beta_{11} \mu}{k_1 k_2} + \frac{\beta_{12}}{k_2^2} + \frac{F \beta_6 + G(\beta_7 + \gamma_2)}{k_3^2} \right] \\ &\quad + b_1 \gamma_1 \left[\frac{\beta_{14}}{k_1^2} + \frac{\mu \beta_{15}}{k_1 k_2} + \frac{\beta_{16}}{k_2^2} - \frac{G \beta_{19}}{k_3^2} \right] - b_1^2 \left[\frac{(\beta_9 + E \beta_{10} + \beta_{13})}{k_1^2} + f \gamma_2 \left(\frac{1}{k_1^2} + \frac{1}{k_2^2} \right) \right] \end{aligned}$$

D. Presentation of kernel coefficients

$$\begin{aligned}
\mathcal{K}_{04}^{(2)} &= f^2 \gamma_2 \left[\frac{b_1}{k_1^2} + \frac{Gk_2^2}{k_1^2 k_3^2} \right] + \frac{b_1}{k_1^2} [f(\beta_9 + E\beta_{10} + \beta_{13}) - \beta_{17}\gamma_1] \\
\mathcal{K}_{11}^{(2)} &= \frac{b_{s^2} S \gamma_1^2}{k_1 k_2} + b_1 \left[\beta_{15}\gamma_1 \mu \left(\frac{1}{k_1^2} + \frac{1}{k_2^2} \right) + \beta_{14}\gamma_1 \left(\frac{k_1}{k_2^3} + \frac{k_2}{k_1^3} \right) + \frac{2\beta_{16}\gamma_1 + \gamma_1^2(1+F)}{k_1 k_2} \right. \\
&\quad \left. - \frac{G(k_1^2 + k_2^2)(\beta_{19}\gamma_1 + 2f\gamma_2)}{k_1 k_2 k_3^2} \right] \\
\mathcal{K}_{13}^{(2)} &= f\gamma_1 \left[-\frac{k_2\beta_{14}}{k_1^3} - \frac{\beta_{15}\mu}{k_1^2} - \frac{\beta_{16}}{k_1 k_2} + Gk_2 \frac{(\beta_{19} - \gamma_1)}{k_1 k_3^2} \right] + b_1 \left[-\gamma_1 \left(\frac{k_2\beta_{17}}{k_1^3} + \frac{\beta_{18}}{k_1 k_2} \right) \right. \\
&\quad \left. + \frac{f}{k_1 k_2} (\beta_8 + 2\beta_9 + 2E\beta_{10} - \gamma_1^2) + 2f^2 \gamma_2 \left(\frac{1}{k_1 k_2} + \frac{k_2}{k_1^3} \right) \right] \\
\mathcal{K}_{15}^{(2)} &= \frac{fk_2}{k_1^3} [\gamma_1 \beta_{17} - \gamma_2] \\
\mathcal{K}_{20}^{(2)} &= -\frac{fb_{s^2} S \gamma_2}{k_2^2} + b_1 \left[\frac{\beta_{16}\gamma_1 - f\beta_{12}}{k_1^2} + \frac{\beta_{14}\gamma_1 - f[\beta_{12} + \gamma_2(1+F)]}{k_2^2} + \mu \frac{(-f\beta_{11} + \gamma_1\beta_{15})}{k_1 k_2} \right. \\
&\quad \left. - f \frac{F\beta_6 + G(\beta_7 + \gamma_2)}{k_3^2} - \frac{fGk_1^2 \gamma_2}{k_2^2 k_3^2} \right] - b_1^2 \left[\frac{\beta_9 + E\beta_{10} + \beta_{13}}{k_2^2} + f\gamma_2 \left(\frac{1}{k_1^2} + \frac{1}{k_2^2} \right) \right] \\
\mathcal{K}_{22}^{(2)} &= f\gamma_1 \left[-(\beta_{14} + \beta_{16}) \left(\frac{1}{k_1^2} + \frac{1}{k_2^2} \right) - \frac{2\beta_{15}\mu}{k_1 k_2} + \frac{2G(\beta_{19} - \gamma_1)}{k_3^2} \right] + f^2 \left[\beta_{12} \left(\frac{1}{k_1^2} + \frac{1}{k_2^2} \right) \right. \\
&\quad \left. + \frac{\beta_{11}\mu}{k_1 k_2} + \frac{F\beta_6 + G(\beta_7 + 2\gamma_2)}{k_3^2} \right] + b_1 \left[(3f^2 \gamma_2 - \beta_{18}\gamma_1) \left(\frac{1}{k_1^2} + \frac{1}{k_2^2} \right) \right. \\
&\quad \left. + f \frac{(k_1^2 + k_2^2)(\beta_9 + E\beta_{10} + \beta_{13} - \gamma_1^2)}{k_1^2 + k_2^2} \right] \\
\mathcal{K}_{24}^{(2)} &= \frac{f}{k_1^2} [\gamma_1 (\beta_{17} + \beta_{18}) + f(-\beta_9 - E\beta_{10} - \beta_{13} + \gamma_1^2) - 2f^2 \gamma_2] \\
\mathcal{K}_{31}^{(2)} &= -f\gamma_1 \left[\frac{k_1\beta_{14}}{k_2^3} + \frac{\beta_{15}\mu}{k_2^2} + \frac{\beta_{16}}{k_1 k_2} - \frac{Gk_1\beta_{19}}{k_2 k_3^2} \right] + [-f\gamma_1^2 + 2f^2 \gamma_2] \frac{Gk_1}{k_2 k_3^2} \\
&\quad + b_1 \left[\frac{k_1}{k_2^3} (-\beta_{17}\gamma_1 + 2f^2 \gamma_2) + f \frac{\beta_8 + 2\beta_9 + 2E\beta_{10} - \gamma_1^2}{k_1 k_2} - \frac{\beta_{18}\gamma_1^2 - 2f^2 \gamma_2}{k_1 k_2} \right] \\
\mathcal{K}_{33}^{(2)} &= \frac{f}{k_1 k_2} [2\beta_{18}\gamma_1 + f(-\beta_8 - 2\beta_9 - 2E\beta_{10} + 2\gamma_1^2) - 2f^2 \gamma_2] \\
\mathcal{K}_{40}^{(2)} &= f^2 \gamma_2 \frac{Gk_1^2}{k_2^2 k_3^2} - b_1 \gamma_1 \frac{\beta_{17}}{k_2^2} + b_1 f \left[\frac{\beta_9 + E\beta_{10} + \beta_{13}}{k_2^2} \right] + b_1 f^2 \frac{\gamma_2}{k_2^2} \\
\mathcal{K}_{42}^{(2)} &= f\gamma_1 \frac{(\beta_{17} + \beta_{18})}{k_2^2} + \frac{f^2}{k_2^2} [-\beta_9 - E\beta_{10}\beta_{13} + \gamma_1^2] - f^3 \frac{2\gamma_2}{k_2^2} \\
\mathcal{K}_{51}^{(2)} &= f \frac{k_1}{k_2^3} [\beta_{17}\gamma_1 - f^2 \gamma_2].
\end{aligned}$$

D. Presentation of kernel coefficients

$$\mathcal{K}_{ab}^{(3)} = \begin{pmatrix} \circ & \bullet & \circ & \bullet & \circ & \bullet \\ \bullet & \circ & \bullet & \circ & \bullet & \circ \\ \circ & \bullet & \circ & \bullet & \circ & \circ \\ \bullet & \circ & \bullet & \circ & \circ & \circ \\ \circ & \bullet & \circ & \circ & \circ & \circ \\ \bullet & \circ & \circ & \circ & \circ & \circ \end{pmatrix}, \quad (\text{D.2})$$

with coefficients,

$$\begin{aligned}
\mathcal{K}_{01}^{(3)} &= \gamma_1 \gamma_2 \frac{b_{s^2} S}{k_1^2 k_2} + b_1 \gamma_1 \left[\frac{\beta_{12} (k_1^2 + k_2^2)}{k_1^2 k_2^3} + \frac{\beta_{11} \mu}{k_1 k_2^2} + \frac{F \beta_6 + G \beta_7}{k_2 k_3^2} \right] + b_1 \gamma_2 \left[\frac{\beta_{14} + \beta_{16}}{k_1^2 k_2} \right. \\
&\quad \left. + \frac{\beta_{15} \mu}{k_1 k_2^2} + \frac{(k_2 \beta_{14} + k_1 \beta_{15} \mu)}{k_1^4} + \frac{\beta_{16}}{k_2^3} - G \beta_{19} \left(\frac{1}{k_2 k_3^2} + \frac{k_2}{k_1^2 k_3^2} \right) \right] + b_1 \gamma_1 \gamma_2 \frac{(1+F)}{k_1^2 k_2} - b_1^2 \frac{(\beta_4 - \beta_3 + E \beta_5)}{k_1^2 k_2} \\
\mathcal{K}_{03}^{(3)} &= - \frac{f \gamma_2}{k_1^2} \left[\frac{k_2 \beta_{14}}{k_1^2} + \frac{\beta_{15} \mu}{k_1} + \frac{\beta_{16}}{k_2} \right] + f \gamma_2 G k_2 \frac{[\beta_{19} - \gamma_1]}{k_1^2 k_3^2} - b_1 \left[\frac{k_2 \beta_{17} \gamma_2}{k_1^4} + [\gamma_2 \beta_{17} - f (\beta_4 - \beta_3 + E \beta_5) \right. \\
&\quad \left. + \gamma_1 (\beta_9 + E \beta_{10} + \beta_{13}) + f \gamma_1 \gamma_2] \frac{1}{k_1^2 k_2} \right] \\
\mathcal{K}_{05}^{(3)} &= f \gamma_2 \frac{k_2 \beta_{17}}{k_1^4} \\
\mathcal{K}_{10}^{(3)} &= \gamma_1 \gamma_2 \frac{b_{s^2} S}{k_1 k_2^2} + b_1 \gamma_1 \left[\frac{(k_1^2 + k_2^2) \beta_{12}}{k_1^3 k_2^2} + \frac{F \beta_6 + G \beta_7}{k_1 k_2^3} + \frac{\beta_{11} \mu}{k_1^2 k_2} \right] + b_1 \gamma_2 \left[\frac{(k_1^2 + k_2^2) \beta_{16}}{k_1^3 k_2^2} \right. \\
&\quad \left. + \frac{(k_1^2 + k_2^2) (k_1 \beta_{14} + k_2 \beta_{15} \mu)}{k_1^2 k_2^4} - G \beta_{19} \frac{(k_1^2 + k_2^2)}{k_1 k_2^2 k_3^2} \right] + b_1 \gamma_1 \gamma_2 \frac{[1+F]}{k_1 k_2^2} - b_1^2 \frac{[\beta_4 - \beta_3 + E \beta_5]}{k_1 k_2^2} \\
\mathcal{K}_{12}^{(3)} &= \gamma_1^2 \left[\frac{\beta_{14}}{k_1^3} + \frac{\beta_{15} \mu}{k_1^2 k_2} + \frac{\beta_{16}}{k_1 k_2^2} - G \frac{\beta_{19}}{k_1 k_3^2} \right] + f \left[-\gamma_1 \frac{(k_1^2 + k_2^2) \beta_{12}}{k_1^3 k_2^2} - \gamma_1 \left(\frac{F \beta_6 + G [\beta_7 + 3 \gamma_2]}{k_1 k_3^2} - \frac{\beta_{11} \mu}{k_1^2 k_2} \right) \right. \\
&\quad \left. + \gamma_2 \left(-\frac{\beta_{14}}{k_1 k_2^2} - \frac{\beta_{15} \mu}{k_1^2 k_2} - \frac{\beta_{16}}{k_1^3} + 3 \frac{G \gamma_2}{k_1 k_3^2} \right) \right] - b_1 \left[\frac{\beta_{13} \gamma_1}{k_1^3} + \frac{-f (\beta_4 - \beta_3 + E \beta_5) + \beta_8 \gamma_1}{k_1 k_2^2} \right. \\
&\quad \left. + \frac{\gamma_1 (2k_1^2 + k_2^2)}{k_1^3 k_2^2} (\beta_9 + E \beta_{10} + f \gamma_2) + \frac{(k_1^2 + k_2^2) \beta_{18} \gamma_2}{k_1^3 k_2^2} \right] \\
\mathcal{K}_{14}^{(3)} &= \gamma_1 \frac{-\beta_{17} \gamma_1 + f^2 \gamma_2}{k_1^3} + f \gamma_1 \frac{[\beta_9 + E \beta_{10} + \beta_{13}]}{k_1^3} + f \gamma_2 \frac{\beta_{18}}{k_1^3} \\
\mathcal{K}_{21}^{(3)} &= \gamma_1^2 \left[\frac{\beta_{14}}{k_2^3} + \frac{\beta_{15} \mu}{k_1 k_2^2} + \frac{\beta_{16}}{k_1^2 k_2} - \frac{G \beta_{19}}{k_2 k_3^2} \right] + f \left[-\frac{(k_1^2 + k_2^2) \beta_{12} \gamma_1}{k_1^2 k_2^3} - \gamma_1 \frac{F \beta_6}{k_2 k_3^2} + G \gamma_1 \frac{-\beta_7 - 3 \gamma_2}{k_2 k_3^2} \right. \\
&\quad \left. + G \gamma_2 \frac{\beta_{19}}{k_2 k_3^2} - \frac{\mu}{k_1 k_2^2} (\gamma_1 \beta_{11} + \gamma_2 \beta_{15}) - \gamma_2 \left(\frac{\beta_{14}}{k_1^2 k_2} + \frac{\beta_{16}}{k_2^3} \right) \right] + b_1 \left[f \frac{(\beta_4 - \beta_3 + E \beta_5)}{k_1^2 k_2} - \gamma_2 \frac{(k_1^2 + k_2^2) \beta_{18}}{k_1^2 k_3^2} \right. \\
&\quad \left. - \gamma_1 \gamma_2 f \left(\frac{1}{k_2^3} + \frac{2}{k_1^2 k_2} \right) - \gamma_1 E \frac{(k_1^2 + 2k_2^2) \beta_{10}}{k_1^2 k_2^3} - \gamma_1 \frac{(k_1^2 + 2k_2^2) \beta_9}{k_1^2 k_2^3} - \gamma_1 \left(\frac{\beta_8}{k_1^2 k_2} + \frac{\beta_{13}}{k_2^3} \right) \right]
\end{aligned}$$

D. Presentation of kernel coefficients

$$\begin{aligned}
\mathcal{K}_{23}^{(3)} &= -\gamma_1^2 \frac{\beta_{18}}{k_1^2 k_2} + f \gamma_1 \frac{[\beta_8 + 3\beta_9 + 3E\beta_{10} + \beta_{13}]}{k_1^2 k_2} + f \gamma_2 \frac{[\beta_{17} + \beta_{18}]}{k_1 k_2^2} + f^2 \frac{[-\beta_4 + \beta_3 - E\beta_5 + 3\gamma_1 \gamma_2]}{k_1^2 k_2} \\
\mathcal{K}_{30}^{(3)} &= -f \gamma_2 \left[\frac{k_1 \beta_{14}}{k_2^4} + \frac{\beta_{15}\mu}{k_2^3} + \frac{\beta_{16}}{k_1 k_2^2} \right] + f \gamma_2 G \frac{k_1 (\beta_{19} - \gamma_1)}{k_2^2 k_3^2} - b_1 \gamma_1 \left[\frac{\beta_9 + E\beta_{10} + \beta_{13}}{k_1 k_2^2} \right] \\
&\quad - b_1 \gamma_2 \frac{(k_1^2 + k_2^2) \beta_{17}}{k_1 k_2^4} + b_1 f \frac{(\beta_4 - \beta_3 + E\beta_5 - \gamma_1 \gamma_2)}{k_1 k_2^2} \\
\mathcal{K}_{32}^{(3)} &= -\gamma_1^2 \frac{\beta_{18}}{k_1 k_2^2} + f \gamma_1 \frac{(\beta_8 + 3\beta_9 + 3E\beta_{10} + \beta_{13})}{k_1 k_2^2} + f \gamma_2 \frac{(\beta_{17} + \beta_{18})}{k_1 k_2^2} - f^2 \frac{(\beta_4 - \beta_3 + E\beta_5 - 3\gamma_1 \gamma_2)}{k_1 k_2^2} \\
\mathcal{K}_{41}^{(3)} &= -\gamma_1^2 \frac{\beta_{17}}{k_2^3} + f^2 \frac{\gamma_1 \gamma_2}{k_2^3} + f \gamma_1 \frac{(\beta_9 + E\beta_{10} + \beta_{13})}{k_2^3} + f \gamma_2 \frac{\beta_{18}}{k_2^3} \\
\mathcal{K}_{50}^{(3)} &= f \gamma_2 \frac{k_1 \beta_{17}}{k_2^4}.
\end{aligned}$$

$$\mathcal{K}_{ab}^{(4)} = \begin{pmatrix} \bullet & \circ & \bullet & \circ & \bullet & \circ \\ \circ & \bullet & \circ & \bullet & \circ & \circ \\ \bullet & \circ & \bullet & \circ & \circ & \circ \\ \circ & \bullet & \circ & \circ & \circ & \circ \\ \bullet & \circ & \circ & \circ & \circ & \circ \\ \circ & \circ & \circ & \circ & \circ & \circ \end{pmatrix}, \quad (\text{D.3})$$

with coefficients,

$$\begin{aligned}
\mathcal{K}_{00}^{(4)} &= \gamma_2^2 \frac{b_{s^2} S}{k_1^2 k_2^2} + b_1 \gamma_2 \left[F \frac{(k_1^2 + k_2^2) \beta_6}{k_1^2 k_2^2 k_3^2} + G \frac{(k_1^2 + k_2^2) \beta_7}{k_1^2 k_2^2 k_3^2} + \frac{(k_1^2 + k_2^2) \beta_{11}\mu}{k_1^3 k_2^3} + \frac{(k_1^2 + k_2^2)^2 \beta_{12}}{k_1^4 k_2^4} \right] \\
&\quad + b_1 \gamma_2^2 \frac{(1+F)}{k_1^2 k_2^2} + b_1^2 \frac{(\beta_1 + E\beta_2)}{k_1^2 k_2^2} \\
\mathcal{K}_{02}^{(4)} &= \gamma_1 \gamma_2 \left[\frac{\beta_{14}}{k_1^4} + \frac{\beta_{15}\mu}{k_1^3 k_2} + \frac{\beta_{16}}{k_1^2 k_2^2} - G \frac{\beta_{19}}{k_1^2 k_2^2} \right] - f \gamma_2 \left[F \frac{\beta_6}{k_1^2 k_3^2} + G \frac{\beta_7}{k_1^2 k_3^2} + \frac{\beta_{11}\mu}{k_1^3 k_2} + \frac{(k_1^2 + k_2^2) \beta_{12}}{k_1^4 k_2^2} \right] \\
&\quad - b_1 f \frac{(\beta_1 + E\beta_2 + \gamma_2^2)}{k_1^2 k_2^2} - b_1 \gamma_1 \frac{(\beta_4 - \beta_3 + E\beta_5)}{k_1^2 k_2^2} - b_1 \gamma_2 \left[\frac{(k_1^2 + k_2^2) \beta_9}{k_1^4 k_2^2} + E \frac{(k_1^2 + k_2^2) \beta_{10}}{k_1^4 k_2^2} + \frac{\beta_{13}}{k_1^4} \right] \\
\mathcal{K}_{04}^{(4)} &= -\gamma_1 \gamma_2 \frac{\beta_{17}}{k_1^4} + f \gamma_2 \frac{(\beta_9 + E\beta_{10} + \beta_{13})}{k_1^4} \\
\mathcal{K}_{11}^{(4)} &= \gamma_1^2 \left[F \frac{\beta_6}{k_1 k_2 k_3^2} + G \frac{\beta_7}{k_1 k_2 k_3^2} + \frac{\beta_{11}\mu}{k_1^2 k_2^2} + \frac{(k_1^2 + k_2^2) \beta_{12}}{k_1^3 k_2^3} \right] - \gamma_2^2 f \frac{2G}{k_1 k_2 k_3^2} + \gamma_1 \gamma_2 \left[\frac{(k_1^2 + k_2^2) \beta_{14}}{k_1^3 k_2^3} \right. \\
&\quad \left. + 2 \frac{\beta_{15}\mu}{k_1^2 k_2^2} + \frac{(k_1^2 + k_2^2) \beta_{16}}{k_1^3 k_2^3} - 2G \frac{\beta_{19}}{k_1 k_2 k_3^2} \right] - b_1 \gamma_1 \frac{(k_1^2 + k_2^2) (\beta_4 - \beta_3 + E\beta_5)}{k_1^3 k_2^3} - b_1 \gamma_2 \left[\frac{(k_1^2 + k_2^2) \beta_8}{k_1^3 k_2^3} \right. \\
&\quad \left. + 2 \frac{(k_1^2 + k_2^2) \beta_9}{k_1^3 k_2^3} + 2E \frac{(k_1^2 + k_2^2) \beta_{10}}{k_1^3 k_2^3} \right] - b_1 f \gamma_2 \frac{(k_1^2 + k_2^2)}{k_1^3 k_2^3}
\end{aligned}$$

D. Presentation of kernel coefficients

$$\begin{aligned}
\mathcal{K}_{13}^{(4)} &= f^2 \frac{\gamma_2^2}{k_1^3 k_2} + f \gamma_1 \frac{(\beta_4 - \beta_3 + E\beta_5)}{k_1^3 k_2} + f \gamma_2 \frac{(\beta_8 + 2\beta_9 + 2E\beta_{10})}{k_1^3 k_2} - \gamma_1^2 \frac{(\beta_9 + E\beta_{10} + \beta_{13})}{k_1^3 k_2} - \gamma_1 \gamma_2 \frac{(\beta_{17} + \beta_{18})}{k_1^3 k_2} \\
\mathcal{K}_{20}^{(4)} &= \gamma_1 \gamma_2 \left[\frac{\beta_{14}}{k_2^4} + \frac{\beta_{15}\mu}{k_1 k_2^3} + \frac{\beta_{16}}{k_1^2 k_2^2} - G \frac{\beta_{19}}{k_2^2 k_3^2} \right] - f \gamma_2 \left[F \frac{\beta_6}{k_2^2 k_3^2} + G \frac{\beta_7}{k_2^2 k_3^2} + \frac{\beta_{11}\mu}{k_1 k_2^3} + \frac{(k_1^2 + k_2^2) \beta_{12}}{k_1^2 k_2^4} \right] \\
&\quad - f \gamma_2^2 \frac{G}{k_2^2 k_3^2} - b_1 \gamma_1 \frac{(\beta_4 - \beta_3 + E\beta_5)}{k_1^2 k_2^2} - b_1 \gamma_2 \left[\frac{(k_1^2 + k_2^2) \beta_9}{k_1^2 k_2^4} + E \frac{(k_1^2 + k_2^2) \beta_{10}}{k_1^2 k_2^4} + \frac{(k_1^2 + k_2^2) \beta_{13}}{k_1^2 k_2^4} \right] \\
&\quad + b_1 f \frac{(\beta_1 - E\beta_2 - \gamma_2^2)}{k_1^2 k_2^2} \\
\mathcal{K}_{22}^{(4)} &= -\gamma_1^2 \frac{(\beta_8 + 2\beta_9 + 2E\beta_{10})}{k_1^2 k_2^2} - \gamma_1 \gamma_2 \frac{2\beta_{18}}{k_1^2 k_2^2} + f \gamma_1 \frac{2(\beta_4 - \beta_3 + E\beta_5)}{k_1^2 k_2^2} + f \gamma_2 \frac{2(\beta_9 + E\beta_{10} + \beta_{13})}{k_1^2 k_2^2} \\
&\quad + f^2 \frac{(\beta_1 + E\beta_2 + 2\gamma_2^2)}{k_1^2 k_2^2} \\
\mathcal{K}_{31}^{(4)} &= f^2 \frac{\gamma_2^2}{k_1 k_2^3} + f \gamma_1 \frac{(\beta_4 - \beta_3 + E\beta_5)}{k_1 k_2^3} + f \gamma_2 \frac{(\beta_8 + 2\beta_9 + 2E\beta_{10})}{k_1 k_2^3} - \gamma_1^2 \frac{(\beta_9 + E\beta_{10} + \beta_{13})}{k_1 k_2^3} - \gamma_1 \gamma_2 \frac{(\beta_{17} + \beta_{18})}{k_1 k_2^3} \\
\mathcal{K}_{40}^{(4)} &= -\gamma_1 \gamma_2 \frac{\beta_{17}}{k_2^4} + f \gamma_2 \frac{(\beta_9 + E\beta_{10} + \beta_{13})}{k_2^4}.
\end{aligned}$$

$$\mathcal{K}_{ab}^{(5)} = \begin{pmatrix} \circ & \bullet & \circ & \bullet & \circ & \circ \\ \bullet & \circ & \bullet & \circ & \circ & \circ \\ \circ & \bullet & \circ & \circ & \circ & \circ \\ \bullet & \circ & \circ & \circ & \circ & \circ \\ \circ & \circ & \circ & \circ & \circ & \circ \\ \circ & \circ & \circ & \circ & \circ & \circ \end{pmatrix}, \quad (\text{D.4})$$

with coefficients,

$$\begin{aligned}
\mathcal{K}_{01}^{(5)} &= \gamma_1 \gamma_2 \left[\frac{(F\beta_6 + G\beta_7)}{k_1^2 k_2 k_3^2} + \frac{\beta_{11}\mu}{k_1^3 k_2^2} + \frac{(k_1^2 + k_2^2) \beta_{12}}{k_1^4 k_2^3} \right] + \gamma_2^2 \left[\frac{\beta_{14}}{k_1^4 k_2} + \frac{\beta_{15}\mu}{k_1^3 k_2^2} + \frac{\beta_{16}}{k_1^2 k_2^3} - G \frac{\beta_{19}}{k_1^2 k_2 k_3^2} \right] \\
&\quad + b_1 \gamma_1 \frac{(\beta_1 + E\beta_2)}{k_1^2 k_2^3} - b_1 \gamma_2 \frac{(k_1^2 + k_2^2) (\beta_4 - \beta_3 + E\beta_5)}{k_1^4 k_2^3} \\
\mathcal{K}_{03}^{(5)} &= -\gamma_1 \gamma_2 \frac{(\beta_9 + E\beta_{10} + \beta_{13})}{k_1^4 k_2} - \gamma_2^2 \frac{\beta_{17}}{k_1^4 k_2} + f \gamma_2 \frac{(\beta_4 - \beta_3 + E\beta_5)}{k_1^4 k_2} \\
\mathcal{K}_{10}^{(5)} &= \gamma_1 \gamma_2 \left[\frac{(F\beta_6 + G\beta_7)}{k_1 k_2^2 k_3^2} + \frac{\beta_{11}\mu}{k_1^2 k_2^3} + \frac{(k_1^2 + k_2^2) \beta_{12}}{k_1^3 k_2^4} \right] + \gamma_2^2 \left[\frac{\beta_{14}}{k_1 k_2^4} + \frac{\beta_{15}\mu}{k_1^2 k_2^3} + \frac{\beta_{16}}{k_1^3 k_2^2} - G \frac{\beta_{19}}{k_1 k_2^2 k_3^2} \right] \\
&\quad + b_1 \gamma_1 \frac{(\beta_1 + E\beta_2)}{k_1^3 k_2^2} - b_1 \gamma_2 \frac{(k_1^2 + k_2^2) (\beta_4 - \beta_3 + E\beta_5)}{k_1^3 k_2^4} \\
\mathcal{K}_{12}^{(5)} &= -\gamma_1^2 \frac{(\beta_4 - \beta_3 + E\beta_5)}{k_1^3 k_2^2} - \gamma_2^2 \frac{\beta_{18}}{k_1^3 k_2^2} - \gamma_1 \gamma_2 \frac{(\beta_8 + 3\beta_9 + 3E\beta_{10} + \beta_{13})}{k_1^3 k_2^2} - f \gamma_1 \frac{(\beta_1 + E\beta_2)}{k_1^3 k_2^2} + f \gamma_2 \frac{(\beta_4 - \beta_3 + E\beta_5)}{k_1^3 k_2^2} \\
\mathcal{K}_{21}^{(5)} &= -\gamma_1^2 \frac{(\beta_4 - \beta_3 + E\beta_5)}{k_1^2 k_2^3} - \gamma_2^2 \frac{\beta_{18}}{k_1^2 k_2^3} - \gamma_1 \gamma_2 \frac{(\beta_8 + 3\beta_9 + 3E\beta_{10} + \beta_{13})}{k_1^2 k_2^3} - f \gamma_1 \frac{(\beta_1 + E\beta_2)}{k_1^2 k_2^3} + f \gamma_2 \frac{[\beta_4 - \beta_3 + E\beta_5]}{k_1^2 k_2^3}
\end{aligned}$$

D. Presentation of kernel coefficients

$$\mathcal{K}_{30}^{(5)} = -\gamma_1 \gamma_2 \frac{(\beta_9 + E\beta_{10} + \beta_{13})}{k_1 k_2^4} - \gamma_2^2 \frac{\beta_{17}}{k_1 k_2^4} + f \gamma_2 \frac{(\beta_4 - \beta_3 + E\beta_5)}{k_1 k_2^4}.$$

$$\mathcal{K}_{ab}^{(6)} = \begin{pmatrix} \bullet & \circ & \bullet & \circ & \circ & \circ \\ \circ & \bullet & \circ & \circ & \circ & \circ \\ \bullet & \circ & \circ & \circ & \circ & \circ \\ \circ & \circ & \circ & \circ & \circ & \circ \\ \circ & \circ & \circ & \circ & \circ & \circ \\ \circ & \circ & \circ & \circ & \circ & \circ \end{pmatrix}, \quad (\text{D.5})$$

with coefficients,

$$\begin{aligned} \mathcal{K}_{00}^{(6)} &= \gamma_2^2 \left[\frac{(F\beta_6 + G\beta_7)}{k_1^2 k_2^2 k_3^2} + \frac{\beta_{11}\mu}{k_1^3 k_2^3} + \frac{(k_1^2 + k_2^2)\beta_{12}}{k_1^4 k_2^4} \right] + b_1 \gamma_2 \frac{(k_1^2 + k_2^2)(\beta_1 + E\beta_2)}{k_1^4 k_2^4} \\ \mathcal{K}_{02}^{(6)} &= -\gamma_1 \gamma_2 \frac{(\beta_4 - \beta_3 + E\beta_5)}{k_1^4 k_2^2} - \gamma_2^2 \frac{(\beta_9 + E\beta_{10} + \beta_{13})}{k_1^4 k_2^2} - f \gamma_2 \frac{(\beta_1 + E\beta_2)}{k_1^4 k_2^2} \\ \mathcal{K}_{11}^{(6)} &= \gamma_1^2 \frac{(\beta_1 + E\beta_2)}{k_1^3 k_2^3} - 2\gamma_1 \gamma_2 \frac{\beta_4 - \beta_3 + E\beta_5}{k_1^3 k_2^3} - \gamma_2^2 \frac{(\beta_8 + 2\beta_9 + 2E\beta_{10})}{k_1^3 k_2^3} \\ \mathcal{K}_{20}^{(6)} &= -\gamma_1 \gamma_2 \frac{(\beta_4 - \beta_3 + E\beta_5)}{k_1^2 k_2^4} - \gamma_2^2 \frac{(\beta_9 + E\beta_{10} + \beta_{13})}{k_1^2 k_2^4} - f \gamma_2 \frac{(\beta_1 + E\beta_2)}{k_1^2 k_2^4}. \end{aligned}$$

$$\mathcal{K}_{ab}^{(7)} = \begin{pmatrix} \circ & \bullet & \circ & \circ & \circ & \circ \\ \bullet & \circ & \circ & \circ & \circ & \circ \\ \circ & \circ & \circ & \circ & \circ & \circ \\ \circ & \circ & \circ & \circ & \circ & \circ \\ \circ & \circ & \circ & \circ & \circ & \circ \\ \circ & \circ & \circ & \circ & \circ & \circ \end{pmatrix}, \quad (\text{D.6})$$

with coefficients,

$$\begin{aligned} \mathcal{K}_{01}^{(7)} &= \gamma_1 \gamma_2 \frac{(\beta_1 + E\beta_2)}{k_1^4 k_2^3} - \gamma_2^2 \frac{(\beta_4 - \beta_3 + E\beta_5)}{k_1^4 k_2^3} \\ \mathcal{K}_{10}^{(7)} &= \gamma_1 \gamma_2 \frac{(\beta_1 + E\beta_2)}{k_1^3 k_2^4} - \gamma_2^2 \frac{(\beta_4 - \beta_3 + E\beta_5)}{k_1^3 k_2^4}. \end{aligned}$$

D. Presentation of kernel coefficients

$$\mathcal{K}_{ab}^{(8)} = \begin{pmatrix} \bullet & \circ & \circ & \circ & \circ & \circ \\ \circ & \circ & \circ & \circ & \circ & \circ \\ \circ & \circ & \circ & \circ & \circ & \circ \\ \circ & \circ & \circ & \circ & \circ & \circ \\ \circ & \circ & \circ & \circ & \circ & \circ \\ \circ & \circ & \circ & \circ & \circ & \circ \end{pmatrix}, \quad (\text{D.7})$$

with coefficient

$$\mathcal{K}_{00}^{(8)} = \gamma_2^2 \frac{(\beta_1 + E\beta_2)}{k_1^4 k_2^4}.$$

E. Squeezed limit of multipoles

These are the leading contributions to the squeezed limits for the multipoles – up to $O(\mathcal{H}/k)$ and $\ell = 3$.

$$B_{0,0} = -2\sqrt{\pi} \frac{P_L P_S}{105} \left[f^4 + \left(-3b_1 - \frac{15}{7} \right) f^3 + \left(-77b_1^2 - 33b_1 - 14b_2 + \frac{14}{3}b_{s^2} \right) f^2 - 105 \left(b_1^2 + \frac{31}{21}b_1 + \frac{4}{3}b_2 - \frac{4}{9}b_{s^2} \right) b_1 f - 195b_1^2 \left(b_1 + \frac{14b_2}{13} - \frac{14b_{s^2}}{39} \right) \right] \quad (\text{E.1})$$

$$B_{1,1} = \sqrt{6\pi} \frac{P_L P_S}{105k_L} \left\{ \gamma_1 f^3 + \left(18b_1\gamma_1 - 9\beta_{14} + 6\beta_{16} - 5\beta_{17} + 2\beta_{18} + \frac{15}{7}\gamma_1 \right) f^2 + \left[49\gamma_1 b_1^2 + (-42\beta_{14} + 56\beta_{16} - 24\beta_{17} + 12\beta_{18} + 18\gamma_1) b_1 + 14\gamma_1 \left(b_2 - \frac{b_{s^2}}{3} \right) \right] f - 35 \left[\left(\beta_{14} - 2\beta_{16} + \frac{3\beta_{17}}{5} - \frac{2\beta_{18}}{5} - \frac{13\gamma_1}{7} \right) b_1 - 2\gamma_1 \left(b_2 - \frac{b_{s^2}}{3} \right) \right] b_1 \right\} \quad (\text{E.2})$$

$$B_{2,0} = -4\sqrt{5\pi} f \frac{P_L P_S}{1155} \left[f^3 + \left(-\frac{55}{14} - \frac{11b_1}{2} \right) f^2 + \left(-110b_1^2 - \frac{429}{7}b_1 - 11b_2 + \frac{11}{3}b_{s^2} \right) f - 231 \frac{b_1}{2} \left(b_1^2 + \frac{23}{21}b_1 + \frac{2}{3}b_2 - \frac{2}{9}b_{s^2} \right) \right] \quad (\text{E.3})$$

$$B_{2,2} = 2\sqrt{30\pi} f \frac{P_L P_S}{1155} \left[f^3 + \left(-\frac{11b_1}{6} - \frac{55}{42} \right) f^2 + \left(-44b_1^2 - \frac{99}{7}b_1 - 11b_2 + \frac{11}{3}b_{s^2} \right) f - 77 \frac{b_1}{2} \left(b_1^2 + \frac{13}{7}b_1 + 2b_2 - \frac{2}{3}b_{s^2} \right) \right] \quad (\text{E.4})$$

$$B_{3,1} = \sqrt{21\pi} \frac{P_L P_S}{165k_L} \left\{ \gamma_1 f^3 + \left[\frac{418}{21}b_1\gamma_1 - \frac{33}{7}\beta_{14} + \frac{22}{7}\beta_{16} - 5\beta_{17} + 2\beta_{18} + \frac{440}{147}\gamma_1 \right] f^2 + \left[\frac{143\gamma_1 b_1^2}{7} + \left(-\frac{99\beta_{14}}{7} + \frac{22\beta_{16}}{7} - \frac{77\beta_{17}}{3} + \frac{242\beta_{18}}{21} + \frac{792\gamma_1}{49} \right) b_1 + \frac{88\gamma_1}{7} \left(b_2 - \frac{b_{s^2}}{3} \right) \right] f - b_1^2 \frac{132}{7} \left(\beta_{17} - \frac{2\beta_{18}}{3} \right) \right\} \quad (\text{E.5})$$

$$B_{3,3} = -f\sqrt{35\pi} \frac{P_L P_S}{1155k_L} \left[\gamma_1 f^2 + \left(\frac{22b_1\gamma_1}{3} - 5\beta_{17} + 2\beta_{18} - 11\beta_{14} + \frac{22\beta_{16}}{3} \right) f - 11 \left(-3b_1\gamma_1 + \beta_{17} - \frac{2\beta_{18}}{3} + 3\beta_{14} - 6\beta_{16} \right) b_1 \right] \quad (\text{E.6})$$

E. Squeezed limit of multipoles

Bibliography

- Abramo L. R., Bertacca D., 2017, Physical Review D, 96
- Aghanim N., et al., 2018
- Alonso D., Ferreira P. G., 2015, Phys. Rev. D, 92, 063525
- Alonso D., Bull P., Ferreira P. G., Santos M. G., 2015a, Mon. Not. Roy. Astron. Soc., 447, 400
- Alonso D., Bull P., Ferreira P. G., Maartens R., Santos M., 2015b, Astrophys. J., 814, 145
- Alonso D., Ferreira P. G., Jarvis M. J., Moodley K., 2017, Phys. Rev. D, 96, 043515
- Ansari R., et al., 2018
- Asorey J., et al., 2020, Mon. Not. Roy. Astron. Soc., 495, 1788
- Bacon D. J., et al., 2020, Publ. Astron. Soc. Austral., 37, e007
- Baldauf T., Seljak U., Senatore L., 2011, JCAP, 1104, 006
- Ballardini M., Matthewson W. L., Maartens R., 2019, Mon. Not. Roy. Astron. Soc., 489, 1950
- Barreira A., 2020, JCAP, 12, 031
- Barreira A., Cabass G., Schmidt F., Pillepich A., Nelson D., 2020, JCAP, 12, 013
- Bartolo N., et al., 2016, Phys. Dark Univ., 13, 30
- Bernal J. L., Breysse P. C., Gil-Marín H., Kovetz E. D., 2019, Phys. Rev. D, 100, 123522
- Bernal J. L., Bellomo N., Raccanelli A., Verde L., 2020, JCAP, 10, 017
- Bernardeau F., Colombi S., Gaztañaga E., Scoccimarro R., 2002, Physics Reports, 367, 1–248
- Bertacca D., 2015, Class. Quant. Grav., 32, 195011
- Bertacca D., Maartens R., Clarkson C., 2014a, JCAP, 09, 037
- Bertacca D., Maartens R., Clarkson C., 2014b, JCAP, 1411, 013

Bibliography

- Bertacca D., Bartolo N., Bruni M., Koyama K., Maartens R., Matarrese S., Sasaki M., Wands D., 2015, *Class. Quant. Grav.*, 32, 175019
- Bertacca D., Raccanelli A., Bartolo N., Liguori M., Matarrese S., Verde L., 2018, *Phys. Rev.*, D97, 023531
- Beutler F., Castorina E., Zhang P., 2019, *JCAP*, 03, 040
- Bharadwaj S., Mazumdar A., Sarkar D., 2020, *Mon. Not. Roy. Astron. Soc.*, 493, 594
- Blas D., Lesgourgues J., Tram T., 2011, *JCAP*, 07, 034
- Bolejko K., Clarkson C., Maartens R., Bacon D., Meures N., Beynon E., 2013, *Phys. Rev. Lett.*, 110, 021302
- Bonvin C., 2008, *Phys. Rev. D*, 78, 123530
- Bonvin C., 2014, *Class. Quant. Grav.*, 31, 234002
- Bonvin C., Durrer R., 2011, *Phys. Rev. D*, 84, 063505
- Bonvin C., Fleury P., 2018, *JCAP*, 05, 061
- Bonvin C., Hui L., Gaztanaga E., 2014, *Phys. Rev. D*, 89, 083535
- Bonvin C., Hui L., Gaztanaga E., 2016, *JCAP*, 08, 021
- Bruni M., Crittenden R., Koyama K., Maartens R., Pitrou C., Wands D., 2012, *Phys. Rev. D*, 85, 041301
- Bruni M., Hidalgo J. C., Meures N., Wands D., 2014, *Astrophys. J.*, 785, 2
- Bull P., Ferreira P. G., Patel P., Santos M. G., 2015, *Astrophys. J.*, 803, 21
- Camera S., Santos M. G., Maartens R., 2015a, *Mon. Not. Roy. Astron. Soc.*, 448, 1035
- Camera S., Maartens R., Santos M. G., 2015b, *Mon. Not. Roy. Astron. Soc.*, 451, L80
- Camera S., Fonseca J., Maartens R., Santos M. G., 2018, *Mon. Not. Roy. Astron. Soc.*, 481, 1251
- Castorina E., Villaescusa-Navarro F., 2017, *Mon. Not. Roy. Astron. Soc.*, 471, 1788
- Castorina E., White M., 2018, *Mon. Not. Roy. Astron. Soc.*, 476, 4403
- Castorina E., et al., 2020
- Celoria M., Matarrese S., 2020, *Proc. Int. Sch. Phys. Fermi*, 200, 179
- Challinor A., Lewis A., 2011, *Phys. Rev. D*, 84, 043516

Bibliography

- Chan K. C., Blot L., 2017, Phys. Rev. D, 96, 023528
- Chen S.-F., Castorina E., White M., Slosar A., 2019, JCAP, 07, 023
- Child H. L., Takada M., Nishimichi T., Sunayama T., Slepian Z., Habib S., Heitmann K., 2018, Phys. Rev. D, 98, 123521
- Chudaykin A., Ivanov M. M., 2019, JCAP, 11, 034
- Clarkson C., de Weerd E. M., Jolicoeur S., Maartens R., Umeh O., 2019, Monthly Notices of the Royal Astronomical Society, 486, L101
- Cunnington S., Pourtsidou A., Soares P. S., Blake C., Bacon D., 2020, Mon. Not. Roy. Astron. Soc., 496, 415
- Dai L., Pajer E., Schmidt F., 2015, JCAP, 10, 059
- Dalal N., Dore O., Huterer D., Shirokov A., 2008, Phys. Rev. D, 77, 123514
- Desjacques V., Jeong D., Schmidt F., 2018a, JCAP, 12, 035
- Desjacques V., Jeong D., Schmidt F., 2018b, Phys. Rept., 733, 1
- Di Dio E., Seljak U., 2019, JCAP, 04, 050
- Di Dio E., Durrer R., Marozzi G., Montanari F., 2014, JCAP, 12, 017
- Di Dio E., Durrer R., Marozzi G., Montanari F., 2016, JCAP, 01, 016
- Di Dio E., Perrier H., Durrer R., Marozzi G., Moradinezhad Dizgah A., Noreña J., Riotto A., 2017, JCAP, 1703, 006
- Di Dio E., Durrer R., Maartens R., Montanari F., Umeh O., 2019, JCAP, 04, 053
- Durrer R., Jalilvand M., Kothari R., Maartens R., Montanari F., 2020, JCAP, 12, 003
- Fonseca J., Camera S., Santos M., Maartens R., 2015, Astrophys. J. Lett., 812, L22
- Fonseca J., Maartens R., Santos M. G., 2017, Mon. Not. Roy. Astron. Soc., 466, 2780
- Fonseca J., Maartens R., Santos M. G., 2018, Mon. Not. Roy. Astron. Soc., 479, 3490
- Fonseca J., Viljoen J.-A., Maartens R., 2019, JCAP, 12, 028
- Gagrani P., Samushia L., 2017, Mon. Not. Roy. Astron. Soc., 467, 928
- Gaztanaga E., Bonvin C., Hui L., 2017, JCAP, 01, 032
- Ghosh A., Mertens F., Koopmans L. V. E., 2018, Mon. Not. Roy. Astron. Soc., 474, 4552

Bibliography

- Giannantonio T., Porciani C., 2010, Phys. Rev. D, 81, 063530
- Gil-Marín H., Percival W. J., Verde L., Brownstein J. R., Chuang C.-H., Kitaura F.-S., Rodríguez-Torres S. A., Olmstead M. D., 2017, Mon. Not. Roy. Astron. Soc., 465, 1757
- Grimm N., Scaccabarozzi F., Yoo J., Biern S. G., Gong J.-O., 2020, JCAP, 11, 064
- Gualdi D., Gil-Marín H., Manera M., Joachimi B., Lahav O., 2019, Mon. Not. Roy. Astron. Soc., 484, L29
- Hall A., Bonvin C., 2017, Phys. Rev. D, 95, 043530
- Hall A., Bonvin C., Challinor A., 2013, Phys. Rev. D, 87, 064026
- Irsič V., Di Dio E., Viel M., 2016, JCAP, 02, 051
- Jalilvand M., Majerotto E., Durrer R., Kunz M., 2019, JCAP, 01, 020
- Jalilvand M., Majerotto E., Bonvin C., Lacasa F., Kunz M., Naidoo W., Moodley K., 2020, Phys. Rev. Lett., 124, 031101
- Jeong D., Komatsu E., 2009, Astrophys. J., 703, 1230
- Jeong D., Schmidt F., 2020, Phys. Rev. D, 102, 023530
- Jeong D., Schmidt F., Hirata C. M., 2012, Physical Review D, 85
- Jolicoeur S., Umeh O., Maartens R., Clarkson C., 2017, JCAP, 09, 040
- Jolicoeur S., Umeh O., Maartens R., Clarkson C., 2018, JCAP, 03, 036
- Jolicoeur S., Allahyari A., Clarkson C., Larena J., Umeh O., Maartens R., 2019, JCAP, 03, 004
- Jolicoeur S., Maartens R., De Weerd E. M., Umeh O., Clarkson C., Camera S., 2020
- Kaiser N., 1987, Mon. Not. Roy. Astron. Soc., 227, 1
- Karagiannis D., Lazanu A., Liguori M., Raccanelli A., Bartolo N., Verde L., 2018, Monthly Notices of the Royal Astronomical Society, 478, 1341–1376
- Karagiannis D., Fonseca J., Maartens R., Camera S., 2020a
- Karagiannis D., Slosar A., Liguori M., 2020b, JCAP, 11, 052
- Kehagias A., Moradinezhad Dizgah A., Noreña J., Perrier H., Riotto A., 2015, JCAP, 08, 018
- Kitayama T., Suto Y., 1996, Astrophys. J., 469, 480
- Koyama K., Umeh O., Maartens R., Bertacca D., 2018, JCAP, 07, 050
- Lepori F., Di Dio E., Villa E., Viel M., 2018, JCAP, 05, 043

Bibliography

- Lepori F., Iršič V., Di Dio E., Viel M., 2020, JCAP, 04, 006
- Lewis A., Challinor A., Lasenby A., 2000, *Astrophys. J.*, 538, 473
- Liguori M., Sefusatti E., Fergusson J. R., Shellard E. P. S., 2010, *Adv. Astron.*, 2010, 980523
- Lopez-Honorez L., Mena O., Rigolin S., 2012, *Phys. Rev. D*, 85, 023511
- Lorenz C. S., Alonso D., Ferreira P. G., 2018, *Phys. Rev. D*, 97, 023537
- Maartens R., Jolicoeur S., Umeh O., De Weerd E. M., Clarkson C., Camera S., 2020, JCAP, 2020, 065–065
- Majumdar S., Pritchard J. R., Mondal R., Watkinson C. A., Bharadwaj S., Mellema G., 2018, *Mon. Not. Roy. Astron. Soc.*, 476, 4007
- Matarrese S., Verde L., 2008, *Astrophys. J. Lett.*, 677, L77
- Matarrese S., Pilo L., Rollo R., 2021, JCAP, 01, 062
- Matsubara T., 2000, *Astrophys. J.*, 535, 1
- McDonald P., 2009, JCAP, 11, 026
- Modi C., White M., Slosar A., Castorina E., 2019, JCAP, 11, 023
- Montanari F., Camera S., 2021, JCAP, 01, 002
- Moradinezhad Dizgah A., Biagetti M., Sefusatti E., Desjacques V., Noreña J., 2020
- Nan Y., Yamamoto K., Hikage C., 2018, JCAP, 07, 038
- Obuljen A., Castorina E., Villaescusa-Navarro F., Viel M., 2018, JCAP, 05, 004
- Oddo A., Sefusatti E., Porciani C., Monaco P., Sánchez A. G., 2020, JCAP, 03, 056
- Okoli C., Scrimgeour M. I., Afshordi N., Hudson M. J., 2017, *Mon. Not. Roy. Astron. Soc.*, 468, 2164
- Pan H., Obreschkow D., Howlett C., Lagos C. d. P., Elahi P. J., Baugh C., Gonzalez-Perez V., 2019
- Philcox O. H. E., Eisenstein D. J., 2020, *Mon. Not. Roy. Astron. Soc.*, 492, 1214
- Pober J. C., 2015, *Mon. Not. Roy. Astron. Soc.*, 447, 1705
- Pober J. C., et al., 2014, *Astrophys. J.*, 782, 66
- Pozzetti L., et al., 2016, *Astron. Astrophys.*, 590, A3
- Raccanelli A., Bertacca D., Doré O., Maartens R., 2014, JCAP, 08, 022
- Raccanelli A., Montanari F., Bertacca D., Doré O., Durrer R., 2016, JCAP, 05, 009

Bibliography

- Raccanelli A., Bertacca D., Jeong D., Neyrinck M. C., Szalay A. S., 2018, Phys. Dark Univ., 19, 109
- Santos M. G., et al., 2015, PoS, AASKA14, 019
- Santos M. G., et al., 2017, in MeerKAT Science: On the Pathway to the SKA. ([arXiv:1709.06099](https://arxiv.org/abs/1709.06099))
- Sargent W. L. W., Turner E. L., 1977, The Astrophysical Journal, 212, L3
- Sarkar D., Bharadwaj S., 2019, Mon. Not. Roy. Astron. Soc., 487, 5666
- Sarkar D., Majumdar S., Bharadwaj S., 2019, Mon. Not. Roy. Astron. Soc., 490, 2880
- Schmit C. J., Heavens A. F., Pritchard J. R., 2019, Mon. Not. Roy. Astron. Soc., 483, 4259
- Scoccimarro R., 2015, Phys. Rev. D, 92, 083532
- Scoccimarro R., Couchman H. M. P., Frieman J. A., 1999, The Astrophysical Journal, 517, 531–540
- Scoccimarro R., Sefusatti E., Zaldarriaga M., 2004, Phys. Rev. D, 69, 103513
- Sefusatti E., Komatsu E., 2007, Phys. Rev. D, 76, 083004
- Sefusatti E., Crocce M., Pueblas S., Scoccimarro R., 2006, Phys. Rev. D, 74, 023522
- Shaw J. R., Sigurdson K., Sitwell M., Stebbins A., Pen U.-L., 2015, Phys. Rev. D, 91, 083514
- Sheth R. K., Tormen G., 1999, Mon. Not. Roy. Astron. Soc., 308, 119
- Sheth R. K., Tormen G., 2002, Mon. Not. Roy. Astron. Soc., 329, 61
- Sheth R. K., Mo H. J., Tormen G., 2001, Mon. Not. Roy. Astron. Soc., 323, 1
- Shirasaki M., Sugiyama N. S., Takahashi R., Kitaura F.-S., 2021, Phys. Rev. D, 103, 023506
- Slepian Z., et al., 2017, Mon. Not. Roy. Astron. Soc., 469, 1738
- Slosar A., et al., 2019
- Smith R. E., et al., 2003, Mon. Not. Roy. Astron. Soc., 341, 1311
- Sugiyama N. S., Saito S., Beutler F., Seo H.-J., 2018, Monthly Notices of the Royal Astronomical Society, 484, 364–384
- Sugiyama N. S., Saito S., Beutler F., Seo H.-J., 2020, Mon. Not. Roy. Astron. Soc., 497, 1684
- Tansella V., Bonvin C., Durrer R., Ghosh B., Sellentin E., 2018, JCAP, 03, 019

Bibliography

- Tellarini M., Ross A. J., Tasinato G., Wands D., 2015, *JCAP*, 07, 004
- Tellarini M., Ross A. J., Tasinato G., Wands D., 2016, *Journal of Cosmology and Astroparticle Physics*, 2016, 014–014
- Tram T., Fidler C., Crittenden R., Koyama K., Pettinari G. W., Wands D., 2016, *JCAP*, 05, 058
- Umeh O., 2017, *JCAP*, 06, 005
- Umeh O., Koyama K., 2019, *JCAP*, 12, 048
- Umeh O., Maartens R., Santos M., 2016, *JCAP*, 03, 061
- Umeh O., Jolicoeur S., Maartens R., Clarkson C., 2017, *JCAP*, 03, 034
- Umeh O., Koyama K., Maartens R., Schmidt F., Clarkson C., 2019, *JCAP*, 1905, 020
- Umeh O., Koyama K., Crittenden R., 2020
- Verde L., Heavens A. F., Matarrese S., Moscardini L., 1998, *Monthly Notices of the Royal Astronomical Society*, 300, 747–756
- Verde L., Wang L.-M., Heavens A., Kamionkowski M., 2000, *Mon. Not. Roy. Astron. Soc.*, 313, L141
- Villa E., Rampf C., 2016, *JCAP*, 1601, 030
- Villaescusa-Navarro F., et al., 2018, *Astrophys. J.*, 866, 135
- Villumsen J. V., 1995
- Wang M. S., Beutler F., Bacon D., 2020, *Mon. Not. Roy. Astron. Soc.*, 499, 2598
- Watkinson C. A., Majumdar S., Pritchard J. R., Mondal R., 2017, *Mon. Not. Roy. Astron. Soc.*, 472, 2436
- Witzemann A., Alonso D., Fonseca J., Santos M. G., 2019, *Mon. Not. Roy. Astron. Soc.*, 485, 5519
- Wolz L., et al., 2015, PoS, AASKA14, 035
- Yankelevich V., Porciani C., 2019, *Mon. Not. Roy. Astron. Soc.*, 483, 2078
- Yoo J., 2010, *Phys. Rev. D*, 82, 083508
- Yoo J., Zaldarriaga M., 2014, *Phys. Rev. D*, 90, 023513
- Yoo J., Fitzpatrick A. L., Zaldarriaga M., 2009, *Phys. Rev. D*, 80, 083514
- Yoo J., Hamaus N., Seljak U., Zaldarriaga M., 2012, *Phys. Rev. D*, 86, 063514
- Zhu H.-M., Pen U.-L., Yu Y., Chen X., 2018, *Phys. Rev. D*, 98, 043511

Bibliography

de Putter R., Doré O., Green D., 2015, JCAP, 10, 024

de Weerd E. M., Clarkson C., Jolicoeur S., Maartens R., Umeh O., 2020, JCAP, 05, 018

List of Figures

3.1.	Overview of the relevant vectors and angles for the Fourier-space bispectrum.	27
3.2.	The absolute value of the bispectrum dipole at $z = 1$ as a function of triangle size, in the flattened (Left, $\theta = 2^\circ$, for intensity mapping bias) and squeezed (Right, $\theta = 178^\circ$, for Euclid-like bias) configurations, with k_3 as the horizontal axis. Red is the $m = 0$ part and blue is $m = \pm 1$. Dashed (and dotted) lines show up to the $\mathcal{O}(\mathcal{H}/k)$ terms considered analytically here, while solid lines indicate larger-scale contributions. For reference the monopole is in black, with the dotted line the Newtonian part. (The zero-crossing in the monopole for the squeezed case is a result of the tidal bias.)	30
3.3.	(Left) We show the dipoles as a function of θ with a bias appropriate for a Euclid-like survey, for $k_1 = k_2 = 0.01 \text{ Mpc}^{-1}$. The left of the plot corresponds to the flattened case where the $m = 0$ (red) dipole reaches 10% of the monopole. (Right) We show the IM signal with $k_1 = k_2 = 0.1 \text{ Mpc}^{-1}$ versus the long mode k_3 . Except for very long modes $\theta \approx \pi$, our $\mathcal{O}(\mathcal{H}/k)$ truncation is a very good approximation in these examples.	31
4.1.	Relevant vectors and angles for the Fourier bispectrum.	36
4.2.	Effect on total relativistic SNR of changing number of φ and μ_1 bins.	42
4.3.	Clustering bias parameters (<i>left</i>), comoving volume and number density (<i>middle</i>) and RSD damping parameter (<i>right</i>). Points are the data from Table 1 in Yankelevich & Porciani (2019).	43
4.4.	Magnification and evolution bias (4.45), (4.46).	45
4.5.	Relativistic SNR per z -bin (<i>left</i>) and cumulative (<i>right</i>) for a Stage IV $H\alpha$ survey.	47
4.6.	Effect of changing k_{\max} on SNR per bin (<i>left</i>) and cumulative SNR (<i>right</i>).	48

List of Figures

4.7.	Effect of changing \mathcal{Q} and b_e on relativistic cumulative SNR.	49
4.8.	Effect of changing k_{\min} on total relativistic SNR.	50
4.9.	As in Fig. 4.5, but showing the effect of omitting the second-order relativistic contribution (4.48) to the bispectrum (dot-dashed curves).	51
4.10.	Marginal errors (cumulative) on the relativistic contribution, growth index and clustering amplitude, using the full bispectrum.	52
4.11.	HI clustering and evolution bias parameters (left) and background temperature (right).	57
4.12.	Schematic of important scales in the k_{\parallel}, k_{\perp} -plane at fixed z . Shading indicates the included region for SD mode (light) and IF mode (dark).	63
4.13.	T_{sys} for the different frequency bands of MeerKAT and SKA1 (from Table 4.4).	67
4.14.	Minimum wavenumbers for the surveys, where k is subject to (4.8) (SD) or (4.92) (IF).	68
4.15.	Physical baseline density models for HIRAX (left) and PUMA (right).	69
4.16.	Noise power spectra of the SD-mode surveys (at $z = 0.4$ for low- z_{\max} bands and $z = 1$ for high- z_{\max} bands) and IF-mode surveys (HIRAX at $z = 1$, PUMA at $z = 2$).	69
4.17.	SNR of the relativistic bispectrum per z -bin (<i>left</i>) and cumulative (<i>right</i>) for SD-mode surveys.	70
4.18.	Cumulative SNR of the relativistic bispectrum for IF-mode surveys.	70
6.1.	Overview of the relevant vectors and angles for the Fourier-space bispectrum.	82
6.2.	Overview of all non-zero multipoles for the bispectrum, which includes ℓ from 0 to 8, and m from $-\ell$ to ℓ ; the pattern here is the same for $m < 0$, so only $m \geq 0$ are displayed. Denoted in the figure are whether components are Newtonian+GR or GR only, triangle shapes indicating whether given components are non-vanishing in flattened (co-linear) or equilateral limits. Note how the dipole is unique in having the equilateral case vanish for every value of m . Also given is which powers of \mathcal{H}/k appear in each of the multipoles.	94
6.3.	Normalised total power for squeezed configuration for Euclid-like (left) and SKA HI intensity mapping (right) surveys. Long mode k_3 is plotted along the x -axis.	100

List of Figures

6.4.	Total power for flattened configuration for Euclid-like (left) and SKA HI intensity mapping (right) surveys. Long mode k_3 is plotted along the x -axis.	100
6.5.	Total power for equilateral configuration for Euclid-like (left) and SKA HI intensity mapping (right) surveys. Since the dipole vanishes in this limit, the $\ell = 1$ line is absent.	101
6.6.	A selection of multipoles of the galaxy bispectrum, $B_{\ell m}$, with $\ell = 0 \dots 3$ and $m = 0 \dots \ell$ as indicated in the figure. Bias model used is that for $H\alpha$ /Euclid-like survey. k_1 is kept fixed, the value of which is given alongside the plot, and the x and y axes vary respectively k_3 and k_2 with respect to the fixed k_1 . The upper left corner of the wedge shape is the squeezed limit, the upper right corner is the equilateral configuration, and the lower corner is the co-linear configuration. Note the difference in range of the colour bars.	102
6.7.	Selected multipoles of the galaxy bispectrum, similar to figure 6.6, but with the bias model appropriate for intensity mapping. The value of fixed k_1 is indicated on the figures. The upper left corner of a wedge shape is the squeezed limit, the upper right corner is the equilateral configuration, and the lower corner is the co-linear configuration.	103
6.8.	Results for the reduced bispectrum $Q_{\ell m}$, where $\ell = 0 \dots 3$ and negative m not shown. The multipoles ℓ, m are indicated on the figure, as well as the value of k_1 which is kept fixed. The colourbar and different colours denote the ratio of k_2/k_1 , where the slightly thicker purple line is the isosceles triangle, which diverges as $\theta \rightarrow \pi$ since there $k_3 \rightarrow 0$	104
6.9.	Total power contained in the relativistic bispectrum normalised by the Newtonian monopole as a function of redshift z ranging from 0.1 to 2. The three panels are the equilateral configuration (left, with $\ell = 1$ vanishing), squeezed (middle) and co-linear flattened configuration (right). Solid lines for $k = 0.1 \text{ Mpc}^{-1}$, and dash-dotted for $k = 0.01 \text{ Mpc}^{-1}$	105
7.1.	$\mathcal{M}^{-1} = \varphi_p/\delta_C^{(1)}$ at $z = 1$	116

List of Figures

- 7.2. Monopole of the reduced bispectrum for a Stage IV H α survey at $z = 1$, for various f_{NL} , with $k_1 = k_2 = 0.1 h/\text{Mpc}$. Shading indicates the 1σ uncertainty (neglecting shot noise) for the $f_{\text{NL}} = 0$ case (solid blue curve). *Left:* Comparing the full relativistic monopole to the Newtonian approximation (dash-dot curves). *Right:* Comparing the full relativistic monopole to the monopole without the GR correction to second-order galaxy bias, (7.32) (dashed curves). 130
- 7.3. Monopole of reduced bispectrum for isosceles triangles, as in Figure 7.2. *Left:* As a function of f_{NL} , for various values of $\theta \equiv \theta_{12}$, where $\theta = \pi$ is the squeezed limit. Dashed curves indicate negative values. *Right:* 2D colour map as a function of f_{NL} and θ/π 131
- 7.4. First few nonzero multipoles for fixed triangle shape as a function of k_3 , with $f_{\text{NL}} = 10$ (solid) and $f_{\text{NL}} = 0$ (dashed). *Left:* Equilateral configuration, $k_1 = k_2 = k_3$. *Middle:* Flattened configuration, $k_1 = k_2 \approx k_3/2$, with $\theta_{12} = 2^\circ$. *Right:* Squeezed configuration with $\theta_{12} = 178^\circ$ and $k_1 = k_2 = k_3/(2 \sin \theta_{12}) \approx 14 k_3$ 132

List of Tables

4.1.	Stage IV $H\alpha$ spectroscopic survey parameters.	46
4.2.	HI intensity mapping survey specifications. (For *, see Appendix stuff.)	65
4.3.	Parameters in (4.100) (from Ansari et al. (2018)).	65
4.4.	System temperatures for MeerKAT and SKA1-MID, used in Figure 4.4 (from Fonseca et al. (2019))	66
4.5.	Total SNR for single-dish mode surveys.	67
4.6.	Total SNR for interferometer-mode surveys.	69
4.7.	Total SNR for single-dish mode surveys with $k_{\parallel\text{fg}} = 0.005 \text{ } h\text{Mpc}^{-1}$. . .	71
4.8.	Total SNR for interferometer-mode surveys with $k_{\parallel\text{fg}} = 0.005 \text{ } h\text{Mpc}^{-1}$. . .	71
B.1.	Individual terms in the observed $\Delta_g^{(2)}(a, \mathbf{x})$ [see (7.56), (7.57)] for $f_{\text{NL}} = 0$ are shown in column 1. The related β_I functions in (7.72) are listed in column 2. The Fourier-space kernels \mathcal{F} corresponding to column 1, given by $\int d\mathbf{k}' \mathcal{F}(\mathbf{k}', \mathbf{k} - \mathbf{k}') \delta_T(\mathbf{k}') \delta_T(\mathbf{k} - \mathbf{k}') / (2\pi)^3$, are shown in column 3. Column 4 gives the coefficients of the terms in $\Delta_g^{(2)}$ (column 1). The line-of-sight derivative is $\partial_{\parallel} = \mathbf{n} \cdot \nabla$ and $\Phi = \Psi$. The superscript (1) on first-order quantities has been omitted and N denotes Newtonian. This table updates the one in Jolicoeur et al. (2017).	141
C.1.	The $f_{\text{NL}} \neq 0$ terms from relativistic projection effects [see (7.74)]. . .	145